Aix*Marseille université
Socialement engagée

NNT: 2024AIXM0414

THÈSE DE DOCTORAT

Soutenue à Aix-Marseille Université
le 29 Novembre 2024 par

Yann Munschy

Physique cinétique et gyrocinétique de l'interaction plasma-paroi dans les tokamaks

Kinetic and Gyrokinetic physics of plasma-wall interaction in tokamaks

Discipline
Physique et Sciences de la Matière

Spécialité
Énergie, Rayonnement et Plasma

École doctorale
ED 352 Physique et Sciences de la Matière

Laboratoire/Partenaires de recherche
CEA-Cadarache - Institut de Recherche sur la Fusion par confinement Magnétique, Saint-Paul-lez-Durance, France

Composition du jury

Tobias GÖRLER Docteur IPP Garching	Rapporteur
Giovanni MANFREDI Directeur de Recherche IPCMS	Rapporteur
David HUGHES Professeur University of Leeds	Examinateur
Claudia NEGULESCU Professeure IMT	Présidente du Jury
Patrick TAMAIN Docteur CEA/IRFM	Examinateur
Guilhem DIF-PRADALIER Directeur de Recherche CEA/IRFM	Directeur de thèse
Yanick SARAZIN Directeur de Recherche CEA/IRFM	Codirecteur

cea irfm

Affidavit

I, undersigned, Yann Munschy, hereby declare that the work presented in this manuscript is my own work, carried out under the scientific supervision of Mr Yanick Sarazin and Guilhem Dif-Pradalier, in accordance with the principles of honesty, integrity and responsibility inherent to the research mission. The research work and the writing of this manuscript have been carried out in compliance with both the french national charter for Research Integrity and the Aix-Marseille University charter on the fight against plagiarism.
This work has not been submitted previously either in this country or in another country in the same or in a similar version to any other examination body.

Aix-en-Provence, 12th December 2024

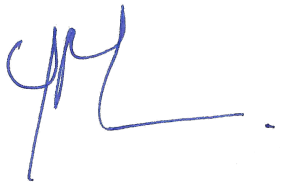

This work is licensed under Creative Commons Attribution NonCommercial - NoDerivatives 4.0 International Public License

Publications and conferences

List of publications produced as part of the thesis project:

- Y. Munschy, E. Bourne, G. Dif-Pradalier, P. Donnel, P. Ghendrih, V. Grandgirard, and Y. Sarazin 2024 *Nuclear Fusion* 64 056027;
- Y. Munschy, E. Bourne, G. Dif-Pradalier, P. Donnel, P. Ghendrih, V. Grandgirard, and Y. Sarazin 2024 *Nuclear Fusion* 64 046013;
- E. Bourne, Y. Munschy, V. Grandgirard, M. Mehrenberger, and P. Ghendrih 2023 *Journal of Computational Physics* 488 112229;
- G. Dif-Pradalier, P. Ghendrih, Y. Sarazin, E. Caschera, F. Clairet, Y. Camenen, P. Donnel, X. Garbet, V. Grandgirard, Y. Munschy, L. Vermare, and F. Widmer 2022 *Communications Physics* 5;

Participation in conferences and summer schools during the thesis period:

- Y. Munschy, G. Dif-Pradalier, Y. Sarazin, P. Donnel, E. Bourne, X. Garbet, P. Ghendrih, L. De Gianni, V. Grandgirard, A. Kara, K. Obrejan and O. Panico 50th European physical society Conference on Plasma Physics, *A penalized model for plasma-wall interaction valid in the gyrokinetic framework* (Poster), July 2024, Salamanca, Spain;
- Y. Munschy, E. Bourne, G. Dif-Pradalier, P. Donnel, P. Ghendrih, V. Grandgirard, Y. Sarazin and the Gysela team International conference on the theory and applications of the Vlasov equation, *Plasma-wall interaction: comparison between kinetic simulations and fluid theory* (Oral), January 2024, Florence, Italy
- Y. Munschy, E. Bourne, G. Dif-Pradalier, P. Donnel, P. Ghendrih, V. Grandgirard, Y. Sarazin and the Gysela team 20th European Fusion Theory Conference, *Vlasov-Poisson system for plasma-wall interaction: simulations, fluid theory, and gyrokinetic implementation* (Invited), October 2023, Padua, Italy;
- Y. Munschy, E. Bourne, G. Dif-Pradalier, Y. Sarazin, P. Ghendrih, V. Grandgirard, P. Donnel and the Gysela team CIRM Workshop Mathematical Justification for the Kinetic and Fluid Equations of Plasmas and Self-Gravitating Systems, *Plasma-wall interaction: comparison between kinetic simulations and fluid theory* (Invited), July 2023, Marseille, France;
- Theory, Simulation, Validation, Verification - Plasma Particle/Heat Exhaust Progress workshop, May 2022, June 2023 and October 2024, Garching, Germany.

Abstract

The interaction between a tokamak plasma and its material boundary affects edge plasma turbulence and thus influences the quality of confinement. Extending gyrokinetic simulations of transport and turbulence up to the very edge of the plasma is a necessary requirement to achieve reliable predictions (i) of the overall plasma confinement and (ii) of possible routes towards improved confinement regimes. However, it is still ongoing work. A critical point is to correctly describe within the gyrokinetic framework the physics of plasma-wall interaction. The present work aims at improving the edge description in the gyrokinetic framework by proposing a model for plasma-wall interaction that is compatible with the gyrokinetic theory.

Prior to proposing such a model, the interaction between charged particles and a solid wall is studied in the two-dimensional—1D in space, 1D in velocity space—framework of the Voice code. The description of the wall is based on immersed boundary conditions, also called penalization technique. Voice shows that penalization allows for the recovery of key aspects of plasma-wall interaction physics: a positively charged region—reminiscent of a Debye sheath—develops at the plasma boundary, which ensures quasineutrality within the plasma. The physics at play within the sheath results in distribution functions departing from Maxwellians. Studying the system using the hierarchy of fluid equations shows that (i) the Bohm criterion is invalid in the kinetic framework, and (ii) the speed of sound used to express this criterion critically depends on the closure of the fluid hierarchy. This last point could bear consequences for fluid codes that use the Bohm criterion as a boundary condition on plasma-facing units. So as to prepare for the future extension of the Gysela code to include plasma-neutral interaction, we describe a so-called *pressure-diffusion* fluid model for neutrals. We couple this neutral fluid model to the kinetic plasma description of Voice, and illustrate the effect of the neutral dynamics on the plasma.

Based on this preliminary study and by reviewing already-existing gyrokinetic plasma-wall interaction models, we propose a sheath model that is compatible with the global framework of the gyrokinetic code Gysela. The model ensures quasineutrality in the plasma withouth solving the characteristic time and spatial scales of the sheath, by matching the electron and ion gyrocenter fluxes on spatial average over the entire surface of the plasma material boundary. The model uses penalization so that the material boundary is immersed within the simulation domain. Performing global simulations shows that the absorption of ions within the material boundary along with the reflection of slow electrons on the boundary surface works as expected. We however observe a mismatch between the electron and ion fluxes at the material boundary. It leads to the buildup of a negative charge in front of the boundary, effectively breaking quasineutrality on timescales too short to study turbulence. We describe possible ways for closing this mismatch and discuss its possible origin.

Résumé

L'interaction entre un plasma et la paroi qui l'entoure influence les niveaux de turbulence dans le bord. L'extension vers des simulations gyrocinétiques décrivant correctement cette région est en cours. Le point critique est de décrire correctement dans le cadre gyrocinétique l'interaction entre le plasma et le mur. Cette thèse est dédiée à l'amélioration de la description du bord dans le cadre gyrocinétique.
Avant de proposer un modèle d'interaction plasma-paroi valide dans le cadre gyrocinétique, cette interaction est étudiée avec le code à deux dimensions—1D en espace, 1D en vitesse—Voice. La description du mur se fait grâce à la technique dite de "pénalisation". On montre que celle-ci permet de reproduire les aspects essentiels de la physique d'interaction plasma-paroi. Une région positivement chargée apparait à l'interface plasma-mur, qui assure la quasineutralité du plasma. La physique cinétique de cette gaine de Debye se traduit par des fonctions de distribution non-Maxwelliennes. En étudiant le système à l'aide des équations fluides, on montre que (i) le critère de Bohm est inopérant dans le cadre cinétique, et (ii) la vitesse du son, nécéssaire pour exprimer ce critère dépend de la fermeture du modèle fluide. Cette dernière observation a des conséquences pour les codes fluides qui imposent le critère de Bohm au niveau des composants face au plasma. Afin de préparer l'extension du code gyrocinétique Gysela à la prise en compte de l'interaction entre particules chargées et neutres, on décrit un modèle fluide de neutres appelé modèle *pressure-diffusion*. On décrit le couplage entre ce modèle fluide de neutres et le modèle cinétique du plasma, et on illustre l'impact qualitatif de la dynamique des neutres sur les propriétés du plasma.
Sur la base de cette étude préliminaire, et en s'appuyant sur des modèles préexistants de gaine gyrocinétique, un modèle sous-maille d'interaction plasma-paroi est détaillé. Celui-ci est compatible avec le cadre global du code gyrocinétique Gysela, et assure la quasineutralité du plasma en ajustant les flux de gyrocentres électroniques et ioniques en moyenne spatiale sur la surface du limiteur. Le limiteur est immergé dans le domaine de simulation. Des simulations produites par le code Gysela montrent que l'absorption des ions et la réflexion des électrons lents sur la surface du limiteur fonctionnent comme attendu. Un écart entre les flux ioniques et électroniques sur la surface du limiteurest en revanche observé. Cet écart conduit à l'accumulation de charges négatives dans la région proche du limiteur, ce qui brise la quasineutralité du plasma sur des temps trop courts pour étudier la turbulence. Les origines de cet écart sont discutées.

Résumé étendu

Cette thèse est dédiée à l'amélioration de la description de la region de *bord* dans les codes gyrocinétiques qui décrivent la dynamique turbulente des plasmas de tokamak. Le *bord* désigne ci-après la région qui s'étend depuis la partie externe du cœur, jusqu'à la séparatrice. Le *cœur* désigne la région confinée du plasma qui s'étend en amont de la séparatrice (dernière surface magnétique fermée), là où les gradients de densité, de température et de potentiel électrique sont généralement forts. La *Scrape-Off Layer* (SOL) comprend au contraire la région où les lignes de champ magnétique sont ouvertes et interceptent des éléments de paroi. Les simulations gyrocinétiques d'un plasma de tokamak sont particulièrement intéressantes pour décrire la turbulence et le transport qui existent dans un tel plasma. L'intensité de la turbulence détermine en effect la qualité du confinement du réacteur, et donc ses performances. Bien que des simulations gyrocinétiques de plasmas de cœur aient été réalisées avec succès lors des vingt dernières années, inclure les régions de cœur, bord et Scrape-Off Layer dans une même simulation reste à l'heure actuelle un défi de taille qui fait l'objet de nombreux efforts au sein de la communauté de fusion. Dans les codes gyrocinétiques, outre le coût numérique, la difficulté physique principale provient de la description de la physique à l'œuvre dans la Scrape-Off Layer, d'une part du fait de l'interaction entre plasma et éléments de parois qui se trouvent à l'extrémité des lignes de champ dans cette région, et d'autre part du fait de l'interaction particules chargées qui composent le plasma et molécules neutres—recyclées depuis le mur ou injectées de manière contrôlée lors de la décharge. La Scrape-Off Layer est ainsi le siège d'une physique riche qui peut influencer les niveaux de turbulence dans la région du bord. Cette observation est d'autant plus vraie que l'accès à des modes de confinement améliorés—tels que le *mode H*—est influencé par les conditions du plasma près de la séparatrice. À titre d'exemple, on montre dans la section (5.1) qu'en régime *sheath-limited*[1] le champ électrique radial peut présenter un changement de signe près de la séparatrice, passant de négatif dans le cœur—du fait de l'équilibre radial des forces du cœur—à positif dans la Scrape-Off Layer—du fait de l'interaction plasma-paroi. Ce changement de signe se traduit par un cisaillement de la vitesse de dérive $E \times B$ projetée dans la direction poloïdale, ce qui réduit l'intensité du transport radial grâce notamment à la décorrélation radiale des cellules de convection turbulentes.

Pour rendre compte de la physique inhérente à la transition entre lignes de champ fermées et ouvertes, il est donc nécessaire d'inclure une description de la physique de l'interaction entre un plasma et une surface solide. Cette description doit être compatible avec les hypothèses du cadre gyrocinétique. Une des difficultés tient au fait que la physique de l'interaction plasma-paroi se traduit—en régime *sheath limited*—par

[1] voir la section (1.3) pour la définition d'un tel régime.

l'apparition d'une couche limite, la *gaine*, qui est positivement chargée et qui s'étend sur une épaisseur de quelques longueurs de Debye à l'interface entre le plasma et la surface solide qui le délimite. Le cadre gyrocinétique ne permet pas de rendre compte de cette physique en la décrivant directement. En effet, cette théorie—qui suppose par construction que la dynamique étudiée est à grande échelle (en temps et en espace) par rapport au mouvement cyclotronique—ne peut pas décrire des phénomènes qui se développent à des échelles aussi petites, et qui ne respectent pas une condition de quasi-neutralité imposée au plasma qu'elle décrit. Inclure un modèle d'interaction plasma-paroi au sein de la théorie gyrocinétique doit donc se faire *via* un modèle *sous-maille*, c'est-à-dire qui ne résout pas les échelles de temps et d'espaces auxquelles la physique de l'interaction plasma-paroi se développe. La présente thèse se propose de décrire un tel modèle. Le modèle proposé est compatible avec la théorie gyrocinétique, et s'appuie sur la technique des *frontières immergées*—décrite ci-dessous—pour modéliser les composants face au plasma. Avant de proposer un tel modèle, un code cinétique qui décrit un espace des phases à deux dimensions est utilisé pour montrer que la technique des frontières immergées décrit de façon convenable la physique de l'interaction entre un plasma et une surface solide. En plus d'aider au développement du modèle gyrocinétique d'interaction plasma-paroi, cette étude préliminaire se révèle riche en enseignements, en particulier en ce qui concerne la validité du *critère de Bohm* et des conditions aux limites imposées au niveau des composants face au plasma dans les codes fluides[2]. Après avoir décrit le modèle sous-maille d'interaction plasma-paroi, une description de l'interaction entre plasma et particules neutres est présentée. Celle-ci est particulièrement importante pour rendre compte des sources de particules et d'un état turbulent stationnaire. Ce dernier modèle est compatible avec une description gyrocinétique du bord, et sera prochainement ajouté au code gyrocinétique GYSELA.

L'interaction plasma-paroi

Lorsqu'un plasma est mis en contact avec une surface solide—que l'on appelle *le mur* dans ce qui suit—les différences de densité et température entre le plasma, chaud et raréfié, et le mur, froid et dense en comparaison, provoque la recombinaison de toute particule chargée (ion ou électron) provenant du plasma qui entre en contact avec le mur. Ce dernier agit donc comme un puits de particules chargées. Du fait de la différence d'inertie entre ions et électrons, ces derniers, plus légers, ont tendance à entrer en contact avec le mur plus facilement que leurs homologues positivement chargés. Une couche limite—la *gaine de Debye*—apparaît alors à l'interface entre le plasma et le mur. La gaine s'étend sur quelques longueurs de Debye. Elle est positivement chargée. Cette charge se traduit par une chute du potentiel électrique dans la gaine, ce qui a deux conséquences. Premièrement, les ions sont accélérés vers le mur par cette chute de

[2]Le critère de Bohm stipule que le flot d'ions doit être supersonique à l'entrée de la gaine, cf. section (3.2). Les *codes fluides* décrivent le plasma au moyen de moments de la fonction de distribution, tels que la densité, le flux de particules, la température, etc. La description fluide d'un plasma est abordée dans la section (3.1)

potentiel. Cette accélération est délétère pour les éléments de paroi car elle augmente leur sputtering (pulvérisation) physique. Deuxièmement, une fraction des électrons les plus lents, dirigés vers le mur, sont réfléchis vers le plasma lors de leur trajectoire dans la gaine. Les électrons les plus rapides surmontent la chute de potentiel de gaine et sont absorbés dans le mur. Cette réflexion sélective des électrons s'ajuste de manière à ce que le plasma ne perde pas de charge et reste quasi-neutre sur des échelles spatiales larges comparées à la longueur de Debye et sur des temps longs comparés à l'inverse de la fréquence plasma électronique. Lorsque la ligne de champ magnétique intercepte le mur avec une incidence non-normale, une couche limite additionnelle apparaît, la *pré-gaine magnétique*. Le rôle de la pré-gaine magnétique est analogue à celui de la gaine de Debye, c'est-à-dire qu'elle assure la quasi-neutralité du plasma. Comme décrit ci-dessous, c'est bien cette propriété de quasi-neutralité que l'on veut retrouver dans le cadre gyrocinétique. Lors de la description d'un modèle d'interaction plasma-paroi valable dans ce cadre, on désignera donc par *gaine* la couche limite composée de la gaine de Debye et de la prégaine magnétique, qui assure la quasi-neutralité du plasma.

Simulations cinétiques avec frontières immergées

Afin de proposer ce modèle d'interaction plasma-paroi sous-maille valide dans le cadre gyrocinétique, la physique de gaine est d'abord étudiée au moyen du code cinétique à deux dimensions—une d'espace, et une de vitesse—VOICE. Ce code décrit la dynamique cinétique d'un plasma le long d'une ligne de champ magnétique. La courbure du champ magnétique, ainsi que toute interaction avec des lignes de champ voisines, sont négligées. Le plasma est en contact avec un mur à chaque extrémité de la ligne de champ. Une source de particule, qui modélise le transport transverse à la ligne de champ, est présente au centre du domaine de simulation. La description du plasma est opérée en résolvant un système Vlasov-Poisson afin de décrire l'évolution temporelle des fonctions de distribution des ions et des électrons. Un opérateur de collision est inclus à l'équation de Vlasov. Cet opérateur rend compte d'interaction Coulombiennes entre deux particules qui n'ont pas nécessairement la même charge. La particularité du code réside dans la description du mur. Celui-ci est immergé dans le domaine de simulation. C'est la technique dite de *pénalisation*, aussi appelée technique des *frontières immergées*. La pénalisation du mur est effectuée par un opérateur de type Bhatnagar-Gross-Krook qui relaxe les fonctions de distribution des ions et électrons vers une fonction cible caractérisée par une densité beaucoup plus faible que celle du plasma ambiant. Du point de vue du plasma, le mur agit alors comme un puits de particules, de quantité de mouvement et d'énergie. En outre, le code VOICE est utilisé comme un banc de test pour maillages non équidistants—particulièrement bien adaptés pour résoudre dans un même code la gaine non-neutre et le plasma quasi-neutre caractérisés pas des échelles de temps et d'espace très disparates—avant l'implémentation de ceux-ci dans le code GYSELA. L'utilisation de maillages non-équidistants montre qu'il est possible de réduire drastiquement le besoin mémoire des simulations par rapport à

des maillages équidistants.
Afin d'évaluer la pertinence de la pénalisation pour décrire la physique de la gaine de Debye, deux opérateurs de pénalisation sont comparés. Avec le premier opérateur, aucune source ou puits de particules chargées ne peut exister dans la région du mur. Le mur agit alors comme un espace de recombinaison, où un ion ou électron ne peut être absorbé que si une particule de charge opposée est absorbée au même moment. C'est le modèle de mur *isolant*, ou *insulating wall*. Le second opérateur autorise l'existence de telles sources de charges dans le mur, et absorbe sans contraintes ions et électrons. C'est le modèle de mur *conducteur*, ou *conducting wall*. Indépendamment du modèle de mur, les caractéristiques principales de la physique de gaine sont retrouvées: une charge positive qui s'étend sur quelques longueurs de Debye se forme à l'extrémité de la ligne de champ. Cette charge positive s'accompagne d'une chute de potentiel qui accélère les ions et réfléchit une partie des électrons les plus lents dans le plasma, alors que les autres, plus rapides, sont absorbés dans le volume du mur. Avec les deux modèles de mur, le plasma reste quasi-neutre sur des échelles spatiales grandes devant la longueur de Debye et sur des temps caractéristiques plus longs que l'inverse de la fréquence plasma électronique. Les dépendances paramétriques du saut de potentiel électrique obtenu dans la gaine ont été étudiées, en variant des paramètres clés tels que le rapport de masse effective entre électrons et ions, la température électronique à l'entrée de la gaine et la longueur de connection magnétique. La comparaison de ces dépendances avec une prédiction pour le saut de potentiel de gaine obtenu au moyen d'un modèle de gaine simple révèle des écarts entre simulations cinétiques et modèle analytique de gaine. Ces écarts sont dus au fait que les fonctions de distribution ne sont pas maxwelliennes à l'entrée de la gaine, ainsi qu'à la réémission d'électrons depuis la région du mur. Cette réémission provient (i) des collisions entre particules chargées dans la gaine de Debye, (ii) de l'amplitude finie de l'opérateur de pénalisation lorsque le mur est conducteur, ou (iii) de la présence d'électrons dans la région pénalisée quand le mur est isolant. Dans le cas du mur conducteur, cette réémission peut être contrôlée et en particulier réduite en augmentant l'amplitude de l'opérateur de pénalisation ainsi qu'en adoptant un masque plus raide pour définir la zone du mur—ce qui implique une meilleure discrétisation et un pas de temps plus faible, augmentant ainsi le coût numérique de la simulation. Le modèle de mur conducteur apparaît alors comme plus approprié que le modèle de mur isolant pour décrire l'interaction plasma paroi. C'est celui qui est retenu pour la suite de l'étude.

Étude des simulations cinétiques au moyen de la théorie fluide

Les simulations cinétiques effectuées dans le cadre du modèle de mur conducteur sont ensuite étudiées au moyen de la hiérarchie d'équations fluides. Ces équations décrivent les propriétés de conservation des moments des fonctions de distribution, telles que la densité, le flux de particules, l'énergie, etc. Il existe une infinité de tels moments, chacun associé à une équation de conservation. Un des résultats qui découlent de l'étude de ces équations de conservation est le *critère de Bohm*, qui stipule que la vitesse

moyenne des ions doit être supersonique à l'entrée de la gaine. La validité de ce critère dans les simulations cinétiques est étudiée. Ce critère est important car il est souvent utilisé en guise de condition à la limite sur la surface des composants face au plasma dans les codes fluides. Ces codes décrivent les plasmas de tokamak en résolvant une partie de la hiérarchie des équations fluides. Les descriptions fluides ont l'avantage d'être moins coûteuses à résoudre numériquement comparées aux modèles cinétiques et gyrocinétiques. Un de ces inconvénients inhérents aux modèle fluides est la nécessité de faire l'hypothèse d'une *fermeture* de la hiérarchie fluide. En effet, pour résoudre un nombre fini d'équations fluides, il est nécessaire de prescrire la valeur du moment d'ordre le plus élevé. En général, les codes fluides résolvent les trois première équations de conservation, i.e. conservation de la masse, quantité de mouvement et énergie, et font la prescription du flux de chaleur.

La physique cinétique obtenue à l'aide du code VOICE se révèle difficile à expliquer au moyen des équations fluides seules, en particulier en ce qui concerne les variations spatiales des flux de chaleur ioniques et électroniques le long de la ligne de champ magnétique simulée par le code. Le flux de chaleur total, obtenu en sommant les flux de chaleur ioniques et électroniques représente 30% du flux d'énergie total[3]. Le flux de chaleur électronique représente environ 50% du flux d'énergie électronique. Ces flux de chaleur importants sont expliqués par la réorganisation des fonctions de distribution via des processus collisionnels entre la zone source, où les particules sont injectées, et le mur. Les collisions tendent à ramener le système vers un équilibre thermodynamique caractérisé par des fonctions de distribution Maxwelliennes, alors que l'injection de particules dans la zone source ainsi que la physique de gaine à l'œuvre près du mur tendent à écarter le système d'un tel état d'équilibre. Les collisions apparaissent également comme un mécanisme indispensable pour atteindre un régime d'équilibre entre injection de particules dans la zone source et absorption au mur: la diffusion des particules dans l'espace des vitesses qu'elles engendrent permettent le dépiégeage collisionnel des électrons lents, qui resteraient sans cela piégés entre les puits de potentiel de gaine aux deux extrémités de la ligne de champ (la turbulence permettrait aussi un tel dépiégeage). En l'absence de collisions, la source de particules alimentant notamment la population d'électrons piégés, la densité de cette population divergerait alors. Cette compétition entre collisions, injection de particules et physique de gaine se traduit par une auto-organisation complexe du système. Cette auto-organisation est par nature cinétique, donc difficile à capturer dans le cadre fluide. Ceci est souligné en calculant les facteurs de transmission de chaleur à l'entrée de la gaine, ou *sheath heat transmission factors*. Le facteur de transmission de chaleur des ions dépasse de 60% la prédiction fluide. Cet écart se révèle être de l'ordre de 35% pour les électrons. Ces écarts sont directement dus aux effets cinétiques détaillés plus haut. De ce fait, il est difficile de prévoir les résultats des simulations cinétiques au moyen de la hiérarchie d'équations fluides. En particulier, la recherche d'une prescription pour la fermeture de

[3]On distingue ici *flux d'énergie* et *flux de chaleur*, le flux d'énergie étant égal à la somme du flux de chaleur—qui découle d'un transfert d'énergie conductif—et du flux d'énergie convectif.

cette hiérarchie portant soit sur le flux de chaleur, ou bien sur un moment d'ordre plus élevé n'a pas permis d'expliquer les résultats cinétiques de la simulation. Une des conséquences qui s'ensuit est qu'il n'est pas possible de prévoir précisément les variations du nombre de Mach dans le plasma. En particulier, le critère de Bohm $M = u_i/c_s = 1$ à l'entrée de la gaine, avec u_i la vitesse moyenne des ions et c_s la vitesse des ondes sonores dans le plasma, n'est pas observé dans les simulations cinétiques. De plus, on montre que l'expression de la vitesse du son c_s dépend de la fermeture considérée pour les équations fluides. Cette observation pourrait avoir des conséquences du point de vue des codes fluides, qui imposent en général la condition $M \geq 1$ sur les composants face au plasma. Il faut noter ici que cette condition à la limite peut être d'autant plus remise en question qu'elle est imposée à l'endroit où les niveaux de flux de chaleur et de particules doivent être calculés de manière pertinente et précise. En général, les codes fluides n'imposent pas la condition à la limite $M \geq 1$ en prenant une expression de la vitesse du son c_s compatible avec la fermeture fluide prise en compte pour résoudre un sous-ensemble des équations fluides. Afin de pallier ce problème, nous proposons une technique qui permet de dériver l'expression de la vitesse du son compatible avec une fermeture quelconque de la hiérarchie fluide. Enfin, le critère de Bohm $M = 1$ n'apparait pas comme une prédiction robuste dans le contexte cinétique. En effet, l'expression de la vitesse du son n'est *à priori* pas connue à l'avance dans la simulation cinétique. En faisant varier la collisionnalité de la simulation d'un facteur aussi large que 5×10^4 par rapport à une collisionnalité typique d'une Scrape-Off Layer en régime sheath-limited, on montre qu'on ne retrouve pas la condition $M = 1$ à l'entrée de la gaine comme cela est pourtant prédit dans le cadre de la fermeture fluide valide à grande collisionnalité.

L'interaction avec les neutres

On prépare ensuite la future extension du code gyrocinétique GYSELA à la description de l'interaction entre particules chargées et neutres dans la Scrape-Off Layer. Cette interaction est cruciale pour décrire notamment les régimes opérationnels de *recyclage* et de *détachement* d'un plasma de tokamak. Dans ces régimes, un fort gradient de température existe entre le point de stagnation et les composants face au plasma. Lorsque ce gradient est suffisamment raide, des processus d'ionisation et de recombinaison se mettent en place proche de ces composants. Pour décrire correctement la physique d'un tel régime, il est alors nécessaire d'inclure un modèle de neutre dans la simulation. On détaille dans le chapter 4 un modèle fluide dit de *pressure-diffusion* qui modélise la dynamique d'une espèce neutre, ainsi que son couplage au modèle cinétique qui décrit le plasma. Ce modèle a été implémenté dans la version `C++` du code VOICE. Ce travail a été fait en partie au travers de l'encadrement d'un stage de deuxième année de Master. En menant une étude préliminaire à une future implémentation dans GYSELA on montre que la physique des neutres peut influencer de manière non-négligeable la dynamique du plasma.

Le modèle de gaine *moyenné en flux* pour une application au cadre gyrocinétique

Le chapitre 5 décrit l'amélioration de la description de la région de bord dans le code gyrocinétique GYSELA par l'inclusion d'un modèle sous-maille d'interaction plasma-paroi. Un modèle fluide pour les particules neutres est également décrit, et implémenté dans le code VOICE, avant une future étude de ce modèle avec le code GYSELA. Le modèle sous-maille permet de rendre compte de la physique de l'interaction plasma-paroi dans le cadre gyrocinétique, sans résoudre les échelles typiques de temps et d'espace de la gaine. La théorie gyrocinétique est dérivée des équations cinétiques en effectuant un développement du modèle cinétique dans la limite des petites valeurs du paramètre $\rho^* = \rho_i/a$, avec ρ_i le rayon de Larmor et a le petit rayon du tokamak. En effectuant ce développement on obtient un modèle indépendant de la phase cyclotronique, qui est donc de dimensionnalité moindre que le modèle purement cinétique (cinq dimensions pour le gyrocinétique, au lieu de six pour le modèle cinétique). Le cadre gyrocinétique est adapté pour décrire la turbulence des tokamaks actuels pour lesquels $\rho^* \ll 1$ ($\rho^*_{\text{ITER}} \approx 10^{-3}$). De nombreuses simulations de la turbulence de cœur ont été effectuées. L'extension de ces simulations vers la zone de bord et Scrape-Off Layer fait l'objet de nombreux travaux à l'heure actuelle. La physique d'interaction plasma paroi est un élément important pour décrire correctement la dynamique des régions de bord et de Scrape-Off Layer. Cette physique ne peut pas être décrite directement par la théorie gyrocinétique car la gaine est positivement chargée, et a une taille petite comparée au rayon de Larmor ionique ρ_i—et ainsi à l'extension typique des cellules turbulentes dans la direction parallèle, donnée par $1/k_\parallel \sim qR$. Pour inclure la physique de la gaine dans un code gyrocinétique, un modèle sous-maille qui rend compte de cette physique est donc nécessaire.
Le principal effet de l'interaction plasma-paroi est d'assurer la quasi-neutralité du plasma. C'est bien cet effect que l'on cherche à intégrer dans une simulation gyrocinétique qui décrirait à la fois le cœur, le bord, et la Scrape-Off Layer. Des modèles d'interaction plasma-paroi existent déjà pour décrire (i) cette physique dans le cadre de l'hypothèse d'électrons adiabatiques, et (ii) dans le cadre d'électrons gyro-cinétiques (en pratique drift-cinétiques). C'est sur ce dernier cas que l'on se focalise. Le modèle de gaine *moyenné en flux*, ou *flux-averaged sheath* dans la texte, proposé dans la présente thèse est présenté et comparé aux modèles de gaine *logique* (logical) et *conductrice* (conducting). Le modèle moyenné en flux propose d'assurer la quasi-neutralité du plasma en imposant l'égalité des flux de gyrocentres ioniques et électroniques en moyenne spatiale sur l'intégralité de la surface face au plasma (le limiteur dans le cadre de GYSELA). Le modèle moyenné en flux s'appuie sur une description du limiteur avec frontières immergées, et est compatible avec le schéma numérique semi-Lagrangien backward de GYSELA. Le modèle pourrait être adapté pour d'autres schémas numériques, tels que les schémas Eulériens ou Lagrangiens. Les trois ingrédient principaux du modèle de gaine moyennée en flux sont détaillés, à savoir (i) l'absorption des ions dans le volume du limiteur grâce à un opérateur de pénalisation, (ii) la réflexion des électrons lents, et

l'absorption des électrons rapides sur la surface du limiteur, et (iii) la procédure de calcul de la vitesse de coupure qui permet de discriminer entre électrons lents et rapides. Puisque le modèle s'appuie sur des frontières immergées, l'équation de quasi-neutralité est modifiée afin de s'assurer qu'aucune charge n'existe dans le limiteur.
L'implémentation du modèle dans le code gyrocinétique GYSELA est explicitée. Les simulations montrent que l'absorption des ions et des électrons rapides, ainsi que la réflexion des électrons lents fonctionne comme prévu. Cependant, malgré la définition de la vitesse de coupure qui devrait assurer l'égalité des flux de gyrocentres ioniques et électroniques à chaque pas de temps en moyenne spatiale sur la surface du limiteur, on observe un écart entre ces deux flux après l'étape d'advection poloïdale, au cours de laquelle la procédure de réflexion sélective des électrons est implémentée. L'écart est tel que trop d'électrons sont réfléchis dans le plasma à chaque itération, ce qui conduit à l'apparition d'une charge négative sur la surface du limiteur. Cela cause l'arrêt de la simulation sur des temps trop courts pour étudier la turbulence de bord. L'origine d'un tel écart n'est pas encore compris à l'heure de rédaction du manuscrit. Des pistes sont néanmoins proposées pour contourner la difficulté.

Conclusion

L'amélioration de la description du bord dans les codes gyrocinétique est un sujet d'une grande importance car les propriétés de la turbulence sont influencées par la physique du bord, et en particulier par la physique de l'interaction plasma-paroi. Cette physique est difficile à intégrer dans un code gyrocinétique du fait des hypothèses faites par cette théorie, mais se révèle cruciale pour assurer la quasi-neutralité du plasma. De la même manière, l'inclusion d'un modèle d'interaction plasma-neutres est nécessaire pour décrire des conditions Scrape-Off Layer proches des conditions expérimentales (régime de recyclage et régime détaché par exemple). L'étude réalisée au cours de la présente thèse a montré tout d'abord qu'un modèle cinétique 1D-1V aux frontières immergées permet de simuler de manière robuste la physique de l'interaction plasma-paroi. On observe dans les simulations cinétiques l'apparition d'une couche limite positivement chargée qui agit de façon similaire à la gaine de Debye. Grâce à cette couche limite, le plasma reste quasineutre. On observe que la physique de la gaine conduit à l'obtention de fonctions de distribution non-Maxwelliennes à l'entrée de la gaine. En étudiant les résultats des simulations par le biais des équations de conservation fluides, on montre que le critère de Bohm est inopérant dans les simulations cinétiques, notamment puisque la vitesse du son—utile pour définir ce critère—dépend du choix de fermeture de la hiérarchie d'équations fluides. Ensuite, afin de préparer l'extension du code gyrocinétique GYSELA à la prise en compte de l'interaction entre particules chargées et neutres, on présente un modèle *pressure-diffusion* pour décrire une espèce neutre au moyen d'un modèle fluide. On explicite le couplage de cette description fluide avec le modèle cinétique du plasma, et on illustre avec des simulations simples l'impact the la physique des neutres sur la dynamique du plasma. Enfin, on décrit un modèle sous-maille d'interaction plasma-paroi valide dans le cadre gyrocinétique. Le

modèle s'appuie sur des frontières immergées pour décrire l'absorption des ions dans le limiteur, et sur le schéma numérique semi-Lagrangien pour décrire la reflection des électrons lents à la surface du limiteur. La distinction entre électrons rapides (absorbés) et lents (réflechis) se fait *via* la vitesse de coupure, qui est calculée de façon à ce que les flux électroniques et ioniques se compensent en moyenne spatiale sur l'intégralité de la surface du limiteur. En réalisant des simulations globales coeur-bord-SOL qui intègrent ce modèle dans le code GYSELA, on observe un écart systématique entre flux ionique et électronique sur la surface du limiteur. Cet écart conduit à l'accumulation de charges négatives dans le plasma, qui brise sa quasineutralité sur des temps trop courts pour étudier les propriétés de la turbulence de bord. On explicite des possibilités concernant l'origine d'un tel écart. De manière générale, afin d'assurer une description correcte de la physique d'interaction plasma-paroi dans le cadre gyrocinétique, celle-ci doit être implémentée via un modèle efficace et robuste. La procédure requise pour calculer la vitesse de coupure, qui sépare les électrons lents et rapides à la surface des composants face au plasma, doit être accompagnée de méthodes permettant de quantifier précisément les écarts entre flux de gyrocentres électroniques et ioniques à la surface du mur, afin d'assurer la quasi-neutralité du plasma sur des temps de simulation suffisamment longs pour observer une saturation de la turbulence. Le développement d'une méthode robuste, adaptée aux spécificités ici recherchées (schéma semi-Lagrangien et frontières immergées) et permettant une auto-correction de l'écart existant entre flux de gyrocentre ioniques et électroniques serait d'une grande valeur. Le développement de tels outils de quantification et de correction de l'erreur avec le code GYSELA demeure une question ouverte.

Remerciements

J'aimerais remercier ici les nombreuses personnes qui ont contribué à l'aboutissement de ma thèse. Les quelques lignes qui suivent ne sauraient refléter fidèlement le soutien que l'on m'a apporté au cours de ces trois ans, je me limiterai donc à exprimer ma profonde gratitude pour tout·es celles et ceux qui ont contribué de près ou de loin à ce travail.

Merci à mes collègues de l'IRFM, et en particulier aux membres de l'équipe GYSELA, avec qui les échanges furent très enrichissants. Côtoyer de brillants (et sympathiques!) collègues est une expérience que je recommande à chacun·e. Je pense notamment à Abdelhadi, Emily, Kévin, Peter, Robin, Virginie, Xavier, et bien évidemment à Guilhem & Yanick, qui furent d'excellents encadrants, tant par leur disponibilité, bienveillance et bonne humeur que par le sérieux avec lequel ils se sont attelés à la (périlleuse) tâche de superviser mon doctorat. Un grand merci aux membres de l'équipe de développement `gyselalibxx` avec qui j'ai travaillé et qui m'ont beaucoup appris—ce que le présent manuscrit ne reflète pas assez à mon goût.

Merci à mes ami·es doctorant·es, qui au cours de ces trois ans sont devenus des ami·es tout court. Vous avez immensément contribué à mon bonheur durant ce séjour provençal. Une (grosse) pensée pour mes *ragazi favoriti* ♡ Emily, Ludovica, Nicolas, Olivier et Virginia. Merci aussi à mes amis d'Aix et d'ailleurs, à ma famille, à tout·es celles et ceux que je ne peux pas citer ici mais pour qui mon cœur balance[4].

I would lastly like to warmly thank all of the members of my PhD defense jury. First, for accepting to be part of it, second, for reading the present manuscript—even though it is over 200 pages long—and third, for your always-relevant questions and remarks, making me question and extend my understanding of aspects of the present work.

Bonne lecture !

yann

[4]Mon coeur ne balance cependant pas pour la majorité des automobilistes provençaux auxquels j'ai eu affaire lors de mes—trop peu nombreuses, souvent trop longues, toujours bienvenues—sorties à vélo dans notre magnifique région.

Contents

1 Introduction **21**
- 1.1 On the fusion reaction . . . 21
- 1.2 The tokamak magnetic configuration . . . 23
  - 1.2.1 Charged particles drifts in the adiabatic limit . . . 24
  - 1.2.2 Tokamak magnetic field and particle trajectories . . . 26
  - 1.2.3 Radial transport in tokamaks . . . 29
- 1.3 Core and edge plasma physics . . . 30
  - 1.3.1 Core plasma . . . 30
  - 1.3.2 Scrape-Off Layer plasma . . . 31
- 1.4 Gyrokinetic edge modeling . . . 33
- 1.5 Numerical developments . . . 35
- 1.6 Outline of the thesis . . . 36

2 Immersed boundary conditions **39**
- 2.1 Fundamentals of plasma-wall interaction . . . 40
  - 2.1.1 The sheath boundary layer . . . 40
  - 2.1.2 Kinetic physics of the sheath and presheath . . . 41
  - 2.1.3 Tilted magnetic field lines and the magnetic presheath . . . 42
- 2.2 Kinetic plasma description . . . 43
- 2.3 Immersed boundary conditions . . . 45
  - 2.3.1 Immersed wall model . . . 46
  - 2.3.2 Electron heat sink in the insulating wall model . . . 48
- 2.4 Source and collisions . . . 49
  - 2.4.1 Plasma source . . . 49
  - 2.4.2 Collisions . . . 50
- 2.5 The Voice code . . . 52
  - 2.5.1 Numerical scheme . . . 52
  - 2.5.2 On the interest of using a non-uniform mesh for the sheath problem 53
  - 2.5.3 Reference simulation parameters . . . 54
- 2.6 Conducting and insulating walls . . . 56
- 2.7 Kinetic physics of the sheath . . . 58
  - 2.7.1 Distribution functions at the sheath entrance . . . 58
  - 2.7.2 Particle trajectories in phase space . . . 60
- 2.8 Parameter scans . . . 62
  - 2.8.1 Potential drop dependence on the ion-to-electron mass ratio value 63

2.8.2 Potential drop dependence on the electron temperature 65
2.8.3 Potential drop dependence on the parallel length 67
2.9 Conclusion of the chapter 68

3 Fluid modeling and kinetic simulations 71
3.1 Fluid description of a plasma 72
3.2 Fluid codes for tokamak power exhaust prediction 73
3.2.1 Mean-field codes 74
3.2.2 Turbulent codes 74
3.2.3 Sheath-like boundary conditions within fluid codes 75
3.3 1D fluid model 76
3.4 Bohm criterion 77
3.4.1 Bohm criterion in the kinetic simulation 78
3.4.2 On the fact that the sound speed depends on the closure of the fluid hierarchy, and on how to derive it 79
3.5 Heat flux 86
3.5.1 Prediction of the variation of plasma quantities assuming a Maxwellian closure 86
3.5.2 Variation of the Mach number in the kinetic simulation 89
3.5.3 Variation of the heat flux in the kinetic simulation 91
3.5.4 Heat transmission factors at the entrance of the sheath 94
3.6 Collisionality scan 96
3.6.1 Impact of collisionality on electron distribution function and heat flux 96
3.6.2 Validity of the Maxwellian closure at high collisionality 97
3.7 Conclusion of the chapter 100

4 Plasma-neutral interaction with Voice 103
4.1 Neutral interaction in the edge 103
4.2 Models for describing neutral particles 104
4.3 Pressure-diffusion model 106
4.4 Reaction rates 109
4.5 Characteristic scales of plasma-neutral interaction 109
4.6 Plasma-neutral interaction with the Voice code 111
4.7 Conclusion of the chapter 115

5 Gyrokinetic plasma-wall interaction 117
5.1 Gyrokinetic edge modeling 118
5.1.1 The necessity of unified core-edge-SOL modeling 118
5.1.2 On the validity of edge gyrokinetic modeling 120
5.1.3 Strategies for edge gyrokinetic modeling 121
5.2 Gyrokinetic description of a plasma 123
5.2.1 Gyrokinetic Vlasov equation 124

5.2.2 Quasineutrality equation . . . 125
5.3 Models for gyrokinetic plasma-wall interaction . . . 127
5.3.1 The necessity of a subgrid model to describe the sheath physics 128
5.3.2 Two subgrid sheath models valid in the gyrokinetic framework . 130
5.3.3 Logical and conducting sheath frameworks . . . 132
5.4 The GYSELA code . . . 136
5.4.1 Code description . . . 136
5.4.2 Numerical scheme . . . 136
5.5 Penalized sheath model valid for BSL codes . . . 138
5.5.1 A penalization operator for ions . . . 138
5.5.2 Electron reflection on the surface of the limiter . . . 140
5.5.3 Matching the electron and ion fluxes on spatial average over the entire limiter surface . . . 143
5.5.4 Implementation of the penalized sheath model in the GYSELA framework . . . 145
5.6 Quasineutrality model . . . 146
5.6.1 On the necessity of a fully kinetic electron response in the Scrape-Off Layer . . . 146
5.6.2 Adapting the quasineutrality equation for the immersed limiter 150
5.7 Results and discussion . . . 151
5.7.1 Simulation without quasineutrality equation . . . 151
5.7.2 Simulation with quasineutrality equation . . . 158
5.8 Conclusion of the chapter . . . 161

6 Conclusion **165**

A Immersed boundary conditions **175**
A.1 Collisions . . . 175
A.2 Verification of the code . . . 176
A.3 Prediction of the potential drop in the sheath . . . 177
A.3.1 Classical potential drop prediction . . . 177
A.3.2 On the electron re-emission from the wall . . . 179
A.4 Sheath entrance and wall definitions . . . 180
A.4.1 Definition of the wall position . . . 180
A.4.2 Definition of the sheath entrance . . . 181

B Plasma-wall interaction: fluid and kinetic analysis **187**
B.1 Bohm criterion with cold ions . . . 187
B.2 Bohm criterion from matching sheath and presheath regions . . . 188
B.3 Plasma sound waves with the polytropic closure . . . 190
B.4 Plasma sound waves with higher moment closure . . . 191
B.5 Prediction for the sheath heat transmission factors . . . 194

C Gyrokinetic plasma-wall interaction **197**
C.1 Alternative models for gyrokinetic plasma-wall interaction 197
C.1.1 Penalization of parallel force balance equation 197
C.1.2 Splitting of poloidal advection 199
C.1.3 Reflection of electrons in field-aligned coordinates 200
C.2 Implementation of the sheath model 202
C.2.1 Reflection of slow electrons 202
C.2.2 Absorption of fast electrons 208
C.2.3 Particle fluxes on the limiter surface 209
C.3 Electron response in the quasineutrality equation 211

1

Introduction



1.1 On the fusion reaction

A fusion reaction is a thermonuclear reaction that involves the fusion of two light nuclei into a heavier one. Figure 1.1 presents the binding energy per nucleon B/A as a function of the number of nuclei A. The binding energy increases for atoms characterized by $A \leq 56$ and decreases above this value. It is therefore possible to harness energy by fusing light nuclei for which $A < 56$ into heavier ones. The fusion reaction with the highest cross-section involves deuterium and tritium, two isotopes of hydrogen. Deuterium (D) has one neutron while tritium (T) has two. Fusing these two elements produces a neutron (n) with an energy of 3.52 MeV, and an alpha (α) particle carrying a kinetic energy of 14.06 MeV. The reaction can be written

$$D \ + \ T \ \longrightarrow \ n \ (14.06\,\mathrm{MeV}) \ + \ \alpha \ (3.52\,\mathrm{MeV}) \tag{1.1}$$

The energy released by D-T fusion is approximately six orders of magnitude above the energy involved in traditional chemical reactions, such as combustion. It is therefore interesting to harvest the energy produced in fusion reactions to produce electricity in fusion reactors[1]. Reaction (1.1) requires particular conditions to happen at a sufficiently high reaction rate. In particular, each particle involved in the reaction must have a high energy level. Fusing two nuclei involves indeed bringing them close enough so that the strong force—that binds nucleons together—becomes dominant over the Coulomb repulsion. One way of overcoming the Coulomb repulsion is to give particles a high thermal energy[2]. As will be detailed in the following, the order of magnitude of the temperature required for D-T fusion is 10 keV, i.e. around 100 million°C. Note that even at such high energies the two nuclei fuse together thanks to quantum tunnelling across the Coulomb potential barrier rather than by just overcoming it. At such temperatures, matter is found in a plasma state, in which electrons are stripped away from

[1] Not all fusion reactors rely on Deuterium-Tritium fusion. Some other reactions can be considered, such as fusing Deuterium and Helium-3 [5], or a proton with a Boron atom [6]. We focus in the following on the D-T reaction as it is the one chosen for the ITER reactor.

[2] Another way consists in accelerating particles and shooting them into a solid target, so as to trigger fusion reactions.

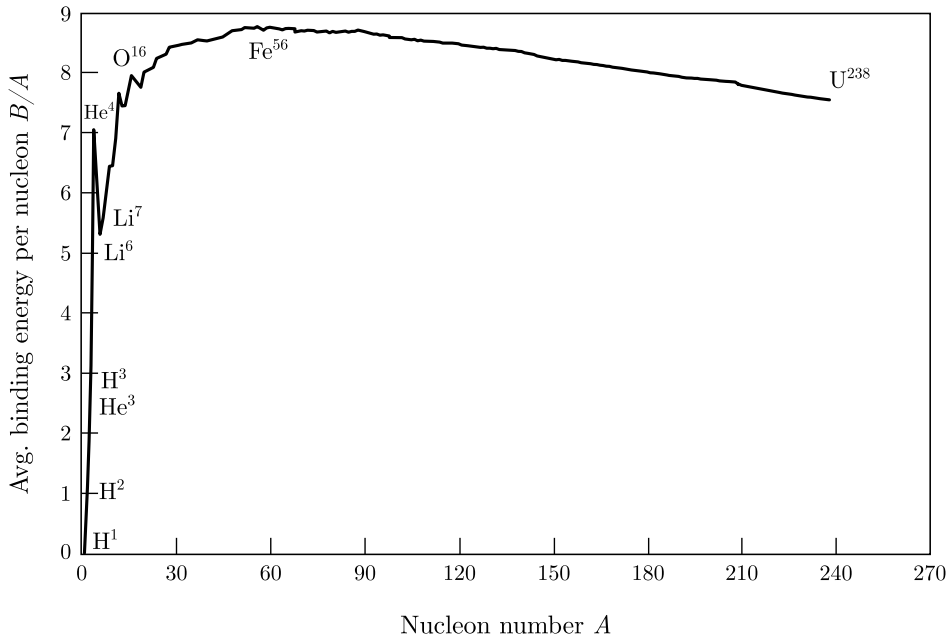

Figure 1.1: Binding energy per nucleon B/A as a function of the nucleon number B, from [7].

their nucleus. A condition for fusion reaction is given by the *Lawson criterion* [8]. To find this criterion, one can write a necessary condition for fusion as

$$\frac{\mathcal{E}}{\tau_E} \leq P_\alpha + P_{\text{aux}}, \tag{1.2}$$

where $\mathcal{E}$ is the energy density of the plasma and τ_E is the energy confinement time. The latter quantity typically represents the average time energy stays within the plasma before being lost to its surroundings. The energy balance given in eq. (1.2) states that the energy lost by the plasma per unit of time $\mathcal{E}/\tau_E$ must be less than the power density carried by alpha particle P_α plus the externally injected power P_{aux}—such as heating via antennas for instance. Note that the above energy balance is expressed per meter cube of plasma, so that $\mathcal{E}$ has the units Jm^{-3}, τ_E is in s and P_α and P_{aux} in Wm^{-3}. Let us introduce the amplification factor Q as

$$Q = \frac{P_{\text{fus}}}{P_{\text{aux}}} = \frac{5P_\alpha}{P_{\text{aux}}}, \tag{1.3}$$

where P_{fus} is the total power density delivered by the fusion reaction, including the contribution from neutrons and alpha particles. Thus $P_{\text{fus}} = P_\alpha + P_n = 5P_\alpha$, with P_n is the power density carried by the neutron, and the factor 5 comes from the ratio between the energy carried by the neutron and by the alpha particle in the D-T reaction. The amplification factor Q represents the ratio between the fusion reaction power output and the externally injected power required to maintain the fusion reaction. In the limit

$Q \to \infty$ the plasma is heated only through the fusion reaction. Such a plasma is called a *burning plasma*. Note that in the balance given in eq. (1.2) the fusion heating power P_α only accounts for alpha particles since the neutron produced in reaction (1.1) does not stay long enough in the plasma to deposit its energy there. By denoting n_D, n_T and n_e respectively the density of deuterium, tritium and electrons in the plasma the energy density is $\mathcal{E} = \frac{3}{2}(n_D + n_T + n_e)\,T$, where T is the plasma temperature—we assumed thermal equilibrium between ions and electrons. Assuming an equal number of deuterium and tritium nuclei in the plasma, and by stating that the plasma is quasineutral we get $n_D = n_T = n_e/2$, thus $\mathcal{E} = 3n_eT$. The power deposited by alpha particles in the plasma can be expressed as

$$P_\alpha = n_D n_T \langle \sigma v \rangle_{\mathrm{DT}} E_\alpha, \tag{1.4}$$

where $E_\alpha = 3.52\,\mathrm{MeV}$ is the energy of the alpha particle and $\langle \sigma v \rangle_{\mathrm{DT}}$ is the average cross section of the DT reaction over a Maxwellian distribution function at the temperature T. This quantity therefore has the unit of a reaction rate in $\mathrm{m^3 s^{-1}}$. By injecting these expressions for the plasma energy density and the fusion power exhaust P_α in the power balance equation we finally arrive at the so-called Lawson criterion that is

$$n_e \tau_E \geq \frac{12T}{E_\alpha \langle \sigma v \rangle_{\mathrm{DT}} \left(1 + \frac{5}{Q}\right)}. \tag{1.5}$$

This gives a necessary requirement for fusion. One has therefore two possible ways of seeking conditions suitable for fusion. The first one consists in working with high densities and relatively small confinement times. This is the *inertial fusion* approach. An example of this approach involves firing a laser beam at a small fuel pellet that implodes on itself, making its constituents fuse together. Another possible solution lies in increasing the energy confinement time τ_E. This is the approach followed by the so-called *magnetic confinement fusion*, on which we will focus in the present work. In magnetic confinement devices, high values for the energy confinement time are achieved by using a magnetic field to confine charged particles in a given region of space. We focus on a specific magnetic configuration called the *tokamak* configuration, that is described in section 1.2. To ease the requirement on the energy confinement time τ_E, one can try working with densities n_e as high as possible. The density n_e in tokamaks reactors is fixed by the ratio between plasma pressure $p = nT$ and magnetic pressure as $\beta = 2\mu_0 p/B^2$, that must stay within a few percent. Increasing β above this threshold results in instabilities that rapidly lead to the loss of plasma confinement. This is the so-called *Greenwald limit* [9]. With the value of the plasma density n_e fixed by this limit, and a magnetic field of the order of a few Teslas, one can demonstrate that the optimal temperature for fusion in tokamaks is around $T = 10\,\mathrm{keV}$ [10].

1.2 The tokamak magnetic configuration

In this section we describe the so-called *tokamak* magnetic configuration, which enables to confine a plasma within a given region of space. As no material can withstand the

contact with a plasma at temperatures close to 10 keV, tokamaks rely on a magnetic field to achieve confinement of charged particles. Studying the confinement quality of tokamak plasmas is of great interest: the higher the confinement time, the better the performance of the fusion device. The main mechanism that degrades the confinement in tokamaks is turbulence [11]. As such, a great deal of research in the fusion community is devoted to study turbulence. As detailed in section 1.4, this work focuses on describing turbulence in the edge of tokamak plasmas. In this section, we describe the tokamak configuration. First, we investigate the motion of charged particles immersed within an electromagnetic field. We then describe the magnetic geometry of tokamaks. Last, we detail how some mechanisms such as turbulence lead to *radial* transport of particles and energy in tokamaks[3].

1.2.1 Charged particles drifts in the adiabatic limit

Let us consider a particle of charge e_s and mass m_s immersed within an electromagnetic field $(\mathbf{E}, \mathbf{B})$. The s subscript refers to the species of the particle, for instance i for ions and e for electrons. The particle is subject to the Lorentz force

$$\mathbf{F} = e_s \left(\mathbf{E} + \mathbf{v}_s \times \mathbf{B} \right),$$

where $\mathbf{v}$ is the velocity of the particle. With the conventions of fig. 1.2 we define the basis $(\mathbf{e}_1, \mathbf{e}_2, \mathbf{b})$, where $\mathbf{b} = \mathbf{B}/B$ is the unit vector in the direction of the magnetic field, E (resp. B) stands for the norm of the electric (resp. magnetic) field, and $(\mathbf{e}_1, \mathbf{e}_2)$ is a set of orthogonal unit vectors in the plane perpendicular to the magnetic field. We consider first the case of a magnetic field uniform in space and of a vanishing electric field. Under these circumstances it is easy enough to show that the motion of the particle is given by the cyclotron motion

$$\mathbf{x} = \mathbf{x}_G + \boldsymbol{\rho}_s,$$

where $\mathbf{x}_s$ is the position of the particle, $\mathbf{x}_G$ is the coordinate of the center of the cyclotron motion—called the guiding-center coordinate in the following—and $\boldsymbol{\rho}_s$ describes the cyclotron motion as

$$\boldsymbol{\rho}_s = \rho_s \left(\cos(\varsigma) \boldsymbol{e}_1 - \sin(\varsigma) \boldsymbol{e}_2 \right).$$

In this last expression the Larmor radius is defined as

$$\rho_s = \frac{m_s v_\perp}{eB},$$

with $v_\perp^2 = \mathbf{v} \cdot \mathbf{v} - v_\parallel^2$ defines the norm of the perpendicular velocity of the particle, and the norm of the parallel velocity is $v_\parallel = \mathbf{v} \cdot \mathbf{b}$. The gyroangle ς is

$$\varsigma = \varsigma_0 + \int_0^t dt' \Omega_c,$$

[3]Radial transport refers to the movement of particles, momentum and energy between magnetic field surfaces from the core plasma towards its edge, see section 1.2.3

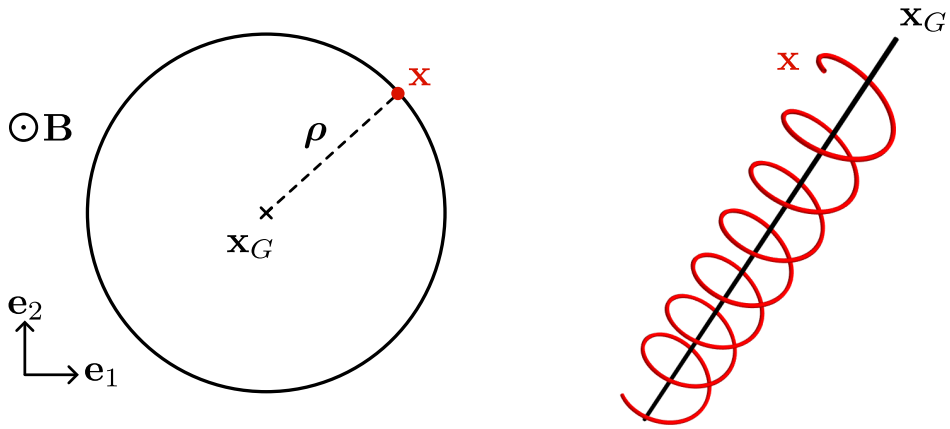

Figure 1.2: Left: simple cyclotron motion of a negatively charged particle. The particle position $\mathbf{x}_s$ can be broken down between the guiding center position $\mathbf{x}_G$ and the Larmor radius $\boldsymbol{\rho}_s$. Right: motion of a particle and of its guiding center in a homogeneous magnetic field.

with ς_0 the initial phase of the particle at $t = 0$ and the cyclotron pulsation

$$\Omega_{cs} = \frac{e_s B}{m_s}.$$

The resulting motion is depicted in fig. 1.2. When a charged particle is immersed in a spatially inhomogeneous and possibly time-varying electromagnetic field, its motion becomes more complicated than the simple cyclotron motion. In general, the resulting motion of the particle can be quite intricate. However in the *adiabatic limit*, it becomes possible to describe the dynamic of the particle as being the sum of a fast cyclotron motion plus some slow drifts applied to the guiding center of the cyclotron motion. These drifts are due to the inhomogeneity of the electromagnetic field. The adiabatic limit refers to the case where (i) the norm of the magnetic field is strong and (ii) when the electromagnetic field varies slowly in time as compared to the cyclotron frequency. These two conditions can be expressed as

$$\frac{1}{|\mathbf{E}|}\frac{\partial|\mathbf{E}|}{\partial t} \approx \frac{1}{|\mathbf{B}|}\frac{\partial|\mathbf{B}|}{\partial t} \ll \Omega_{cs}, \tag{1.6}$$

and

$$\frac{\nabla \cdot \mathbf{B}}{|\mathbf{B}|} \ll \rho_s^{-1}. \tag{1.7}$$

When these conditions are satisfied, it can be shown that the guiding center motion can be approximated by the following formula [12]

$$\mathbf{v}_G = v_{\parallel}\mathbf{b} + \mathbf{v}_D + \mathbf{v}_E. \tag{1.8}$$

The magnetic drift velocity is defined in the low β limit, with $\beta = 2\mu_0 p/B^2$ as

$$\mathbf{v}_D = \frac{m_s v_\parallel^2 + \mu_s B}{e_s B_\parallel^* B^2} \mathbf{B} \times \nabla B \tag{1.9}$$

and the $E \times B$ drift velocity, also called electric drift is

$$\mathbf{v}_E = \frac{1}{B_\parallel^*} \frac{\mathbf{E} \times \mathbf{B}}{B}. \tag{1.10}$$

In eq. (1.8) we identified the parallel velocity of the particle $v_\parallel$ with the parallel velocity of the guiding center[4]. In the expressions of the drifts, we introduced the magnetic moment of the particle $\mu_s = \frac{1}{2} m_s v_\perp^2 / B$ and the modified magnetic field

$$\mathbf{B}^* = \mathbf{B} + \frac{m_s v_\parallel^2}{e_s} \nabla \times \mathbf{b}, \tag{1.11}$$

and $B_\parallel^* = \mathbf{B}^* \cdot \mathbf{b}$. In the expression of the magnetic drift velocity, the modified magnetic field appears along with the magnetic field itself. This can be understood from the following point: when writing the drifts velocities $\mathbf{v}_D$ and $\mathbf{v}_E$ that apply to the guiding center rather than to the particle itself, one must take into account that fact that these two coordinates differ by a Larmor radius. Thus the guiding center does not experience the same field as the particles. The modified magnetic field is reminiscent of this mismatch. The time evolution of the guiding center parallel velocity can be expressed at leading order as

$$m_s \frac{\mathrm{d}v_\parallel}{\mathrm{d}t} = -\mathbf{b} \cdot \nabla \left(e_s \phi + \mu_s B \right) + m_s v_\parallel \mathbf{v}_E \cdot \frac{\nabla B}{B}. \tag{1.12}$$

The first force term $-e\mathbf{b} \cdot \nabla \phi$ that appears in this equation corresponds to the electric part of the Lorentz force projected in the parallel direction. The second one $-\mu \mathbf{b} \cdot \nabla B$ is the consequence of inhomogeneities of the magnetic field. As particles gyrate around the position of their guiding center, they behave similarly to small magnets. As such, they experience a force induced by inhomogeneity of the magnetic field. This force is sometimes called the *mirror force*, as it can result in the trapping of particles near a minimum of the norm of the magnetic field. The last term $m_s v_\parallel \mathbf{v}_E \cdot \nabla B / B$ originates from a synergy of the electric and magnetic drifts.

1.2.2 Tokamak magnetic field and particle trajectories

Let us first introduce the toroidal geometry depicted on fig. 1.3. The radial direction stands for the direction carried by the unit vector $\mathbf{e}_r$, the poloidal direction by the unit vector $\mathbf{e}_\theta$ and the toroidal direction is obtained by revolving around the axis defined by the $\mathbf{e}_Z$ unit vector. The coordinate along the toroidal direction is the angle φ. The minor radius of the torus is a, and the major radius is R_0.

[4]Strictly speaking, the parallel velocity of the guiding center is not the same quantity as the parallel velocity of the particle. One can however show that these two quantities differ by a term which is small compared to $(\rho_c \nabla \cdot \mathbf{E}) / |\mathbf{E}|$—or any small parameters constructed from eqs. (1.6) and (1.7)

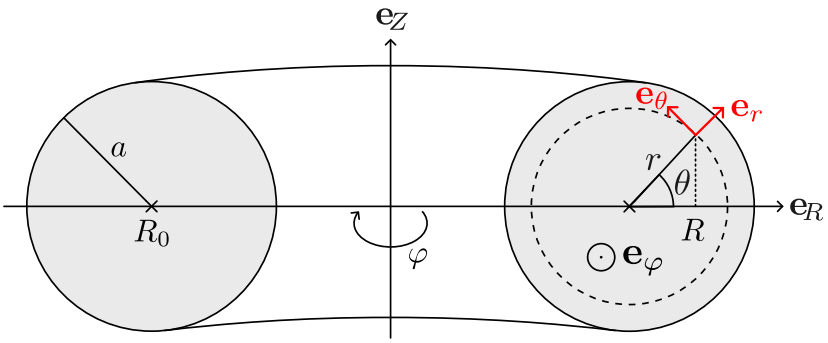

Figure 1.3: Toroidal geometry. Each unit vector is associated with its correponding coordinate, the radius r for $\mathbf{e}_r$, poloidal angle θ for $\mathbf{e}_\theta$, etc.

Magnetic field In the tokamak magnetic configuration, the magnetic field can be decomposed at leading order between a toroidal and a poloidal component. Such magnetic field can be approximated as

$$\mathbf{B}(r,\theta) = B_0 \left(\frac{r}{qR}\mathbf{e}_\theta + \frac{R_0}{R}\mathbf{e}_\varphi \right), \tag{1.13}$$

with $R = R_0 + r\cos\theta$ and B_0 is a constant. With this expression for the magnetic field, field lines are helical, as depicted on the right graph of fig. 1.4. More precisely, they adopt the shape of helixes that lie on nested torus surfaces. Altogether, magnetic field lines located at a given value of the radius r generate a magnetic surface that adopt a torus shape. In eq. (1.13) the safety factor q measures the helicity of the magnetic field lines. This factor represents the number of poloidal turns per toroidal turn and is defined as

$$q(r,\theta) = \left. \frac{\mathbf{B}\cdot\nabla\varphi}{\mathbf{B}\cdot\nabla\theta} \right|_{\text{field line}}. \tag{1.14}$$

In practice, the toroidal component of the field along the $\mathbf{e}_\varphi$ direction is obtained by using a set of poloidal coils, as represented on the leftmost graph of fig. 1.4. The poloidal component of the magnetic field is obtained by inducing a current in the toroidal direction in the plasma, as show on fig. 1.4, middle graph. This current can be created by several means, including *ohmic heating*, *non-inductive current drive* and can result as well from the *bootstrap current*[5]. A last remark is that the coils represented on fig. 1.4, right graph are usually completed by additional coils that can be used for (i) generating a vertical magnetic field to compensate some magnetohydrodynamic[6] forces

[5]Ohmic heating consists in considering the tokamak itself as the secondary of a transformer, and discharging a central solenoid located on the vertical axis in the center of the torus—along the $\mathbf{e}_Z$ direction on fig. 1.3—to induce the toroidal current. Non-inductive current drive refers to the injection of toroidal momentum using neutral beam injection, or radiofrequency current drive. The bootstrap current is self-generated by the plasma as a result of neoclassical effects [13, 14]

[6]Magnetohydrodynamics study the interaction between the plasma and an electromagnetic field. The plasma is described using a fluid model in this case. The system *plasma+magnetic field* of

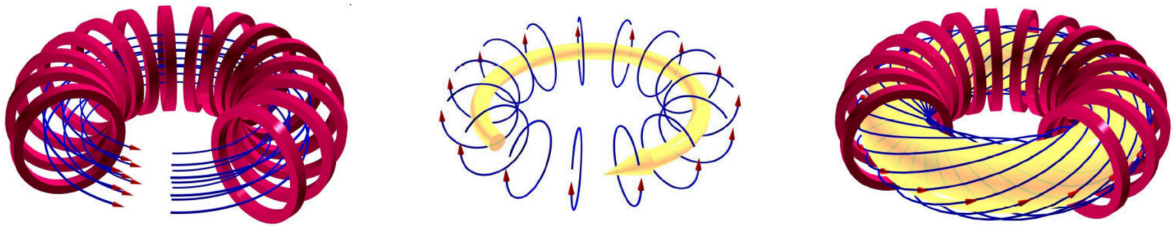

Figure 1.4: Left: purple poloidal coils create the blue toroidal magnetic field. Middle: the yellow toroidal current creates a blue poloidal field. Right: the combination of the toroidal and poloidal fields gives helical field lines. Images taken from [15].

felt by the plasma (such as the so-called tire tube and $1/R$ forces), (ii) shaping the poloidal cross section of the magnetic surfaces, and (iii) contributing to the generation of the toroidal current.

Particle trajectories In the adiabatic limit detailed in section 1.2.1, it is possible to fully determine the trajectories of charged particles in the tokamak magnetic configuration [12]. These trajectories are best studied using the invariants and symmetries of the problem. Three invariants can be identified: (i) the magnetic moment of a particle $\mu = \frac{1}{2}mv_\perp^2/B$, (ii) its energy $\mathcal{E} = \frac{1}{2}m_s v_\parallel^2 + \mu_s B + e_s\phi$, and (iii) the canonical toroidal momentum $P_\varphi = m_s R v_\varphi + e_s\psi$. In this last expression v_φ is the toroidal velocity of the particle, and ψ is the poloidal magnetic flux defined as $\psi = \frac{1}{2\pi}\int_{\mathcal{S}} \mathbf{B}\cdot d\mathbf{S}$, with $\mathcal{S}$ a surface contained in the poloidal plane and bounded by a magnetic field surface—for instance, the surface defined by $r =$ constant on fig. 1.3. In the following we investigate the trajectories of particles in the limit of a vanishing electric field[7]. One can thus write using the invariants that $v_\parallel^2 = 2(\mathcal{E} - \mu_s B)/m_s$. The magnetic moment μ_s is conserved, and the magnetic field possesses a maximum on the high field side of the device. Therefore, the last expression for $v_\parallel^2$ shows that there exist two classes of particles in a tokamak

1. The first class encompasses particles that have parallel velocities that never vanish during the motion. These are the so-called *passing particles*, as they explore both high and low field sides of the machine during their motion.

2. The second class of particles is composed of the ones for which this condition is not satisfied. Their parallel velocity vanishes during the motion. These are called

tokamak devices is subject to MHD activity. Indeed, the poloidal component of the magnetic field in the tokamak configuration is created by a toroidal current flowing in the plasma. On the contrary to tokamaks, stellarator devices do not rely on such a plasma toroidal current. Rather, these devices operate with twisted poloidal coils. The level of MHD activity is therefore much reduced in stellarators as compared to tokamaks.

[7]Considering a finite electric field does not change the nature of the particles trajectories detailed here. Indeed, in this case one may write that $\mathcal{E} - e_s\phi(\psi_*)$ remains constant at leading order in ρ_* during the particle motion, thus the rest of the analysis is unchanged. ψ_* denotes the magnetic flux surface the particle stays close to, see [12, p.14]

trapped particles.

An important remark is that the motion of both passing and trapped particles remains close to a given magnetic flux surface. Thus, in the limit of the adiabatic theory the tokamak magnetic configuration achieves confinement of charged particles in a closed region of space.

1.2.3 Radial transport in tokamaks

In tokamaks devices there exist mechanisms that lead to the breaking of the invariants presented in section 1.2.2. The breaking of the invariants of motion translates into radial transport. We understand radial transport as the movement of particles, momentum and energy across magnetic flux surfaces, from the core of the tokamak plasma towards its edge. Three main causes for radial transport can be identified in tokamaks

1. Modifications of the magnetic field topology introduced in section 1.2.2. For instance, magnetic ripple—a variation of the norm of the magnetic field in the toroidal direction—results in the breaking of the toroidal symmetry of the device. Magnetic ripple is due to the finite number of poloidal coils. Turbulent fluctuations of the magnetic field can lead to the connection of two magnetic flux surfaces, thus to radial transport. Turbulence is detailed in the third point below;

2. Coulomb collisions between particles, that imply that the magnetic moment of a particle μ_s can no longer be considered as invariant. In magnetized plasmas, collisions are mediated by the interaction between particles via the Coulomb force at the sub-Debye scale. Collisions deflect the trajectories of particles in any direction. The study of radial transport mediated by Coulomb collisions is called *neoclassical transport* [14];

3. Turbulence. Time variation of the electromagnetic field breaks the invariance of energy. Because of this time variation, electromagnetic turbulence appears, resulting in cross-field transport. In particular, turbulent fluctuations of the radial electric field leads to radial transport through the $E \times B$ drift velocity. Free energy sources—for instance density and temperature gradients—present in the system lead to the exponential growth of microscale electromagnetic turbulence.

Overall, the mechanism that dominates radial transport in tokamaks is turbulence [11]. The study of microscale turbulence is therefore critical to understand and predict confinement properties of a tokamak. A relevant framework to study turbulence is given by the gyrokinetic theory—which is essentially a reduction of a six-dimensional kinetic model to a five-dimensional one. We detail the gyrokinetic theory in section 5.2. Gyrokinetic simulations have produced a great variety of results concerning the study of tokamak turbulence [16–19]. As discussed in section 5.1, the correct description of turbulence in tokamaks requires to perform global simulations that describe the entire

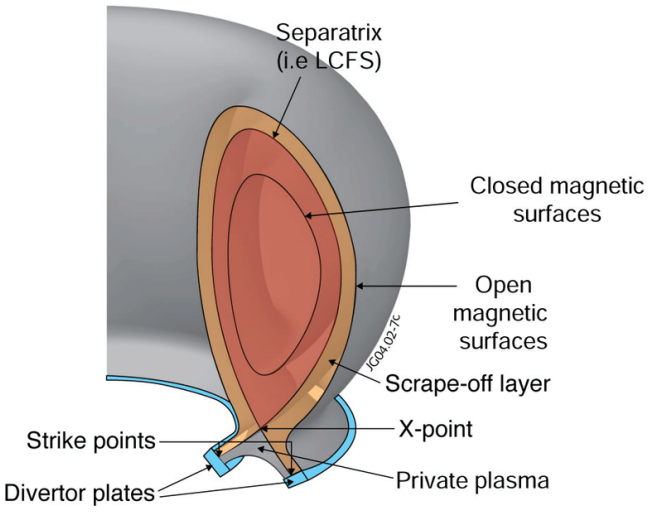

Figure 1.5: Core and Scrape-Off Layer region in a realistic tokamak device. Magnetic field lines in the Scrape-Off Layer hit the solid surface of the divertor.

plasma, from the plasma core to its edge. The present work mainly aims to improve the description of the edge region in gyrokinetic simulations.

1.3 Core and edge plasma physics

There exist two distinct regions in a tokamak: the core, and the Scrape-Off Layer. We now describe these two regions, along with the edge region. The *core* is characterized by closed magnetic field surfaces, whereas the *Scrape-Off Layer* is characterized by open field lines that intersect solid surfaces of the device. The magnetic flux surface that separates the core and Scrape-Off Layer regions is called the *separatrix*, or *Last Closed Flux Surface* (LCFS). The *edge* refers to a loosely defined region spanning from the outer core up to the separatrix. fig. 1.5 shows the core and Scrape-Off Layer regions, in the so-called divertor plasma configuration—see section 1.3.2 for more details about the divertor and for other possible magnetic configurations. We now give a brief description of the core and Scrape-Off Layer physics.

1.3.1 Core plasma

Parallel transport is much more efficient than cross-field transport. Thus the plasma density and temperature are nearly homogeneous on each closed field surface in the core. The core is the place where fusion reactions take place in a fusion reactor. Therefore, challenges related to the core plasma are (i) ensuring a high enough triple product to enable for fusion reactions and (ii) evacuate the fusion products—such as alpha particles—towards the plasma edge. The quality of confinement in the core plasma is mainly governed by turbulence. When going from the central region of the core

towards the edge plasma, the density and temperature decrease. These radial gradients represent sources of free energy for instabilities. As a result, microscale turbulent modes grow and result in a turbulent plasma state. Two key plasma instabilities for the establishment of turbulence in the core plasma. These are the *ion temperature gradient* (ITG) and *trapped electron modes* (TEM). Both instabilities are interchange-like. The ion temperature gradient instability arises on the low field side of the tokamak. It results from the combined effect of the temperature and magnetic field gradients. Trapped electron modes are the result of the resonant interaction between the toroidal precession of trapped particles and perturbations of the electric field [20]. TEMs are a key instability: they are thought to play a key role in how plasma shaping—in particular negative triangularity—influences confinement time.

1.3.2 Scrape-Off Layer plasma

In the Scrape-Off Layer region of a tokamak, magnetic field lines are open and intersect a solid material. We refer to this material by the *wall*, the *plasma-facing units*, or the *target plates*.

Magnetic configuration There are two main magnetic configurations of the Scrape-Off Layer in tokamak devices. These two configurations are visible on the two leftmost graphs of fig. 1.6. In the first one, the radial expansion of the core plasma is limited by a solid material tangent to the last closed field surface[8]. This is the *limiter* configuration. The second magnetic configuration for the Scrape-Off Layer is the *divertor* configuration. In this configuration, coils are used to divert magnetic field lines of the Scrape-Off Layer to a solid target located further away from the plasma. The solid target is called the divertor. The divertor configuration is the one adopted in modern tokamak devices and in particular in ITER. Plasma properties in the Scrape-Off Layer are very different from those of the plasma core. The main difference lies in the solid material that bounds each magnetic field line of the Scrape-Off. As detailed in section 2.1, solid surfaces act as perfect sinks for the plasma. This implies that plasma particles brought from the core to the Scrape-Off Layer—via cross-field transport for instance—will quickly reach the solid target by traveling in the direction parallel to the magnetic field lines and will be absorbed, see fig. 1.6, right graph. As transport in the direction parallel to the magnetic field is much faster than cross-field transport, the Scrape-Off Layer typical radial extension—denoted generally λ_q—is rather small. In ITER, it is predicted to be of the order of 1 mm [21]. This small width causes strong engineering constraints. Indeed, all the power coming out from the core is deposited on a very small surface of the limiter/divertor. The predicted heat flux resulting from this power deposition should not exceed $10\,\mathrm{MW/m^2}$ for ITER [22]. This value is very

[8] Because of radial transport, a plasma has the natural tendency to expand. It will therefore eventually reach a region where magnetic field lines intersect an element of the tokamak reactor walls. There is thus always a Scrape-Off Layer region within a tokamak device

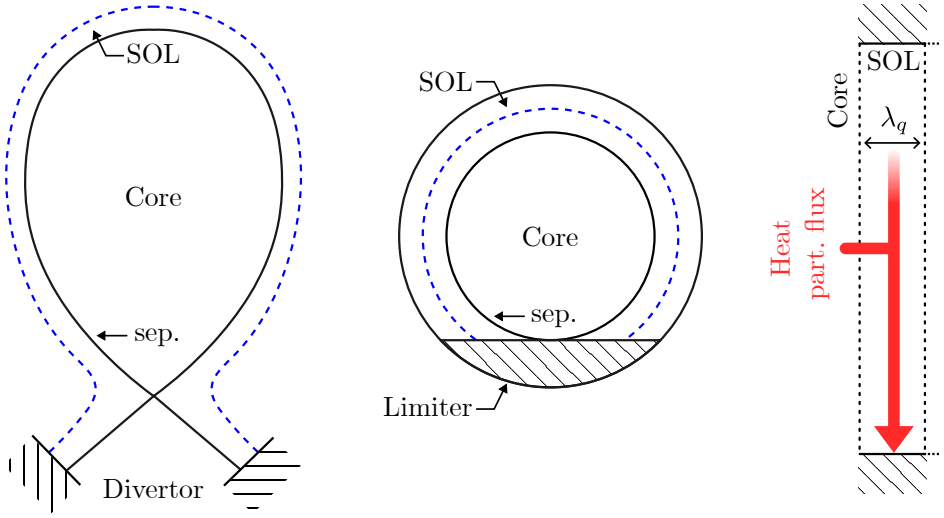

Figure 1.6: Leftmost graph: divertor magnetic configuration. Center: limiter magnetic configuration. On both graph, the separatrix (sep.) is represented, along with a magnetic field line in the Scrape-Off Layer in dashed blue. Rightmost graph: simplified Scrape-Off Layer geometry.

close to what can be handled by a solid material. Correct predictions of the Scrape-Off Layer width, along with assessing the magnitude of the heat flux reaching the divertor targets is key for designing a fusion reactor. As the λ_q width is directly linked to the levels of turbulent cross-field transport at the separatrix, a correct description of turbulence in the plasma edge is therefore critical.

Scrape-Off Layer regimes Depending on the operational parameters of a tokamak, several Scrape-Off Layer regimes can be identified. We use the simplified SOL geometry of fig. 1.6, right graph to study these regimes, where magnetic field lines have been straightened. In between the two target plates, there exists necessarily a point where the plasma mean velocity vanishes. This is the stagnation point. Plasma quantities evaluated at the stagnation point are denoted with the u subscript, for upstream. The same quantities at the solid target are denoted with a t subscript. We divide the different Scrape-Off Layer regimes into the following categories [23]. The transition between them is driven by the increase of the upstream density n_u. The regimes are

1. The *sheath-limited* regime, where the Scrape-Off Layer exhibits small temperature gradients in the parallel direction. This regime is characterized by a low collisionality. In this regime the particle flux at the target Γ_t is nearly proportional to the upstream plasma density n_u, i.e. $\Gamma_t \propto n_u$, and the plasma properties in the Scrape-Off Layer are governed by the physics of plasma-wall interaction that takes place close to the target. On the contrary to the conduction-limited regimes described hereafter, the interaction between the plasma and neutral particles in the Scrape-Off Layer is negligible in the sheath limited regime.

2. The *conduction-limited* regime, where the Scrape-Off Layer exhibits strong temperature gradients in the parallel direction. These gradients build up as a result of the parallel conductivity being small as compared to the sheath-limited regime. This regime can be further divided into distinct sub-regimes. When temperature gradient are strong enough so that the plasma close to the target plates become colder than typically 13.5 eV, ionization of neutral particles[9] become important. This is the *recycling* regime. When the upstream density further increases and the target temperature drops below 2 eV, the incoming plasma recombines before reaching the wall. Said differently, the ionization front moves from the wall surface and to the plasma volume. This is the *detached* divertor regime.

In the *detached* regime, the extraction of power exhaust by neutrals—or said differently the friction between plasma and neutral particles—effectively reduces the heat and particle fluxes levels at the plasma facing units by capturing part of the momentum and energy of the incoming ions. The detached regime proves to be particularly interesting for future fusion devices to operate with heat fluxes levels at plasma-facing units that remain within acceptable range. The ITER reactor for instance plans to operate in detached divertor regime [24].
In the spirit of improving the description of the edge Scrape-Off Layer regions in gyrokinetic simulations, this work mainly focusses on the sheath-limited regime, where the dominant player of the physics at play in the Scrape-Off Layer is plasma-wall interaction. Given the importance of plasma-neutral interaction for the study of experimental conditions that are relevant for future fusion devices, it is mandatory to include a description of plasma-neutral interaction in the gyrokinetic framework as well. We touch upon this point in section 4.1.

1.4 Gyrokinetic edge modeling

In this section we detail the reason why gyrokinetic simulations that encompass both core, edge and Scrape-Off Layer regions of the plasma are valuable to investigate tokamak performances.

Improved confinement regimes Tokamak plasmas notably self-organize and can bifurcate towards *improved confinement regimes*. An example of such regimes is the *high confinement mode* (H-mode). It is characterized by an increase of roughly a factor two of the plasma confinement time as compared to a plasma operating in a standard regime[10] [25]. This improved confinement regime is characterized by a steep gradient of plasma temperature and density—referred to as the *pedestal*—located in the edge

[9] Neutrals can be found close to the target plates due to two main mechanisms. The first one is the recycling process, where an impinging ion gets neutralized and injected back into the plasma. The second one is the injection of neutral particles close to the plasma-facing units by external means.

[10] The standard plasma confinement regime before bifurcating towards H-mode is usually referred to as *L-mode*, for low confinement mode.

plasma region, see [26] for a comparison of typical density and temperature profiles in low and high confinement regimes. The formation of the pedestal is the footprint of an underlying transport barrier, i.e. a localized region in the vicinity of the separatrix where turbulent transport is reduced. The study of such improved confinement regime is of uttermost importance for future fusion devices. In addition to maximizing the fusion output—by achieving the highest possible density and temperature in the core region—a crucial point is to operate the plasma in regimes compatible with engineering constraints. Although the high density and temperature of the top-pedestal region drives the improved performance of H-mode plasmas [27], this comes at a non-negligible cost. The high confinement mode is accompanied by intermittent bursts of plasma released in the Scrape-off through quasi-periodic relaxations of the pedestal—the so-called *Edge Localized Modes* (ELMs) [28, 29]. Mitigating the consequences of these bursts is crucial so that particle and heat fluxes levels at the plasma facing units remain within acceptable range to avoid damaging the solid wall. This mitigation can be achieved by several means. The ITER reactor plans for instance to use shallow pellet injection and possible suppression of ELMs using resonant magnetic perturbations. ITER is also planned to operate in detached divertor conditions with injection of neutrals to control the heat and particle fluxes at the plasma facing units. Another possibility regarding the mitigation of drawbacks of the high confinement mode consists in resorting to other scenarii for bifurcated plasma states. Other improved confinement regimes have been reported experimentally, such as the *I-mode* or *quiescent H-mode*[11]. Overall, the plasma condition in the edge and Scrape-Off Layer appears as critical for the safe operation of the device and for understanding self-organization processes. As a result, turbulent simulations including core, edge and Scrape-Off Layer regions would give very valuable insights concerning the properties of turbulence and radial transport in the edge region, helping to understand mechanisms underlying confinement properties of tokamaks, and possibly allowing for the study of improved confinement regimes.

Gyrokinetic modeling An adapted framework to study turbulence in tokamak plasmas is given by the gyrokinetic theory [32, 33], that is in essence a reduction of a six-dimensional phase space kinetic model to a five-dimensional one. The reduction is performed by expanding a kinetic equation with the small parameter $\rho^* = \rho_i/a$—with ρ_i the ion Larmor radius and a the minor radius of the device. The resulting equation does not depend on the cyclotron phase. This reduction in dimensionality enables to perform simulations of tokamak plasmas, that would otherwise be too intensive in terms of computational resources if performed with a fully kinetic model. Gyrokinetic codes have been largely used to perform simulations of core plasmas. A review of main

[11] The I-mode regime is characterized by a pedestal for the electron temperature while densities and ion temperature profiles are similar to those of a L-mode plasma [30]. The quiescent H-mode regime is a type of H-mode regime without ELMs [31]. Plasmas in quiescent H-mode are characterized by a toroidal rotation stronger than H-mode plasmas. This rotation drives a continuous MHD mode at the edge.

results obtained with such simulations can be found in [16]. Results include the study of large scale structures created by turbulence, such as *Zonal Flows*, *streamers* and *avalanches*[12]. All these mechanisms affect radial transport in core tokamak plasmas. As explained in section 5.1, there are sustained efforts in the gyrokinetic community to include the edge and Scrape-Off Layer regions within a single gyrokinetic simulations[13]. Capturing the transition from closed field lines in the core to open field lines in the Scrape-Off Layer is critical to correctly describe turbulence levels in the edge region, see section 5.1 and [4] in particular. Describing the edge in the gyrokinetic framework is not straightforward due to (i) the possible breakdown of some assumptions of the gyrokinetic theory in the edge, see section 5.1.2, and (ii) by the physics at play in the Scrape-Off Layer that is the interaction between the plasma and its boundary, and possibly with neutrals, see section 5.1.

1.5 Numerical developments

The extension of gyrokinetic core simulations to global simulations that encompass both core and Scrape-Off Layer regions raises several numerical challenges. One of these many challenges consists in resolving the entire range of plasma temperatures from the core—where temperature are in the range of 10 keV—to the vicinity of material boundaries—where temperatures can be as low as a few eVs. Given that the typical width of the distribution functions scales like the square root of the temperature, such a temperature gradient requires using non-uniform meshes in velocity space to correctly resolve both hot (broad) and cold (narrow) distribution functions. Developing algorithms to handle efficiently such non-equidistant meshes within the Backward semi-Lagrangian framework of GYSELA[14] is a research topic in itself. In particular, the spline interpolation step used by the GYSELA code must be adapted for such non-uniform meshes (using non-equidistant cubic splines in particular). So as to test these new numerical techniques in a simplified framework, the two-dimensional VOICE code used to perform plasma-wall interaction simulations—see chapters 2 and 3—has been used to investigate the performance of non-uniform splines. The results of this study can be found in [3] and are detailed in section 2.5.2.
Moreover, performing global simulations in the gyrokinetic framework requires *exascale supercomputers*[15]. Gyrokinetic codes must be massively parallelized, and opti-

[12]Zonal flows are fluctuations of the flux-surface averaged plasma poloidal velocity [34], streamers are convective cells that are elongated in the radial direction [35] and avalanches are intermittent burst of plasma turbulence propagating radially outwards [36]

[13]Examples of such efforts include the EUROfusion projects E-TASC/TSVV1 TSVV4 lead by T. Görler and D. Told respectively, focussing on the topics *Physics of the L-H transition and Pedestals*, and *Particle/heat Exhaust: Gyrokinetic/Kinetic Edge Codes*. The E-TASC acronym stands for *EUROfusion-Theory and Advanced Simulation Coordination* and TSVV for *Theory, Simulation, Validation and Verification*.

[14]see section 5.4 for a description of the GYSELA code and its numerical algorithm.

[15]Such computers are capable of performing at least 10^{18} double-precision operations per second [37], and are the next generation of supercomputers.

mized for the architecture it is executed on. The adaptation of the code so that it can be run efficiently on different parallelized architectures: CPU, GPU, from different manufacturers, is a challenge. Developing *high performance computing* codes—such as GYSELA—that are massively parallelized for such a variety of hardware configurations, without having a separate version of the code dedicated to each specific architecture, is mandatory. Indeed, having for instance a MPI+OpenMP version of the code used for a parallel CPU execution and a CUDA version of the code used for GPU execution is not possible, due to the difficulty for maintaining each version of the code. Overall, including advanced numerical schemes—such as non-uniform meshes—in an exascale code adaptable to several architectures requires advanced coding tools. The current version of the GYSELA code is written in the FORTRAN 90 language, and is not compatible with an execution on a GPU architecture. This has motivated the porting of the code to the modern `C++` programming language. This re-writing phase is ongoing. The switch to the `C++` language allows for instance for using advanced libraries such as the `DDC` and `Kokkos` libraries [38, 39]—for efficient manipulation of multi-dimensional arrays, and multi-architecture parallelization with a single version of the code—or the `GoogleTest` framework [40] for convenient unitary testing. Integrating such tools into the GYSELA framework requires a complete redevelopment of the code. The adopted strategy for such redevelopment is to start from building a two-dimensional version of the code identical to the VOICE code—described in section 2.5—and then progressively increase the dimensionality and complexity of the model towards a five-dimensional gyrokinetic code. During my PhD I have been much involved in the development of the two-dimensional version of the `C++` GYSELA code.

1.6 Outline of the thesis

The present work focuses (i) on the study of plasma-wall interaction using a kinetic model with immersed boundary conditions, (ii) on the extension of the model to describe the interaction between charged and neutral particles with a fluid neutral model, and (iii) on the improvement of the description of the edge and Scrape-Off Layer regions in the global, full-f and flux-driven GYSELA code [41]. We first use the two-dimensional (1D in space, 1D in velocity space) VOICE code to investigate the interaction between a plasma and a solid surface by means of immersed boundary condition. With this technique the main features of plasma wall interaction are recovered, see chapter 2. Namely, we recover a positively charged region that forms in front of the solid wall that is reminiscent of the Debye sheath. The positively charged region translates into a drop of the electric potential, that repels a fraction of the slowest electrons back into the plasma and accelerates ions towards the wall. Overall, the physics at play in the Debye sheath ensures that quasineutrality holds within the plasma. Next, in chapter 3 we investigate the kinetic simulation results using the hierarchy of fluid equations. By doing so, we find that the validity of the Bohm criterion—that states that the ion flow at the entrance of the sheath must be supersonic—can be questioned. More precisely,

(i) the Bohm criterion does not appear to be applicable in the kinetic framework, and (ii) the speed of sound waves used to express the Bohm criterion appear to critically depend on the choice of the closure for the fluid hierachy. This last observation bears consequences for fluid codes that rely on such a criterion. In chapter 4 we extend the kinetic description of the plasma to include its interaction with neutrals, modeled using a fluid *pressure-diffusive* model. Last, in chapter 5, using the knowledge obtained from studying plasma-wall interaction with the reduced kinetic model, and by taking advantage of already-existing models for gyrokinetic plasma wall interaction, we propose a new approach using immersed boundary conditions to model the wall region. When dealing with this model, only the sheath-limited regime is considered, where the interaction between plasma and neutrals is neglected. A particularity of the considered plasma-wall model is that is uses immersed boundary conditions, and is compatible with Backward semi-Lagragian numerical schemes. The model aims to ensure that the most important feature of plasma-wall interaction is reproduced without solving the characteristic spatial and time scales of the Debye sheath, namely that the plasma remains quasineutral. This is achieved by (i) absorbing ions and fast electrons incoming on the material boundary surface and (ii) reflecting a portion of the slowest electrons on this surface. The transition between slow and fast electrons is defined by a cutoff velocity, obtained by matching the electron and ion fluxes on spatial average over the entire material boundary surface. We investigate the validity of this model within the GYSELA framework, discuss its current limitations and explore possible ways forward.

2

Kinetic plasma-wall interaction using immersed boundary conditions



Contents

2.1 Fundamentals of plasma-wall interaction 40
2.2 Kinetic plasma description 43
2.3 Immersed boundary conditions 45
2.4 Source and collisions 49
2.5 The VOICE code 52
2.6 Conducting and insulating walls 56
2.7 Kinetic physics of the sheath 58
2.8 Parameter scans 62
2.9 Conclusion of the chapter 68

Summary

In the perspective of proposing a model for including realistic plasma boundary conditions at the limiter/divertor surface in the gyrokinetic framework, we first study the kinetic physics of plasma-wall interaction, using immersed boundary conditions—or penalization—to describe the solid wall that bounds a plasma. This technique has already been successfully used to include the subgrid physics of plasma-wall interaction within fluid codes. The majority of the results presented in this chapter have been published in [1]. To assess the robustness of the penalization technique we investigate two different models for describing the immersed wall region, that either allow or forbid currents to exist in the wall. In both cases we retrieve important kinetic features of the Debye sheath physics: a positively charged region—that we refer to as *the sheath*—which is a few Debye lengths wide appears in front of the solid boundary. This positively charged region translates into a drop of the electric potential. This drop reflects a portion of the slowest electrons back into the plasma, while the fastest are absorbed in the wall region. The potential drop further translates into an acceleration of ions, and overall the electron and ion fluxes are equal at the plasma boundary, hence the plasma remains quasineutral on scales typically larger than the Debye length. Both

wall models however exhibit a flux of electrons that is emitted from the wall region back into the plasma. This is an undesirable artefact that result from the immersed boundary condition technique. We assess whether or not it is possible to control this electron re-emission for both wall models. We then quantify the impact of this re-emission on the electric potential drop that exists in the sheath by comparing the simulated drop with a simple analytical prediction.

2.1 Fundamentals of plasma-wall interaction

In this section we describe the basic physics of the interaction between a plasma and a solid surface. In particular we describe the physics at play in the so-called sheath and presheath layers. Last, we touch upon how the physics of plasma-wall interaction is modified when accounting for a tilt angle between the magnetic field line and the solid wall.

2.1.1 The sheath boundary layer

Any solid surface—sometimes referred to as *a wall* in the following—surrounding a plasma acts as a perfect sink of plasma particles, momentum and energy. Indeed, a wall has a large density and low temperature compared to the hot and less dense plasma. This property governs a prompt recombination of any plasma ions impinging the solid boundary. The plasma disappears into the wall material, thus driving a plasma flow into it. It is generally assumed that the boundary material is at constant conditions and grounded. It thus acts as a thermal bath and as an infinite reservoir of particles. Due to the inertia difference between electrons and ions, the former tend to be lost in the wall more easily than the latter. As a consequence, a boundary layer—called the *sheath*—appears in front of the wall. The sheath layer can be understood as a region of space where a positive charge develops. This charge creates a drop of the electric potential that confines bulk—i.e. low-velocity—electrons in the plasma, and accelerates ions up to the wall. We give a precise definition of *bulk electrons* below. The sheath potential drop regulates the ion and electron fluxes to the wall so that no charge separation appears in the plasma on scales larger than the Debye length. The Debye length λ_D corresponds to the typical length scale of the sheath boundary layer [23]. It is expressed as

$$\lambda_D = \sqrt{\frac{\varepsilon_0 T}{ne^2}}, \tag{2.1}$$

where n and T are the plasma typical density and temperature. The typical timescale that sets the relaxation time of a perturbation that would appear in the sheath—for instance a perturbation of the electric potential—is given by the inverse of the electron plasma frequency ω_{pe}^{-1}, with

$$\omega_{pe} = \sqrt{\frac{ne^2}{m_e \varepsilon_0}}. \tag{2.2}$$

A prediction for the electric potential drop that exists in the sheath can be found in [23]. The derivation is recalled in appendix A.3.1. This prediction gives

$$\Delta\phi_{\mathrm{sh}} = \frac{T_e}{2e}\log\left(2\pi\frac{m_e}{m_i}\left(1+\frac{T_i}{T_e}\right)\right), \tag{2.3}$$

where m_e and m_i stand for the electron and ion mass, T_e and T_i are the electron and ion temperatures. This potential drop is localized between the entrance of the sheath and the wall. We give a precise definition of the entrance of the sheath in appendix A.4. For now it is understood as the approximate position on the considered magnetic field line where the charge density becomes non negligible so that the plasma cannot be considered as quasineutral. Assuming equipartition $T_i = T_e$ gives for a plasma composed of Deuterium ions $e\Delta\phi_{\mathrm{sh}}/T_e \approx -2.8$. The sheath boundary layer is preceded on the magnetic field line by a quasineutral region called *presheath*. In the presheath exists a small positive electric field. A typical value for the electric potential drop in the presheath is $e\Delta\phi_{\mathrm{pre.}}/T_e \approx -0.7$. The presheath electric field is very small compared to the sheath electric field since its typical scale is given by the parallel extension of the magnetic field line $L_\parallel \approx qR \approx 50\,\mathrm{m}$ for ITER-like values of the major radius R and safety factor q. Note that the discussion presented above is valid when the considered magnetic field line impacts the solid wall with a normal incidence. In the case whith oblique incidence, an additional layer called *presheath* is present as well. We comment on this oblique incidence case in section 2.1.3.

2.1.2 Kinetic physics of the sheath and presheath

The positive electric field that exists in the sheath repels electrons and accelerates ions. Due to the repulsive Coulomb force that acts on electrons in the sheath, the electron population can be understood as being split into two classes that are the *bulk* and *fast* electrons. Bulk electrons are the ones that do not possess enough kinetic energy to overcome the sheath potential drop given in eq. (2.3). We sometimes refer to these electrons as *slow* electrons. Electrons that have high enough kinetic energy to reach the wall are called *fast*. These electrons are therefore absorbed in the wall. In the absence of sources or sink of particles in the sheath, and without collisional processes the energy of an electron is conserved in the sheath. Therefore from the sheath potential drop we can compute a threshold velocity $v_c = \sqrt{2e\Delta\phi_{\mathrm{sh}}/m_e}$. Slow electrons have velocities $v \leq v_c$ at the entrance of the sheath, while fast electrons are characterized by $v > v_c$. Positive velocities correspond here to particles traveling towards the wall. We see here that the physics at play within the sheath physics is inherently kinetic: depending on their velocity electrons will, or will not reach the wall during their motion in the sheath.
The electric field that exists in the sheath accelerates ions up to the wall. From a rapid energy balance one gets that the kinetic energy gained by ions in the sheath exactly balances the kinetic energy lost by fast electrons as they are slowed down in the sheath by the electric field. Bulk electrons do not contribute to this energy balance as they

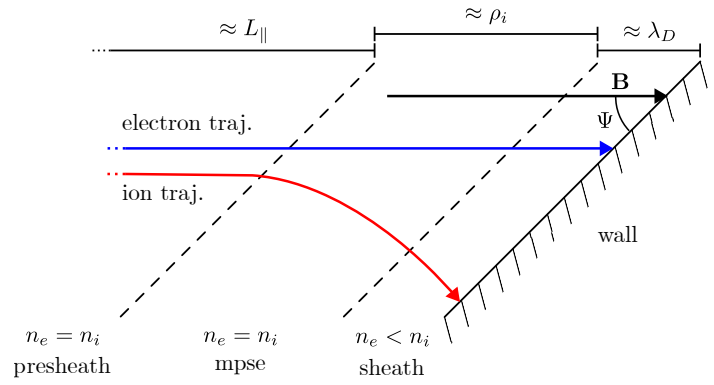

Figure 2.1: The magnetic presheath (mpse) is located in between the presheath and the Debye sheath. The motion of electrons remain undisturbed by the magnetic presheath.

bounce back to the plasma. For the same reason, these slow electrons do not contribute to the electron flux that reaches the wall. As stated above, the main effect of the sheath is to ensure that no charge separation appears in the plasma on scales larger than the sheath typical scale—the Debye length. When neglecting transport across field lines, and assuming a grounded wall this is equivalent to stating that the flux of fast electrons must balance the flux of ions at the entrance of the sheath. When cross-field transport is taken into account, this equality of fluxes is not necessarily verified. Indeed in this case current loops between different parts of the wall may exist. On spatial average over the entire plasma solid boundary, and time average over times larger than ω_{pe}^{-1} the equality of electron and ion fluxes must however be verified so that the plasma remains quasineutral.
The physics at play in the presheath is very similar to the one in the sheath: electrons are slowed down by the drop of the electric potential that exists in this region, while ions are accelerated. A famous result concerning the presheath physics is that the presheath electric field must accelerate ions so that they reach the entrance of the sheath with supersonic velocities. This is the Bohm criterion. It is discussed in detail in Chapter 3.

2.1.3 Tilted magnetic field lines and the magnetic presheath

Tokamak devices operate with an angle ψ between the magnetic field and the plasma facing components close to 0°. This grazing magnetic field angle allows for reducing the heat flux deposited on the plasma-facing components. By denoting $q_\parallel$ the heat flux in the direction of the magnetic field $\mathbf{B}$, one can write that the heat flux received by the solid plasma boundary q_w is $q_\mathrm{w} = q_\parallel \sin\psi$. Because of this tilt angle, an additional boundary layer develops at the plasma-wall interface. This layer is the *magnetic presheath*, or *Chodura sheath* [42]. The Chodura sheath has a typical width of the order of the ion larmor radius ρ_i, which it is large compared to the Debye

sheath—that has a typical width of the order of λ_D. In section 5.3 we show that taking typical values for the density and temperature of a Scrape-Off Layer plasma leads to $\rho_i/\lambda_D \approx 50$. As a result, the magnetic presheath is quasineutral. It is located in between the presheath and the Debye sheath, as depicted on fig. 2.1. The main effect of the magnetic presheath is to divert the parallel motion of ions such that their motion becomes orthogonal to the solid wall at the entrance of the Debye sheath, see fig. 2.1. It can be shown that the potential drop across the magnetic presheath $\Delta\phi_{\mathrm{MPS}}$ typically scales like

$$\frac{e\Delta\phi_{\mathrm{MPS}}}{T_e} \approx \log(\sin\psi)\,. \tag{2.4}$$

In the present work we largely ignore the effect of the magnetic presheath on the plasma properties. The combined effect of the {magnetic presheath + sheath} layers on the plasma is to ensure equality of electron and ions fluxes on spatial and time average at the plasma boundary. When the magnetic field line is tilted with respect to the wall, a fraction of the potential drop that exists in the sheath is transferred to the magnetic presheath so that the ion gyromotion is distorted as explained above, so that the equality of fluxes is satisfied. Therefore, as far as the quasineutral plasma—without the magnetic presheath—is concerned, there is fundamentally no difference between (i) tilted magnetic field lines bounded by a magnetic presheath and sheath layers, and (ii) field lines with a normal incidence bounded by a sheath. In both cases, the plasma remains quasineutral. Moreover, as both sheath and magnetic presheath cannot be described by the usual gyrokinetic theory, we chose to include the combined effect of the magnetic presheath and sheath layers on the plasma by proposing in Chapter 5 a subgrid model that effectively ensures the equality of electron and ion fluxes at the plasma facing units.

2.2 Kinetic plasma description and simplified magnetic geometry

In this section we give the equations that describe a plasma from a kinetic standpoint. Then, we introduce the simplified one-dimensional kinetic model we use later on to study the interaction between a plasma and a solid surface. A kinetic description of a plasma is given by the Boltzmann equation

$$\partial_t f_s + \mathbf{v}\cdot\nabla_{\mathbf{x}} f_s + \frac{e_s}{m_s}\left(\mathbf{E}+\mathbf{v}\times\mathbf{B}\right)\cdot\nabla_{\mathbf{v}} f_s = \mathcal{C}(f_s) + \mathcal{S}(f_s), \tag{2.5}$$

where e_s and m_s are the charge and mass of species s. The distribution function $f_s(\mathbf{x},\mathbf{v},t)$ is defined in 6-dimensional phase space $(\mathbf{x},\mathbf{v})$, where $\mathbf{x}$ is the spatial coordinate in phase space and $\mathbf{v}$ is the velocity coordinate. This distribution function measures the probability density of particles within an infinitesimal volume $d^3\mathbf{x}\,d^3\mathbf{v}$ centered on $(\mathbf{x},\mathbf{v})$. In order to get a closed system eq. (2.5) must be complemented

by Maxwell's equations that describe the dynamic of the mean field $(\mathbf{E}, \mathbf{B})$[1]. Kinetic descriptions require however too much computational power to provide a practical way of describing an entire tokamak plasma. In order to describe such a system, one has to further reduce the dimensionality of the problem. Examples of such simplifications are given by fluid models, see Chapter (3), or gyrokinetic models, see Chapter 5. Kinetic modeling is however suited for lower dimensionality studies such as the one presented here.

For the present chapter, we study the interaction between a plasma and a solid surface using a two-dimensional model. We consider a single Scrape-Off Layer magnetic field line, with a geometry represented on fig. 2.2, left graph. This field line is connected to the divertor wall at its both ends. Curvature effects are neglected and the field line is flattened, giving the geometry of fig. 2.2, top right graph. We assume that this straight line impacts the divertor with a normal incidence. The effect of cross-field transport is modeled by a particle source term described in section 2.4.1. The problem is now one-dimensional in position space and one dimensional in velocity space. We use the x variable to specify the considered position on the field line. The v variable expresses the parallel velocity of the considered particle. The distribution function of species s is thus $f_s(x, v, t)$. The subscript s denotes the species the quantity refers to: e for electrons, i for ions. We assume the magnetic field to be constant and homogeneous along the considered field line. Under these circumstances the Boltzmann equation given in eq. (2.5) reduces to

$$\partial_t f_s + v\partial_x f_s - \frac{e_s}{m_s}\partial_x\phi\,\partial_v f_s = \mathcal{C}(f_s) + \mathcal{S}(f_s). \tag{2.6}$$

The $\mathcal{C}(f_s)$ term accounts for self species collisions and electron-ion momentum and energy exchanges. Collisions are described in detail in section 2.4.2. The $\mathcal{S}(f_s)$ operator represents sources and sinks. For the present model it is composed of up to three distinct entities $\mathcal{S} = \mathcal{S}_{\text{sink,n}} + \mathcal{S}_{\text{sink,T}} + \mathcal{S}_{\text{src}}$. The sink term $\mathcal{S}_{\text{sink,n}}$ characterizes the wall region and is described in section 2.3.1. The heat sink term $\mathcal{S}_{\text{sink,T}}$ is included in the model only for a particular description of the wall region, see section 2.3.2. The source term $\mathcal{S}_{\text{src}}$ is described in section 2.4.1. We work in the electrostatic limit where the electric field is $-\partial_x\phi$. We thus close eq. (2.6) by complementing it with the following Poisson equation

$$-\varepsilon_0\partial_x^2\phi = \rho_c \quad \text{with} \quad \rho_c = \sum_{\text{species}} e_s n_s, \tag{2.7}$$

where we introduced the charge density ρ_c and the local density n_s of species s. This last quantity is defined as the integral over the velocity space $n_s = \int dv\, f_s$. The Boltzmann-

[1]Similarly to the distribution function, the mean electromagnetic field present in a Boltzmann equation results of an averaging process conducted over a large number of realizations of the considered system. As a result, the mean electric field $\mathbf{E}$ for instance does not contain information about the electric potential created by each individual particle, that goes as $\phi \propto e_s/r$ with r the distance to the charge e_s.

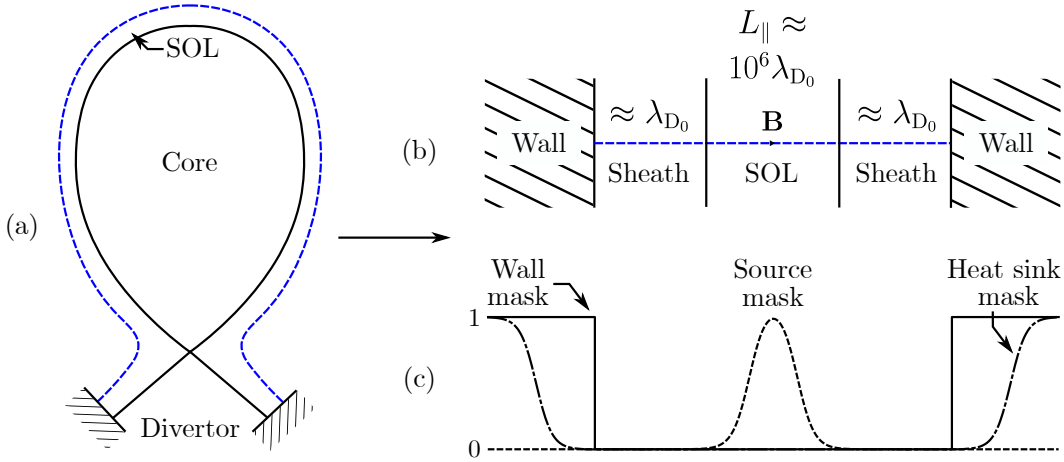

Figure 2.2: (a) Poloidal projection of a tokamak magnetic geometry. (b) Simplified geometry with no curvature. The field line represented as a dashed blue line hits the divertor walls at both ends. (c) Masks used to define the wall and plasma regions.

Poisson system is normalized to time and length scales relevant to study plasma-wall interaction. We use a reference density n_0 and temperature T_0. Time is normalized to the inverse of the electron plasma frequency $\omega_{pe_0} = \sqrt{n_0 e^2/m_e\varepsilon_0}$. The space variable x is normalized to the Debye length $\lambda_{D_0} = \sqrt{\varepsilon_0 T_0/n_0 e^2}$. The electrostatic potential is normalized to T_0/e. The phase space velocity variable v is normalized to the thermal velocity of each species $v_{T_{0s}}$ as $v_s = v/v_{T_{0s}}$, with the thermal velocity of species s written as $v_{T_{0s}} = \sqrt{T_0/m_s}$. Particle distribution functions are normalized to the reference particle density in phase space $n_0/v_{T_{0s}}$. We use the notation $A_s = m_e/m_s$ to express the mass ratio between electrons and species s (in particular $A_e = 1$). The normalized charge of species s is written as $Z_s = e_s/e$. The normalized Boltzmann-Poisson system then reads as follows

$$\partial_t f_s + \sqrt{A_s}\,(v_s \partial_x f_s - Z_s \partial_x \phi\, \partial_v f_s) = \mathcal{C}(f_s) + \mathcal{S}(f_s) \tag{2.8}$$

$$\partial_x^2 \phi = -\rho_c \quad \text{with} \quad \rho_c = \sum_{\text{species}} Z_s n_s, \tag{2.9}$$

where all variables are normalized, but we kept the same notations as in the dimensional expressions for the sake of simplicity. In the following we write by default all quantities in their dimensional form. If a reference to some normalized quantity is needed, it will be explicitly pointed out.

2.3 Immersed boundary conditions

In this section we detail the technique we use to model plasma-wall interaction, that is the immersed boundary conditions—or penalization—technique. This solution has already been successfully used to include plasma-wall interaction in fluid descriptions

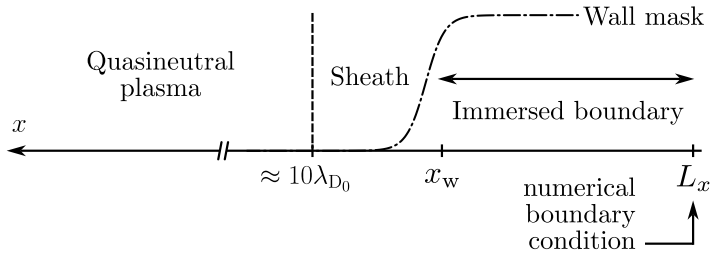

Figure 2.3: Treatment of the material boundary. The mathematical boundary condition is relegated away from the region of interest where the plasma-wall transition takes place. The wall region acts as a particle, momentum and energy sink. This region plays the role of an immersed boundary condition from the plasma point of view.

of a plasma—see [43, 44] and section 3.2—without resolving the characteristic spatial and time scales of the sheath. In the spirit of using the same solution within the gyrokinetic framework, we first show that it is possible to use penalization to simulate plasma-wall interaction. We detail in the present section two penalized models for the wall region, that either allow for current to exist in the wall or does not.

2.3.1 Immersed wall model

Using immersed boundary conditions to simulate plasma-wall interaction consists in including the wall in the simulation domain. The wall is described using the same system of equations as the one used for describing the plasma, i.e. in our case the Boltzmann-Poisson system given in eqs. (2.8) and (2.9). The difference between plasma and wall regions lies in the fact that in the wall region, a sink of particles, momentum and energy is contained in the source term $\mathcal{S}$ of the Boltzmann equation. This source term models the atomic recombination processes at play in the wall, so that the plasma boundary effectively acts as a sink of particles, momentum and energy. The absorbing wall boundary condition is therefore "immersed" in the simulation box. In other words, from a numerical point of view the wall appears in the simulations as a plasma with altered (i.e. penalized) dynamics. The boundary layer at the wall interface then develops independently of the numerical boundary conditions. These boundary conditions are still necessary to solve the Boltzmann-Poisson system in the mathematical sense. They are imposed at $x = 0$ and $x = L_x$ (with L_x the spatial length of the simulation box), far from the sheath region, see fig. 2.3. The immersed boundary condition is introduced in the Boltzmann eq. (2.8) using the particle sink term $\mathcal{S}_{\text{sink,n}}$, a Bhatnagar-Gross-Krook operator—or BGK operator [45]. It acts as a particle, momentum and energy sink. It is written as

$$\mathcal{S}_{\text{sink,n}}(f_s) = -\mathcal{M}_{\text{w}}\nu_s\left(f_s - f_{\text{ws}}\right). \tag{2.10}$$

Target function The structure of this operator is that of a restoring force that drives the distribution function f_s towards the target distribution f_{ws}. We chose this target

function as a Maxwellian. This target function is

$$f_{\mathrm{w}s}(v) = \frac{n_{\mathrm{w}}}{\sqrt{2\pi T_{\mathrm{w}}/m_s}} \exp\left(-\frac{m_s v_s^2}{2T_{\mathrm{w}}}\right). \tag{2.11}$$

This function does not depend on the spatial coordinate x. The density n_{w} and temperature T_{w} are constant in space and time. The wall target density n_{w} is orders of magnitude smaller than the plasma typical density, so the operator acts as a particle sink. Typically we take $n_{\mathrm{w}} \approx 10^{-9}$ in the simulations, while the plasma has a density close to unity far from the wall region[2]. For sufficiently small values of the wall target density n_{w}, one can expect the plasma-wall interaction physics to be independent of this density. We have checked that it is indeed the case with the chosen value of wall density. As an example, the potential drop in the sheath region is independent of the particular value of n_{w}. The target temperature T_{w} is a free parameter. The typical value taken for this temperature does not however influence the properties of the plasma. Indeed, the temperature T_{w} governs the typical width of the target function f_{w}. Given that this target function has a very low density, we can write $\mathcal{S}_{\mathrm{sink,n}}(f_s) \approx -\mathcal{M}_{\mathrm{w}}\nu_s f_s$, an expression that is independent of the wall temperature. At first order, the wall effect is to relax f_s towards zero, thus effectively absorbing plasma particles, momentum and energy. Similarly, one could take a target function characterized by a non-vanishing mean velocity without impacting the plasma characteristics.

Wall mask The particle sink operator is localized in the wall region using the mask function $\mathcal{M}_{\mathrm{w}}$. It is this function that defines the wall region in the simulation domain. It is expressed as

$$\mathcal{M}_{\mathrm{w}}(x) = 1 - \frac{1}{2}\left\{\tanh\left(\frac{x - x_{\mathrm{w}}^{\ell}}{d_{\mathrm{w}}}\right) - \tanh\left(\frac{x - x_{\mathrm{w}}^{r}}{d_{\mathrm{w}}}\right)\right\}.$$

This function is represented on fig. 2.2, bottom left graph. The x_{w}^{ℓ} and $x_{\mathrm{w}}^{\mathrm{r}}$ parameters define the spatial positions where the mask function is equal to $1/2$ as it steps down from 1 in the wall to 0 in the plasma. The wall region is therefore defined by $\mathcal{M}_{\mathrm{w}}(x) = 1$ while the plasma region is such that $\mathcal{M}_{\mathrm{w}}(x) = 0$. Intermediate values characterize gray regions where the wall sink is active but the plasma density is still larger than the target value n_{w}. The characteristic width of this intermediate region is d_{w}, typically a

[2]The choice for the particular value taken for n_{w} is arbitrary, but is nevertheless motivated by physical and numerical considerations. The density of the wall should be small compared to the plasma typical density, so that the wall effectively acts as a sink of particles. From a numerical point of view, it is easier to take $n_{\mathrm{w}} \neq 0$ to avoid negative values of the distribution function in the wall region. Indeed, as the Voice code uses a semi-Lagrangian scheme for solving the advective part of a Boltzmann equation, an interpolation method is required, see section 2.5.1 Typically we use cubic spline interpolation to perform this procedure. Interpolating data points that are very close to zero may lead to negative values as the spline often shows small oscillations around the interpolated data points. To avoid this, the chosen value for the wall density is non-zero.

fraction of the Debye length, see section 2.5.3. In the simulations we take the maximum steepness which is compatible with the chosen discretization refinement and timestep[3]. The steepness of the wall mask that we have considered has been checked to be large enough, that the observed sheath physics becomes independent of this parameter.

Restoring force magnitude The third parameter in the chosen restoring force eq. (2.10) is the species-dependent amplitude ν_s. We always take a constant value ν_i for the ions restoring force, hence fixing the recombination rate for this species. We address two different restoring force for the electrons, corresponding to two different wall models. The first wall model consists in setting $\nu_e = \nu_i$, therefore constant in time and space. In the following, we refer to this wall model with equal sink amplitude as the *conducting wall* because it is found to exhibit an electrical current with reduced charge density, as will be shown in section 2.6. This naming is only for convenience because neither the wall resistivity nor any electrical current properties of the wall are addressed in the chosen reduced wall model. The second choice is to ensure that the wall particle sink does not generate any charge. For an electron and singly charged ion plasma according to eq. (2.10) the normalized charge source is $\mathcal{S}_\rho = -\mathcal{M}_\mathrm{w}\left\{\nu_\mathrm{e}\left(n_\mathrm{e}(x,t) - n_\mathrm{w}\right) - \nu_\mathrm{i}\left(n_\mathrm{i}(x,t) - n_\mathrm{w}\right)\right\}$. Thus, setting

$$\nu_\mathrm{e}(x,t) = \nu_\mathrm{i}\,\frac{n_\mathrm{i}(x,t) - n_\mathrm{w}}{n_\mathrm{e}(x,t) - n_\mathrm{w}} \tag{2.12}$$

enforces the charge source to be vanishing. We refer to this case as the *insulating wall* model, as in this case a negative charge exists within the wall region, see section 2.6.

2.3.2 Electron heat sink in the insulating wall model

When using the insulating wall model, a heat sink $\mathcal{S}_\mathrm{sink,T}$ is included in the source term of Boltzmann equation, i.e. $\mathcal{S} = \mathcal{S}_\mathrm{sink,n} + \mathcal{S}_\mathrm{sink,T} + \mathcal{S}_\mathrm{src}$ in this case. We stress that when using the conducting wall description, this operator is not included in the wall model. The reason for adding such a heat sink is the following. One can notice in the constraint eq. (2.12) that when the ion density is close to the wall target density $n_\mathrm{i}(x,t) \approx n_\mathrm{w}$ then $\nu_\mathrm{we}(x,t) \approx 0$. Therefore, deep in the wall region where plasma ions have been all absorbed, the absorption of fast electrons—that have overcome the sheath potential barrier and reached the wall—stops. Therefore, the remaining electrons propagate into the wall. To avoid that these electrons interact with the numerical boundary conditions

[3]The maximum steepness of the wall mask is constrained by the refinement of the spatial grid, and by the chosen timestep. The more points used to describe the wall mask transition region, the steeper the wall mask can be. On the other hand, the steepness of the wall is also limited by the value of the timestep adopted in the simulation. The VOICE code used to perform the simulations operates with a splitting of Strang to solve the Boltzmann equation, see section 2.5.1. This splitting is no longer valid if the effect of the source term $\mathcal{S}(f_s)$ on the particles trajectories cannot be neglected when performing the advection step. This can happen if the timestep if too large, or if the source term $\mathcal{S}(f_s)$ presents a very steep spatial variation, as is case when the wall mask is too steep.

imposed at the end of the simulation domain—i.e. at the end of the wall $x = L_x$, we include a heat sink term in the wall to ensure that these remaining electrons adopt a low temperature Maxwellian distribution function. The heat sink is taken as a BGK operator of the form

$$\mathcal{S}_{\mathrm{sink,T}}(f_e) = -\mathcal{M}_{\mathrm{sink,T}}\nu_{\mathrm{sink,T}}\left(f_e - f_{\mathrm{sink,T}s}\right). \tag{2.13}$$

The mask $\mathcal{M}_{\mathrm{sink,T}}$ is similar to the wall mask of section 2.3.1 but restricted to the deeper half portion of each wall, see fig. 2.2. This is to ensure that the heat sink term does not interplay with the plasma-wall transition region. This heat sink only acts on electrons in the insulating wall model. The amplitude $\nu_{\mathrm{sink,T}}$ of the restoring force is chosen constant. The target function $f_{\mathrm{sink,T}s}$ is a Maxwellian written as

$$f_{\mathrm{sink,T}s}(v) = \frac{n_{\mathrm{sink,T}}}{\sqrt{2\pi T_{\mathrm{sink,T}}/m_s}}\,\exp\left(-\frac{m_s v^2}{2T_{\mathrm{sink,T}}}\right). \tag{2.14}$$

It is characterized by a density $n_{\mathrm{sink,T}}$ equal to the electron density $n_{\mathrm{sink,T}}(x,t) = \int f_{\mathrm{e}}(x,v,t)\,dv$. This operator thus conserves density locally, it does not absorb particles. We set the temperature of the target distribution function $T_{\mathrm{sink,T}}$ equal to a fraction of the electron temperature at the wall position: $T_{\mathrm{sink,T}}(t) = \alpha T_{\mathrm{e}}(x_{\mathrm{w}}, t)$, where x_{w} is the position where the wall mask defined by section 2.3.1 steps from zero to one. Typically we take $\alpha = 1/3$. This operator then acts as an energy and momentum sink for the remaining electrons in the wall. Furthermore, it forces the electron distribution function to relax towards a Maxwellian.

2.4 Source and collisions

In this section we describe the source of particles $\mathcal{S}_{\mathrm{src}}$ included in the source term $\mathcal{S}$ of Boltzmann eq. (2.6), and the model adopted to describe collisional processes $\mathcal{C}$ in the plasma. These two elements are crucial to reach an equilibrium state between the plasma and the wall sink.

2.4.1 Plasma source

In this section we describe the particle source $\mathcal{S}_{\mathrm{src}}$ included in the source term of the Boltzmann equation given in eq. (2.8), i.e. $\mathcal{S} = \mathcal{S}_{\mathrm{sink,n}} + \mathcal{S}_{\mathrm{sink,T}} + \mathcal{S}_{\mathrm{src}}$. In the SOL region, cross-field turbulent transport along with ionization of neutrals governs the injection of particles and heat on the considered field line. In tokamak devices the balance of particles on a given field line is also influenced by neutrals ionization and plasma recombination. We choose to ignore plasma-neutral interaction in the present chapter. In section 4.2 we present a model to take this physics into account. Plasma-neutral interaction is usually neglected when the Scrape-Off Layer operates in

the sheath-limited regime[4]. Thus, the term $\mathcal{S}_{\rm src}$ models cross-field turbulent transport only. It can be understood as being the divergence of the cross-field turbulent fluxes. Considering that turbulent transport is observed to be ballooned to the low field side of the tokamak device, it is reasonable to address a localized source term. For the sake of simplicity, we do not consider in the present work sources of momentum, charge and pure sources of energy. To model the source we use a Maxwellian with zero mean velocity, and therefore no momentum transfer, written as

$$\mathcal{S}_{\rm src}(f_s) = \frac{\mathcal{M}_{\rm src}(x)}{\int_0^{L_x} \mathcal{M}_{\rm src}(x)\,dx} \frac{s_{\rm k}}{\sqrt{2\pi T_{\rm src}/m_s}} \exp\left(-\frac{m_s v_s^2}{2T_{\rm src}}\right). \tag{2.15}$$

The mask $\mathcal{M}_{\rm src}$ plotted on fig. 2.2 localizes the source region in the central part of the plasma. It has the same form as the wall mask, see section 2.3.1. The source temperature $T_{\rm src}$ and the source magnitude $s_{\rm k}$ determine the rate of energy transfer and particle transfer into the plasma. These two control parameters are chosen here to be constant both in space and time. The source temperature is taken equal for both species except in section 2.8.2 where we perform simulations with different electron and ion particle source temperatures. Note that the ratio between the source and wall temperature $T_{\rm src}/T_{\rm w}$ does not influence the direction of the energy transfer, which always happens to be from plasma to wall as one would expect. Indeed, the target distribution function in the wall region $f^{\rm T}_{\rm sink}$ is characterized by a density which is very small compared to the plasma typical density. Therefore, the leading effect of the wall penalization term is to absorb particles, thus energy, independently of the value of the wall temperature. The choice of the precise value for the source and wall temperatures is therefore of no critical importance. We typically take $T_{\rm src}/T_{\rm w} = 3$ in the simulations.

2.4.2 Collisions

As discussed in section 3.6, it is critical to include a self scattering mechanism in the considered system so that a steady state can be reached. The collisional regularizing operator in velocity space must handle cases with large departure from Maxwellian distributions. Furthermore, to investigate the possible role of collisions on the sheath physics, it must address a regime characterized by variations on the Debye scale. While the non-linear Landau and Lenard-Balescu collision operators do not prescribe near Maxwellian distributions [46], their derivation assumes spatial scale separability, *i.e.* that each distribution function only depends on velocities at the Debye scale. To our knowledge, there is no published closure of the kinetic hierarchy allowing the calculation of a collision operator that would remain valid in conditions with plasma inhomogeneity on the Debye scale. Further collisional issues are met when stepping to realistic SOL conditions where electron-impurity and ion-neutral collisions become particularly important in the high recycling and detached divertor regime. As we chose to address the

[4]The sheath-limited regime is described in section 1.3.2. When the Scrape-Off Layer temperature is above 13.5 eV, ionization processes are negligible, thus particle and heat fluxes are extracted from the Scrape-Off Layer only through the sheath and not via plasma-neutral interaction [23].

so-called sheath-limited regime in the gyrokinetic simulations of turbulent transport, we thus consider a low-collisionality SOL regime where such complex atomic processes can be ignored. As a result, to model the kinetic physics of plasma-wall interaction we take into account collisions with two linearized operators, one specific to inter-species collisions $\mathcal{C}_{ss'}$, and the other for collisions within particles of the same species $\mathcal{C}_{ss}$. The latter has the property Coulomb collision operators, namely that the collision frequency decreases with increasing particle velocity. This is most important in determining the electron heat diffusivity, which is a key point to address the divertor regimes. The chosen expression is devised to satisfy the fundamental conservation properties of elastic binary collisions.

The self-collision operator $\mathcal{C}_{ss}$ is inspired from [47]. It conserves density, momentum and energy and Maxwellian distribution functions belong to its kernel. A complete description is given in appendix A.1. In normalized units it is written as

$$\mathcal{C}_{ss}(f_s) = \nu^{\star}_{\mathrm{D0}} \frac{\partial}{\partial v_s}\left\{ D_v f_{Ms} \frac{\partial}{\partial v_s}\left(\frac{f_s}{f_{Ms}}\right)\right\}. \tag{2.16}$$

The f_{Ms} function is a Maxwellian characterized by a mean velocity u_{Ms} and a thermal energy T_{Ms} computed at each time step and at each spatial position to constrain momentum and thermal energy conservations. Note that when the distribution function f_s is a Maxwellian, then u_{Ms} and T_{Ms} are equal to the mean velocity and temperature of f_s. The normalized diffusion coefficient in velocity space D_v is defined in eq. (A.3). It is proportional to $\nu^{\star}_{ss} = \sqrt{A_s} Z_s^4 n_s / T_s^{3/2}$, eq. (A.4). It exhibits the $|v_s|^{-3}$ velocity dependence of the Landau and Lenard-Balescu non-linear operators [46]. The control parameter ν^{*}_{D0} is the reference collision frequency normalized by the plasma frequency. It is further discussed below.

The inter species collision operator is adapted from [48] and fully described in appendix A.1. It is set to drive distribution functions towards thermal equipartition and equal mean velocities. Its normalized expression is

$$\mathcal{C}_{ss'}(f_s) = \nu^{\star}_{\mathrm{D0}} \left\{ \frac{C^{ss'}_{\mathcal{E}}}{n_s T_s}\left(\frac{(v_s-u_s)^2}{T_s} - 1\right) + \frac{C^{ss'}_{\Gamma}}{n_s T_s^{1/2}} \frac{v_s - u_s}{\sqrt{T_s}} \right\} F_{Ms}, \tag{2.17}$$

where F_{Ms} is a normalized Maxwellian distribution that has the same first three moments as f_s: density n_s, mean velocity u_s and temperature T_s. The term proportional to C^s_{Γ} accounts for momentum exchange between species s and s', hence a friction force, while the term proportional to $C^s_{\mathcal{E}}$ stands for the energy transfer, leading to equipartition. These two terms expressed in dimensional units are given by

$$C^{ss'}_{\Gamma} = -n_s m_s \nu_{ss'} \left(u_s - u_{s'}\right), \tag{2.18}$$

$$C^{ss'}_{\mathcal{E}} = -3 n_s \frac{m_s}{m_s + m_{s'}} \nu_{ss'} \left(T_s - T_{s'}\right) - u_s C^{ss'}_{\Gamma}. \tag{2.19}$$

With the inter species operator given in eq. (2.17) one therefore has in dimensional units $C_\Gamma^{ss'} = \int dv\, m_s v\, \mathcal{C}_{ss'}(f_s)$ and $C_\mathcal{E}^{ss'} = \int dv\, \frac{1}{2} m_s v^2\, \mathcal{C}_{ss'}(f_s)$. The inter-species collision frequency is given in appendix A.1. The collisionality is set using $\nu_0^\star$ as control parameter, such that $\nu_0^\star = \nu_{\mathrm{D}0}^\star L_\parallel / \lambda_{\mathrm{D}0}$, see eq. (2.20). The control parameter $\nu_0^\star$ can be read as the collisional mean free path divided by the reference field line length in the SOL. Expressing the dimensionless parameter $\nu_0^\star$ as a function of dimensional quantities yields

$$\nu_0^\star = \frac{4\sqrt{\pi}}{3}\Big(\frac{e^2}{4\pi\varepsilon_0}\Big)^2 \frac{n_0}{T_0^2} \log\Lambda\; L_\parallel = \nu_{\mathrm{D}0}^\star \frac{L_\parallel}{\lambda_{\mathrm{D}0}} = \frac{L_\parallel}{L_{\mathrm{coll}}} \tag{2.20}$$

where $\log\Lambda$ is the Coulomb logarithm. The control parameter $\nu_0^\star$ does not depend on particle mass. Collisional processes influence the plasma characteristics even for small values of the collisionality $\nu_0^\star \leq 1$. Indeed, the amplitude of the collision operator may become large whenever the derivative of the distribution function in the velocity direction becomes large. As will be shown in the following, this is precisely the case in the vicinity of the Debye sheath where particle absorption by the wall tends to generate steep gradients in the velocity direction.

2.5 The Voice code

In this section we detail the implementation within the Voice code of the numerical scheme that solves the Boltzmann-Poisson system (2.6-2.7) with immersed boundary conditions. We discuss another interesting feature of the code that is studying non uniform meshes. We then discuss the parameters used in the reference simulation.

2.5.1 Numerical scheme

The Voice acronym stands for *Vlasov Open boundary Ion Coupling to Electrons*. Along with plasma-wall interaction, this code can be used for instance to study Landau damping, the so-called bump-on-tail instability, or plasma-neutral interaction. The numerical scheme implemented in Voice is very similar to the one of the gyrokinetic code Gysela [41]. The Voice code describes a two dimensional phase space—one dimension of real space and one dimension of velocity—with possibly non uniform meshes in both spatial and velocity directions, see section 2.5.2. The code is fully ported to GPU. The coupling between Boltzmann and Poisson equations is solved using a predictor corrector scheme. Several solvers for Poisson equation are available, for instance Fourier transform when the considered spatial domain is periodic, or a finite element solver when it is not. The Boltzmann equation solver further involves a Strang splitting, with a semi-Lagrangian method to describe the advections. The procedure for advancing the distribution function from time t to $t + \Delta t$ can be summarized as

1. Solve $\partial_t f_s = \mathcal{S}(f_s) + \mathcal{C}(f_s)$ on $\Delta t/2$;
2. Solve $\partial_t f_s = -v\partial_x f_s - q_s E/m_s \partial_v f_s$ on Δt;

3. Solve $\partial_t f_s = \mathcal{S}(f_s) + \mathcal{C}(f_s)$ on $\Delta t/2$;

Steps 1. and 3. are subdivided into sub-steps to solve independently the sources and collision operators. Similarly, the advection step 2. is generally divided into an advection in the x direction described by the evolution equation $\partial_t f_s = -v\partial_x f_s$ and an advection in the v direction described by $\partial_t f_s = -q_s E/m_s \partial_v f_s$. Both advections are solved using a *backward semi-Lagrangian scheme* [49]. This numerical scheme is halfway between an Eulerian and a Lagrangian code. It allows for using higher values of the timestep Δt compared to an Eulerian code, while avoiding numerical noise found in low-density regions of phase space when using a Lagrangian method. In the absence of source and collisions, the Vlasov equation simply states that the distribution function is invariant along the trajectories of particles in phase space [46]. The backward semi-Lagrangian scheme takes advantage of this observation. In order to compute the value of the distribution function at time $t + \Delta t$ and position (x_i, v_j)—where x_i and v_j are two points of the mesh used to discretize phase space—we write that

$$f_s(x_i, v_j, t + \Delta t) = f_s(x_i^\star, v_j^\star, t)$$

Where $\left(x_i^\star, v_j^\star\right)$ is called the *foot of the characteristics*. This point is computed by solving the equations of motion of a virtual particle located at $(x_i^\star, v_j^\star)$ at time t and (x_i, v_j) at time $t+\Delta t$. Denoting by $(X(t), V(t))$ the position of such a particle in phase space, these equations are in the electrostatic case

$$\frac{\mathrm{d}X}{\mathrm{d}t} = V, \qquad m_s \frac{\mathrm{d}V}{\mathrm{d}t} = e_s E,$$

with e_s and m_s the particle charge and mass. The characteristics are thus traced back in time, hence the denomination *backward*. Most of the time, the foot $(x_i^\star, v_j^\star)$ does not coincide with a mesh point, thus an interpolation method is required to compute $f_s(x_i^\star, v_j^\star, t)$. Both VOICE and GYSELA codes use cubic spline interpolation for this purpose, which is a common choice [50, 51]. Some elements concerning the verification of the VOICE code are presented in appendix A.2.

2.5.2 On the interest of using a non-uniform mesh for the sheath problem

As discussed in section 1.5, another topic relevant to gyrokinetic modeling of the tokamak edge physics is the use of non-uniform meshes. In tokamak devices the plasma temperature typically goes from 10 keV in the core region to a few electronvolts close to the plasma facing units. Solving this temperature gradient within the gyrokinetic framework while keeping reasonable computational times implies refining the discretization in the velocity direction of phase space in the Scrape-Off Layer. A first step towards using such non-uniform meshes in the GYSELA code consists in studying them in the simplified two-dimensional framework of VOICE. Indeed, the sheath physics at play close to the wall region leads to very strong gradients, in both spatial and velocity directions. To correctly capture the sheath physics, non-uniform spline schemes that are

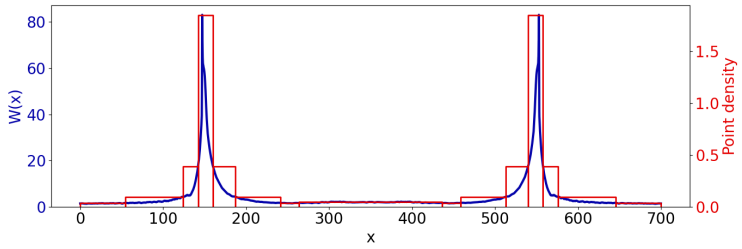

Figure 2.4: Example of a non-uniform point discretization of the spatial direction when applied to the sheath problem [3]. The steeper the space gradient and curvature of the distribution function are, the higher the weight function $W(x)$ is. A high value of the weight function therefore translates to a high point density of the spatial mesh.

compatible with an efficient GPU implementation have been developed. An example of a non uniform mesh in the spatial direction used in VOICE is visible on fig. 2.4. The study of non-uniform splines within the VOICE code is detailed in [3]; we summarize the main results here. By comparing a non-uniformly meshed simulation with a uniformly meshed simulation that produces the same results—in the sense that the numerical errors of the two simulations are comparable—, the study showed that (i) the use of a non-uniform mesh reduces the memory requirement by 89% and (ii) the non-uniform simulations run 5.5 times faster than the uniform one, despite the reduction in performance associated with non-uniform spline schemes. These two reductions in required memory and time execution are a direct consequence of the fact that with a non-uniform mesh, one can use less grid points than in the uniform case. Another observation from this work is that the best choice for the degree of splines appears to be three. Higher-order splines lead to spurious oscillations of the interpolated quantity close to boundaries of the interpolation domain, whereas lower order splines are less accurate. The successful implementation of a non uniform spline schemes in the VOICE code opens interesting perspectives for using this scheme within the five-dimension gyrokinetic framework of the GYSELA code.

2.5.3 Reference simulation parameters

A list of the parameters used in the reference simulation that is analyzed in the present chapter can be found in Table (2.1). A number $N_x = 1500$ points are used to discretize the spatial direction. Most of these points are placed in the vicinity of the sheath, where steep gradients develop, see fig. 2.4. Conversely, the quasineutral plasma and the wall region are discretized with a lower density of points since the distribution function is more regular there. A similar non-uniform mesh is used for the velocity dimension, with a total of $N_v = 700$ to discretize this dimension. The maximum resolved velocity $v_{\max}$ is six thermal velocities, i.e. $v_{\max} = 6v_{T_0}$. Typical SOL plasma density and temperature in a fusion plasma are $n_0 = 2.5 \times 10^{19}\,\mathrm{m}^{-3}$ and $T_0 = 100\,\mathrm{eV}$. These values correspond to the sheath-limited regime, close to the transition to the high re-

Quantity	L_x	$L_\parallel$	n_{src}	T_{src}	d_{w}	n_{w}	T_{w}	$\nu_0^\star$
Unit	$\lambda_{\mathrm{D}0}$	$\lambda_{\mathrm{D}0}$	n_0	T_0	$\lambda_{\mathrm{D}0}$	n_0	T_0	$L_\parallel^{-1}$
VOICE value	700	406	1	1	0.2	10^{-9}	1/3	50
SOL value		$\approx 10^6$						50

Table 2.1: Reference simulation parameters and comparison with the connection length $L_\parallel$ and collisionality ν_0^* of a typical Scrape-Off Layer magnetic field line. A typical density $n_0 = 2.5 \times 10^{19}\,\mathrm{m}^{-3}$ and $T_0 = 100\,\mathrm{eV}$ have been used along with a connection length $L_\parallel = 15\,\mathrm{m}$. The collisionality $\nu_0^\star$ represents the number of collisions experienced by a particle when traveling a distance $L_\parallel$. It is taken in the VOICEsimulation to be equal to its typical value for a Scrape-Off Layer field line. This effectively results in the simulated plasma being much more collisional than what is found experimentally.

cycling regime. One then finds that the typical Debye length is $\lambda_{\mathrm{D}_0} \approx 1.5 \times 10^{-5}\,\mathrm{m}$, and therefore $L_\parallel = 10^6 \lambda_{\mathrm{D}_0}$ for a typical connection length $L_\parallel \approx 15\,\mathrm{m}$. Modeling an entire SOL magnetic field line with the present one-dimensional kinetic model is out of reach because of the required computational resources. We therefore simulate a field line of reduced length $L_\parallel = 406\,\lambda_{\mathrm{D}_0}$. In section 2.8.3 we vary the connection length and show that this parameter has no impact on the potential drop that exists in the sheath. This hints at the fact that the considered connection length is large enough so that the sheath physics can be properly studied by the present model, especially regarding scale separation between the quasineutral and non neutral plasma regions. The total size of the simulation box is given by L_x. The quantity $L_{\mathrm{w}} = L_x - L_\parallel$ represents the spatial extent of the walls in the simulation box. Each wall (left and right) has a length $L_{\mathrm{w}}/2$. The width of the transition region between plasma and wall conditions is set to $d_w = 0.2\,\lambda_{\mathrm{D}_0}$. We have checked that the transition is sharp enough that the simulation behavior does not depend on this parameter. As stated in section 2.3.1, the normalized target wall density n_{w} is much smaller than unity so that evanescent plasma conditions are enforced in the wall, and we chose a source temperature T_{src} that is higher than the wall target temperature T_{w}.

The choice of collisionality is made according to a constraint on the velocity mesh resolution. Let us first address the collisionality regime for the chosen plasma parameters. Given the definition of the Debye scale λ_{D_0} and that of $\nu_0^\star$, one obtains the expression of the mean free path $L_{\mathrm{coll}} = \lambda_{\mathrm{D}_0}^2/\lambda_{\mathrm{L}_0}(3\sqrt{\pi}/\log\Lambda)$, where the Landau scale $\lambda_{\mathrm{L}_0} = (e^2/(4\pi\varepsilon_0))/T_0$ is the distance of closest approach of two particles. With $\lambda_{\mathrm{L}_0} \approx 10^{-11}\,\mathrm{m}$ and $\lambda_{\mathrm{D}_0} \approx 1.5 \times 10^{-5}\,\mathrm{m}$ one obtains for $L_\parallel = 10^6\,\lambda_{\mathrm{D}_0}$ the collisionality $\nu_0^\star \approx 50$. However, for $L_\parallel \approx 400\lambda_{\mathrm{D}_0}$, one finds $\nu_0^\star \approx 10^{-2}$. Taking this latter value which is consistent with the chosen connection length for the simulation is however not possible. Indeed, the smaller $\nu_0^\star$, the smaller the grid step Δv required to resolve steep gradients. Balancing the time scale for collisional diffusion on the scale Δv by a

time scale that characterizes the advection, one finds that the number of mesh point in the velocity space scales typically like $1/\sqrt{\nu_0^{\star 5}}$. The cost to use realistic values of $\nu_0^\star$ is therefore a factor 70 increase in the number of points required to mesh the velocity space. Such an increase of grid points cannot be afforded, thus we kept a value of $\nu_0^\star \approx 50$ in the reference simulation. The increase of collisionality by a factor 5×10^3 in the simulation has implications on the simulated plasma properties. These are assessed in section 3.6.1.

2.6 Conducting and insulating wall behavior

In this section we show that the two wall models presented in section 2.3.1—the conducting and insulating models—successfully reproduce the main features of plasma-wall interaction. We then assess the differences in the simulated sheath physics that originate from the difference between the two wall models. We summarize below the key characteristics of the two models, see section 2.3.1 for a detailed description.

1. In the *conducting wall* model, the solid boundary is described using a BGK operator of the form $S_{\text{sink}}(f_s) = -\nu_s \mathcal{M}_w \left(f_s - f_t\right)$, where the magnitude of the restoring force ν_s is a constant $\nu_e = \nu_i = \text{cte}$. The wall mask localizes the sink to the wall region, and the target function f_t is a low density Maxwellian, see eq. (2.11) and section 2.3.1;
2. The *insulating wall* model uses the same BGK operator except that the magnitude of the restoring force for electrons ν_e is adjusted at each spatial coordinate and timestep so that no sink of charge is found in the wall. This is achieved by taking $\nu_i = \text{cte.}$, and $\nu_e(x,t) = \nu_i(n_i - n_w)/(n_e - n_w)$.

Charge densities We first focus on the charge densities represented on fig. 2.5, right graph. For both wall models we observe a positive charge density that builds up between the entrance of the sheath and the wall. The entrance of the sheath is understood as the approximate position where the charge density ρ_c departs from zero.

[5] One can write indeed that collisions have an influence on the plasma if they displace a particle by at least Δv in the velocity direction when the considered particle travels a distance $L_\parallel$ within the plasma. We take a particle with a typical velocity $v_T = \sqrt{T_0/m_s}$ for the present calculation. The condition for collisions to be effective can therefore be written as

$$\frac{\Delta v^2}{D_0} < \frac{L_\parallel}{v_T},$$

with $D_0 \sim v_T^2 \nu_0$ the collisional diffusion coefficient and ν_0 the collisionality. Rearranging the above equation one gets

$$\frac{\Delta v^2}{v_T^2} < \frac{L_\parallel \nu_0}{v_T}$$

By definition $\nu_0^* = L_\parallel \nu_0 / v_T$, thus one obtains that $v/\Delta v \gtrapprox 1/\sqrt{\nu_0^*}$. The typical number of points to discretize the velocity direction $v/\Delta v$ scales like $1/\sqrt{\nu_0^*}$.

The wall position is the spatial location where the charge density reaches a maximum. The precise definition of these two positions is discussed in appendix A.4. For both wall models this positive charge density is accompanied by a drop of the electric potential. We call this positively charged layer the Debye sheath, as it repels bulk electrons in the plasma and accelerates ions up to the wall. We see for both wall models that a negative charge density exists in the wall region. This charge is a consequence of the immersed wall model. It has a different origin in the insulating and conducting cases:

- In the conducting wall case, the magnitude of the restoring force ν_s is the same for ions and electrons. Because the latter are much more mobile than the former, they can penetrate deeper in the wall region before being absorbed. This results in a negative charge in the wall. This inertia difference is also the cause of the negative current that exists in this region for the conducting wall model, see below.
- In the insulating wall case charge conservation is enforced so that $\mathcal{S}_\rho = 0$. In practice, $\mathcal{S}_\rho = 0$ means that a particle of given charge is absorbed in the wall only if another particle of opposite charge can be absorbed as well, similarly to a recombination process. As no source of charge exists in the quasineutral plasma either, the total charge density integrated over the entire simulation domain {plasma + wall} must vanish $\int_0^{L_x} dx\, \rho_c = 0$. Therefore, the positive charge density that exists in the sheath must be balanced by a negative charge density in the wall.

Currents We now focus on currents represented on fig. 2.5, left graph. The current is defined in dimensional units as $j_{\rm tot} = e_{\rm e}\Gamma_{\rm e} + e_{\rm i}\Gamma_{\rm i}$, where Γ_s is the particle flux of species s. On the aforementioned figure the current is normalized by the ion saturation current at the sheath entrance which is $j_{\rm sat}^{\rm sh} = e_{\rm i}\Gamma_{\rm i}^{\rm sh}$, where $\Gamma_{\rm i}^{\rm sh}$ the flux of ions at the entrance of the sheath. In both conducting and insulating wall cases, the total current computed at the entrance of the sheath and wall positions is negligible compared to the ion saturation current. In both cases, the sheath effectively enforces the matching of the ion and electrons fluxes at the plasma boundary, so that the plasma remains quasineutral on scales larger than the Debye length. In the wall region, both wall models give rise to different values for the current. In the insulating wall case, we observe that the current remains small compared to $j_{\rm sat}^{\rm sh}$, while in the conducting case the total current reaches approximately 40% of the ion saturation current in the wall. To understand this, let us first write the equation expressing the charge balance in the wall as

$$\partial_x j_{\rm tot} = \mathcal{S}_\rho = -\mathcal{M}_{\rm w}(\nu_{{\rm w}i}(n_i - n_{\rm w}) - \nu_{\rm we}(n_e - n_{\rm w})) \tag{2.21}$$

Thus:

- In the insulating wall case one has $\mathcal{S}_\rho = 0$. Given that $j_{\rm tot}$ vanishes in the plasma due to the sheath physics at play at the plasma boundary, integration of eq. (2.21) gives that $j_{\rm tot}$ must vanish in the wall as well;

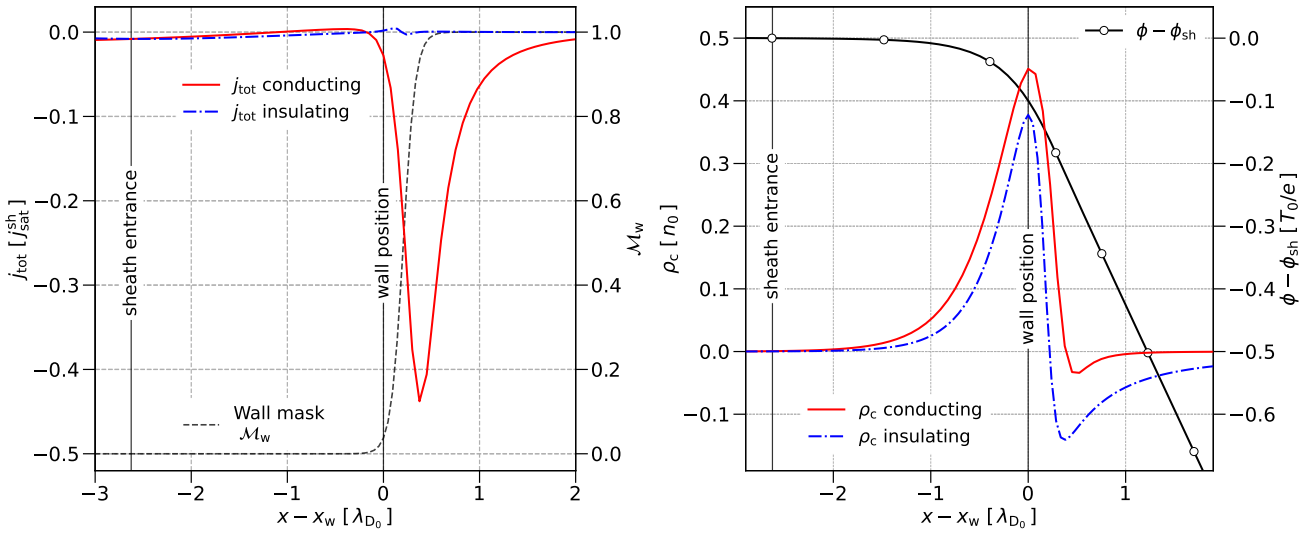

Figure 2.5: The spatial axis of both plots has been renormalized so that the sheath entrance and wall position coincide in the conducting and insulating wall cases. Left: total current normalized to the ion saturation current. Right: charge densities. The potential is represented in the conducting wall case. The spatial shape of the potential has a similar shape in the insulating wall case.

– In the conducting wall case one has $\mathcal{S}_\rho \neq 0$, thus driving a non vanishing current there. This current has the same origin as the negative wall charge that exists in the wall region for this same conducting wall: as electrons are lighter than ions, they penetrate deeper into the wall before being absorbed, thus creating a strong negative current—or equivalently a positive flux of electrons—there.

2.7 Kinetic physics of the sheath

In this section we comment on the distribution function of ions and electrons. Studying these distributions shows that we recover the key kinetic features of plasma-wall interaction detailed in section 2.1. Both conducting and insulating wall models however exhibit discrepancies compared to this idealized picture. We detail the origin of these discrepancies here.

2.7.1 Distribution functions at the sheath entrance

Both ion and electron distribution functions taken at the entrance of the sheath are visible on fig. 2.6, for both conducting (left graph) and insulating (right graph) wall models. Let us comment first on the ion distribution function. It has a similar shape for both wall models. It is shifted towards positive velocities. This is a consequence of the presheath acceleration in the quasineutral plasma, and is reminiscent of the Bohm criterion. This last point is addressed in detail in section 3.4.1. Let us remark that even

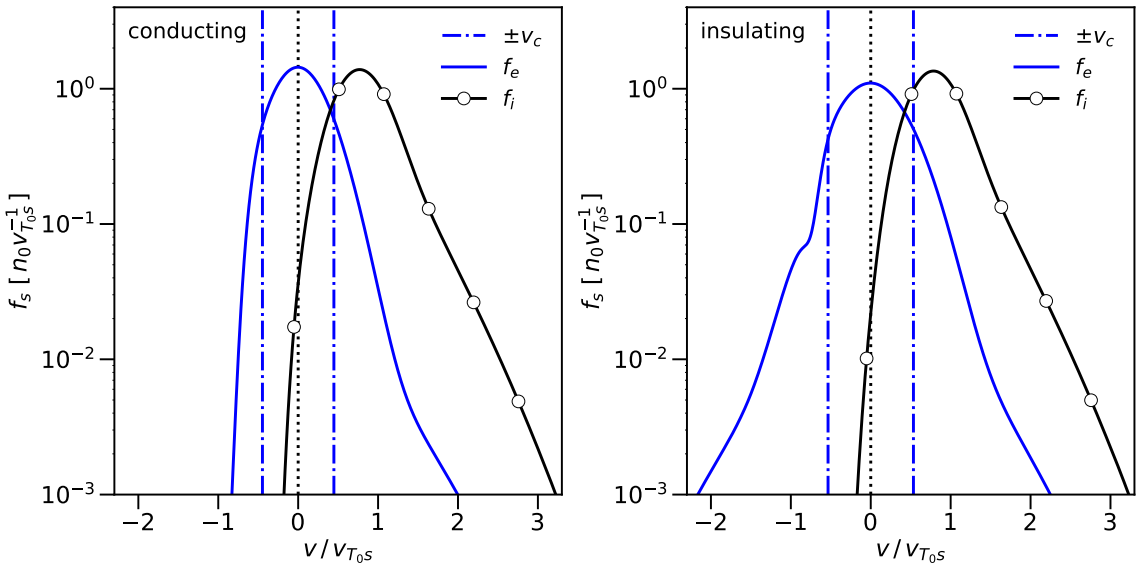

Figure 2.6: Distribution function computed at the entrance of the sheath, with the critical velocity. Left: conducting wall mode, right: insulating wall model.

though there is no source of particle within the sheath region, there are some ions at the entrance of the sheath with negative velocities $v \leq 0$. This is a direct consequence of collisional processes at play in the sheath layer. As the ion distribution function departs from a Maxwellian, collisions replenish the $v \leq 0$ part of the distribution function, hence resulting in ions coming back from the sheath to the plasma.

We now focus on electron distribution functions. On both graphs the cutoff velocity $v_c = \sqrt{-2e\Delta\phi_{\text{sh}}/m_e}$ has been represented, along with its opposite $-v_c$. The sheath potential drop is defined as $\Delta\phi_{\text{sh}} = \phi(x_w) - \phi(x_{\text{sh}}) < 0$. Electron distribution functions in the velocity range $[-v_c,\, v_c]$ are approximately symmetric. This is expected, as these velocities correspond to bulk electrons that are reflected in the sheath back into the plasma: in the absence of collisions and sources of particles in the sheath region, the energy of a particle $H_s = \frac{1}{2}m_s v^2 + e_s\phi$ is conserved during its motion in the sheath. Electrons for which $0 \leq v \leq v_c$ therefore do not possess enough kinetic energy to overcome the sheath potential barrier and are thus reflected in the plasma. We notice that there are more fast electrons going towards the wall for which $v \geq v_c$ than fast electrons coming back to the plasma characterized by $v < -v_c$. We retrieve a key feature of the kinetic physics at play within the sheath: fast electrons for which $v \geq v_c$ possess enough kinetic energy to reach the wall and thus be subject to the particle sink at play there. The amount of electrons lost in the wall is adjusted through the potential drop in the sheath so that overall the ion and electron fluxes match[6]. One can remark however that there are still some electrons at the entrance of the sheath with velocities

[6]To be more precise, due to the physics at play in the Debye sheath the electron and ion fluxes match on timescales typically larger than the inverse of the electron plasma frequency $\omega_{pe}^{-1} = \sqrt{m_e\varepsilon_0/(ne^2)}$.

$v < -v_c$, and that the amount of these electrons is larger in the insulating wall case. The presence of these electrons with $v \leq -v_c$ at the entrance of the sheath is the result of two distinct processes. First, similarly to ions, collisional processes in the sheath tend to replenish the velocity part $v < -v_c$ of the distribution function. Second, for both wall models there exists a negative charge density in the wall, see fig. 2.5. For both wall models, a non vanishing electric field exists in the wall. This electric field has the same sign as in the sheath: it is positive, hence tends to repel electrons present in the wall back to the plasma, thus leading to the presence of fast electrons $v \leq -v_c$ at the entrance of the sheath. We call these the *re-emitted* electrons. On the contrary to fast electrons $v < -v_c$ present at the sheath entrance due to collisions, electrons re-emitted from the wall are unphysical. These re-emitted electrons are the result of the penalization technique only. There are much more electrons re-emitted by the wall in the insulating wall case compared to the conducting case. This is no surprise: the negative charge density that builds up in the wall is larger in the insulating wall case compared to the conducting wall case, see section 2.6 and fig. 2.5. In the conducting wall case, the re-emission of electron can be controlled, while it is not true with the insulating wall model. Indeed, with the conducting wall the negative charge density that exists in the wall is the result of the finite magnitude ν_s of the penalization operator presented in eq. (2.10). Since ν_s is finite, electrons can penetrate the wall before being absorbed. By increasing the chosen value for ν_s this re-emission can be reduced, although at the cost of a smaller timestep to resolve the faster absorption dynamic in the wall. In the insulating wall model, the excess of electrons present in the wall is not constrained by the restoring force of the penalization operator, see section 2.6—hence justifying the use of the heat sink term presented in section 2.3.2. One has therefore no easy way of reducing the electron re-emission in this case. The insulating wall model appears therefore less relevant to describe plasma-wall interaction than the conducting wall model. In section 2.8 we further show that this larger re-emission of the insulating wall compared to the conducting one results in larger discrepancies between the simulated sheath potential drop and analytical predictions.

2.7.2 Particle trajectories in phase space

On fig. 2.7 are shown plots of the ion and electron distribution functions in the entirety of (x, v) phase space. The simulation has been performed with the conducting wall model. Both electron and ion distribution functions tend to vanish in the two wall regions, as the sink of particles from eq. (2.10) absorbs particles there. On each graph iso-contours of the Hamiltonian $H_s = \frac{1}{2}m_s v^2 + e_s\phi$ are superimposed on the distribution functions as red lines. These iso-contours give the trajectories of particles in phase space in the absence of collisions, source and sink terms. For positive velocities, corresponding to the top half of each plot, the iso-contours are to be followed from left to right. For negative velocities (bottom half of each plot), it is the opposite. The two graphs on the right of fig. 2.7 show a zoom of phase space in the vicinity of the sheath near the right wall. The following discussion focuses on the physics of the right part of the

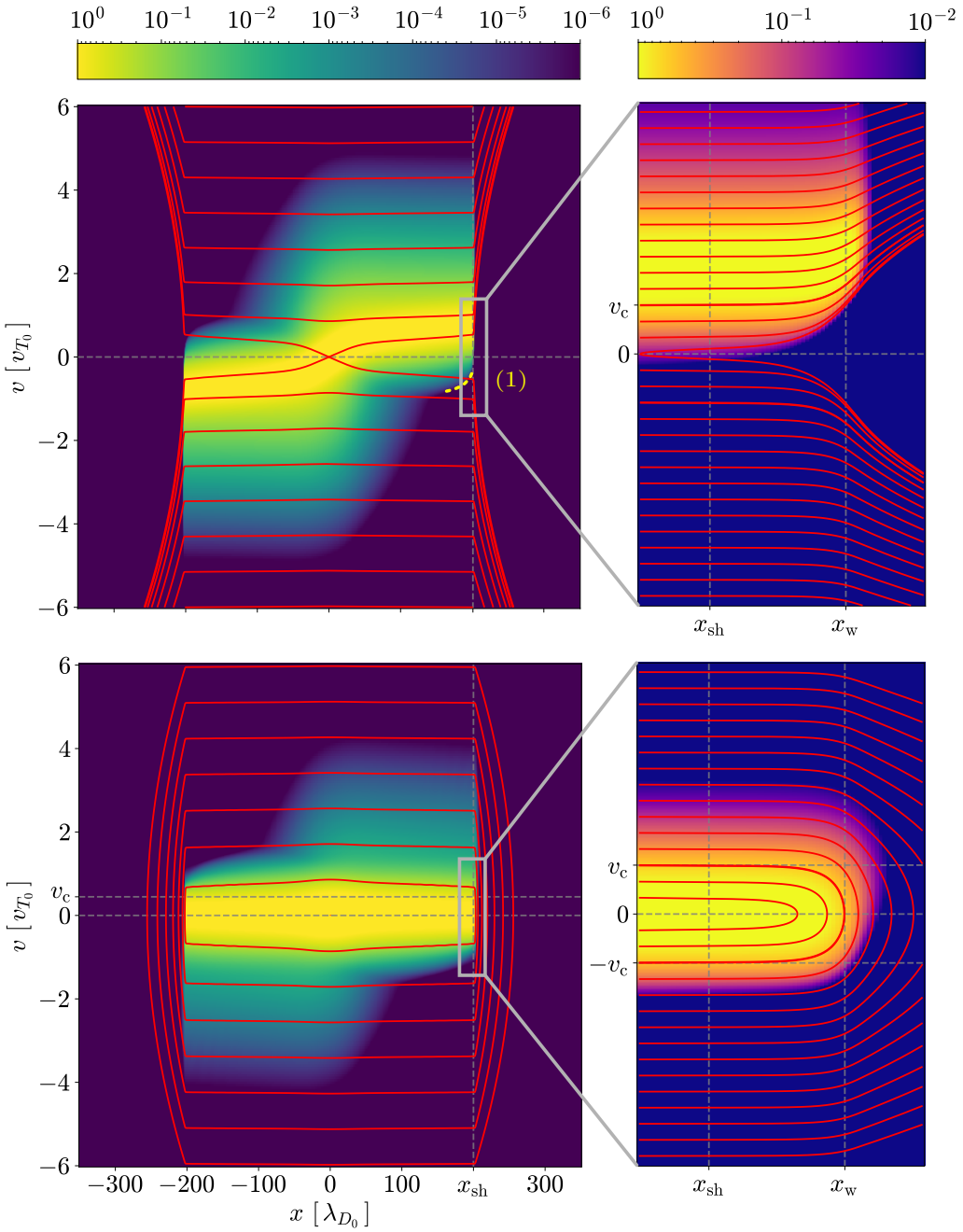

Figure 2.7: Distribution functions in phase space. Top left: ion distribution function, bottom left: electron distribution function. The right graphs represent a zoom of both distribution functions in the vicinity of the sheath. For clarity a different color scale is used in the zoomed graphs as compared to the two left graphs. The gray boxes on the two left graphs remind the reader that the right graphs are a zoom of some portion of the initial left graphs. The boxes do not however cover the exact zoomed area, but are drawn bigger to make them more visible.

plasma, for which $x \geq 0$. The $x < 0$ region is the symmetrical of the $x \geq 0$ region. Ions experience an acceleration in both plasma, sheath and wall regions. The acceleration in the quasineutral plasma is negligible as compared to the one in the sheath and the wall, where the iso-contours bend towards large velocities. This is a consequence of the steep drop of the electric potential that exists there. Electrons are slowed down by this potential drop. The passing electrons for which $v \geq v_{\mathrm{c}}$ at the sheath entrance overcome the potential barrier of the sheath and penetrate the absorbing wall region. On the contrary, electrons with $v \leq v_{\mathrm{c}}$ are reflected in the sheath and thus are "trapped" in the plasma. As explained in the previous section, we see that some of the passing electrons are able to come back in the plasma region, as a result of collisional processes and the finite strength of the penalization operator. The effect of collision can be viewed directly on the ion distribution function: in the area denoted by the dashed yellow line near the (1) marker we see that the ion distribution function presents an increasing number of particles with negative velocities going from the wall towards the plasma center. As no particle source exists in this region of phase space, this effect can therefore only be attributed to collisions.

2.8 Influence of relevant plasma parameters on the potential drop in the sheath region

In this section we perform several simulations varying three key simulation parameters that are the ion-to-electron mass ratio m_i/m_e, the temperature of the particle source T_{src} and the magnetic connection length $L_{\parallel}$. We compare the potential drop obtained in the sheath for all investigated cases with a reference potential drop that is derived using a simplified sheath kinetic model. Discrepancies between the simulated potential drop and the prediction stem from two causes: the re-emission of electrons from the wall, and the departure of the electron distribution function from a Maxwellian at the entrance of the sheath. These discrepancies reveal to be larger in the insulating wall case compared to the conducting wall case.

In the following we use a well known prediction for the electric potential drop that exists in the sheath region [23]. The derivation of this potential drop is recalled in appendix A.3.1. It assumes that the distribution functions at the entrance of the sheath can be described by a Maxwellian distribution function non vanishing for positive velocities only for ions, and a centered Maxwellian truncated for velocities $v \leq -v_c$ for electrons. The cutoff v_c is defined such that the electron flux matches the ion flux at the entrance of the sheath. This leads to the prediction for the potential drop

$$\Delta\phi_{\mathrm{sh}}^{\mathrm{pred.}} = \frac{T_{\mathrm{e}}^{\mathrm{sh}}}{2e} \log\left(2\pi \frac{m_{\mathrm{e}}}{m_{\mathrm{i}}} M^2 \left(1 + \frac{T_{\mathrm{i}}^{\mathrm{sh}}}{T_{\mathrm{e}}^{\mathrm{sh}}}\right)\right), \tag{2.22}$$

where the ion and electron temperatures are supposed to be taken at the sheath entrance, as indicated by the *sh* superscript. The Mach number M is defined as

$M = u_i/c_{\mathrm{s}}^{\mathrm{iso.}}$ for the present section only, with u_i the mean ion velocity defined in section 3.1, and the velocity of plasma sound waves computed in the isothermal closure framework $c_{\mathrm{s}}^{\mathrm{iso.}} = c_{\mathrm{s}} = \sqrt{(T_{\mathrm{i}} + T_{\mathrm{e}})/m_{\mathrm{i}}}$[7].

2.8.1 Potential drop dependence on the ion-to-electron mass ratio value

We assess here the dependence of the sheath potential drop with the ion-to-electron mass ratio value. This mass ratio $m_{\mathrm{i}}/m_{\mathrm{e}}$ is fixed by the respective electron and ion masses, for instance $m_i/m_e \approx 3600$ for a Deuterium plasma. In global gyrokinetic codes it is common practice to use a different ratio, corresponding to heavy electrons, or equivalently lighter ions. This allows for resolving the ion and electron timescales at a numerical cost that remains affordable. The main constraint lies in making sure that the physics observed with an adapted mass ratio value is similar to the one that would be obtained with a realistic value. We assess in the following the relevance of immersed boundary conditions for retrieving the expected dependence of the sheath potential drop on the ratio m_i/m_i. We investigate mass ratios in the range $\{40, 100, 400, 1835, 3600\}$. The $m_i/m_e = 1836$ value corresponds to a hydrogen plasma, while $m_i/m_e = 3600$ is similar to that of a deuterium plasma as stated above. To compare simulations performed with different mass ratios we define an *effective* potential drop as

$$\overline{\Delta}\phi_{\mathrm{sh}} = \frac{e\Delta\phi_{\mathrm{sh}}}{T_{\mathrm{e}}^{\mathrm{sh}}} - \log\left(\sqrt{2\pi M^2\left(1 + \frac{T_{\mathrm{i}}^{\mathrm{sh}}}{T_{\mathrm{e}}^{\mathrm{sh}}}\right)}\right). \tag{2.23}$$

From eq. (2.22) we see that a prediction for this effective potential drop is simply

$$\overline{\Delta}\phi_{\mathrm{sh}}^{\mathrm{pred.}} = \frac{1}{2}\log\left(\frac{m_{\mathrm{e}}}{m_{\mathrm{i}}}\right). \tag{2.24}$$

It only depends on the ratio m_i/m_e. This effective potential drop is referred to on fig. 2.8 for both conducting and insulating wall models as the *baseline* scenario. We

[7] In Chapter 3 we show that the definition of the Mach number in the kinetic simulation is subject to discussions. This definition does however not matter for the present discussion. Indeed, from appendix A.3.1 the quantity inside the logarithm of eq. (2.22) is simply the ratio between the ion flux and the forward flux of electrons computed at the entrance of the sheath, that is to say

$$\Delta\phi_{\mathrm{sh}}^{\mathrm{pred.}} = \frac{T_{\mathrm{e}}^{\mathrm{sh}}}{e}\log\left(\frac{\Gamma_{\mathrm{i}}^{\mathrm{sh}}}{\Gamma_{\mathrm{e}}^{\mathrm{sh+}}}\right) = \frac{T_{\mathrm{e}}^{\mathrm{sh}}}{e}\log\left(\frac{\Gamma_{\mathrm{i}}^{\mathrm{sh}}}{n_{\mathrm{e}}^{\mathrm{sh}}}\sqrt{\frac{2\pi m_{\mathrm{e}}}{T_{\mathrm{e}}^{\mathrm{sh}}}}\right),$$

where $\Gamma_{\mathrm{e}}^{\mathrm{sh+}}$ is the forward electron flux at the entrance of the sheath

$$\Gamma_{\mathrm{e}}^{\mathrm{sh+}} = \int_0^{+\infty} dv\, v f_{\mathrm{e}}^{\mathrm{sh}}(v).$$

The quantity $\Gamma_{\mathrm{i}}^{\mathrm{sh}}/\Gamma_{\mathrm{e}}^{\mathrm{sh+}}$ is independent of the choice of the definition for the speed of sound waves, as we have $\Gamma_{\mathrm{i}}^{\mathrm{sh}} = n_{\mathrm{i}}^{\mathrm{sh}} M c_{\mathrm{s}} = n_{\mathrm{i}}^{\mathrm{sh}} u_{\mathrm{i}}^{\mathrm{sh}}$ whatever the definition of c_{s}.

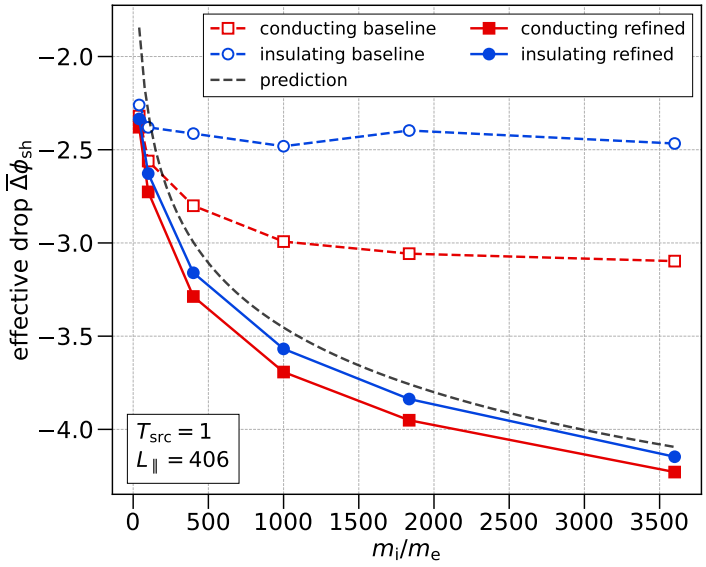

Figure 2.8: Sheath potential drop dependence on the value of the ion-to-electron mass ratio. The red squares and blue circles correspond to conducting and insulating walls respectively. The effective potential drop defined in eq. (2.23) and the refined potential drop defined in section 2.8.1 are both represented. The dashed grey curve corresponds to the prediction, which is the same in both effective and refined cases.

see non negligible discrepancies between effective potential drops and the prediction, for both wall models. The discrepancy is higher at high ion-to-electron mass ratios, and is more significant in the insulating wall case as compared to the conducting wall case. We expect the effective potential drop to become more negative as m_i/m_e increases towards realistic values: as electrons become lighter with respect to ions, a more negative potential drop in the sheath is required to confine bulk electrons in the plasma. The effective potential drop in the conducting wall case exhibits the correct tendency, it decreases when inceeasing m_i/m_e. This is not the case for the insulating wall model, as the effective potential drop remains almost constant when varying m_i/m_e. In both conducting and insulating wall cases, the discrepancy between the effective potential drop and the prediction can be explained by the re-emission of electrons from the wall. To show this, let us adapt the prediction of the potential drop given by eq. (2.22) to account for the electron re-emission. The derivation is detailed in appendix A.3.2. It leads to the following formula for the prediction of the potential drop

$$\Delta\phi_{\mathrm{sh}}^{\mathrm{pred,\,ref.}} = \frac{T_{\mathrm{e}}^{\mathrm{sh}}}{e}\log\left(\sqrt{2\pi\frac{m_{\mathrm{e}}}{m_{\mathrm{i}}}M^2\left(1+\frac{T_{\mathrm{i}}^{\mathrm{sh}}}{T_{\mathrm{e}}^{\mathrm{sh}}}\right)}\left(1+\frac{\Gamma_{\mathrm{e}}^{-}}{\Gamma_{\mathrm{i}}^{\mathrm{sh}}}\right)\right). \tag{2.25}$$

This prediction is labeled *refined* or simply *ref.* in the following to highlight the fact that it takes the electron re-emission into account. In this latter expression Γ_{e}^{-} is the flux of electrons re-emitted by the wall, computed at the sheath entrance. It is

expressed as

$$\Gamma_{\mathrm{e}}^{-} = -\int_{-\infty}^{-v_{\mathrm{c}}} dv\, v f_{\mathrm{e}}^{\mathrm{sh}}(v). \tag{2.26}$$

In a similar fashion as what has been done in eq. (2.23), we define a *refined effective* potential drop as

$$\overline{\Delta}\phi_{\mathrm{sh}}^{\mathrm{ref.}} = \frac{e\Delta\phi_{\mathrm{sh}}}{T_{\mathrm{e}}^{\mathrm{sh}}} - \log\left(\sqrt{2\pi M^2\left(1+\frac{T_{\mathrm{i}}^{\mathrm{sh}}}{T_{\mathrm{e}}^{\mathrm{sh}}}\right)}\left(1+\frac{\Gamma_{\mathrm{e}}^{-}}{\Gamma_{\mathrm{i}}^{\mathrm{sh}}}\right)\right), \tag{2.27}$$

The interest of defining this quantity is that its prediction is the same as in the *baseline* case, that is to say

$$\overline{\Delta}\phi_{\mathrm{sh}}^{\mathrm{pred,\,ref.}} = \overline{\Delta}\phi_{\mathrm{sh}}^{\mathrm{pred.}} = \frac{1}{2}\log\left(\frac{m_{\mathrm{e}}}{m_{\mathrm{i}}}\right). \tag{2.28}$$

Hence it is possible to represent on the same figure the effective potential drops simulated in the *refined* and *baseline* cases—i.e. with or without electron re-emission—along with their common prediction. This is done on fig. 2.8. When taking the electron re-emission into account, we find a good agreement for both wall models between the effective potential drop and the prediction. This shows that the potential drop in the sheath obtained from the kinetic simulation departs from the simple analytical model for this drop detailed in the beginning of the present section mainly due to the electron re-emission from the wall. The origin of this electron re-emission has been unraveled in section 2.7. We now understand the larger discrepancy observed in the insulating wall case when comparing the effective potential drop to its prediction in the baseline case, i.e. without correcting for electron re-emission: this re-emission is larger in the insulating wall case, see section 2.7 and fig. 2.6. For both wall models, the electron re-emission tends to lower the potential drop in the sheath region. This was expected: emitting electrons from the wall region lowers the drop of the electric potential required to ensure the equality of ion and electron fluxes $\Gamma_i = \Gamma_e$ at the entrance of the sheath.

2.8.2 Potential drop dependence on the electron temperature

The radial variation of the electric potential in the Scrape-Off Layer of tokamak devices is found to be proportional to the electron temperature in the sheath-limited regime, see section 5.1.1. This is a direct consequence of plasma-wall interaction. This proportionality is retrieved when looking at the prediction for the sheath potential drop, as one can rewrite it as $\Delta\phi_{\mathrm{sh}}^{\mathrm{pred.}} = \Lambda T_{\mathrm{e}}^{\mathrm{sh}}/e$ from eq. (2.22), with

$$\Lambda = \frac{1}{2}\log\left(2\pi\frac{m_{\mathrm{e}}}{m_{\mathrm{i}}}M^2\left(1+\frac{T_{\mathrm{i}}^{\mathrm{sh}}}{T_{\mathrm{e}}^{\mathrm{sh}}}\right)\right). \tag{2.29}$$

We show in the following that we retrieve the proportionality between the sheath potential drop and the electron temperature in the kinetic simulations, for both wall models, provided that we take into account (i) the electron re-emission from the wall

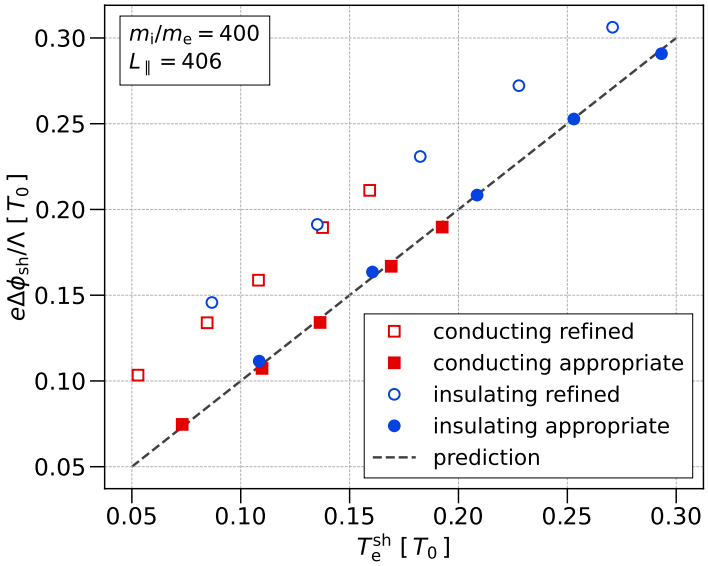

Figure 2.9: Potential drop dependence on electron temperature at the sheath entrance, for conducting (red squares) and insulating (blue circles) walls. The dashed line corresponds to the potential drop prediction.

and (ii) the departure from thermal equilibrium of the electron distribution function at the entrance of the sheath. We assess the dependence of the potential drop in the sheath with the electron temperature by varying the electron temperature of the particle source, which is defined in section 2.4.1. We investigate temperatures in the range $T_{\mathrm{src,e}} \in \{0.5, 0.75, 1, 1.25, 1.5\}$. The temperature of the ion source remains constant in all of these simulations. The other parameters remain equal to the ones presented in Table (2.1). On section 2.8.2 is plotted the variation of the quantity $e\Delta\phi_{\mathrm{sh}}/\Lambda$ for different values of the proportionality coefficient Λ. We call this quantity the *normalized* potential drop in the following. When taking into account the re-emission of electron from the wall at the entrance of the sheath the Λ coefficient is

$$\Lambda^{\mathrm{ref.}} = \log\left(\sqrt{2\pi\frac{m_{\mathrm{e}}}{m_{\mathrm{i}}}M^2\left(1+\frac{T_{\mathrm{i}}^{\mathrm{sh}}}{T_{\mathrm{e}}^{\mathrm{sh}}}\right)}\left(1+\frac{\Gamma_{\mathrm{e}}^{-}}{\Gamma_{\mathrm{i}}^{\mathrm{sh}}}\right)\right), \tag{2.30}$$

following the prediction given in section 2.8.1, so that a prediction for the normalized potential drop is $e\Delta\phi_{\mathrm{sh}}^{\mathrm{pred.}}/\Lambda^{\mathrm{ref.}} = T_e$. The normalized potential drop computed with Λ^{ref} is labeled as *refined*. It is plotted for both wall models on section 2.8.2. We observe the expected linear dependence of the normalized potential drop $e\Delta\phi_{\mathrm{sh}}/\Lambda^{\mathrm{pred.}}$ with the electron temperature at the sheath entrance, for both wall models. The slope of the plotted data is in good agreement with the predicted slope of 1. A constant offset exists between the values obtained from the simulation and the prediction. It can be mainly explained by the departure of the electron distribution function from a Maxwellian at the sheath entrance. Indeed, in appendix A.3.1 to derive the prediction of the sheath potential drop of section 2.8.1 we write the equality of ion and electrons fluxes at the

sheath entrance as

$$\Gamma_{\mathrm{i}}^{\mathrm{sh}} = \Gamma_{\mathrm{e}}^{+\mathrm{pred.}} - \Gamma_{\mathrm{e}}^{-},$$

where

$$\Gamma_{\mathrm{e}}^{+\mathrm{pred.}} = \int_{v_{\mathrm{c}}}^{+\infty} dv\, v n_e^{\mathrm{sh}} \sqrt{\frac{m_{\mathrm{e}}}{2\pi T_{\mathrm{e}}^{\mathrm{sh}}}} e^{-\frac{m_{\mathrm{e}} v^2}{2T_{\mathrm{e}}^{\mathrm{sh}}}} \tag{2.31}$$

is the predicted forward flux of electrons with velocities $v \geq v_{\mathrm{c}}$, and Γ_e^- is the electron re-emission flux. When the electron distribution function departs from a Maxwellian, eq. (2.31) fails to predict the actual value of the forward flux of electrons at the entrance of the sheath. As shown on fig. 2.6 electron distribution functions for both insulating and conducting wall are not Maxwellian for velocities higher than v_{c}. They actually look like a superposition of two Maxwellians of different temperatures. This superposition is the result of the competition between collisional processes and the injection of particles by the source. We discuss this bi-Maxwellian feature in detail in section 3.6.1. By approximating $f_{\mathrm{e}}^{\mathrm{sh}}$ as the sum of two Maxwellians of different temperatures and densities, we can adapt the temperature used in the predicted flux expression of eq. (2.31), so that the predicted forward flux matches the forward flux of electrons found in the simulation. This corresponds to taking the temperature of the best Maxwellian fit for the $v \geq v_{\mathrm{c}}$ part of the electron distribution function at the sheath entrance. By doing so we obtain the *appropriate* set of points on fig. 2.9. These corrected points now do not exhibit any offset with respect to the prediction, as compared to the *refined* case, for both wall models.

2.8.3 Potential drop dependence on the parallel length

Lastly, we assess the dependence of the sheath potential drop with the magnetic connection length $L_\parallel$. We investigate lengths in the range $L_\parallel \in \{406, 706, 1305, 2506\}$. The fraction of the simulation box that accounts for the wall region is kept constant between these simulations, and the collisionality $\nu_0^\star$ is kept constant as well. Looking at the prediction for the potential drop given in eq. (2.22) one notices no dependence with this connection length. On fig. 2.10 we plot the effective potential drop defined in eq. (2.23) in the *baseline* scenario—i.e. without taking corrections for re-emitted electrons or departures from Maxwellian state—for both conductive and insulating wall models. The same scale is used as in the mass ratio scan of fig. 2.8. We see that the effective potential drop exhibits a weak dependence with $L_\parallel$ and stays approximately constant when varying this quantity. The discrepancy between the prediction of the effective potential drop given in eq. (2.24) can be explained once again by the electron re-emission from the wall and by the departure from a Maxwellian of the electron distribution function. Correcting the effective potential drop by taking these two effects into account we get the *appropriate* set of data points for the effective potential drop. As represented of fig. 2.10, the appropriate potential drop follows closely the prediction and stays constant when varying the connection length $L_\parallel$.

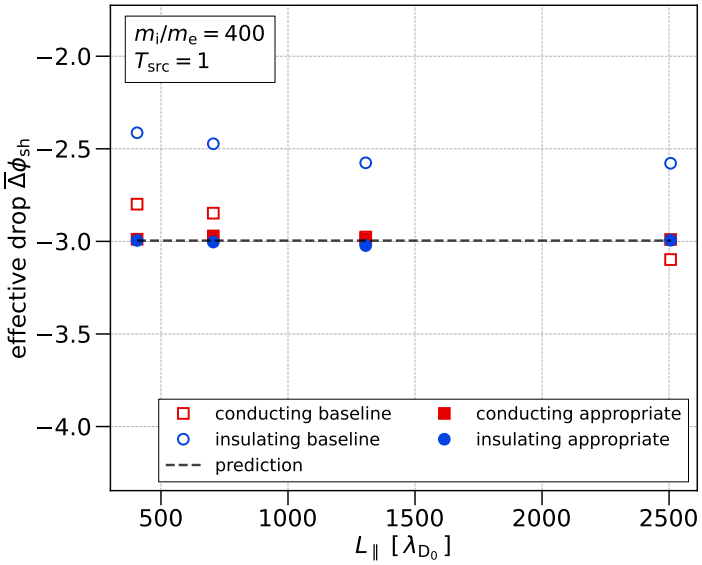

Figure 2.10: Effective potential drop dependence on magnetic field line length $L_\parallel$, for conducting (red squares) and insulating (blue circles) walls. The effective potential drop definition is the one used in the mass ratio scan, i.e. eq. (2.23).

2.9 Conclusion of the chapter

In this chapter we used a penalization technique to simulate the interaction between a plasma and a material boundary. With this technique a solid wall region—potentially of arbitrary shape, even though normal incidence only has been investigated—is immersed in the simulation domain. We investigated two different models to describe this immersed boundary region. With the first wall model that we called *conducting wall*, currents exist in the wall region, along with a small negative charge density. The second wall model—called *insulating wall*—forbids the existence of these currents by enforcing that no source of charge exists within the wall. This however comes at the price of a larger negative charge compared to the conducting wall case. For both wall models, we retrieve the fundamental features of the sheath physics. Namely, a positively charged region of typical width given by the Debye length appears in front of the wall. This sheath layer regulates the electron outflow to the wall so that the electron and ion fluxes match at the plasma boundary. The flux of electron to the wall is regulated by the sheath potential drop which reflects slow electrons back into the plasma. We compared the potential drop obtained in the sheath from the kinetic simulation with an analytical prediction derived with a simple kinetic model for the sheath. By varying relevant parameters of the simulation, we showed that the observed discrepancies between kinetic simulation and the prediction are explained by the departure from a Maxwellian state of the electron distribution function at the entrance of the sheath, but more importantly by the re-emission of electrons from the wall region. This re-emission is the consequence of (i) collisional processes happening in the sheath, and

(ii) of the presence of electrons in the wall region. As more electrons can be found in the wall in the insulating wall case compared to the conducting one, the potential drop in the insulating framework exhibits a larger discrepancy with the prediction compared to the conducting case.
Given the flexibility offered by the penalization technique to deal with complex wall geometries, and provided one can control the re-emitted electron emission from the wall into the plasma, the immersed boundary condition technique proves to be a good candidate to include the sheath physics into the gyrokinetic framework. In the conducting wall case, the re-emission of electrons can be reduced by using more absorbent walls, at the price however of a reduced timestep to absorb electrons more efficiently in the wall. In the insulating case on the contrary there is no means to control this re-emission, thus the insulating wall appears less relevant than the conducting one. In Chapter 5 we present a technique that takes advantage of the penalization technique investigated in the present chapter to propose a subgrid sheath model, that is free from electron re-emission.

3

Fluid modeling of plasma-wall interaction and comparison with kinetic simulations

Contents

3.1 Fluid description of a plasma 72
3.2 Fluid codes for tokamak power exhaust prediction 73
3.3 1D fluid model 76
3.4 Bohm criterion 77
3.5 Heat flux 86
3.6 Collisionality scan 96
3.7 Conclusion of the chapter 100

Summary

After having studied the sheath properties obtained from kinetic simulations in the previous chapter, we now investigate the quasineutral plasma, in the conducting wall framework. We use the hierarchy of fluid conservation equations to do so. The majority of the results presented in this chapter have been published in [2]. A general result from fluid theory is the Bohm criterion, which states that the flow of ions at the entrance of the sheath must be supersonic. This criterion is of interest since it is used as a boundary condition for the plasma at the limiter/divertor surface in fluid codes that use a subgrid sheath model. We investigate the validity of this criterion in the kinetic framework. We find in the kinetic simulation heat transmission factors at the entrance of the sheath 50% higher than usually predicted. This is due to the departure of distribution functions from Maxwellians at the entrance of the sheath. We show that the variations of fluid moments such as the ion mean velocity is driven by a non-vanishing heat flux. The heat flux is particularly high for electrons and accounts for 50% of the electron energy flux impinging the wall in the reference kinetic simulation. By performing several simulation varying the collisionality, we show that the observed heat flux levels result from the competition between collisions that tends to bring the system back to a Maxwellian equilibrium, and the injection of particles in the source region, along with the physics at play in the Debye sheath layer, that both tend to make the distribution functions depart from Maxwellians.

3.1 Fluid description of a plasma

Fluid models describe the time evolution of velocity-averaged plasma quantities, called fluid moments, such as the plasma density, temperature, pressure, etc. These quantities are defined as moments of the particle distribution function of species s written f_s. The plasma density n_s and mean velocity $\mathbf{u}_s$ are defined as

$$n_s(\mathbf{x},t) = \int d^3\mathbf{v}\, f_s(\mathbf{x},\mathbf{v},t), \tag{3.1}$$

$$\mathbf{\Gamma}_s(\mathbf{x},t) = \int d^3\mathbf{v}\, \mathbf{v} f_s(\mathbf{x},\mathbf{v},t). \tag{3.2}$$

Where the integrals are performed over 3D velocity space. We define the plasma mean velocity as $\boldsymbol{u}_s(\mathbf{x},t) = \mathbf{\Gamma}_s/n_s$. We further define the pressure tensor $\bar{\bar{P}}_s$ and energy flux $\mathbf{Q}_s$ as

$$\bar{\bar{P}}_s(\mathbf{x},t) = \int d^3\mathbf{v}\, m_s\,(\mathbf{v}-\mathbf{u}_s)\otimes(\mathbf{v}-\mathbf{u}_s)\, f_s(\mathbf{x},\mathbf{v},t), \tag{3.3}$$

$$\mathbf{Q}_s(\mathbf{x},t) = \int d^3\mathbf{v}\, \frac{1}{2} m_s\,|\mathbf{v}|^2\, \mathbf{v} f_s(\mathbf{x},\mathbf{v},t), \tag{3.4}$$

and the heat flux $\mathbf{q}_s$ is

$$\mathbf{q}_s(\mathbf{x},t) = \int d^3\mathbf{v}\, \frac{1}{2} m_s\,|\mathbf{v}-\mathbf{u}_s|^2\,(\mathbf{v}-\mathbf{u}_s)\, f_s(\mathbf{x},\mathbf{v},t). \tag{3.5}$$

In the above expressions $\otimes$ denotes the outer product. The pressure tensor is commonly decomposed as the sum of the scalar pressure $p_s = \frac{1}{3}\,\mathrm{tr}(\bar{\bar{P}}_s)$ and of the stress tensor $\bar{\bar{\pi}}_s$ as

$$\bar{\bar{P}}_s = p_s\mathbb{I} + \bar{\bar{\pi}}_s. \tag{3.6}$$

Where $\mathbb{I}$ is the identity tensor and $\mathrm{tr}(A)$ is the trace of tensor A. To obtain the set of equations that governs the time evolution of fluid quantities, one has to multiply the Vlasov/Boltzmann equation by powers of the velocity variable $\mathbf{v}^{\otimes k}$ and then integrate it against this variable. In this last expression $\mathbf{v}^{\otimes k}$ refers to the tensor of rank k obtained by applying the outer product k times to the vector $\mathbf{v}$. For $k=0$ we obtain a fluid equation expressing the conservation of mass which is

$$\partial_t n_s + \nabla\cdot\mathbf{\Gamma} = S_n, \tag{3.7}$$

where S_n refers to any source or sink of particles. No collision term appears here since, in the absence of neutrals, collisions conserve the number of particles in the plasma. For $k=1$ we get an equation expressing the conservation of momentum which is

$$n_s m_s\left(\partial_t\mathbf{u}_s + \nabla\cdot(\mathbf{u}_s\otimes\mathbf{u}_s)\right) = n_s e_s\left(\mathbf{E}+\mathbf{u}_s\times\mathbf{B}\right) - \nabla\cdot\bar{\bar{P}}_s + \mathbf{S}_{us} + \mathbf{R}_{us}. \tag{3.8}$$

Where the $\mathbf{S}_{us}$ term encompasses momentum sources—including the $m_s\mathbf{u}_s S_n$ term—and $\mathbf{R}_{us}$ momentum exchanges due to collisions between species s and any other species.

For $k = 2$, neglecting off-diagonal term of the pressure tensor, and assuming isotropy of the pressure, we get the conservation of energy which is

$$\partial_t \left(\frac{3}{2} p_s + \frac{1}{2} m_s n_s \left| \mathbf{u}_s \right|^2 \right) + \nabla \cdot \mathbf{Q}_s = e_s \mathbf{\Gamma}_s \cdot \mathbf{E} + \mathbf{S}_{hs} + \mathbf{R}_{hs}, \tag{3.9}$$

where then $\mathbf{S}_{hs}$ and $\mathbf{R}_{hs}$ terms represent energy sources and collisional energy exchange. There exists an infinite number of such fluid equations. By defining the moment of order k as

$$M_k^s(\mathbf{x}, t) = \int d^3\mathbf{v}\, \mathbf{v}^{\otimes k} f_s(\mathbf{x}, \mathbf{v}, t), \tag{3.10}$$

multiplying Boltzmann equation by the tensor $\mathbf{v}^{\otimes k}$ then integrating against $\mathbf{v}$, one finds an equation that links the moment of order k with the moment of order $k+1$. In practice, solving a fluid model requires truncating the hierarchy of fluid equations at some order N, and prescribing a value for the moment of order $N+1$. In most cases only the first three fluid equations written in eqs. (3.7) to (3.9) are solved numerically and the value of the heat flux $\mathbf{q}_s$ is prescribed. This prescription is referred to as the *closure* of the fluid hierarchy. The main reason for closing the hierarchy at $k = 3$ is that there exists no clear physical interpretation of moments of order higher than the heat flux. Thus, giving a prescription for these moments reveals arduous. The choice of the closure is a critical step as many properties of the system depends on this choice. In section 3.4.2 we show for instance that the speed of sound waves in the plasma depends on this closure.

3.2 Fluid codes for tokamak power exhaust prediction

An important step in the design of tokamak devices is to predict correctly the particle and heat fluxes deposited on the plasma facing components. Too high these fluxes, and operating the device without damaging the walls surrounding the plasma becomes impossible. A powerful tool to study this power exhaust problem is solving numerically fluid models to describe a tokamak plasma. There exist several such fluid codes. They reveal useful to (i) explore the physics of tokamak discharges by matching some aspects of experimental data, trying to understand the underlying causal relations or trying to provide evidence for unmeasurable quantities, and (ii) provide a predictive capability to ease the design of future fusion devices. Fluid codes stand at an intermediate level of plasma modeling complexity, between integrated modeling[1] and gyrokinetic codes. As

[1]Integrated modeling tools aim to find the best compromise between first-principle descriptions of the physics at play in tokamaks devices, and reduced models of this physics that can be solved extremely fast numerically. These tools usually assume a scale separation between the fast transport timescale and the slower timescale of currents equilibration. Most of the time they couple different codes into a *workflow*, each code being devoted to the simulation of a specific phenomenon, such as the computation of equilibrium currents, of plasma transport, etc. Integrated modeling tools can be used to predict and understand the behavior of fusion reactors. For a description of integrated modeling the reader can see [52]

such, they require less numerical resources compared to gyrokinetic codes, but provide a more accurate description of the plasma than integrated modeling tools. Fluid codes can be separated into two main categories, mean-field codes and turbulent codes. These two types of codes differ by the method they use to estimate radial transport fluxes resulting from turbulence, denoted $\mathbf{\Gamma}_{\text{turb}}$ in the following.

3.2.1 Mean-field codes

Mean-field fluid codes assume a toroidal symmetry of the plasma system and model radial transport as a random walk process. Therefore, they assume $\mathbf{\Gamma}_{\text{turb}} = -D_{\text{turb}}\nabla_{\perp}n$, where D_{turb} is a cross-field diffusion coefficient that encompasses turbulent processes in the plasma. As the name suggests, mean-field codes do not give access to the fluctuations of the electromagnetic field and plasma characteristics due to turbulence, but only to the mean value of these quantities. Mean-field models are light to run, include relevant tokamak geometries and some mechanisms or properties hard to consistently model in more complex (non mean field approaches), such as diverted plasmas with X-point, etc. They usually rely on a Braginskii closure valid at high collisionality and large ion-to-electron mass ratio. Recent improvements of mean-field codes led to the implementation of the Zhdanov closure which is suited for describing plasmas with high impurity content, realistic ion-to-electron mass ratio and plasmas with strong seeding[2] [53]. Examples of mean-field codes are SOLPS-ITER [54], SOLEDGE-3X [55, 56][3], EDGE2D [57] and GBS [58]. Mean-field codes have been used as predictive tools to assess particle and heat flux levels in ITER, along with studying plasma contamination by erosion of metallic walls for instance. The inherent weakness of mean fluid codes lies in the estimation of the coefficient D_{turb}. As this coefficient is a free parameter of the simulation, it must be estimated prior to running the code. Estimating such a coefficient is a difficult task, especially for future machines where scaling laws for the diffusion coefficient have to be used, since no experimental data is available yet.

3.2.2 Turbulent codes

As they provide a predictive tool that does not rely on the estimation of a diffusion coefficient, turbulent fluid codes have become the norm of fluid modeling. In these codes, the turbulent cross-field flux comes directly from solving for the turbulent fluctuations of the plasma density and mean velocity. These codes are therefore flux-driven, and do not assume any scale separation between equilibrium quantities and their fluctuations. Examples of turbulent fluid codes are BOUT++ [59], FELTOR [60], GRILLIX [61]. SOLEDGE3X [55, 56]. In the past, these turbulent codes did not include all of the physics available in mean-field codes, such as realistic geometry or plasma-wall

[2]Strong seeding refers to a plasma regime where impurities are injected in the far-SOL region so that they radiate a fraction of the core power. This effectively decreases heat loads on plasma facing components.

[3]Note that SOLEDGE-3X can be run in either mean-field or turbulent configuration, see section 3.2.2.

interaction. Recent efforts have made this statement less true. In particular, turbulent codes such as SOLEDGE3X include the effect of the 3D magnetic geometry in a divertor configuration. Coupling to solvers for neutrals physics has also been shown. Turbulent codes gives information about the effective turbulent diffusion coefficient that can be recomputed during the post-processing phase of the simulation. They enable studying the SOL width when varying experimentally relevant parameters, such as the divertor leg length, or the gas puff rate for instance. One of the main shortcomings of turbulent fluid codes lies in the necessary prescription of a closure for the fluid hierarchy, either on the heat flux or on the highest-order moment resolved by the code.

3.2.3 Sheath-like boundary conditions within fluid codes

In order to gain a predictive capability for particle and energy fluxes on plasma-facing components of a tokamak, fluid codes need to account for the geometry of solid plasma boundaries—such as the shape of the limiter/divertor and the first wall. This is no easy task since in general the walls of a tokamak can be of quite complicated shape. Possible solutions to overcome this challenge can be for instance adopting a mesh to discretize the simulated domain that is aligned with the plasma solid boundaries, or using immersed boundary conditions to model the solid wall region. This last technique has successfully been applied to modeling the SOL region of a tokamak while accounting for relevant divertor physics—such as plasma-neutral interaction [62]—and we applied this technique in Chapter 2 of the present work to model plasma-wall interaction in a one-dimensional simple magnetic geometry. In both cases, with immersed boundary conditions or with an aligned mesh, fluid codes need to account for plasma-wall interaction without solving the sheath characteristic time and spatial scales. Fluid codes describe the time evolution of several fluid moments, possibly for several charged species of the plasma. Providing boundary conditions at the divertor/limiter surface is therefore required for all of the moments described by the fluid model. We mainly focus hereafter on the boundary conditions imposed on the mean velocity $\mathbf{u}_s$ and energy flux $\mathbf{Q}_s$ of species s, and on the electrostatic potential ϕ as these are constrained at the limiter/divertor surface by the sheath physics at play. The boundary conditions usually imposed on these quantities by fluid codes can be summarized as [62–64]

1. The electric potential ϕ at the solid wall boundary is fixed at a value given by the prediction for the sheath potential drop. This prediction can be the one given by eq. (2.22), or a modified version of this prediction, that accounts for instance for a non-vanishing current at the plasma boundary;

2. The energy flux $\mathbf{Q}_s$ is fixed by the energy exhaust balance $\mathbf{Q}_s = \gamma_s \mathbf{\Gamma}_s T_s$, where γ_s is the sheath heat transmission factor for species s. Typical values for this factor are $\gamma_e = 4.8$ and $\gamma_i = 3.5$, see section 3.5.4 for the derivation of these values and for a discussion on the sheath heat transmission factors observed in the kinetic simulation;

3. The boundary condition for the particle flux is fixed using Bohm criterion which is of the form $\mathbf{u}_s \cdot \mathbf{n}_\mathrm{w} \geq c_s \mathbf{b} \cdot \mathbf{n}_\mathrm{w}$, where $\mathbf{b}$ denotes the unit vector in the direction parallel to the magnetic field, $\mathbf{n}_\mathrm{w}$ is the local unit vector normal to the solid wall, and c_s is the speed of sound. We recall here that the Bohm criterion results from a positive charge building up in the presheath region that accelerates ions up to supersonic speeds at the entrance of the sheath, see section 2.1.2.

These boundary conditions can be improved to account for instance for a plasma composed of several ion species, see [65], or to account for the magnetic presheath, see [66]. We focus hereafter on the boundary condition imposed on the ion mean velocity through the Bohm criterion. We show in the present chapter that the speed of sound waves in the plasma c_s strongly depends on the closure used to truncate the hierarchy of fluid equations. Therefore, to impose a relevant boundary condition on the ion mean velocity one needs to compute the value of the speed of sound that is consistent with the chosen closure. More precisely, as discussed in details in section 3.4.2 the speed of sound used to impose the Bohm criterion at the plasma-facing units must be derived taking into account the prescribed expression of the heat flux used to close the hierarchy of fluid equations—or equivalently, taking into account the prescription on the highest-order moment resolved by the fluid model. This observation seems quite relevant as the value of the speed of sound is used to give a lower bound for the mean speed of ions $u_i > c_s$ in a region where one is very much interested in assessing correct levels of energy and particle fluxes. To our knowledge, most of the time a generic value for the sound speed is used in fluid codes, such as the sound speed obtained in the framework of the isothermal closure $c_s = \sqrt{(T_e + T_i)/m_i}$, or the polytropic sound speed $c_s = \sqrt{\gamma_p (T_e + T_i)/m_i}$, see section 3.4.2. In both cases these sound speeds are not necessarily consistent with the chosen closure adopted in each specific model. We present in section 3.4.2 a technique that could in principle be applied to 3D fluid models to compute a speed of sound that is internally consistent with the choice of closure.

3.3 One dimensional fluid model of a plasma along a magnetic field line

In this section we write the fluid moments and conservation equations with the simplified magnetic geometry presented in section 2.2. This geometry is the one used in the VOICE code, and describes a single magnetic field line bounded by two walls. In this framework the fluid equations expressing the conservation of density, momentum and energy reduce to

$$\partial_t n_s + \partial_x \Gamma_s = S_n^s \tag{3.11}$$

$$m_s \partial_t \Gamma_s + \partial_x \Pi_s = -e_s n_s \partial_x \phi + C_\Gamma^s \tag{3.12}$$

$$\partial_t \mathcal{E}_s + \partial_x Q_s = -e_s \Gamma_s \partial_x \phi + C_\mathcal{E}^s + S_\mathcal{E}^s \tag{3.13}$$

where the fluid moments are defined as in eqs. (3.1) to (3.4) except the integrals are now one-dimensional. We further write the particle flux as $\Gamma_s = n_s u_s$ with u_s the mean velocity of species s. The momentum flux Π_s is defined as

$$\Pi_s = \int_{-\infty}^{+\infty} dv\, m_s v^2 f_s = n_s T_s + m_s n_s u_s^2 = 2\mathcal{E}_s \tag{3.14}$$

This last expression also defines the energy $\mathcal{E}_s$ and temperature T_s. We write the pressure as $p_s = n_s T_s$. The energy flux Q_s can be decomposed as the sum of the convective energy flux $Q_s^c = u_s(p_s + \mathcal{E}_s)$ and the heat flux q_s as $Q_s = q_s + Q_s^c$. In one dimension the heat flux is $q_s = \int dv\, \frac{1}{2} m_s (v - u_s)^3 f_s$. As stated in section 3.1, a closure of the fluid eqs. (3.11) to (3.13) consists in prescribing an expression for the heat flux q_s, the higher-order moment considered that appears in these equations. Furthermore, in the fluid equations (3.11-3.13), the S_n^s term describes the particle source defined as

$$S_n^s = \int_{-\infty}^{+\infty} dv\, \mathcal{S}(f_s), \tag{3.15}$$

with $\mathcal{S}$ the source term in Boltzmann eq. (2.6) and $S_\mathcal{E}^s$ is the energy source term

$$S_\mathcal{E}^s = \int_{-\infty}^{+\infty} dv\, \tfrac{1}{2} m_s v^2 \mathcal{S}(f_s). \tag{3.16}$$

Remember that the source term $\mathcal{S}(f_s)$ appearing in Boltzmann eq. (2.6) does not inject any momentum, thus there is not momentum source in eq. (3.12). Lastly, C_Γ^s and $C_\mathcal{E}^s$ represent collisional momentum and energy transfers obtained by taking the moments of the collision operator $\mathcal{C}(f_s)$ in a similar fashion as eqs. (3.15) to (3.16), i.e. $C_\Gamma^s = \int dv\, m_s v\, \mathcal{C}(f_s)$ and $C_\mathcal{E}^s = \int dv\, \frac{1}{2} m_s v^2\, \mathcal{C}(f_s)$.

3.4 On the difficulty of applying the Bohm criterion in a kinetic framework

In this section we analyse the kinetic simulation results from the VOICE code, using the conducting wall model. Section 3.4.1 shows that the Bohm criterion is not satisfied at the entrance of the sheath in the kinetic simulation. In section 3.4.2 we show that the expression of the speed of plasma sound waves depends on the closure of the fluid hierarchy by computing the sound speed for several closure schemes. In all graphs presented hereafter, only the right half of the simulation box of the plasma is represented, which spans from the stagnation point at $x = 0$ up to the sheath entrance at $x \approx 200$. The left half of the simulation box is the symmetric of the right part.

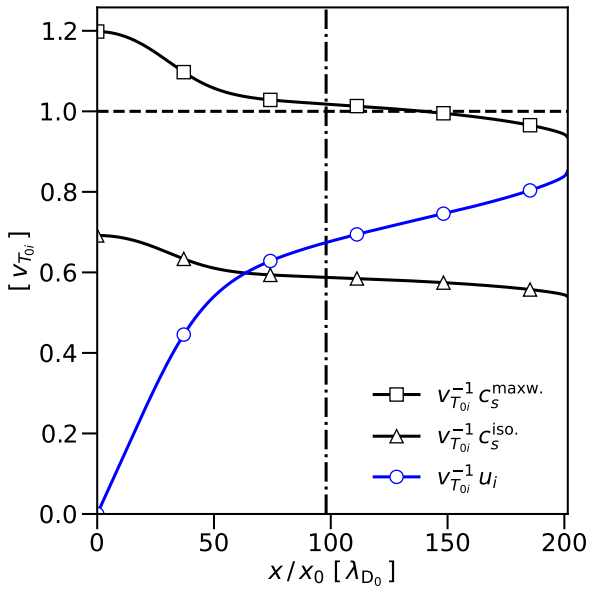

Figure 3.1: Normalized ion mean velocity $u_i/v_{T_0 i}$ with ion thermal velocity $v_{T_0 i} = \sqrt{T_0/m_i}$, alongside with the normalized speed of sound in the isothermal $c_s^{\text{iso}}/v_{T_0 i}$ and maxwellian $c_s^{\text{maxw}}/v_{T_0 i}$ cases. The leftmost region of the graph delimited by the vertical dashed line corresponds to the region where the source of particles is active. The quantities visible in the figure are computed using the reference kinetic simulation from the VOICE code.

3.4.1 Bohm criterion in the kinetic simulation

One of the most famous theoretical results concerning the physics of plasma-wall interaction is the so-called Bohm criterion. This result dates back from 1949 and states that ions must penetrate in the sheath region with a velocity that is superior or equal to the speed of sound in the plasma [67]. From a fluid standpoint, this acceleration comes from the presheath potential drop that exists within the quasineutral plasma. This presheath accelerates ions during their travel from the stagnation point up to the plasma facing components, where they are supposed to reach supersonic speeds. In the following, we distinguish between the Bohm criterion in its marginal form $M = 1$ and in its less constraining form $M \geq 1$ at the entrance of the sheath. We refer to the $M = 1$ constraint at the sheath entrance as the *marginal Bohm criterion*, and to the $M \geq 1$ constraint simply as *the Bohm criterion*. The mach number M is defined as

$$M = u_i/c_s, \tag{3.17}$$

where u_i is the mean ion velocity and c_s is the speed of sound waves in the plasma, whose expression is left undefined for now. There exist numerous demonstrations of the Bohm criterion, two of them being detailed in appendix B.1 and (B.2). The first derivation assumes cold ions and gives the Bohm criterion $M \geq 1$ at the entrance of the sheath, while the second one assumes that the sheath layer is infinitely small as compared to the plasma parallel connection length and gives the marginal Bohm criterion $M = 1$ at the

sheath entrance. Stepping to the analysis of the kinetic simulation results, fig. 3.1 shows the spatial variation of the normalized ion mean velocity $u_i/v_{T_0 i}$—defined with the ion thermal velocity $v_{T_0 i} = \sqrt{T_0/m_i}$. In section 3.4.2 we show that the speed of sound waves in the plasma is expressed as $c_s^{\text{iso}} = \sqrt{(T_e + T_i)/m_i}$ when assuming isothermal ions, and $c_s^{\text{maxw}} = \sqrt{3(T_e + T_i)/m_i}$ when assuming a Maxwellian plasma[4]. The spatial variation of these two expressions for the speed of sound waves are represented on fig. 3.1. The normalized ion mean velocity $u_i/v_{T_0 i}$ increases steeply in the plasma region where the particle source is active, roughly in between $x \approx 0$ and $x \approx 100$. It then increases in a slower fashion in the rest of the plasma that we call the free streaming region. Conversely, the two sound speeds decrease going from the stagnation point at $x = 0$ to the wall. When assuming an expression for the speed of sound waves compatible with a Maxwellian plasma, we find that the Bohm criterion is not satisfied, i.e. $u_i/c_s^{\text{maxw.}} < 1$ everywhere in the simulation box. When considering a sound speed compatible with isothermal ions, we find that the marginal Bohm criterion $M = 1$ is satisfied in the quasineutral plasma, close the position $x \approx 60$, well before the entrance of the sheath that is located at $x \approx 200$. Thus at the entrance of the sheath the condition $M \geq 1$ is satisfied in this case. Note that at the entrance of the sheath, $u_i/v_{T_0 i}$ is not equal to either of the sound speeds values, computed with the isothermal or Maxwellian hypothesis.

3.4.2 On the fact that the sound speed depends on the closure of the fluid hierarchy, and on how to derive it

In this section we show that the expression of the speed of sound waves computed within the fluid framework depends on the closure of the hierarchy of fluid equations. We present a technique that allows for computing the value of the sound speed with a general closure. Then, we apply this technique to relevant closure schemes and write the obtained expressions for the sound speed. The dependence of the sound speed on the closure has two main consequences. The first one is that it becomes difficult to assess whether or not the Bohm criterion is verified in the kinetic framework. Indeed, we do not know *a priori* the value of the sound speed in the simulation. The second consequence concerns fluid codes. These codes generally enforce the Bohm criterion at the plasma boundary, see section 3.2.3, but use an expression for the speed of sound that is in general not compatible with the closure of the fluid hierarchy.

A general technique for computing the speed of sound within the fluid framework

By linearizing the first three fluid conservation equations, and then projecting the system in Fourier space one is left with a dispersion relation. This relation can be solved for finding the velocities a perturbation can propagate with in the plasma. We

[4]We use the denomination *Maxwellian plasma* to describe a plasma characterized by distribution functions of charged species that are Maxwellian.

perform this computation in a simplified one dimensional framework. This could in principle be adapted to higher dimensions, with an arbitrary closure scheme. Let us consider a quasineutral plasma composed of electrons and singly-charged ions. From quasineutrality the plasma density n relates to the densities of electrons and ions as $n_e = n_i = n$. We assume that no ionization source exists within this plasma, i.e. the electron and ion density source terms are equal $S_n^e = S_n^i$ in the mass conservation eq. (3.11). By combining the mass conservation equations for electrons and ions we obtain

$$\partial_x \left(e\Gamma_i - e\Gamma_e \right) = 0.$$

Therefore the plasma current $j = e\Gamma_i - e\Gamma_e$ must be equal to a constant in the quasineutral part of the plasma. The present model is considered one dimensional and the plasma is bounded by two walls. We consider these two solid surfaces to be at the same potential. Thus there is no current flowing in the plasma, $\Gamma_i = \Gamma_e = \Gamma$. One therefore also has $u_e = u_i = u$. We further assume that there exists a large inertia difference between ions and electrons $m_i \gg m_e$. By summing the conservations equations of momentum eq. (3.12) for ions and electrons and by neglecting the electron inertia terms we obtain

$$m_i \partial_t \Gamma + \partial_x (\Pi_i + \Pi_e) = 0.$$

We further define the sum of generalized electron and ion pressures as $\Pi = \Pi_e + \Pi_i$, and since $m_i \gg m_e$ this term reduces to $\Pi = p_e + p_i + m_i n u_i^2$. By defining the total energy flux as $Q = Q_e + Q_i$ and by summing the energy conservation equations for both species we arrive to the system

$$\partial_t n + \partial_x \Gamma = S_n \tag{3.18}$$

$$\partial_t \Gamma + \partial_x (\Pi / m_i) = 0 \tag{3.19}$$

$$\partial_t (\Pi / m_i) + \partial_x (2Q / m_i) = 2(S_{\mathcal{E}}^e + S_{\mathcal{E}}^i) \tag{3.20}$$

Let us remark that the collisional momentum and energy transfer terms C_Γ^s and $C_{\mathcal{E}}^s$ do not appear in this system since collisional processes between electrons and ions leave the plasma momentum and energy unchanged, i.e. we have $C_\Gamma^e = -C_\Gamma^i$ and $C_{\mathcal{E}}^e = -C_{\mathcal{E}}^i$. Let us linearize this system by considering fluctuations of the density, momentum and total pressure around steady state solutions of eqs. (3.18) to (3.20) for these quantities as $n = n_0 + \tilde{n}$, $\Gamma = \Gamma_0 + \tilde{\Gamma}$ and $\Pi = \Pi_0 + \tilde{\Pi}$. The steady state quantities—also referred to as equilibrium quantities in the following—may depend on space. The perturbations denoted by the tildes are small compared to their corresponding equilibrium quantities. Rewriting eqs. (3.18) to (3.20) for the perturbed quantities leads to

$$\partial_t \tilde{n} + \partial_x \tilde{\Gamma} = 0 \tag{3.21}$$

$$\partial_t \tilde{\Gamma} + \partial_x (\tilde{\Pi} / m_i) = 0 \tag{3.22}$$

$$\partial_t (\tilde{\Pi} / m_i) + \partial_x (2\tilde{Q} / m_i) = 0 \tag{3.23}$$

Next, we linearize the perturbed part of the energy flux by expressing it as a function of the lower order moments as

$$\frac{2Q}{m_i} = \frac{2Q_0}{m_i} + \frac{2\tilde{Q}}{m_i}, \tag{3.24}$$

with

$$\frac{2\tilde{Q}}{m_i} = a_n\tilde{n} + a_\Gamma\tilde{\Gamma} + a_\Pi\tilde{\Pi}/m_i, \tag{3.25}$$

and

$$a_n = \partial_n\left(\frac{2Q}{m_i}\right)\bigg|_0, \quad a_\Gamma = \partial_\Gamma\left(\frac{2Q}{m_i}\right)\bigg|_0, \quad a_\Pi = \partial_{\Pi/m_i}\left(\frac{2Q}{m_i}\right)\bigg|_0 \tag{3.26}$$

where the 0 subscript indicates that the corresponding partial derivative is evaluated at $(n_0, \Gamma_0, \Pi_0/m_i)$. By writing such an expression, we projected $\tilde{Q}$ on the vector space spanned by the first three equilibrium moments (n_0, Γ_0, Π_0). Thus, we neglected any dependence of the perturbed energy flux on higher order moments. We Fourier transform the system (3.21-3.23) in space and time assuming modes characterized by the phase $ikx - i\omega t$. To study a particular mode, the time derivatives are replaced by $-i\omega$ and the spatial derivatives by ik. The determinant of the system must vanish so that non-trivial solutions exist, that is to say we shall have

$$\begin{vmatrix} -c & 1 & 0 \\ 0 & -c & 1 \\ a_n & a_\Gamma & a_\Pi - c \end{vmatrix} = 0,$$

where the phase velocity c of the considered mode is defined as $c = \omega/k$. This dispersion relation can be recast as

$$c^3 - a_\Pi c^2 - a_\Gamma c - a_n = 0. \tag{3.27}$$

Therefore, finding the expression of the a_n, a_Γ and a_Π coefficients and then solving this third order polynomial yields the velocities that a perturbation can propagate within the plasma. To summarize, in order to find the speed of sound waves in a plasma that is compatible with the considered fluid hierarchy and closure scheme, one can use the following approach.

1. Decompose fluid moments between equilibrium and fluctuating quantities. The equilibrium quantities are defined as steady state solutions of the fluid equations. Write the fluid equation expressing the time evolution of the fluctuations;

2. The linearization of the energy flux Q involves the a_n, a_Γ and a_Π coefficients defined in eq. (3.26). Specifying a closure of the fluid hierarchy on the third order moment involves prescribing an expression for the heat flux. With this expression, one can compute the a_n, a_Γ and a_Π coefficients[5];

[5]Note that the present technique can be adapted as well to closures on moments of order higher than the heat flux. This is done in appendix B.4 for instance.

3. Project the system of fluid equations describing the dynamics of the fluctuations in Fourier space, by considering a mode with phase $ikx - i\omega t$. In order for the system to admit non-trivial solutions, its determinant must vanish;

4. This determinant depends on the phase velocity $c = \omega/k$ of the considered Fourier mode. Finding values of c such that this determinant vanishes gives possible velocities of a perturbation within the plasma.

Plasma sound waves with vanishing heat flux

In this section we solve the dispersion relation given in eq. (3.27) using a simple closure which consists in assuming a vanishing heat flux for both species, i.e. $q_i = q_e = 0$. This heat flux is defined in eq. (3.5). The situation of vanishing heat flux is encountered when assuming the ion and electron distribution functions to be Maxwellians. This situation is encountered when the plasma collisionality is very large such that thermal equilibrium is reached. Let us now express the total energy flux $Q = Q_e + Q_i$ in the limit of a vanishing heat flux and large ion-to-electron mass ratio. We have $Q = Q_c^e + Q_c^i$. We neglect the $\frac{1}{2} m_e n_e u_e^2$ term compared to $\frac{1}{2} m_i n_i u_i^2$. Since quasineutrality holds in the plasma one can write $n_e = n_i = n$. By the physics at play within the sheath, given that we neglect transport with adjacent field lines we additionally have $\Gamma_e = \Gamma_i = \Gamma$ and $u_e = u_i = u$. Therefore the total energy flux is

$$Q = \Gamma \left(\frac{3}{2} T + \frac{1}{2} m_i u_i^2 \right),$$

with the total temperature T defined as $T = T_e + T_i$. Similar arguments lead to the following expression for the total pressure $\Pi = nT + m_i n u^2$ and thus

$$\frac{3}{n} \frac{\Pi}{m_i} = \frac{3T}{m_i} + 3u^2 = \frac{3T}{m_i} + \frac{3\Gamma^2}{n^2}$$

Thus the total energy flux $Q = Q_e + Q_i$ can be rewritten as

$$\frac{2Q}{m_i} = \Gamma \left(\frac{3}{n} \frac{\Pi}{m_i} - \frac{2\Gamma^2}{n^2} \right).$$

We write the fluctuations of the total temperature as $T = T_{\rm eq} + \tilde{T}$. Computing the a_n, a_Γ and a_Π coefficients defined by eq. (3.24) leads to

$$\begin{aligned} a_n &= \Gamma_0 \left(-\frac{3}{n_0^2}\frac{\Pi_0}{m_i} + 4\frac{\Gamma^2}{n_0^2} \right) \\ &= u_0 \left(-3\left(\frac{T_{\rm eq}}{m_i} + u_0^2 \right) + 4u_0^2 \right) \\ &= u_0 \left(u_0^2 - \frac{3T_{\rm eq}}{m_i} \right), \end{aligned} \tag{3.28}$$

$$\begin{aligned} a_\Gamma &= \left(\frac{3}{n_0}\frac{\Pi_0}{m_i} - \frac{2\Gamma_0^2}{n_0^2} \right) - 4\frac{\Gamma_0^2}{n_0^2} \\ &= 3\left(\frac{T_{\rm eq}}{m_i} + u_0^2 \right) - 6u_0^2 \\ &= 3\left(\frac{T_{\rm eq}}{m_i} - u_0^2 \right), \end{aligned} \tag{3.29}$$

and $a_\Pi = 3u_0$. With these expressions it is easy to check that the dispersion relation of eq. (3.27) admits u_0 as a solution. Thus, the polynomial can be recast in the following form

$$(c - u_0)(c^2 - 2u_0 c + u_0^2 - 3T_{eq}/m_i) = 0.$$

Its two other roots are

$$c_\pm = u_0 \pm \sqrt{3T_{eq}/m_i}.$$

Therefore, in the reference frame of the plasma that moves with velocity u_0, perturbations may propagate either towards increasing or decreasing values of the x variable. The speed of these perturbations corresponds to the value of the speed of sound in the framework of a vanishing heat flux closure, which is therefore

$$c_s^{\rm maxw.} = \sqrt{\frac{3\left(T_e + T_i\right)}{m_i}},$$

where the *maxw.* superscript indicates the closure used to compute the speed of sound, and we replaced the sum of the plasma equilibrium temperatures T_{eq} by its expression as a function of the electron and ion temperatures $T_e + T_i$.

Comparison of the sound speed obtained with various closure schemes

The speed of sound waves derived for various closures of the fluid hierarchy can be found in Table (3.1). For each of these expressions, we give a reference to a section of the present work or to a paper where the derivation can be found. The investigated closure are

- An *isothermal closure*, where the temperature of the electron and ions is considered constant along the considered field line;
- A *Maxwellian* closure that assumes a Maxwellian distribution function for the ions and electrons. This closure implies that the heat flux of both species vanishes;
- A *cold ions* closure, that assumes monoenergetic ions, i.e. $T_i = 0$;
- A *polytropic closure*, where the variations of plasma pressure are related to the variations of plasma density through the polytropic coefficient γ_p as $\frac{dp}{p} = \gamma_p \frac{dn}{n}$;
- A *non-collisional* closure, first proposed by *Hammet-Perkins* [68, 69]. This closure projects the heat flux q_s on lower order moments of the distribution function, and gives the coefficients that appear in section 3.4.2 by matching the density fluctuations response in the kinetic and fluid framework. One of its essential merits is to encapsulate Landau damping within a fluid framework.
- A *higher-order moment* closure, which consists in assuming that the moment of order ℓ of the distribution function vanishes, i.e. $N_\ell = 0$. The moment of order ℓ is defined in this case by eq. (B.13).

Note that other closures could have been investigated as well. In particular, most fluid models assume a collisional parallel heat flux driven by the temperature gradient of the form $q_s = -\kappa_s \nabla_\parallel T_s$, with κ_s the thermal conductivity of the plasma for species s. While the computation of the speed of sound could easily be done—at least in the present one-dimensional framework—we chose not to present it here for the simple reason that such a closure cannot be used to match the reference kinetic simulation. Indeed, as detailed in section 3.6.1, the kinetic simulation exhibits a positive electron heat flux at a slightly positive electron temperature gradient, ruling out any relation of the form $q_e = -\kappa_e \nabla_\parallel T_e$ with $\kappa_e > 0$. The positive electron temperature gradient can be seen on fig. 3.7, left graph, for the simulation with a collisionality value $\nu_0^* = 5$. The electron heat flux is positive as well where $\nabla T_e > 0$, as can be seen on fig. 3.6, right graph[6].

The marginal Bohm criterion $M = 1$ at the entrance of the sheath is not recovered by any of the expressions for the sound speed. fig. 3.1 rules out $u_i = c_s$ for the Maxwellian and isothermal sound speeds. It is not so surprising given that the temperature is not constant along the field line, see fig. 3.7, and the heat flux is not vanishing, see section 3.5.3. We additionally have $c_s^{\text{cold}} < c_s^{\text{iso.}}$ thus the cold ion hypothesis does not enable for recovering the Bohm criterion, not so surprising either since ions are not monoenergetic in the kinetic simulation. The polytropic closure could lead to find $u_i = c_s^\gamma$ at the entrance of the sheath for a well-chosen value of the polytropic coefficient

[6]Note that a situation with $\kappa_e < 0$ could be encountered. The system would in this case exhibit an anti-diffusive behavior that would lead to a temporary instability. This instability is however no observed in the simulations.

Closure	Sound speed	Main assumptions	Derivation
Isothermal	$c_s^{\text{iso.}} = \sqrt{\dfrac{T_e + T_i}{m_i}}$	$T_s = \text{cte.}$	[44]
Maxwellian	$c_s^{\text{maxw.}} = \sqrt{\dfrac{3\,(T_e + T_i)}{m_i}}$	$q_s = 0$	section 3.4.2
Cold Ions	$c_s^{\text{cold}} = \sqrt{\dfrac{T_e}{m_i}}$	$T_i = 0$	appendix B.1
Polytropic	$c_s^{\gamma} = \sqrt{\dfrac{\gamma_p\,(T_e + T_i)}{m_i}}$	$\dfrac{dp}{p} = \gamma_p \dfrac{dn}{n}$	appendix B.3
Hammet-Perkins	$c_s^{\text{HP}} > c_s^{\text{maxw.}}$	Projection of q_s	[2]
Closure at order ℓ	$c_s^{\ell} = \left(\ell \dfrac{N_{\ell-1}}{n}\right)^{1/(\ell-1)}$	$N_\ell = 0$	appendix B.4

Table 3.1: Speed of plasma sound waves computed with various closures of the fluid hierarchy.

γ_p. In appendix B.3 we compute the polytropic coefficient from the kinetic simulation results using the definition of the polytropic coefficient $\gamma_p = \frac{n}{p}\frac{dp}{dn}$. By doing so one gets fig. B.1. We thus find that the polytropic coefficient is not constant: it varies within the plasma, ruling out the polytropic closure. The Hammet-Perkins closure does not seem to lead to a better prediction of the kinetic simulation result since it gives a sound speed higher than the one computed in the framework of the vanishing heat flux closure, $c_s^{\text{HP}} > c_s^{\text{maxw.}}$. Closing the hierarchy at order ℓ does not seem to be satisfactory either, since one has no physical insight on the physical meaning of the moment of order ℓ. In particular, one cannot expect the moment N_ℓ to approach zero as $\ell \to +\infty$. Indeed, when considering for instance a Maxwellian distribution function, one has $N_\ell = 0$ for odd values of ℓ, and $N_\ell > 0$ for even values of ℓ. The fact that none of the investigated closures results in finding $u_i = c_s$ at the entrance of the sheath does not necessarily imply that the marginal Bohm criterion does not apply. Two options are possible; either the marginal Bohm criterion does not apply indeed, or it does but the value of the sound speed at the sheath entrance is unknown. Let us additionally note that for some of the investigated expressions of the sound speed, the Bohm criterion $M \geq 1$ appears to be satisfied at the entrance of the sheath. It is the case for instance with the isothermal ion sound speed, where one observes on fig. 3.1 that $u_i > c_s^{\text{iso}}$ at the sheath entrance. The Bohm criterion $M \geq 1$ does not however appear to be a robust tool to study a kinetic simulation: depending on the chosen expression of the

sound speed, the criterion is satisfied at different locations in the plasma, or is simply not satisfied. Therefore, what the present analysis shows is that the Bohm criterion is very difficult to apply in the kinetic framework as a prognostic quantity.
As stated in section 3.4.2, the dependency of the sound speed on the closure of the fluid hierarchy may have consequences for fluid codes. In most cases indeed, the sound speed c_s used to impose the Bohm criterion $M = u_i/c_s \geq 1$ at the plasma boundary—typically at the divertor surface—is not consistent with the closure of the fluid hierarchy. To resolve this inconsistency one could use the technique presented in section 3.4.2 to derive an expression for the speed of sound that is compatible with the chosen closure. In principle, the technique could be applied to a three-dimensional case with any closure scheme, although calculations will obviously be more complex than in the one-dimensional case considered for the present study. Prior to conducting such an analytical work, one could assess the dependency of the Bohm criterion $M \geq 1$ imposed in fluid codes with the expression of the sound speed c_s. More precisely, one could consider for instance a sound speed of the form $c_s^\chi = \sqrt{\chi(T_e + T_i)/m_i}$, and perform several simulations varying the factor χ. If quantities of interest such as heat and particle fluxes on the plasma facing units exhibit a non-negligible dependency on the parameter χ, a recommendation would then consists in deriving an expression for the speed of sound that is compatible with the chosen closure. The steps required for deriving such a sound speed adapted to a given closure are detailed in section 3.4.2.

3.5 Heat flux influence on steady state plasma characteristics

In this section, we show that the kinetic simulation exhibits non-negligible heat flux levels, in particular for the electron species for which the heat flux accounts for approximately 50% of the electron energy flux. Using the analytical prediction from the Maxwellian closure, we show that this non-vanishing heat flux is responsible for the variations of fluid moments such as the ion mean velocity in the free streaming region of the simulation box. We then propose an explanation for the origin of such a non-vanishing heat flux, as being the consequence of the injection of particles in the source region, and of the sheath physics at play close to the wall.

3.5.1 Prediction of the variation of plasma quantities assuming a Maxwellian closure

To assess the impact of the heat flux on the fluid quantities, we study the system of the first three fluid equations presented in eqs. (3.11) to (3.13) assuming a vanishing heat flux closure—or equivalently, a plasma that has a Maxwellian distribution function. With this closure, the spatial evolution of all fluid moments is analytical and can be expressed as a function of a single control parameter A. Note that the following analysis is very similar to the one presented in [70] which assumes an isothermal closure. We thus assume $q_s = 0$ and work with a large ion-to-electron mass ratio $m_i \gg m_e$. When steady-state is reached the time derivatives that appear in the fluid conservation

equations vanish and the system can be recast as

$$\partial_x \Gamma = S_n \tag{3.30}$$

$$\partial_x (\Pi / m_i) = 0 \tag{3.31}$$

$$\partial_x (2Q_c / m_i) = 2\left(S^e_{\mathcal{E}} + S^i_{\mathcal{E}}\right) \tag{3.32}$$

Where $Q_c = \Gamma(\frac{3}{2}T + \frac{1}{2}m_i u_i^2)$ is the convective part of the energy flux. Inside the plasma the source term $\mathcal{S}(f_s)$ has a Maxwellian shape and can be expressed as

$$\mathcal{S}(f_s) = \frac{S_n}{\sqrt{2\pi T_{\text{src}}/m_s}} \exp\left(-\frac{m_s v^2}{2T_{\text{src}}}\right). \tag{3.33}$$

where T_{src} represents the temperature of the source, and S_n gives the spatial profile of the particle source. With this expression the sum of the energy source terms that appear in eq. (3.32) reduces to $S^e_{\mathcal{E}} + S^i_{\mathcal{E}} = T_{\text{src}} S_n$. As the one-dimensional plasma domain is symmetric all fluid moments of odd order—such as the particle and energy fluxes—vanish at the stagnation point $x = 0$. By integrating the system (3.30-3.32) between $x = 0$ and a particular position along the magnetic field line we get

$$\Gamma = \int_0^x S_n(y)\, dy \tag{3.34}$$

$$\Pi = \text{cte.} \tag{3.35}$$

$$\Gamma\left(3T + m_i u_i^2 - 2T_{src}\right) = 0. \tag{3.36}$$

The first equation simply expresses the fact that the particle flux builds up going towards the wall as a consequence of the particle source term. The second equation states that the total pressure of the plasma stays constant. This is nothing else than the conservation of the plasma total energy as $\Pi = \Pi_e + \Pi_i = 2(\mathcal{E}_e + \mathcal{E}_i)$. Lastly, eq. (3.36) states that the thermal energy $2T_{\text{src}}$ injected in the plasma by the particle source splits up between the plasma thermal energy $3T/2$ and kinetic energy $m_i u_i^2/2$. We further substitute the mach number $M = u_i / c_s^{\text{maxw.}}$ in eq. (3.36). We take the sound speed compatible with the Maxwellian closure $c_s^{\text{maxw.}} = \sqrt{3T/m_i}$, see Table 3.1. eq. (3.36) can thus be used to express the plasma temperature T as a function of the Mach number as

$$T = \frac{2T_{\text{src}}}{3\left(1 + M^2\right)}. \tag{3.37}$$

We now seek a similar expression for the total pressure Π. This quantity can be recast as

$$\Pi = \Pi_{qn} - (n_i - n_e)T_e,$$

Where $\Pi_{qn} = n_i T + n_i m_i u_i^2$ is the total pressure in the quasineutral plasma region, i.e. $\Pi = \Pi_{qn}$ when $n_i = n_e$. We focus on this region in the following, where $n_e = n_i = n$

and since $\Gamma_e = \Gamma_i = \Gamma$ holds, we further write $u_i = u_e = u$. The total pressure is thus $\Pi_{qn} = nT(1 + 3M^2)$. We replace in this last expression the density n by

$$n = \frac{\Gamma}{u} = \frac{\Gamma}{M}\sqrt{\frac{m_i}{3T}}. \tag{3.38}$$

Thus the total pressure can be written as

$$\Pi_{qn} = \frac{\Gamma}{M}\sqrt{\frac{m_i T}{3}}\left(1 + 3M^2\right).$$

Injecting the expression for the temperature given in eq. (3.37) we arrive to

$$\Pi_{qn}^2 = \frac{2}{9} m_i T_{\mathrm{src}} \Gamma^2 \frac{\left(1 + 3M^2\right)^2}{M^2\left(1 + M^2\right)}, \tag{3.39}$$

where we squared the whole expression for the sake of simplicity. At the entrance of the sheath in the framework of the Maxwellian closure the marginal Bohm criterion is satisfied, see the end of the present section. Using the fact that the total pressure is a constant—from eq. (3.31)—and plugging $M = 1$ in the last expression we obtain the value of the total pressure in the quasineutral plasma

$$\Pi_{qn} = \frac{4}{3}\sqrt{m_i T_{\mathrm{src}}}\Gamma^\star, \tag{3.40}$$

where $\Gamma^\star$ is the value of the particle flux at the entrance of the sheath—or equivalently at the wall position since there is no particle source in the sheath—i.e.

$$\Gamma^\star = \int_0^{x^\star} S_n \, dx'.$$

Note that the plasma total pressure Π_{qn} is set by the integrated particle source $\Gamma^\star$ and the marginal Bohm criterion at the sheath entrance. The last equations (3.39) and (3.40) provide two different expressions for the total pressure Π_{qn}. By equating them, we find an expression for the quantity $\Gamma/\Gamma^\star$ which is

$$\frac{\Gamma}{\Gamma^\star} = \sqrt{\frac{8M^2\left(1 + M^2\right)}{\left(1 + 3M^2\right)^2}} = \frac{4}{3}\sqrt{m_i T_{\mathrm{src}}}\frac{\Gamma}{\Pi_{qn}}. \tag{3.41}$$

We use this last expression to define the control parameter A as

$$A = \frac{4}{3}\sqrt{m_i T_{\mathrm{src}}}\frac{\Gamma}{\Pi_{qn}}, \tag{3.42}$$

we therefore have

$$A = \sqrt{\frac{8M^2\left(1 + M^2\right)}{\left(1 + 3M^2\right)^2}}, \tag{3.43}$$

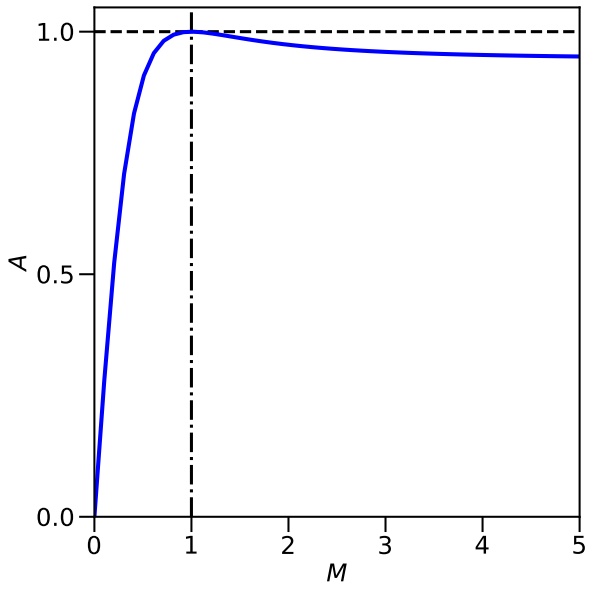

Figure 3.2: Control parameter dependence on the Mach number value given by eq. (3.43) (Maxwellian closure characterized by a vanishing heat flux). This figure has been produced by evaluating eq. (3.43) for values of the Mach number in the range $[0, 5]$.

and in the quasineutral plasma the following equality holds: $A = \Gamma/\Gamma^\star$. This last relation is however not valid in the sheath where quasineutrality breaks down. The variation of the control parameter in the quasineutral plasma region is driven solely by the particle flux, thus by the particle source. From there, eq. (3.43) can be solved to find the value of the Mach number at any spatial location in the quasineutral plasma. This in turns gives the value of the density through eq. (3.38) and temperature through eq. (3.37). Before stepping to the analysis of the kinetic simulation using the predictions developed in the present section, let us remark that the control parameter A can be used to study the supersonic transition happening at the entrance of the sheath. Plotting eq. (3.43) we obtain fig. 3.2. In the quasineutral plasma region $A = \Gamma/\Gamma^\star$ increases from a vanishing value at the stagnation point up to $A = 1$ at the sheath entrance, where all of the particle source contributions have been integrated in the expression of the particle flux given in eq. (3.34). Therefore in the quasineutral plasma region we have $M \leq 1$, the ion flow must stay subsonic. Additionally, if the particle source does not span the entire quasineutral plasma region up to the entrance of the sheath, we expect the Mach number to be constant in the region where the particle source vanishes. In the sheath, it can be shown that the departure from quasineutrality drives the increase of the Mach number to values above unity, see [2].

3.5.2 Variation of the Mach number in the kinetic simulation

In this section we analyze the spatial variation of the Mach number in the reference kinetic simulation at steady state, in the quasineutral plasma. Figure 3.3 shows the

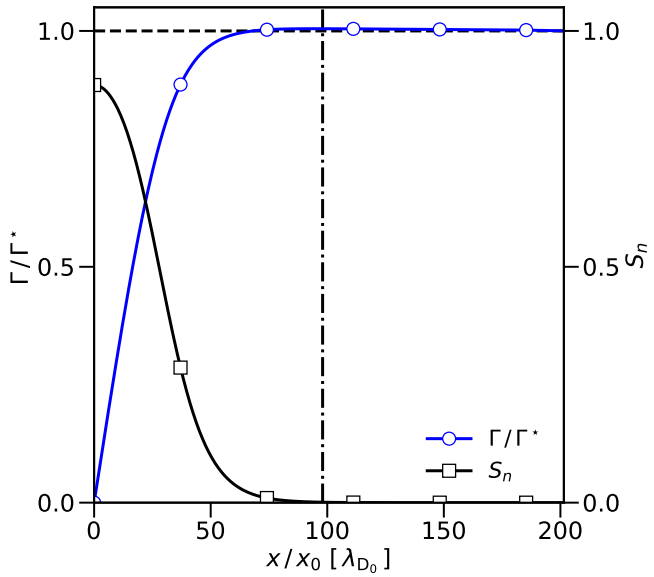

Figure 3.3: Left axis: particle flux Γ in the quasineutral plasma in the reference VOICE simulation. Right axis: profile of the particule source S_n. The particle flux is normalized to the reference particle flux $\Gamma_0 = \int_0^{x_w} dx\Gamma$ with x_w the wall position. The ratio Γ/Γ_0 should be equal to the control parameter A given in eq. (3.43) if the Maxwellian closure leading to eq. (3.43) would hold. The quantities visible in the figure are computed using the reference kinetic simulation from the VOICE code.

expected dependence of the particle flux with the source: the particle flux increases from a vanishing value at the stagnation point $x = 0$ up to a value very close to $\Gamma^\star$ after the source region and then stays constant there. Note that the values of both electrons and ions particles fluxes are very close to each other, see section 2.6. The total pressure of the plasma stays constant as $\Pi/\Pi_0 = 1.1814 \pm 3 \times 10^{-4}$ in the plasma with Π_0 the total pressure at $x = 0$. Here we see that the relative difference between Π and Π_0 is around 18%. The fact that $\Pi \neq \Pi_0$ is no surprise since the Π_0 quantity is computed by evaluating eq. (3.40), which is derived assuming a Maxwellian closure, and assuming that $u_i/c_s^{\text{maxw.}} = 1$ holds at the entrance of the sheath, with the Maxwellian sound speed $c_s^{\text{maxw.}}$ given in Table 3.1. In the present section and in section 3.5.3 we show that these two hypotheses are not fulfilled in the reference simulation. Given that the total pressure can be considered as constant with a good approximation in the simulation box, we however find that eq. (3.34) and (3.31) are verified in the kinetic simulation. This is not surprising, as these two equations are independent of any choice for the closure of the fluid hierarchy, but rather a consequence of the Boltzmann eq. (2.6) being solved correctly by the VOICE code. These two conservations can be viewed as a further verification of the code.

From the definition of the control parameter given in eq. (3.42) and fig. 3.3 we can state that A is proportional to the particle flux, as the total pressure stays constant in

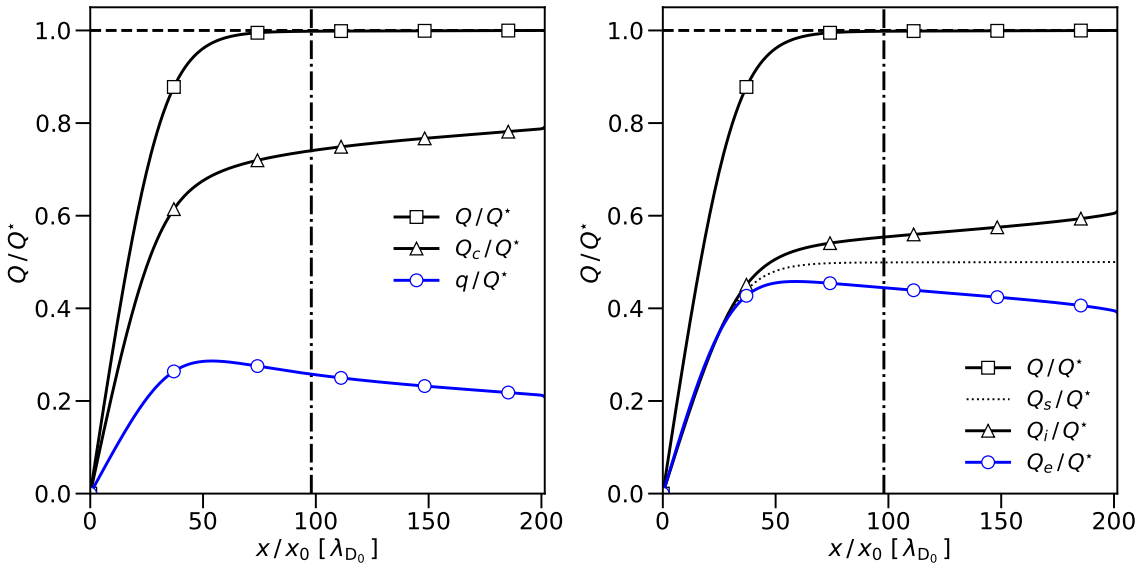

Figure 3.4: Left: plasma energy flux Q and breakdown between convective energy flux Q_c and heat flux q. The transfer between heat and convective fluxes is attributed to collisional reorganization of the system. Right: plasma energy flux and breakdown between ion and electron energy flux. The transfer from electrons to ions energy flux is attributed to Joule heating of the ions. The Q_s term corresponds to the equipartition energy flux $Q_s = Q/2$. The quantities visible in the figure are computed using the reference kinetic simulation from the Voice code.

the quasineutral plasma. Therefore, in the free streaming region A is a constant, as the particle flux Γ is constant as well there. Hence, by eq. (3.43) the Mach number should be constant as well in the quasineutral region—and because we expect the marginal Bohm criterion to be satisfied at the entrance of the sheath then $M = 1$ should hold in the free streaming region. As explained in section 3.4.1 and illustrated on fig. 3.1 this is not the case at all. The normalized ion mean velocity $u_i/\sqrt{T_0/m_i}$ increases in the free streaming region, while the sound speed computed in the vanishing heat flux framework $c_s^{\text{maxw.}}$ decreases there. Overall, the mach number increases in the free streaming region, while the control parameter A remains constant. Therefore, M cannot only depend on A. The Maxwellian closure does not allow for recovering the results of the kinetic simulation. From the analysis conducted in the framework of the vanshing heat flux closure, we conclude that it is the non-vanishing value of the heat flux in the quasineutral plasma that drives the variation of fluid quantities—and in particular of the Mach number M—outside the particle source region.

3.5.3 Variation of the heat flux in the kinetic simulation

In this section we comment on the energy and heat flux levels obtained in the kinetic simulations. On fig. 3.4 the plasma energy flux $Q = Q_e + Q_i$ is represented, along with its constituents: the plasma heat flux $q = q_e + q_i$ and convective energy flux

$Q_c = Q_e^c + Q_i^c$. The increase of the plasma energy flux Q in the source region is the direct consequence of the injection of energy by the source there, as expressed by eq. (3.32), i.e. $\partial_x Q/m_i = 2T_{\rm src}S_n$. The plasma energy flux plateaus in the free streaming region since there is no particle source there, thus no energy injection. The heat flux accounts for roughly 20% of the plasma energy flux at the wall position. It increases in the source region, exhibits a maximum value at the end of this region, and then starts to decrease. This decrease is mirrored by an equal increase of the convective energy flux Q_c, since $Q = Q_c + q$. The origin of the non-zero heat flux levels observed in the plasma is twofold: the particle source and the sheath drive the system out of thermal equilibrium. This is quite obvious for the sheath: the absorption of fast electrons at the wall position—and the reflection of slow electrons—imply that the electron distribution function departs from a Maxwellian at the entrance of the sheath. This has been explained in section 2.7.1 and can be seen on fig. 2.6. Therefore one can fairly expect non-vanishing values for the heat flux in the vicinity of the wall. The source of particles also makes distribution functions depart from Maxwellians. This is somewhat counter-intuitive since the source itself has a Maxwellian shape in velocity space, see eq. (3.33). To understand this fact, let us rewrite the Boltzmann equation (2.5) that describes the time evolution of a distribution function f in the quasineutral plasma as

$$\partial_t f + v\partial_x f = \mathcal{S}(f), \tag{3.44}$$

where we neglected collisions and the influence of the electric field on the dynamics of the system. This last hypothesis implies that particles travel with a constant velocity v during their motion in phase space. By looking at the trajectories of particles in phase space depicted on fig. 2.7 we see that it is a reasonable assumption for ions with $v \neq 0$ and for electrons. To simplify the following expressions let us consider that the mass of the considered species is unity, along with the temperature of the source $T_{\rm src} = 1$. The source is therefore $\mathcal{S} = S_n(x)/\sqrt{2\pi}e^{-v^2/2}$. Under these circumstances the above Boltzmann equation can be integrated using the method of characteristics. Its solutions for any velocity $v \neq 0$ are given by

$$f(x,v,t) = f(x-vt,v,0) + \frac{1}{v\sqrt{2\pi}}e^{-v^2/2}\int_{x-vt}^{x} dx' S_n. \tag{3.45}$$

The first term $f(x-vt,v,0)$ expresses the fact that particles are advected at a constant velocity v, while the second term encompasses the effect of the source. Let us further assume that the spatial shape of the source term is a Dirac function $S_n(x) = \delta(x)$—the particular shape of this term does not change the discussion below, but the dirac function gives simple expressions. We thus have

$$f(x,v,t) = f(x-vt,v,0) + \frac{1}{v\sqrt{2\pi}}e^{-v^2/2}. \tag{3.46}$$

Therefore, even if the distribution function at initial time $f(x,v,0)$ is a Maxwellian and the source has a Maxwellian shape in velocity space, the advection of particles

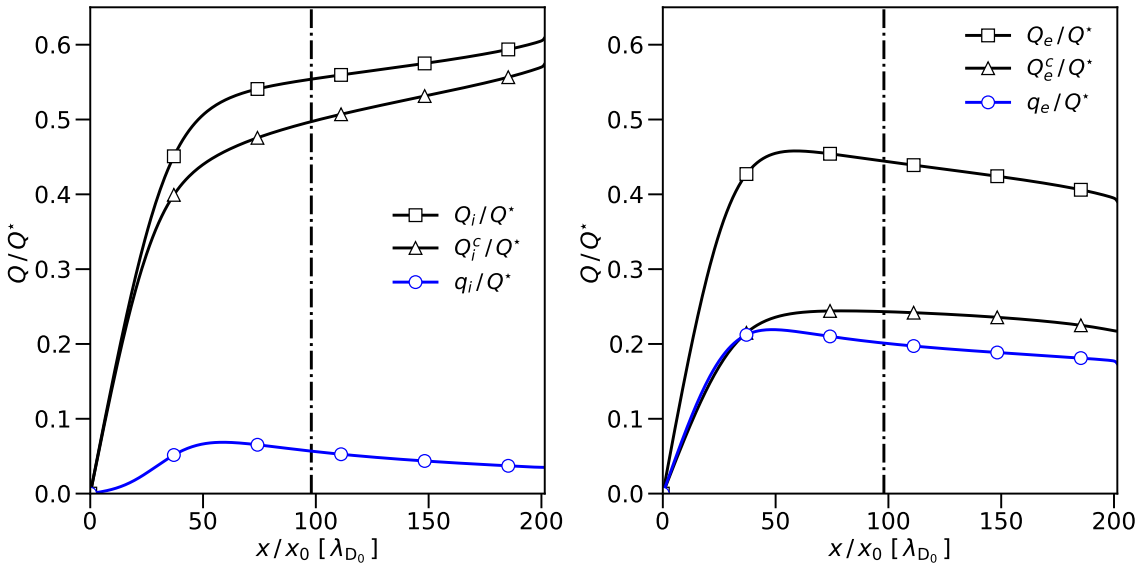

Figure 3.5: Left: Ion energy flux Q_i and breakdown between convective energy flux Q_{ci} and ion heat flux q_i. Right: same quantities for the electron species. The ion heat flux levels remain low on the contrary to the electron heat flux levels. The quantities visible in the figure are computed using the reference kinetic simulation from the VOICE code.

injected by the source drives the distribution function away from the initial Maxwellian equilibrium. This explains the increase of the heat flux in the source region observed on fig. 3.5. Let us additionally remark that eq. (3.46) further highlights the importance of collisional processes to reach a steady state for the system. The solution exhibits a singularity at $v = 0$: particles injected by the source with velocities close to zero tend to accumulate. The electric field contributes to reducing the accumulation of particles close to $v = 0$, except at the center of the plasma where by symmetry the electric field vanishes. Therefore at this singular point $(x = 0, v = 0)$ collisions are the only mechanism at hand to prevent the accumulation of slow particles. Lastly, the decrease of the heat flux observed on fig. 3.4 in the free streaming region is the consequence of collisional reorganization of the system. As the particle source is not active there, collisions drive the system back to Maxwellian equilibrium as we approach the wall.

The left graph of fig. 3.4 shows a net energy transfer from the electron to the ion species as we approach the wall. This net energy transfer is carried by the Joule heating term $e_s\Gamma E$ visible in the equation of energy conservation (3.13). The other mechanism at hand that could be held responsible for inter-species energy transfer is collisions between electrons and ions. This last mechanism can be ruled out since as shown in fig. 3.7 in the reference collisionality case $\nu_0^\star = 50$ the electron temperature is lower than the ion temperature in the plasma. Therefore the thermal energy exchange from collisions rather transfers energy from ions to electrons. Looking at fig. 3.5, left graph we see that the ion energy flux is essentially of convective nature, q_i is small compared to Q_i. It is not the case at all for electrons, as the electron heat flux accounts for nearly

50% of the electron energy flux. The fact that the ion heat flux is smaller than the electron heat flux is no surprise. Indeed, as shown in section 2.7.1 the trajectories in phase space of particles of opposite charges are fundamentally different. The ions follow a rather simple trajectory from the particle source region where they are injected to the wall where they are absorbed. Electrons trajectories are more intricate: the fastest are absorbed in the wall, the slowest are reflected back and forth between the two walls. The absorption of fast electrons at the wall location drives the system out of thermodynamical equilibrium. The sheath makes the electron distribution depart from a Maxwellian state, resulting in heat flux levels greater than the one observed for ions.

3.5.4 Heat transmission factors at the entrance of the sheath

We compute hereafter the so-called *sheath heat transmission factors* from the reference kinetic simulation and compare the obtained values with some predictions for these quantities. The sheath heat transmission factor γ is defined by the relation

$$Q_{\mathrm{sh}} = \gamma \Gamma_{\mathrm{sh}} T_e^{\mathrm{sh}}, \tag{3.47}$$

where the *sh* subscript (or superscript) indicates that the considered quantity is evaluated at the entrance of the sheath, and $Q_{\mathrm{sh}} = Q_e^{\mathrm{sh}} + Q_i^{\mathrm{sh}}$ stands for the total energy flux at the entrance of the sheath. In tokamak devices, the estimation of the total energy flux Q_{sh} deposited on the plasma-facing units is of great interest—we consider in the present section a sheath-limited Scrape-Off Layer with no sources in the sheath thus $Q_{\mathrm{sh}} = Q_{\mathrm{w}}$ with Q_{w} the energy flux deposited on the solid wall. This is especially true for the ITER project, where the power deposited on the divertor target must stay around $10\,\mathrm{MW/m^2}$ in steady state [22]. Given that the values of the electron temperature and particle flux can be obtained experimentally—using Langmuir probes for instance—having a prediction for the heat transmission factor γ gives access to an estimate of the energy flux deposited on the plasma facing components Q_{sh}. In appendix B.5 we recall a derivation of a prediction for the sheath heat transmission factor γ. This derivation can be found as well in various references such as [23]. More precisely, the derivation gives predictions for the electron and ion heat transmission factors γ_e and γ_i that are defined as

$$Q_e^{\mathrm{sh}} = \gamma_e \Gamma_{\mathrm{sh}} T_e \quad \text{and} \quad Q_i^{\mathrm{sh}} = \gamma_i \Gamma_{\mathrm{sh}} T_i. \tag{3.48}$$

And thus $\gamma \approx \gamma_e + \gamma_i$ provided $T_e \approx T_i$. Using the results from the kinetic simulation to compute the energy fluxes for both species along with particle fluxes and temperatures, one can use the above relations to estimate the heat transmission factors at the entrance of the sheath in the reference kinetic simulation. The results obtained by doing so, along with the predictions for the transmission factors are visible in Table (3.2). Note that the predictions depend on the dimensionality of the problem along with the value for the ion-to-electron mass ratio m_i/m_e. The table gives the values for the predictions at different mass ratios and dimensionalities. The reference kinetic

	γ	γ_i	γ_e
1D prediction $m_i/m_e = 400$	5.2	2.5	2.7
1D-1V simulation $m_i/m_e = 400$	7.8	4	3.8
3D prediction $m_i/m_e = 400$	5.2	3.5	3.7
3D prediction $m_i/m_e = 3600$	5.2	3.5	4.8

Table 3.2: Prediction for the sheath heat transmission factors for different values of the ion-to-electron mass ration m_i/m_e and different dimensionalities. Their values at the entrance of the sheath computed from the reference kinetic simulation are given as well. The total heat transmission factor is computed as $\gamma = \gamma_e + \gamma_i$.

simulation has been performed in a one-dimensional framework (1D in space) and with $m_i/m_e = 400$ thus we compare the values of the heat factors with the predictions derived with the corresponding dimensionality and mass ratio. We find that the sheath heat transmission factor γ is approximately 53% higher in the kinetic simulation as compared to the prediction. The electron factor γ_e is approximately 35% higher than the predicted value, while the ion factor γ_i is 60% higher than the predicted value. It is no surprise that we find such discrepancies between the prediction and the results from the VOICE code. The derivation for the predicted heat transmission factors assumes at the entrance of the sheath (i) that the ion distribution function is a Maxwellian shifted towards positive velocities, and (ii) that the electron distribution function is a Maxwellian truncated for high velocity electrons coming back from the wall. As explained in section 2.7.1 the ion and electron distribution functions depart from these simplified shapes. In the kinetic simulation one therefore finds that the energy flux impinging the wall cannot be linked to temperatures and particle fluxes with a simple prediction for the sheath heat transmission factor. We observe indeed in the kinetic simulation $Q_{\text{sh}} > \gamma_{\text{pred.}} \Gamma T_e^{\text{sh}}$. The departure of the distribution function from the quasi-Maxwellian state assumed by the prediction for γ_e and γ_i leads to a higher energy flux impinging the wall as compared to a situation where the $Q_{\text{sh}} = \gamma_{\text{pred.}} \Gamma T_e^{\text{sh}}$ relation holds.

To summarize, at least with the parameters considered in the reference kinetic simulation, one obtains an energy flux impinging the wall that is approximately 50% higher than what would be obtained by assuming a relation of the form $Q_{\text{sh}} = \gamma_{\text{pred.}} \Gamma T_e^{\text{sh}}$ with a usual value for $\gamma_{\text{pred.}}$. One can put this observation in perspective with the fact that most fluid codes assume a boundary condition of the form $Q_s = \gamma_s \Gamma_s T_s$ at the surface of plasma facing units to prescribe a value for the energy flux Q_s, see section 3.2.3. We do not claim that based on the present kinetic simulation one should use higher values for heat transmission factors in fluid codes. Indeed one can reasonably expect

that parameters such as the dimensionality of the simulation, or the physics at play close to the wall boundary—the interaction between charged species and neutrals for instance—will result in different values for the heat transmission factors as compared to the present one-dimensional case. However, in a similar fashion to the discussion presented in section 3.4.2, one could assess the dependency of key observables—such as heat and particle fluxes—with the values of γ_e, γ_i used as boundary condition in the simulation, by performing several simulations with different values for these parameters. If these key observables exhibit a strong dependency with the heat transmission factors, one could consider taking safety margins for γ_s when imposing the boundary condition $Q_s = \gamma_s \Gamma_s T_s$, so as to account for underlying kinetic effects not resolved by the code.

3.6 Influence of collisionality on the kinetic equilibrium

In this section we investigate the influence of collisionality on the simulation by performing a scan in this parameter. The investigated collisionality values are $\nu_0^\star \in \{5,\ 50,\ 500,\ 5 \times 10^4\}$. The maximum value of collisionality investigated in the present work $\nu_0^\star = 5 \times 10^4$ is set by numerical constraints, as discussed in the following in section 3.6.2.

3.6.1 Impact of collisionality on electron distribution function and heat flux

First, let us highlight again that collisional processes are critical for the system to reach an equilibrium. As discussed in section 3.5.3, collisions are essential to limit the accumulation of particles in the vicinity of the $(x = 0, v = 0)$ coordinate in phase space. They are essential as well to allow for a balance to exist between the sources and sinks of particles in the system. To illustrate this, let us write the potential drop between $x = 0$ and the wall position as $\phi(0) - \phi(x_\mathrm{w}) = \Delta\phi_\mathrm{tot.}$. In the absence of collisional processes all electrons injected by the source with velocities v such that $|v| < \sqrt{2e\Delta\phi_\mathrm{tot.}/m_e}$ are trapped within the plasma and cannot reach the wall. Typical values for the presheath and sheath potential drop give $\Delta\phi_\mathrm{tot.} \approx \Delta\phi_\mathrm{presheath} + \Delta\phi_\mathrm{sheath} \approx 3.7 T_e/e$. Assuming $T_e \approx T_\mathrm{src}$ we can compute that 99% of electrons are injected by the Maxwellian source given in eq. (3.33) in the trapped region of phase space. Collisions are responsible for the detrapping of all these electrons so that in steady state the injection of particles exactly balances the sink in the wall region. The electron distribution function is plotted for different values of the collisionality parameter $\nu_0^\star$ on fig. 3.6. At low collisionality the distribution function resembles a sum of two Maxwellian with different temperatures and densities: a cold bulk Maxwellian with temperature $T_e^c \approx 0.09 \approx T_e(x = 0)$ and density $n_e^c = 2.64$, and a hot Maxwellian characterized by $T_e^h \approx 0.80$ and density $n_e^h \approx 0.04$. The hot tail of the electron distribution function has a temperature close to the source temperature $T_\mathrm{src} = 1$. When increasing the collisionality, the whole distribution becomes Maxwellian: the hot tail disappears as the high energy electrons

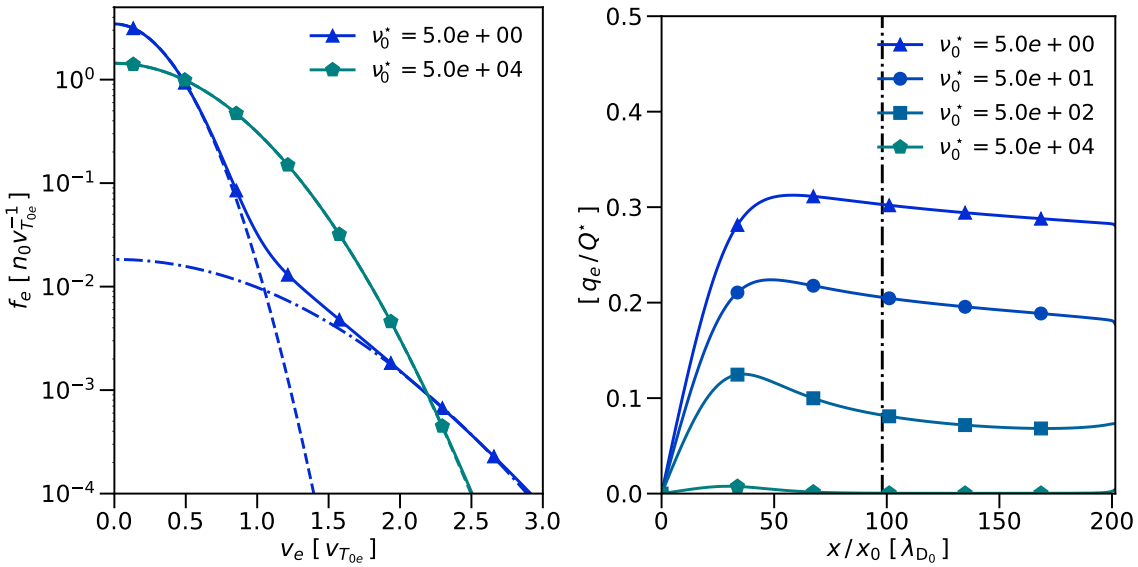

Figure 3.6: Left: positive velocity $v > 0$ part of the electron distribution function at the center of the plasma $x = 0$. Only the maximum and minimum collisionality cases have been represented for more clarity. The dashed line corresponds to the best Maxwellian fit for the whole distribution $v \in [-v_{\max}, v_{\max}]$. This fit is performed for both collisionalities. In the case $\nu_0^\star = 5 \times 10^4$ the fitted Maxwellian overlaps almost perfectly the distribution function. The dash-dotted line corresponds to the best Maxwellian fit of the high velocity part of the distribution function $v \in [v_{\text{crit.}}, v_{\max}]$, with $v_{\text{crit}} \approx 1$ in the low collisionality case. Right: electron heat flux q_e normalized to the energy flux at the wall $Q^\star$ for different collisionality values. The quantities visible in the figure are computed using the reference kinetic simulation from the Voice code.

that compose it are thermalized in the bulk of the distribution function more efficiently than in the low collisionality case. As expected, we find that increasing the collisionality drives the system back to thermal equilibrium, i.e. Maxwellian state. The effect on the heat flux is clear: on fig. 3.6, right graph, we clearly see that the electron heat flux decreases when the collisionality increases. When the collisionality is high enough $\nu_0^\star \in \{500, 5 \times 10^4\}$ we clearly see the influence of the collisional reorganization in the free streaming region on the heat flux. q_e increases in the vicinity of the source region and of the sheath, where the system is driven out of thermal equilibrium.

3.6.2 Validity of the Maxwellian closure at high collisionality

Since the heat flux vanishes when $\nu_0^\star \to +\infty$, one can expect the predictions formulated in section 3.5.1 assuming a Maxwellian closure to become valid. We expect for instance the variation of the total temperature $T = T_e + T_i$ to be described by eq. (3.37) and the Mach number by eqs. (3.42) to (3.43). Looking first at the prediction for the temperature, at high collisionality we expect equipartition of thermal energy between electrons and ions to become valid. A prediction for the electron and ion temperature

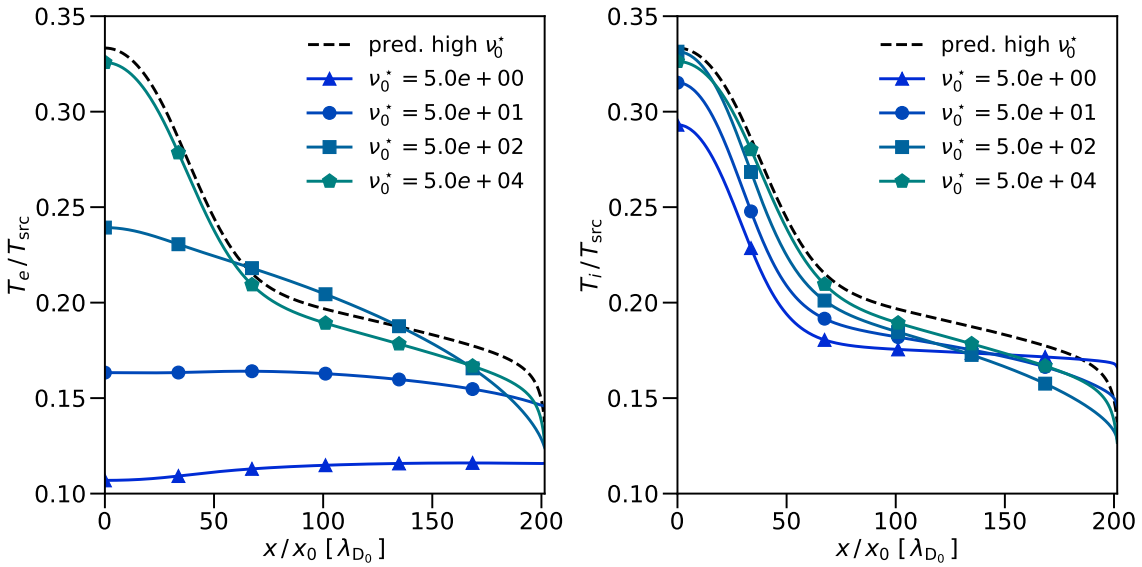

Figure 3.7: Spatial profile of electron (left) and ion (right) temperatures for different values of the collisionality $\nu_0^\star$. The prediction at high collisionality given in eq. (3.49) is visible on both graphs, while a prediction for the electron temperature performed by balancing the energy flux at the wall position is visible on the left graph. The quantities visible in the figure are computed using the reference kinetic simulation from the VOICE code.

valid at high collisionality is thus

$$T_e = T_i = \frac{T_{\text{src}}}{3\,(1+M^2)}. \tag{3.49}$$

The electron and ion temperature are plotted for different values of the collisionality on fig. 3.7. We indeed see that for both species the prediction given in eq. (3.49) is recovered for $\nu_0^\star = 5 \times 10^4$. The spatial shape of the ion temperature stays pretty similar at high and low collisionality. The same is not true at all for electrons: the electron temperature is almost flat at low collisionality. This illustrates the difference between the ion and electron dynamics. At high collisionality, the electron temperature is fixed by the ion temperature profile via collisional energy transfer between the two species. At low collisionality, the electron temperature is fixed by the sheath physics. Slow energy electrons circulate back and forth in the plasma between the two adjacent walls, effectively driving the electrons towards an isothermal state. This low collisionality regime could be called *sheath-limited*. Let us remark that at low collisionality we observe a positive electron heat flux at vanishing, or even slightly positive electron temperature gradient. On fig. 3.7, left graph we indeed see that with the collisionality of the reference simulation $\nu_0^* = 5$ the electron temperature increases when going towards the wall, i.e. $\nabla T_e > 0$. This rules out any closure of the form $q_e = -\kappa_e \nabla T_e$.

We now assess the dependence of the Mach number on the collisionality. The sound speed used to compute the Mach number is the one obtained in the framework of the

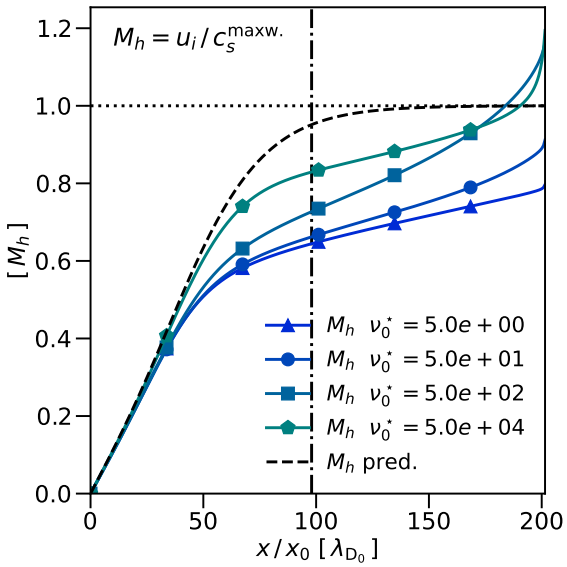

Figure 3.8: Dependence of the Mach number with the collisionality parameter $\nu_0^\star$, with the prediction at high collisionality given by eqs. (3.42) to (3.43). The quantities visible in the figure are computed using the reference kinetic simulation from the Voice code.

Maxwellian plasma $c_s^{\text{maxw.}} = \sqrt{3(T_e + T_i)/m_i}$. The prediction for the Mach number valid at high collisionality is given by the implicit equation

$$A = \sqrt{\frac{8M^2\left(1+M^2\right)}{\left(1+3M^2\right)^2}} = \frac{4}{3}\sqrt{m_i T_{\text{src}}}\frac{\Gamma}{\Pi_{qn}}, \tag{3.50}$$

On fig. 3.8 the prediction obtained from this equation is represented, along with the value of the Mach number for different values of the collisionality. Even at the highest value for the collisionality, the spatial variation of the Mach number does not follow the prediction. In particular, the Mach number increases to a value smaller than the one predicted at the end of the source region. It becomes higher than unity before the entrance of the sheath. One could however argue that the spatial shape of the Mach number profile gets closer to the prediction when the collisionality increases. Let us emphasise that the discrepancy between the prediction obtained at high collisionality and the Mach number profile obtained from the simulation can only originate from non vanishing values of the heat flux, as explained in section 3.5.1. Therefore, we do not recover the high-collisional prediction for the only reason that $\nu_0^\star = 5 \times 10^4$ is not a high-enough value of the collisionality. Going to higher values of the collisionality is challenging numerically. Indeed, in the vicinity of the sheath, the electron distribution function departs from a Maxwellian due to the absorption of fast electrons. Increasing the collisionality in this region counters this effect. When $\nu_0^\star \to +\infty$ one can reasonably argue that no equilibrium solution exists for the plasma. A perfectly Maxwellian distribution function in the sheath is not compatible with the absorption of fast electrons at the wall. Increasing the collisionality of the simulations to values higher than

$\nu_0^\star = 5 \times 10^4$ is possible, provided one decreases the value of the timestep and possibly increases the mesh discretization in the vicinity of the sheath. This would however provide little physical insight, as the system is predicted to follow the analytical predictions presented in this section in the limit $\nu_0^\star \to +\infty$. The interest of performing such a collisionality scan is rather to unveil the sensibility of the Mach number on the heat flux. As discussed above, on fig. 3.6 we saw that the electron heat flux is negligible in the case of maximum collisionality as compared to the other less collisional cases. The spatial profile of the Mach number appears nevertheless to be very sensitive to the heat flux: a small heat flux translates into a large deviation of the Mach number from the prediction. Going back to the condition $M = 1$ at the entrance of the sheath, we can conclude that at least in the one-dimensional case, it appears that the marginal Bohm criterion is not a robust feature of the kinetic simulation: even at very high collisionality values, the criterion is not recovered.

3.7 Conclusion of the chapter

In this chapter we presented the hierarchy of fluid equations, and explained the interest of using fluid codes that solve such equations to predict plasma characteristics—such as the heat loads on the plasma facing units—that are useful for the design of future tokamak devices. As such codes enforce the Bohm criterion $M \geq 1$ at the surface of the plasma facing units, we investigated the validity of this criterion with the kinetic model. Studying the quasineutral plasma from a reference kinetic simulation performed with the conducting wall model showed that the Bohm criterion in either of its $M = 1$ or $M \geq 1$ form is not an effective criterion in the kinetic framework, at least for the range of parameters investigated in the present work. By studying the hierarchy of fluid equations, we indeed observed that the speed of plasma sound waves critically depends on the closure chosen to truncate this hierarchy. In order to show this, we presented a general technique to compute the speed of sound from fluid equations, and applied this technique to several closure schemes. The fact that the sound speed depends on the closure has consequences for fluid models. Within fluid codes, the Bohm criterion is enforced at the surface of the limiter/divertor without using an expression of the speed of sound waves compatible with the considered closure. The aforementioned technique to compute the sound speed could be used to improve the relevance of the boundary conditions used in the fluid framework. We found heat transmission factors at the entrance of the sheath in the reference kinetic simulation approximately 50% higher than usually predicted. This is due to the departure of distribution functions from quasi-Maxwellian shapes usually assumed to derive predictions for the heat transmission factors.

Studying the quasineutral plasma obtained from the kinetic model by comparing it with fluid predictions formulated with the Maxwellian—vanishing heat flux—closure, we showed that the variation of the Mach number outside of the region where particle

sources are active can only be attributed to a non-vanishing heat flux. This heat flux is found to account for nearly 50% of the electron energy flux, and is due to the departure of the electron distribution function from a Maxwellian in the source region and in the vicinity of the sheath. Lastly, by varying the collisionality of the plasma we showed that even at very large values of this parameter—where both ion and electron distribution functions are Maxwellian and the heat flux almost vanishes—we do not retrieve the fluid predictions formulated with the vanishing heat flux closure. In particular, we do not retrieve the Bohm criterion. As a result, the Bohm criterion does not appear to be a robust sheath feature in the kinetic framework.

4

Plasma-neutral interaction with VOICE

Contents

4.1 Neutral interaction in the edge 103
4.2 Models for describing neutral particles 104
4.3 Pressure-diffusion model 106
4.4 Reaction rates 109
4.5 Characteristic scales of plasma-neutral interaction 109
4.6 Plasma-neutral interaction with the VOICE code 111
4.7 Conclusion of the chapter 115

Summary

In this chapter we detail the coupling between a kinetic description of a plasma and a fluid description for a neutral species. The retained fluid model for neutral is called a *pressure-diffusion* model. We implement this model along with its coupling to the kinetic model within the VOICE code. Performing a few simple *proof-of-concept* simulations highlights the impact of the neutral dynamic on the plasma close to the target. More precisely, in the investigated case where ionization is dominant, density is found to increase at the plasma boundary. This increase of density is mirrored by a decrease of the ion Mach number. Rather than providing a detailed investigation of plasma-neutral interaction with the VOICE code, this chapter aims to demonstrate the feasibility of the coupling between the fluid neutral and kinetic plasma model. This opens up the road for the future integration of such a fluid neutral model within the GYSELA code.

4.1 Including the interaction with neutrals in the edge treatment

In addition to plasma-wall interaction, an important piece of edge physics is the interaction between the plasma and neutrals particles. Neutrals can be found in the edge and Scrape-Off Layer plasmas due to two main mechanisms. The first one is the so-called *recycling* mechanism, where charged particles impinging on the wall interact with it and are subsequently released back into the plasma. Secondly, neutrals can

be injected close to the plasma-facing units. This controlled injection is of interest since the friction between the hot plasma coming from the upstream Scrape-Off Layer and neutrals leads to an effective reduction of the particle and heat flux levels at the plasma facing units. Furthermore, when the density of neutrals in front of plasma facing units is high enough, the plasma may become *detached* [71]. A detached plasma is no longer connected to the solid wall, in the sense that charged particles do not reach the wall surface. This results in a reduced particle and energy flux impinging on the wall as compared to an attached plasma scenario. The study of detached plasmas is of uttermost importance especially since the ITER reactor is expected to operate at partially detached divertor regime [24]. Thus, the inclusion of plasma-neutral interaction in the gyrokinetic framework is an important cornerstone for describing edge plasmas correctly with gyrokinetic codes and for reaching a steady-state from a particle balance perspective. As a first step towards the future implementation of plasma-neutral interaction in the GYSELA code, we detail below a one-dimensional fluid model for neutrals compatible with a kinetic description of the plasma. Prior to its inclusion in the GYSELA gyrokinetic framework, the model for neutrals has been implemented in the VOICE code. We give a brief overview of some preliminary results obtained with this model. This work has been performed with the SOLEDGE-3X team. For a reference paper concerning the implementation of a pressure-diffusive model for neutrals in the SOLEDGE-3X code the reader can see [72]. A significant portion of the work presented in the following section was conducted during the Master of Science intership of Josu Blanco at IRFM. I was involved in this intership as a co-supervisor. Last, let us remark that all of the simulations with plasma-neutral interaction have been run with a `C++` version of the VOICE code, on the contrary to plasma-wall interaction simulations investigated in chapters 2 and 3 that have been performed with the `Fortran` version of this code. To perform the simulations presented below it was thus necessary to port the VOICE code to modern `C++` and to parallelize it so that it can be exectuded on a GPU architecture. To do so the new VOICE code uses the DDC library [38], that handles multi-dimensional arrays and parallelization compatible with a variety of architectures (GPU and CPU in particular). I have been much involved in this porting and redevelopment work during my PhD.

4.2 Models for describing neutral particles

The interaction between charged particles and neutrals is mediated mainly by the following reactions. As usual, we consider ions with a single positive charge, and a neutral species that is of the same atomic number than the ion—for instance, deuterium and ionized deuterium. The reactions are

1. The *ionization* reaction, where a neutral particle A gets ionized into a positively charged particle A^+. This reaction emits an electron, and is endothermic, as a given amount of energy is required to free the electron from its previously bound

state. The reaction can be written as

$$A \rightarrow A^+ + e^-.$$

2. The *recombination* reaction, which is the opposite of the ionization reaction. An ion captures an electron to give a neutral particle. The reaction is exothermic and can be written as
$$A^+ + e^- \rightarrow A.$$

3. The *charge-exchange* reaction, where a positively-charged ion A^+ collides with a neutral B, and transfers its charge to the neutral particle. This reaction leads to the transport of neutrals. This transport can be viewed as a diffusion process if the mean free path of the charge-exchange reaction is small with respect to a characteristic length of the system [1]. The charge exchange reaction can be written as
$$A^+ + B \rightarrow A + B^+.$$

The ionization and recombination reactions account for a transfer of particles, momentum and energy between the plasma and neutrals. As an elastic collision process, the charge-exchange reaction results in an effective momentum and energy exchange between the ion and the neutral particle. To model these reactions, several models are available. The first one consists in using a kinetic description, i.e. solving a Boltzmann-like equation to model the neutrals dynamic. An example of a code that integrates such a kinetic description is the IRENE code [73]. The code uses a Monte-Carlo approach to solve the kinetic model. This approach has two main drawbacks. First, Monte-Carlo codes exhibit a high level of numerical noise resulting from the probabilistic sampling of phase space. Second and most importantly, the computational time required to solve the kinetic model becomes large when one is interested by describing detached cases, where charge-exchange reactions are dominant[2]. The fact that charge-exchange reactions are dominant at low temperature can be viewed on fig. 4.1. To model highly-collisional regimes while keeping the required numerical cost within acceptable range, one can adopt a fluid description of neutrals. This description can be solved deterministically at a small numerical cost. In the following we adopt a fluid description of neutrals.

Fluid models for neutrals can be of varying degrees of complexity. A review of such models and a comparison of their performances can be found in [74]. The simplest models, such as the one presented hereafter, solve a so-called *pressure-diffusion* equation [75–78]. This equation is obtained by balancing the pressure gradient of neutrals with

[1] This regime can be achieved at low Knudsen number $K_n \ll 1$: it corresponds to a highly collisional regime where the fluid approach becomes valid to describe the neutral dynamics

[2] In low-temperature detached plasmas, charge-exchange reactions dominates. Thus it is necessary to describe a large number of ion-neutral collisions before reaching an equilibrium in the Monte Carlo solver

the momentum source from plasma-neutral interaction, see section 4.3. Using such a pressure-diffusion equation to describe the neutral dynamics gives satisfactory results concerning the source of charged particles resulting from plasma-neutral interaction [74]. This pressure-diffusion model has been applied to realistic ITER-like geometries in [79]. Fluid models can be improved by resolving an additional equation such as the parallel momentum conservation equation [76, 80–82], or a fully three-dimensional momentum equation [76, 83]. Note that the mean free path of neutrals greatly varies within the fusion reactor. Thus, a fluid model for neutrals is not valid everywhere. For instance, kinetic effects are important to model the recycling at play at the interface with the main chamber wall, away from plasma facing units. When one is interested in describing such physics, a solution consists in using a hybrid fluid-kinetic model to describe the dynamics of neutrals [84, 85].

4.3 Pressure-diffusion model

We present in this section the pressure-diffusion model implemented in the VOICE code. We use the simplified one dimensional geometry to describe a plasma on a single magnetic field line, with the wall being modeled using immersed boundary conditions. Overall the geometry can be viewed on fig. 2.2 and has already been described in chapters 2 and 3. The pressure-diffusion model is introduced in [74, 79]. We write n_N, $\mathbf{\Gamma}_\mathrm{N}$ and T_N the neutral density, particle flux and temperature. The equation expressing the conservation of density for the neutral species reads as follows

$$\partial_t n_\mathrm{N} + \nabla \cdot \mathbf{\Gamma}_\mathrm{N} = -S_{n,\mathrm{N}}, \tag{4.1}$$

where $S_{n,\mathrm{N}}$ is a particle source term—as indicated by the first subscript n—for the neutral species—as indicated by the second subscript N. The $S_{n,\mathrm{N}}$ term is taken as negative when the interaction between plasma and neutrals is dominated by recombination, effectively leading to a positive source $-S_{n,\mathrm{N}}$ in the above equation. This source term accounts for ionization and recombination processes, and can thus be expressed as

$$S_{n,\mathrm{N}} = n_\mathrm{N} n_e K_\mathrm{i} - n_i n_e K_\mathrm{r}.$$

The $K_\mathrm{r} = \langle \sigma v \rangle_\mathrm{recomb.}$ and $K_\mathrm{i} = \langle \sigma v \rangle_\mathrm{ion.}$ are the reaction rates for the recombination and ionization processes. They mainly depend on the electron temperature, and to a lesser extent, on the plasma density. We cover the computation of the reaction rates in section 4.4. The mass continuity equation (4.1) is closed by assuming that the gradient of the neutral pressure balances the neutral momentum source term as

$$\mathbf{S}_{m,\mathrm{N}} = \nabla p_\mathrm{N}, \tag{4.2}$$

where $p_\mathrm{N} = n_\mathrm{N} T_\mathrm{N}$ is the pressure of neutrals, and $\mathbf{S}_{m,\mathrm{N}}$ is the momentum source term. This last term originates from all three ionization, recombination and charge-exchange reactions. As such it can be expressed as

$$\mathbf{S}_{m,\mathrm{N}} = m_\mathrm{N} \left(n_i n_e K_\mathrm{r} + n_\mathrm{N} n_i K_\mathrm{cx} \right) \mathbf{u}_i - m_\mathrm{N} \left(n_e K_\mathrm{i} + n_i K_\mathrm{cx} \right) \mathbf{\Gamma}_\mathrm{N}. \tag{4.3}$$

In this last expression, $K_{\rm cx} = \langle \sigma v \rangle_{\rm cx}$ is the reactivity of the charge-exchange reaction, that depends on the electron temperature. The mass of neutral particles is $m_{\rm N}$, and as usual $\mathbf{u}_i$ is the ion mean velocity. Combining eqs. (4.2) and (4.3) we arrive to the following expression for the neutral particle flux

$$\mathbf{\Gamma}_{\rm N} = n_{\rm N,eq}\mathbf{u}_i - D_p^{\rm N}\nabla p_{\rm N}, \tag{4.4}$$

With the following definitions:

$$n_{\rm N,eq} = \frac{n_i n_e K_{\rm r} + n_{\rm N} n_i K_{\rm cx}}{n_i K_{\rm cx} + n_e K_{\rm i}} \tag{4.5}$$

$$D_p^{\rm N} = \frac{1}{m_{\rm N}(n_i K_{\rm cx} + n_e K_{\rm i})} \tag{4.6}$$

By injecting the expression of the neutral particle flux $\mathbf{\Gamma}_{\rm N}$ in the mass continuity equation (4.1) we arrive to the so-called pressure-diffusion equation

$$\partial_t n_{\rm N} + \nabla \cdot (n_{\rm N,eq}\mathbf{u}_i - D_p^{\rm N}\nabla p_{\rm N}) = -S_{n,{\rm N}}. \tag{4.7}$$

Note that in the reduced 1D1V framework of the VOICE code, the gradient operator ∇ reduces to the derivative in the x direction along the field line ∂_x. By assuming a constant neutral temperature, this last equation can be solved numerically for the neutral density $n_{\rm N}$. The solver implemented in VOICE uses splines to evaluate the spatial derivatives, along with an explicit Runge-Kutta method of order two for the time integration. Last, a source term $\mathcal{S}_{\rm N}$ is added to the right-hand side of the Vlasov equation that describes the plasma dynamics—see eq. (2.6). In principle, this source term should ensure the conservation of density, momentum and energy for the global system composed of charged and neutral particles. In our case, we design the $\mathcal{S}_{\rm N}$ source term so as to ensure the conservation of mass, and choose the following form

$$\mathcal{S}_{\rm N}(f_s, n_{\rm N}) = \frac{S_{n,{\rm N}}}{\sqrt{2\pi T_{\rm sc}/m_s}} \left(\frac{3}{2} - \frac{m_s v^2}{2T_{\rm src}} \right) \exp\left(-\frac{m_s v^2}{2T_{\rm src}} \right). \tag{4.8}$$

With this expression, we have that $\int dv\, \mathcal{S}_{\rm N}(f_s) = S_{n,{\rm N}}$, hence the conservation of mass is fulfilled for the {plasma + neutral} system. The peculiar shape for the source term given in eq. (4.8) ensures that particles are injected (or removed) with no injection (or absorption) of momentum and energy. Note that this source term cannot account for any transfer of momentum between plasma and neutral particles as $\int dv\, v\mathcal{S}_{\rm N}(f_s) = 0$. Even though neutrals may have a non-vanishing mean velocity $u_N = \mathbf{\Gamma}_{\rm N}/n_{\rm N} \neq 0$, the momentum of ionized neutrals cannot be transferred through the plasma when neutrals are ionized. There is in that sense an inconsistency between the fluid model for neutrals and the kinetic source term given in eq. (4.8). This inconsistency could be solved for instance by modifying this source term so that $\int dv\, v\mathcal{S}_{\rm N}(f_s) = S_{m,{\rm N}}$.

	α_k^{i}	β_k^{i}	α_k^{cx}	β_k^{cx}	α_k^{r}	β_k^{r}
$k=0$	0.06478416786452716	0.053216546399122204	0	0.25125030648153424	-0.03713312941661376	-1.1497231886316353
$k=1$	-0.06283835812957501	1.4939944926753081	0	0.03849324670136343	0.03849324670136343	-5.117013348529228
$k=2$	0.0533047026400489	-1.8156125022306027	0	-0.009966677207985306	0	0
$k=3$	-0.02412714188219726	1.269858057577872	0	0.017922185310747015	0	0
$k=4$	0.005377140897108906	-0.468107496181505	0	-0.010699854255929037	0	0
$k=5$	-0.0004718012889316646 6	0.06406763661421713	0	0	0	0

Table 4.1: Coefficients for the polynomial fitting of the ionization, charge-exchange and recombination reaction rates. The normalization coefficients visible in eq. (4.9) are $n_0 = 10^{20}\,\mathrm{m}^{-3}$, $T_0 = 10\,\mathrm{eV}$ and $K_0 = K_{\mathrm{cx}}(n_0, T_0) \approx 10^{-14}\,\mathrm{m}^3 s^{-1}$.

4.4 Reaction rates

The reaction rates K_i, K_r and K_cx are modeled using the ADAS database [86]. We consider the variation of these quantities over a range of parameters suitable for the study of Scrape-Off Layer plasma, i.e. plasma density in the range $n \in [5 \cdot 10^{13}, 2 \cdot 10^{21}]$ m^3 and electron temperature in the range $T_e \in [0.1, 100]$ eV. Note that in the present section we assume that quasineutrality holds within the plasma, hence $n_e = n_i = n$. So as to be integrated in the VOICE framework efficiently, the variation of the reaction rates over the investigated range of densities and temperature are approximated by polynomials in logarithmic scale. More precisely, we write

$$\log_{10}\left(\frac{K_a}{r_K K_0}\right) = \sum_{k=0}^{N_a} \left(\alpha_k^a \log_{10}\left(\frac{n}{n_0}\right) + \beta_k^a\right) \log_{10}^k\left(\frac{T_e}{T_0}\right), \tag{4.9}$$

where the subscript a indicates the considered reaction, i.e. $a \in \{\mathrm{i}, \mathrm{r}, \mathrm{cx}\}$. The N_a integer stands for the degree of the polynomial, and the α_k^a and β_k^a coefficients are defined for $k \in [0, N_a]$ in Table 4.1 for all three reaction rates. The degree of the polynomial fit for the recombination rate is $N_\mathrm{r} = 5$, while it is $N_\mathrm{cx} = 4$ for the charge-exchange reaction, and $N_\mathrm{i} = 1$ for the recombination reaction. Note additionally that the charge-exchange reaction rate does not depend on the plasma density, thus $\alpha_k^\mathrm{cx} = 0 \,\forall k$. The normalization coefficient K_0 that appears in eq. (4.9) is defined as the value the charge exchange rate at the reference density[3] $n_0 = 10^{20}\,\mathrm{m}^{-3}$ and temperature $T_0 = 10\,\mathrm{eV}$, i.e. $K_0 = K_\mathrm{cx}(n_0, T_0) \approx 10^{-14}\,\mathrm{m^3 s^{-1}}$. The r_K coefficient is an input parameter of the code that allows for artificially increasing or decreasing reaction rates in the simulations, i.e. at $n_0 = 10^{20}\,\mathrm{m}^{-3}$ and $T_0 = 10\,\mathrm{eV}$ we have $K_a = r_K K_0$. Equation (4.9) should be evaluated numerically to compute the normalized rate K_a/K_0 from the normalized density and temperature n/n_0 and T_e/T_0. The justification for this observation is twofold, (i) in the code all quantities are normalized, hence it is necessary to specify the normalization coefficients n_0, T_0 and K_0, and (ii) the renormalization ensures that all three ratios n/n_0, T_e/T_0 and K_a/K_0 remain close to unity so as to reduce the numerical errors. With the polynomial fit presented above, the error between the reaction rates from the ADAS database and the fitted values is under a percent. The reaction rates are plotted on fig. 4.1 for a value of the density $n = 10^{20}\,\mathrm{m}^{-3}$.

4.5 Characteristic scales of plasma-neutral interaction

Let us consider a density and temperature of a plasma where charge-exchange reactions are dominant, i.e. $n_0 = 10^{20}\,\mathrm{m}^{-3}$ and $T_0 = 1\,\mathrm{eV}$, see fig. 4.1. The associated rate for the charge-exchange reaction is $K_0 = K_\mathrm{cx}(n_0, T_0) \approx 10^{-14}\,\mathrm{m^3 s^{-1}}$. We take a typical velocity of neutrals equal to the ion thermal velocity $v_{T_0\mathrm{i}} = \sqrt{T_0/m_i}$: charge-exchange

[3] Note that a typical density of a Scrape-Off Layer plasma would rather be of the order of $10^{19}\,\mathrm{m}^{-3}$, which is smaller than the reference density considered here.

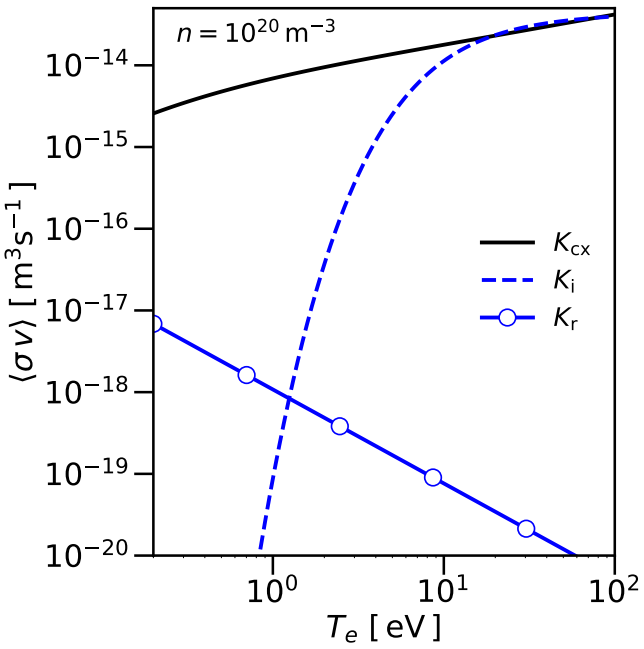

Figure 4.1: Ionization, recombination and charge-exchange reaction rates fitted using the polynomial defined in eq. (4.9) with a value of density $n = 10^{20}\,\mathrm{m}^3$.

collisions ensure that velocities of neutral particles are close to typical ions velocities. The time dynamics of the charge-exchange reaction is therefore given by the frequency

$$\omega_{\mathrm{cx}} = K_0 n_0, \tag{4.10}$$

and the mean free path of neutrals between two charge-exchange collisions is

$$L_{\mathrm{cx}} = \frac{v_{T_0\mathrm{i}}}{K_0 n_0}. \tag{4.11}$$

Evaluating these two quantities with the aforementioned values of density and temperature one gets $\omega_{\mathrm{cx}} \approx 1\,\mathrm{MHz}$ and $L_{\mathrm{cx}} \approx 10\,\mathrm{mm}$. By comparison the time and spatial scales of plasma-wall interaction are given by the electron plasma frequency and Debye length. In the present case $\omega_{\mathrm{pe}} \approx 500\,\mathrm{GHz}$ and $\lambda_D \approx 1\,\mu\mathrm{m}$. Thus the neutral dynamics dominated by charge-exchange reactions develops on time and spatial scales very large compared to the electron plasma frequency and the Debye length, i.e. $\lambda_D \ll L_{\mathrm{cx}}$ and $\omega_{\mathrm{pe}} \gg \omega_{\mathrm{cx}}$. In order to investigate the neutral dynamics within the VOICE code, we modify the typical time and spatial scales of the interaction between charged and neutral particles. To do so, we normalize the pressure-diffusion eq. (4.7) with the normalization of the VOICE code. The normalization procedure of the VOICE code is detailed in section 2.2. For the present section let us recall that the spatial variable x is normalized to $\lambda_D = \sqrt{\varepsilon_0 T_0 / n_0 e^2}$, time to $\omega_{\mathrm{pe}} = \sqrt{n_0 e^2 / m_e \varepsilon_0}$ and the ion velocity u_i to $\sqrt{T_0/m_i}$. Densities and temperatures are normalized to the reference n_0 and T_0 values, the neutral mass m_{N} is normalized to m_e and reaction rates to K_0. We denote

normalized quantities with a hat in the following, for instance $\hat{x} = x/\lambda_D$ for normalized spatial position variable. The normalized pressure-diffusion equation reads as follows

$$\partial_{\hat{t}}\hat{n}_{\mathrm{N}} + \partial_{\hat{x}}\left(\hat{n}_{\mathrm{N,eq}}\hat{\mathbf{u}}_i - \frac{\omega_{\mathrm{pe}}}{\omega_{\mathrm{cx}}}\hat{D}_p^{\mathrm{N}}\partial_{\hat{x}}\hat{p}_{\mathrm{N}}\right) = -\frac{\omega_{\mathrm{cx}}}{\omega_{\mathrm{pe}}}\hat{S}_{n,\mathrm{N}}, \tag{4.12}$$

with the normalized source term $\hat{S}_{n,\mathrm{N}} = \hat{n}_{\mathrm{N}}\hat{n}_e\hat{K}_{\mathrm{i}} - \hat{n}_i\hat{n}_e\hat{K}_{\mathrm{r}}$ and

$$\hat{n}_{\mathrm{N,eq}} = \frac{\hat{n}_i\hat{n}_e\hat{K}_{\mathrm{r}} + \hat{n}_{\mathrm{N}}\hat{n}_i\hat{K}_{\mathrm{cx}}}{\hat{n}_i\hat{K}_{\mathrm{cx}} + \hat{n}_e\hat{K}_{\mathrm{i}}}, \tag{4.13}$$

and

$$\hat{D}_p^{\mathrm{N}} = \frac{1}{\hat{m}_{\mathrm{N}}(\hat{n}_i\hat{K}_{\mathrm{cx}} + \hat{n}_e\hat{K}_{\mathrm{i}})}. \tag{4.14}$$

The normalized pressure-diffusion equation given in eq. (4.7) involves the ratio between the plasma-wall interaction and charge-exchange typical frequencies $\omega_{\mathrm{pe}}/\omega_{\mathrm{cx}}$. With the values for densities and temperatures of a plasma mentioned at the beginning of this section, one finds that $\omega_{\mathrm{pe}}/\omega_{\mathrm{cx}} \gg 1$ and the diffusion term $\omega_{pe}/\omega_{\mathrm{cx}}\hat{D}_p^{\mathrm{N}}\partial_{\hat{x}}\hat{p}_{\mathrm{N}}$ is dominant in the normalized charge-exchange reaction. So as to be able to solve eq. (4.12) numerically, or said differently to be able to study plasma-neutral interaction on the scales investigated within VOICE, we perform simulations with an altered value of $\omega_{\mathrm{pe}}/\omega_{\mathrm{cx}}$ compared to a realistic value. We however retain the fact that the neutral dynamics is slow with respect to the dynamics of plasma wall interaction, thus we use $\omega_{\mathrm{pe}}/\omega_{\mathrm{cx}} = 10$ in the following.

4.6 Plasma-neutral interaction with the VOICE code

In this section we perform simulations of plasma-neutral interaction with the VOICE code. The simulation setup is similar to the one used for describing plasma-wall interaction in chapters 2 and 3. Namely, the spatial domain is one dimensional in space and models a single magnetic field line that connects two solid walls. Any interaction with adjacent field lines is neglected, and so is the magnetic field curvature. The plasma dynamics is described by the Vlasov-Poisson system given by eqs. (2.6) and (2.7) and neutrals by the pressure-diffusion model described in section 4.3. We illustrate how the interaction of charged particles with the neutral species affects plasma-wall interaction. As usual, the wall is immersed in the simulation domain. We perform three simulations: a first one without neutrals, a second one with neutrals and a normalization coefficient for the reaction rates—visible in eq. (4.9)—that is taken as $r_K = 1$, and a third one with $r_K = 5$. For both simulations with neutrals, a normalization coefficient $\omega_{\mathrm{pe}}/\omega_{\mathrm{cx}} = 10$ is considered, see section 4.5. The plasma equilibrium temperature is $T_0 = 10\,\mathrm{eV}$ and density $n_0 = 10^{20}\,\mathrm{m}^{-3}$. In this regime recombination is negligible as compared to ionization, see fig. 4.1. With these parameters and using eq. (4.11) the

mean free path of neutrals between two charge exchange collisions is

$$\frac{L_{\rm cx}}{\lambda_D} = r_K \sqrt{\frac{m_e}{m_i}} \frac{\omega_{\rm pe}}{\omega_{\rm cx}},$$

i.e. $L_{\rm cx}/\lambda_D = r_K/2$. Lastly, let us remark that we do not seek here quantitative predictions for the plasma-neutral interaction physics at play close to the target plates in a recycling or detached Scrape-Off Layer regime. We rather illustrate on a short transient case on a small domain that the neutral physics can affect significantly the plasma dynamics. We consider a magnetic connection length of $L_\parallel = 30\lambda_{D_0}$, and run the simulation until time $t = 20\,\omega_{\rm pe}^{-1}$.

Plasma density For both simulations with the pressure-diffusion model, the initial density of neutrals is taken as

$$n_{\rm N} = n_0 \left(1 - \frac{1}{2}\left\{\tanh\left(\frac{x - x_{\rm N}^\ell}{d_{\rm N}}\right) - \tanh\left(\frac{x - x_{\rm N}^r}{d_{\rm N}}\right)\right\}\right)$$

with n_0 the normalization density. In this expression the initial density of neutral vanishes for spatial positions $x \in \left[x_{\rm N}^\ell,\, x_{\rm N}^{\rm r}\right]$, and transitions smoothly to unity outside of this interval. The smoothness of the transition is controlled by the $d_{\rm N}$ parameter, and we take $d_{\rm N} = 1.5$. The transitions are defined as $x_{\rm N}^\ell = 0.25L_x$ and $x_{\rm N}^\ell = 0.75L_x$, with L_x the simulation box length—that includes the wall—that is $L_x = 100$. In the simulation box, the wall region where the penalization operator is active[4] is defined by the wall mask given in section 2.3.1. This wall mask has a hyperbolic tangent shape similar to the one given in eq. (4.15). The plasma is therefore defined by the positions $x \in \left[x_{\rm w}^\ell,\, x_{\rm w}^{\rm r}\right]$ with $x_{\rm w}^\ell = 0.2L_x$ and $x_{\rm w}^\ell = 0.8L_x$.
At the start of the simulation, neutral particles can be found in a region that encompasses the wall and a part of the plasma, in the vicinity of the wall. On fig. 4.2, left graph the ion density is plotted for the two simulations with neutrals and $r_K \in \{1,\, 5\}$, and for the simulation without neutrals—that we label the $r_K = 0$ simulation for convenience. Only half of the plasma is represented, i.e. spatial positions $\tilde{x} = x - x_{\rm h} \in [0, 15]$ with $x_{\rm h}$ the coordinate of the stagnation point $x_{\rm h} = L_x/2$. The $\tilde{x} \in [-15, 0]$ part of the plasma is the symmetric of the $\tilde{x} \in [0, 15]$ part. The position $\tilde{x} = 15$ stands for the location where the penalization mask equals one half. This position represents approximately the beginning of the wall region, which is located at positions $\tilde{x} > 15$. On the left graph of fig. 4.2 we see that when considering the interaction with neutrals, the ion density is non-monotonic as compared to the reference case without neutrals $r_K = 0$. The increase of the ion density in the vicinity of the wall is a direct consequence of the ionization process at play there. On the right graph of fig. 4.2, neutral densities at initial time and at the end simulation time $t = 20\,\omega_{\rm pe}^{-1}$ for both investigated values

[4]Let us recall that this operator acts as a sink of particles, momentum and energy. Its form is given in eq. (2.10). The wall model considered for the present simulations is the conducting one, see 2.3.1

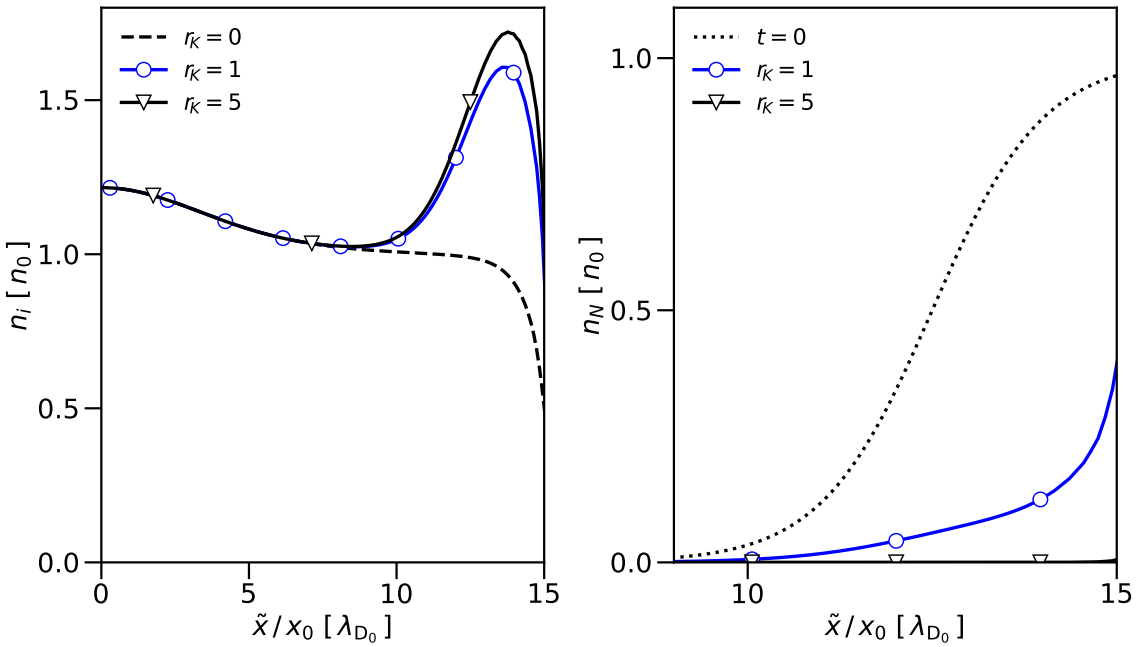

Figure 4.2: Left: ion density profiles in the plasma for a simulation with no neutrals $r_K = 0$, and two simulations with neutrals and with different values for this coefficient $r_K \in \{1, 5\}$. The profiles are recorded at the final simulation time $t = 20\,\omega_{\mathrm{pe}}^{-1}$. Right: neutral density in the vicinity of the wall at initial time $t = 0$ and final time for both values of the normalization rate r_K.

of r_K are represented in the vicinity of the wall. At $t = 20\,\omega_{\mathrm{pe}}^{-1}$, for both $r_K = 1$ and $r_K = 5$ cases the neutral density has decreased compared to its initial value. This ionization translates into (i) a net loss of neutrals through the $S_{n,\mathrm{N}} = n_{\mathrm{N}} n_e K_{\mathrm{i}} - n_i n_e K_{\mathrm{r}}$ term of the pressure-diffusion eq. (4.7), and (ii) a positive source of charged particles through the source term given in eq. (4.8). When the normalization coefficient is taken as $r_K = 5$, the final neutral density is lower compared to the $r_K = 1$ case, given that increasing this coefficient increases the effective rate of ionization, see eq. (4.9).

Ion mean velocity A feature of plasma-wall interaction investigated in chapter 3 is that the ion mean velocity increases monotonically from the stagnation point up to the wall. On fig. 4.3 the normalized ion mean velocity $u_i/\sqrt{T_0/m_i}$ is represented for the considered simulations. Looking first at the $r_K = 0$ case, one observes as expected a sharp increase of the ion mean velocity in the vicinity of the wall. This is a consequence of the electric potential that drops in this region, due to the positive charge density of the Debye sheath, see chapter 3. In the $r_K = 0$ case the ion mean velocity is positive in the entirety of the plasma. One can observe a slight negative gradient of the $u_i/\sqrt{T_0/m_i}$ quantity close to the $\tilde{x} = 5$ position. This is due to the plasma not having reached a steady state at the investigated simulation time. The injection of particles in the source region approximately between $\tilde{x} = 0$ and $\tilde{x} = 5$

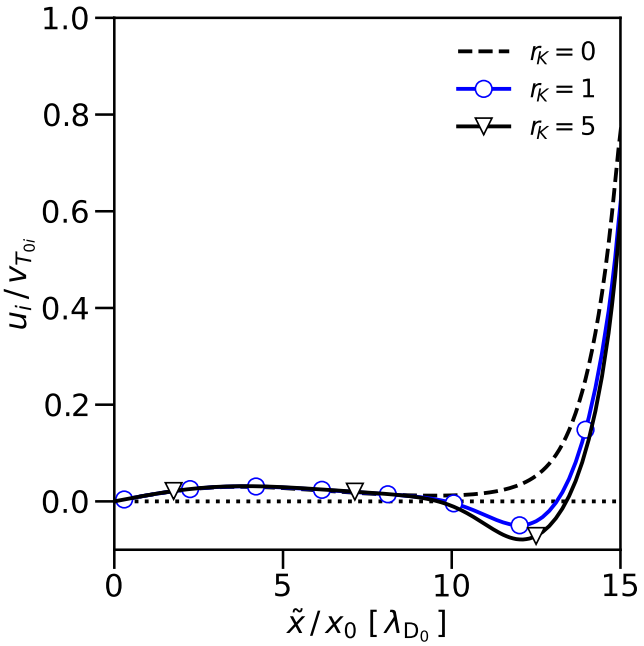

Figure 4.3: Normalized ion mean velocities $u_i/v_{T_{0i}}$ with $v_{T_{0i}} = \sqrt{T_0/m_i}$ in the case with no neutrals $r_K = 0$, and with neutrals $r_K = 1$, and $r_K = 5$.

drives an increase of the ion mean velocity there. Due to the short simulation time, these injected ions did not influence yet the part of the plasma for $\tilde{x} > 5$. Looking now at the $r_K > 0$ cases, on notices a peculiar behavior of the ion mean velocity close to the wall. In both $r_K = 1$ and $r_K = 5$ cases, the ion mean velocity becomes negative in the $\tilde{x} \in [10, 13]$ region. This is again a direct consequence of the ionization process at play there. The ionization of neutrals produces charged particles that are characterized by a Maxwellian distribution function, i.e. ionization produces as many ions with parallel velocities $v > 0$ as ions with $v < 0$ [5]. The ions with positive parallel velocities reach the wall and are absorbed, while the negative velocity ions travel towards the plasma. Given that the value of the $u_i/\sqrt{T_0/m_i}$ quantity is relatively small in the $r_K = 0$ case, the flux of ionized neutrals coming back towards the stagnation point appears as being strong enough to drive the ion mean velocity towards negative values. In the $r_K = 5$ case, the ion mean velocity is more negative than in the $r_K = 1$ case, given that the ionization process is larger in the former case than in the latter.

With the simple simulation setup described in the present section, one observes a strong modification of the plasma density and ion mean velocity profiles when comparing a

[5] Note that this situation is the direct consequence of the definition of the source term given in eq. (4.8) that has a vanishing momentum $\int dv\, v\mathcal{S}_{\mathrm{N}}(f_s) = 0$, i.e. no momentum can be transferred from neutral to plasma particles through ionization processes. When considering more realistic source terms than the one given in eq. (4.8) one can reasonably expect the mean velocity of the plasma to be different with respect to the situation visible on fig. 4.3

case without plasma-neutral interaction, and a case where this interaction is simulated. With the investigated plasma temperature and density $T_0 = 10\,\mathrm{eV}$ and $n_0 = 10^{20}\,\mathrm{m}^{-3}$ the ionization is dominant as compared to recombination. Therefore, any neutral particle present at the start of the simulation gets quickly ionized and neutrals are depleted. This is the reason why the simulations above have been performed up to $t = 20\,\omega_{\mathrm{pe}}$ only. The pressure-diffusion model described in the present section is to be adapted to the gyrokinetic GYSELA framework in future work.

4.7 Conclusion of the chapter

In the present chapter we described a fluid model for neutrals based on a pressure-diffusion equation. This work prepares for future improvement of the GYSELA edge physics capabilities to include such a neutral model. The pressure-diffusion model embarks realistic reaction rates taken from the ADAS database for ionization, recombination and charge-exchange. We described the coupling of the model to the kinetic plasma description of the VOICE code. The implementation has been performed so that simulations can be run efficiently on GPU architectures. Proof-of-concept simulations have been performed to illustrate how the neutral dynamics affects density and ion Mach number profiles in the vicinity of the target plates. In the simulated regime where ionization is dominant, this process leads to an increase of plasma density close to the immersed wall region. Given that the source term that models the coupling between neutral and charged particles has a vanishing momentum, ionization leads to a decrease of the ion Mach number in the vicinity of the wall. The expression of this source term could be improved to better account for momentum transfer between plasma and neutrals.

5

A subgrid model for gyrokinetic treatment of plasma-wall interaction

Contents

5.1 Gyrokinetic edge modeling 118
5.2 Gyrokinetic description of a plasma 123
5.3 Models for gyrokinetic plasma-wall interaction 127
5.4 The Gysela code 136
5.5 Penalized sheath model valid for BSL codes 138
5.6 Quasineutrality model 146
5.7 Results and discussion 151
5.8 Conclusion of the chapter 161

Summary

We present in this chapter a model for integrating plasma-wall interaction in the gyrokinetic framework. The model is compatible with the global, full-f and flux-driven gyrokinetic code Gysela. The model shares similarities with already-existing techniques modelling plasma-wall interaction in the gyrokinetic framework, namely the so-called logical and conducting sheath. We review these two approaches and compare them to the present model which consists in matching the electron and ion gyrocenter fluxes on spatial average over the material boundary surface. This *flux-averaged* sheath approach is implemented in the Gysela code, and adapted for immersed boundary conditions and a Backward semi-Lagrangian numerical scheme. It consists of three distinct elements that are (i) a penalization operator that absorbs ions in the solid material volume—the limiter in our case—(ii) a reflection procedure for slow electrons and absorption of fast ones so as to match the electron and ion fluxes on spatial average over the material boundary surface, and (iii) a modification of the quasineutrality equation to account for immersed boundary conditions. While the absorption of ions and fast electrons, and the reflection of slow electrons gives satisfactory results, the ion and electron gyrocenter fluxes appear to display a persistent mismatch at the limiter surface, eventually causing the simulation to break down. We investigate possible reasons for this mismatch, which remains of unclear origin as of today.

5.1 Gyrokinetic edge modeling

The gyrokinetic theory provides a framework to study tokamak plasmas with an intermediate level of computational complexity that sits in-between a fully-kinetic model and a fluid description. We give an overview of the gyrokinetic theory in section 5.2. Gyrokinetic models are derived from the kinetic model by eliminating the dependence of the kinetic equation with the cyclotron phase. This is achieved by performing an expansion of the fully-kinetic equation with the small parameters $\rho^* = \rho_i/a$ and ω/Ω_{ci}. These parameters are defined in section 5.2. At leading order, the resulting equation does not depend on the cyclotron phase. As a result, particles described using the gyrokinetic theory evolve in five-dimensional phase space, composed of three dimensions of real space and two dimensions of velocity space. This reduction from 6D—the dimensionality of a fully kinetic model—to 5D enables to perform simulations of tokamak plasmas at relatively affordable computational costs. The gyrokinetic theory provides an appropriate framework to describe core turbulence in tokamak plasmas. As a result, gyrokinetic codes have been largely used to perform turbulent simulations of core plasmas, and are now extended towards the edge and SOL plasma regions. The degree of validity of the gyrokinetic theory in the edge of tokamak plasmas, where strong gradients and large magnitude fluctuations develop, remains however an open issue. Historically the core and edge regions were treated by distincts gyrokinetic codes. Examples of gyrokinetic codes adapted for modeling the core region are CGYRO [87], GENE [88], GKNET [89], GKW [90], GT5D [91], GYSELA [41] and ORB5 [92]. An extensive review of some important results obtained from gyrokinetic simulations of core plasmas can be found in [16]. Some other gyrokinetic codes describe an open field line plasma region. GKEYLL [93, 94] or PICLS [95] are suited to describe a limiter configuration, while XGC [33, 96] or COGENT [97] describe an open field line region with a divertor configuration. There are currently sustained efforts in the gyrokinetic community to include both core and Scrape-Off Layer regions within a single simulation.

5.1.1 The necessity of unified core-edge-SOL modeling

The main reason for including both core, edge[1] and Scrape-Off Layer regions within a single simulation is to study the formation of edge transport barriers, and the possible bifurcation towards improved confinement regimes. The edge is indeed a critical region where a transport barrier—the so-called *pedestal*—forms when a plasma bifurcates towards an improved confinement regime [98, 99]. There is strong evidence suggesting that the development of flow shear in the edge region plays a central role in the establishment of a transport barrier [100–102][2]. Flow shear in the edge plasma contributes to the reduction of turbulence levels and hence the improvement of confinement [103].

[1] We understand the edge in the present work as a loosely defined region spanning from the outer core up to the separatrix.

[2] Magnetic shear is found to play a role as well. We choose to focus on the effect of flow shear on the formation of transport barriers in the present work.

The poloidal rotation of turbulent eddies is mainly governed by the poloidal component of the $E \times B$ flow, i.e. by the radial electric field E_r. The shear of the radial electric field is expected to be particularly large at the transition between closed and open field lines, that is to say at the magnetic separatrix. The radial electric field is indeed found experimentally to change sign when going from the core to the edge region [104]. We give here some elements to understand this sign reversal. In the core, the radial electric field adjusts so that the following radial force balance equation is satisfied

$$n_i e \left(E_r + v_{\theta i} B_\varphi - v_{\varphi i} B_\theta\right) = \partial_r p_i,$$

where n_i, p_i stand respectively for the ion density and scalar pressure. The ion mean poloidal and toroidal velocities are $v_{\theta i}$ and $v_{\varphi i}$. In the absence of externally injected torque, the toroidal component of the ion mean velocity $v_{\varphi i}$ is expected to remain small [105]. When the radial electric field is dominated by neoclassical effects, the poloidal velocity $v_{\theta i}$ is the result of the detrapping of particles due to collisions [14]. We neglect the effect of the poloidal velocity in the radial force balance. Therefore, a rough estimate of the radial electric field in the plasma core leads to

$$E_r \approx \frac{\partial_r p_i}{e n_i}. \tag{5.1}$$

Given that pressure is a decreasing function of r, one finds that the radial electric field is negative in the core region in the absence of strong poloidal and toroidal flows. In the Scrape-Off Layer, the physics that governs E_r is drastically different. In the sheath-limited regime, the potential remains fairly constant in the direction parallel to a given magnetic field line. As a consequence, at a given radial position in the SOL, the electric potential is fixed by the potential drop located in the Debye sheath, close to the material boundary of the plasma [23]. One can therefore write in the Scrape-Off Layer that[3]

$$E_r^{\mathrm{SOL}} = -\partial_r \phi \approx \partial_r \Delta\phi_{\mathrm{sh}}. \tag{5.2}$$

With the prediction of the sheath potential drop given in eq. (2.3), one can recast this last expression as

$$E_r^{\mathrm{SOL}} \approx \frac{\Lambda}{2e} \partial_r T_e,$$

where we have introduced the quantity

$$\Lambda = \log\left(2\pi \frac{m_e}{m_i}\left(1 + \frac{T_i}{T_e}\right)\right). \tag{5.3}$$

When writing eq. (5.2) we neglected the small radial variation of Λ when the electron and ion temperatures vary radially given the logarithmic dependence of Λ with these temperatures. The electron temperature decreases from the separatrix at $r/a = 1$ to the

[3] Indeed $\partial_r \phi = \partial_r \left(\phi - \phi_w\right) \approx -\partial_r \Delta\phi_{\mathrm{sh}}$ with ϕ_w the potential of the material boundary, and $\Delta\phi_{\mathrm{sh}}$ is the sheath potential drop defined in eq. (2.3).

wall at $r/a > 1$, and Λ is negative: $m_i/m_e \approx 3600$ for a Deuterium plasma. Therefore in the Scrape-Off Layer one finds that $E_r^{\mathrm{SOL}} > 0$. On the basis of the arguments mentioned above, the radial electric field is thus expected to change sign in the vicinity of the separatrix. Hence the poloidal component of the $E \times B$ velocity—that we denote $v_{E\theta}$—is also expected to exhibit a significant shear in this region: $v_{E\theta}$ is negative in the Scrape-Off Layer, while it is positive in the core. This shear flow influences turbulence levels in the edge plasma. To summarize, in order to properly describe turbulence and its regulation mechanisms in the edge plasma, one needs to correctly compute the radial electric field. Given that the radial electric is much influenced by the transition from closed to open field lines, a gyrokinetic simulation including both edge and core regions is required to assess precisely turbulence levels in the edge region. Hence, one needs to account within the gyrokinetic framework for the physics of plasma-wall interaction at play at the plasma solid boundary in the Scrape-Off Layer region. Note that plasma-wall interaction in the Scrape-Off Layer is not the only player that may lead to the establishment of a strong E_r shear at the edge of the plasma. Namely, the loss of ions in solid walls due to the finite excursion of their cyclotron motion in the perpendicular direction plays a role as well [106, 107]. A model for the L-H transition based on this physics has been proposed in [108]. Moreover, the radial variation of neoclassical coefficients in the edge where steep density and temperature gradient exist may cause bifurcations of turbulent transport as well, see [109].

5.1.2 On the validity of edge gyrokinetic modeling

In order to model the edge plasma by means of the gyrokinetic theory, one has to verify first that the assumptions the gyrokinetic theory is based upon are valid in the edge. We give a brief overview of these hypotheses in section 5.2. Under some circumstances, these assumptions break down in the edge. More specifically:

- Turbulent fluctuations—of density for instance, usually written $\delta n/n$—are found to be larger in the edge than in the core plasma [110, 111]. When these fluctuations are large enough, the position of the gyrocenter may depart significantly from the position of the guiding center [112]. This invalidates the construction of the magnetic moment μ that is required for building a gyrokinetic theory. Similarly, when turbulent fluctuations of the electrostatic potential $e\delta\phi/T_0$ become large[4]—with T_0 the equilibrium plasma temperature—one cannot assume anymore that the drift velocity $\mathbf{v}_E$ remains small compared to the thermal velocity of a given species $v_{T_0 s} = \sqrt{T_0/m_s}$. Lastly, high level of fluctuations also invalidate the linearization required to derive collision operators included in gyrokinetic codes [113, 114];
- The formation of a transport barrier in the vicinity of the separatrix—such as the so-called *pedestal* that appears in a bifurcated H-mode plasma—leads to a

[4]Large compared to the expansion parameter $\rho^* = \rho_i/a \ll 1$.

large effective beta parameter $\beta_{\text{eff}} = \beta(qR/L_p)^2$, with L_p the typical length of the pressure gradient and β the ratio of plasma pressure to magnetic pressure $\beta = 2\mu_0 p/B^2$. In such regimes, the electromagnetic nature of the electron response, including Alfvén waves, cannot be ignored: the electrostatic model is insufficient to capture the associated physics [110]. In this last expression we introduced L_p the typical length of the pressure gradient and β the ratio of plasma pressure to magnetic pressure $\beta = 2\mu_0 p/B^2$. In the vicinity of a transport barrier this gradient length may become comparable to the ion Larmor radius ρ_i. In this case, the assumption of an electrostatic response of the plasma is questionable. More generally, gradients length $L_p \approx \rho_i$ contradicts the expression of the polarization density in the long wavelength approximation that appears in the quasineutrality eq. (5.15), see section 5.2.2 and eq. (5.13).

Given these limitations, one can legitimately question the relevance of using a gyrokinetic description of the edge and Scrape-Off Layer plasmas, and in particular an electrostatic one when transport barriers with steep gradients develop. A more adapted description would be given by a fully-kinetic and electromagnetic model. Running simulations with such a model is however out of the current scope of numerical capabilities due to the enormous computational power required to solve a 6D kinetic model coupled to Maxwell's equations. As a consequence, the gyrokinetic theory remains nevertheless the most appropriate framework to study turbulence in the edge plasma. Anyhow, given the difficulty of performing global core-edge-SOL simulations using a full-f gyrokinetic code in the flux-driven framework, the inclusion of an even very simple model allowing for describing the physics at play at the plasma solid boundary in the Scrape-Off Layer would represent a significant improvement.

5.1.3 Strategies for edge gyrokinetic modeling

We review here available options for describing an open field line region of a plasma within the gyrokinetic framework. Let us first make the distinction between gyrokinetic models that assume an adiabatic response for electrons, and models that do not. We detail in appendix C.3 what is precisely meant by *adiabatic electron response*. For now let us consider that it corresponds to the limit where electrons respond infinitely fast to any variation of the electric potential. Depending on whether or not the electron response is considered adiabatic, models for plasma-wall interaction are radically different.

Adiabatic electron response A possible solution for including the physics of plasma-wall interaction in the adiabatic electron limit is given by the penalization technique. This technique was first introduced in the computational fluid dynamics community [115, 116], and then adapted to plasmas [117–119]. Examples of results obtained from using this penalization technique can be found in [4, 120], where the GYSELA code is used to study edge turbulence, or in ORB5 to study the impact of plasma shaping on

confinement [121]. We briefly describe hereafter the penalization technique used in [4, 120] and highlight some prominent results. When applied to plasma-wall interaction in the adiabatic electron limit, the penalization technique consists in (i) modeling the limiter as a sink of thermal energy, and (ii) introducing a penalization term in the quasineutrality eq. (5.15). The penalization of the potential ϕ ensure the relaxation of its average component towards $\frac{1}{2}\Lambda T_e/e$ in the SOL to model the effect of the (non-resolved) sheath at the limiter surface. The limiter can be grounded $\phi_{\text{lim}} = 0$ or biased $\phi_{\text{lim}} = \phi_{\text{bias}}$. The thermal sink in the limiter is introduced using a heat sink term in the right-hand-side of the gyrokinetic eq. (5.5). The penalization technique is very convenient in this case since it allows for treating plasma solid boundaries of any shape, without adapting the numerical mesh close to these boundaries.
The application of such a penalization technique in [4, 120] to model plasma turbulence highlights the influence of the edge region on the plasma properties. In particular, the production of turbulent eddies in the edge is enhanced when taking plasma-wall interaction into account. The interaction between the plasma and its boundaries appears as a source of free energy that destabilizes the edge and is responsible for an increased turbulent activity. This edge destabilization modifies the properties of the core region through the propagation of eddies from the edge to the core. This propagation is somehow reminiscent of the usual picture of the core turbulence *spreading* towards the edge, although the inverse situation is encountered here, with turbulence spreading from the edge to the core. This increased turbulence level in the edge could also help explaining the discrepancy between edge turbulence levels measured in experiments—where fluctuations are observed to increase when going from the core towards the edge plasma [11]—and results obtained from gyrokinetic computations that do not include proper descriptions of the edge region—where the edge is found to be linearly stable [122].

Non-adiabatic electron response Going towards a more realistic electron response is required to study properly radial particle and heat transport. When assuming an adiabatic response for electrons, the resulting turbulence leads to a vanishing flux-averaged $E \times B$ transport of particles in the radial direction [16]. In order to model radial particle transport, one has to relax the adiabatic electron assumption. In addition, considering a non-adiabatic electron response allows for trapped-electron modes (TEM) to grow. These modes are supposed to play a major role in the transport of heat and particles in the core and edge regions of tokamaks.
As soon as one is interested by giving a description within the gyrokinetic framework of a region where field lines are open and impact a solid material, a model for plasma wall interaction is required. Indeed, the solid wall that bounds the plasma can be considered as a sink of particles, momentum and energy. Because of the inertia difference between electrons and ions, the former tend to be lost in the wall much more easily than the latter. This mechanism is exactly the one described in section 2.1 and is responsible for the formation of the Debye/Chodura sheath at the boundary of plasmas. The problem that arises here is that a positively charged sheath cannot by any mean

be described within the gyrokinetic framework, see section 5.3. As a result, a model for plasma-wall interaction is required. There are currently to our knowledge two different models for including such physics within the gyrokinetic framework. These are the so-called *logical* and *conducting* sheath approaches [123, 124]. We give a detailed description of these techniques in section 5.3.2. The logical and conducting sheath approaches have been broadly used in gyrokinetic codes that describe open field line regions, and can be applied to a variety of numerical schemes. These simulations allow for studying turbulence production in open field line regions, sometimes taking into account an electromagnetic response for the plasma. Examples of such simulations can be found in [93, 94, 125–131]. In order to bridge the gap between core and SOL gyrokinetic codes, one needs to incorporate both open and closed field line regions within a single simulation. A first possible approach consists in coupling a core gyrokinetic code with a Scrape-Off Layer gyrokinetic code, as done in [132, 133]. The approach followed in the present work is rather to extend the simulation domain of the GYSELA code to include an open field line region within the domain. This, to our knowledge, has never been achieved. In this chapter, we therefore propose a model for plasma wall interaction valid in the GYSELA framework that takes into account a kinetic electron response in the Scrape-Off Layer. The present work is therefore an extension of the penalized SOL and limiter model valid with adiabatic electrons described in [4, 119, 120] .

5.2 Gyrokinetic description of a plasma

In this section we give a brief overview of the gyrokinetic theory. In tokamak plasma the breaking of the three invariants presented in section 1.2.3—the magnetic moment μ , canonical toroidal momentum P_φ and particle energy $\mathcal{E}$—leads to the trajectories of particles becoming chaotic and effectively induces radial transport. Describing such a system with a six-dimensional kinetic model is out of reach, given the computational power involved. A possible reduction in dimensionality—hence in required computational power—is given by the *gyrokinetic theory*. This model consists in performing an expansion of a kinetic model with the small order parameters $\rho^* = \rho_i/a$ and ω/Ω_{ci}, with ρ_i the ion Larmor radius, a the minor radius of the tokamak, Ω_{ci} the cyclotron frequency, and ω the characteristic frequency of the system dynamics. At leading orders, the equation obtained from this expansion procedure does not depend on the cyclotron phase. The elimination of the fast cyclotron motion renders gyrokinetic models easier to solve as compared to fully kinetic models. Such a reduction comes with some restrictions. The gyrokinetic theory is suited for describing phenomena that have typical frequencies that are small compared to the cyclotron frequency, so that the ratio ω/Ω_{ci} remains small. Similarly, the parameter $\rho^* = \rho_i/a$ must be small as well for the gyrokinetic expansion to the valid: the radial extent of the tokamak device a must be large compared to the Larmor radius ρ_i. The gyrokinetic theory additionally assumes that fluctuations of the electromagnetic field remains small. One can summarize the

ordering assumed by the gyrokinetic theory as

$$\frac{\omega}{\Omega_c} \sim \frac{e\delta\phi}{T_0} \sim \frac{\delta B}{B} \sim \frac{\rho_i}{a} \ll 1, \tag{5.4}$$

where T_0 is the plasma equilibrium temperature, $\delta\phi$ and δB stand for fluctuations of the electromagnetic field. In the following we describe in distinct sections the two equations that allow for describing the dynamics of gyrocenters in the electrostatic limit. These are the gyrokinetic equivalent of the Vlasov equation, described in section 5.2.1 and the quasineutrality equation, described in section 5.2.2. For a more detailed and rigorous derivation of the gyrokinetic model, the reader can see [16, 32, 112, 134].

5.2.1 Gyrokinetic Vlasov equation

The first step consists in deriving a gyrokinetic equivalent of the Vlasov equation. This is achieved by defining a new adiabatic invariant that is associated with a virtual particle that is called a *gyrocenter*. The position of the gyrocenter slightly differs from the position of the particle guiding center—see section 2.7.2 for a definition of a particle guiding center—so as to ensure that the new magnetic moment is indeed an invariant of motion. After averaging over the cyclotron motion, one is left with the following gyrokinetic equation that describes the time evolution of the distribution function of gyrocenters F_s—related to species s—as

$$\frac{\partial F_s}{\partial t} + \frac{d\mathbf{x}}{dt} \cdot \nabla_{\mathbf{x}} F_s + \frac{dv_\parallel}{dt} \nabla_{v_\parallel} F_s = \mathcal{S}(F_s) + \mathcal{C}(F_s). \tag{5.5}$$

The distribution function of gyrocenters $F_s(\mathbf{x}, v_\parallel, \mu, t)$ depends on five coordinate plus time. These coordinates are the position of the gyrocenter $\mathbf{x}$ in real space—it is a three dimensional quantity—the magnetic moment μ of the gyrocenter, and its parallel velocity $v_\parallel$. The right-hand side of the gyrokinetic equation describes collisions $\mathcal{C}$ and sources $\mathcal{S}$. Note that collisions modify the value of the magnetic moment of the gyrocenters μ over time. The equation that describes the motion of gyrocenters in real space is

$$\frac{d\mathbf{x}}{dt} = v_\parallel \mathbf{b}^*_\parallel + \mathbf{v}_E + \mathbf{v}_D, \tag{5.6}$$

where the electric drift $\mathbf{v}_E$ and magnetic drift $\mathbf{v}_D$ in the gyrocenter coordinates are written as

$$\mathbf{v}_E = \frac{\bar{\mathbf{E}} \times \mathbf{B}}{B^*_\parallel B} \quad \text{and} \quad \mathbf{v}_D = \frac{m_s v_\parallel^2 + \mu B}{e_s B^*_\parallel B^2} \mathbf{B} \times \nabla B, \tag{5.7}$$

where $\bar{\mathbf{E}} = \nabla \bar{\phi}$ is the electric field averaged over a cyclotron motion, and the gyroaverage electric potential is $\bar{\phi} = \mathcal{J}\phi$. $\mathcal{J}$ is the operator that expresses this averaging procedure. It is called the gyroaveraging operator—or simply gyroaverage—and is expressed for a given function g as

$$\mathcal{J} g = \frac{1}{2\pi} \int_0^{2\pi} g \, d\varsigma, \tag{5.8}$$

where ς is the cyclotron phase. The modified magnetic field is

$$\mathbf{B}_\parallel^* = \mathbf{B} + \frac{m_s v_\parallel}{e_s B} \nabla \times \mathbf{B}, \tag{5.9}$$

and its norm is $B_\parallel^* = \mathbf{B}_\parallel^* \cdot \mathbf{B}/B$. The unit vector $\mathbf{b}_\parallel^*$ is defined as $\mathbf{b}_\parallel^* = \mathbf{B}_\parallel^*/B_\parallel^*$. The modified magnetic field represents the magnetic field felt by the gyrocenters during their motion. In the low-β limit, the time evolution of the gyrocenter parallel velocity $v_\parallel$ can be expressed as

$$m_s \frac{dv_\parallel}{dt} = -\mu \mathbf{b}_\parallel^* \cdot \nabla B - e_s \mathbf{b}_\parallel^* \cdot \nabla \bar{\phi} + \frac{m_s v_\parallel}{B} \mathbf{v}_E \cdot \nabla B. \tag{5.10}$$

The different forces that appear in eq. (5.10) are reminiscent of the mirror force with the $-\mu \mathbf{b}_\parallel^* \cdot \nabla B$ term, of the electrostatic force $-e\mathbf{b}_\parallel^* \cdot \nabla \bar{\phi}$ and the last term originates from a synergy between two previous forces involving the electric field and the inhomogeneity of B.

5.2.2 Quasineutrality equation

The gyrokinetic equation given in eq. (5.5) involves terms that depend on the electromagnetic field $(\mathbf{E}, \mathbf{B})$. As a consequence, to solve the gyrokinetic equation one must complement it with Maxwell's equations. Maxwell's equations are however written in terms of charge and current densities of *particles*, whereas the gyrokinetic equation involves quantities relative to *gyrocenters*. Therefore, the second step in deriving a gyrokinetic theory consists in expressing the charge and current densities of particles as functions of the charge and current densities of gyrocenters. In the present work we focus on the electrostatic regime, thus we solve the gyrokinetic equation along with the Poisson equation, while considering that the magnetic field is constant in time. Let us write the normalized Poisson equation as

$$\left(\frac{\lambda_D}{L_\parallel}\right)^2 \tilde{\nabla}_\parallel^2 \tilde{\phi} + \left(\frac{\lambda_D}{L_\perp}\right)^2 \tilde{\nabla}_\perp^2 \tilde{\phi} = \frac{(n_e - e_i n_i)}{e n_0}. \tag{5.11}$$

In this expression, the normalized potential is $\tilde{\phi} = e\phi/T_0$ with T_0 a reference temperature, n_0 is a reference density and e is the elementary charge. We consider the situation of a plasma composed of a single ion species of charge e_i for the sake of simplicity. The Debye length is $\lambda_D = \sqrt{\varepsilon_0 T_0/(n_0 e^2)}$. $\tilde{\nabla}_\parallel^2$ (resp. $\tilde{\nabla}_\perp^2$) stands for the normalized Laplacian operator in the direction parallel (resp. transverse) to the magnetic field. The Laplacian in the parallel direction is normalized to a given length scale $L_\parallel$ while the perpendicular Laplacian is normalized to $L_\perp$. In order to study turbulence in tokamak plasmas, we choose the $L_\parallel$ and $L_\perp$ factors to be comparable to the typical spatial extent of turbulent eddies in the parallel and transverse directions. For interchange or drift wave turbulence, the typical size of turbulent eddies in the transverse plane is given by the ion Larmor radius $L_\perp \approx \rho_i$, whereas eddies are very elongated in the

parallel direction $L_\parallel \approx qR \gg L_\perp$. In both directions eddies are much bigger than the Debye length $L_\parallel \gg \lambda_D$ and $L_\perp \gg \lambda_D$: in section 5.3 we compute λ_D and ρ_i by taking typical values of density and temperature in the Scrape-Off Layer region. The results are visible in Table 5.1. One finds that $L_\perp \approx \rho_i \approx 50\,\mu\text{m} \gg \lambda_D \approx 1.3\,\mu\text{m}$ and $L_\parallel \approx qR \approx 24\,\text{m} \gg \lambda_D$, taking ITER-like values for the major radius $R = 6.2\,\text{m}$ and safety factor at the separatrix $q_{95} = 3$ [135]. Therefore one finds that up to second order in the small parameter $\lambda_D/L_\perp$, Poisson eq. (5.11) reduces to the quasineutrality equation

$$\frac{(n_e - e_i n_i)}{e n_0} = 0. \tag{5.12}$$

This equation is at first glance independent of the electrostatic potential ϕ. In the framework of the gyrokinetic theory, one can however write that the density of species s written n_s is related to the gyrocenter distribution function F_s as

$$n_s = \int d^3v\, \mathcal{J} F_i(\mathbf{x}, v_\parallel, \mu, t) + n_{pol,s},$$

where $n_{pol,s}$ is the so-called polarization density. It represents the mismatch between gyrocenter and particle densities. Indeed, these two quantities are not equal: as the gyrocenter and particle position differ by a Larmor radius, one may observe a particle in a given volume of real space while the gyrocenter is outside this volume. Let us now express the polarization density. As the electron Larmor radius is small compared to the ion Larmor radius, it is usual practice to neglect the electron polarization density. There exist several approximations of the ion polarization density. In the *long wavelength limit*[5], the polarization term is

$$n_{pol,i} \approx \nabla_\perp \cdot \left(\frac{m_i \bar{n}_{eq,i}}{e_i B^2} \nabla_\perp \phi \right). \tag{5.13}$$

Where $\bar{n}_{eq,i}$ represents the equilibrium ion density on a given magnetic flux surface, i.e. ,

$$\bar{n}_{\text{eq},i} = \langle n_i \rangle_{\text{FS}}\,. \tag{5.14}$$

A rigorous derivation of the transformation from gyrocenter to particles densities—and currents—can be found in [32]. The gyrokinetic quasineutrality equation can therefore be written in dimensional units as

$$-\nabla_\perp \cdot \left(\frac{m_i \bar{n}_{eq,i}}{e Z_i B^2} \nabla_\perp \phi \right) = Z_i \int d^3v\, \mathcal{J} F_i(\mathbf{x}, v_\parallel, \mu, t) - n_e, \tag{5.15}$$

[5]The long wavelength limit consists in assuming that variations of the electrostatic potential ϕ have a typical size in the plane transverse to the magnetic field that is much larger than the ion Larmor radius. This is equivalent to writing that the perturbation of the electrostatic potential verifies $k_\perp \rho_i \ll 1$, where $k_\perp$ is the wavevector of the perturbation in the transverse plane. Note that the $k_\perp \rho_i \ll 1$ hypothesis is violated in both core and Scrape-Off Layer regions. Core turbulence resulting from ITG and TEM instabilities have a spectrum that peaks around $k_\perp \rho_i \approx 0.3$ and $k_\perp \rho_i \approx 1$ respectively. In the Scrape-Off Layer, gradients length can be of the order of ρ_i, see section 5.1.2. To alleviate these issues a better approximation of the polarization density, such as a Padé approximation, can be used instead. For some reference the reader can see [136].

	Debye sheath	Gyrokinetic plasma
Characteristic length scale	$\lambda_{D_0} = \sqrt{\frac{\varepsilon_0 T_0}{n_0 e^2}} \approx 1.3\,\mu\text{m}$	$\rho_i = \frac{m_i v_{T_{0i}}}{eB} \approx 50\,\mu\text{m}$
Characteristic frequency	$\omega_{pe0} = \sqrt{\frac{n_0 e^2}{m_e \varepsilon_0}} \approx 200\,\text{GHz}$	$\Omega_{ci} = \frac{eB}{m_i} \approx 100\,\text{MHz}$
Charge density	$\rho_{\text{sh}} > 0$	Quasineutral

Table 5.1: Typical spatial scales and characteristic frequencies of the Debye sheath physics as compared to a plasma described by means of the gyrokinetic theory—that we abusively call a *gyrokinetic plasma* in the present table. Typical values of density and temperature of a Scrape-Off Layer plasma $n_0 \approx 10^{19}\,\text{m}^{-3}$ and $T_0 \approx 30\,\text{eV}$ have been used to compute the values presented in the table.

where $Z_i = e_i/e$ is the normalized charge of the ion species. As this formulation of the quasineutrality equation involves the electrostatic potential ϕ, one can solve this equation for it. There are several possibilities to compute the electron density n_e from the electron distribution function F_e. In section 5.6 we detail these possibilities, and show that not all of them are suitable to include plasma-wall interaction within the gyrokinetic framework.

5.3 Models for gyrokinetic plasma-wall interaction

Let us first highlight that the sheath layer cannot be resolved within the gyrokinetic framework. The physics at play within the Debye sheath is indeed incompatible with the gyrokinetic theory. Taking a typical density and temperature of a sheath-limited Scrape-Off Layer plasma $n_0 \approx 10^{19}\,\text{m}^{-3}$ and $T_0 \approx 30\,\text{eV}$ [23] one gets the values presented in Table 5.1 for the characteristics length scale and frequencies of the physics at play within the Debye sheath and within a quasineutral plasma described by means of the gyrokinetic theory. The sheath physics develops on spatial scales smaller than the Larmor radius, with characteristic frequencies extremely large compared to the cyclotron frequency. Besides, quasineutrality breaks down in the sheath region. As a consequence, describing the Debye sheath within the gyrokinetic framework is out of reach. From a theoretical standpoint, $\lambda_{D_0} \ll \rho_i$, $\omega_{pe0} \gg \Omega_{ci}$ and the breakdown of quasineutrality within the sheath are in contradiction with the fundamental hypotheses of the gyrokinetic theory, see section 5.2. From a numerical standpoint, refining a mesh

to describe the sheath scale while lowering the timestep to account for frequencies of the order of the electron plasma frequency would be too costly numerically.

5.3.1 The necessity of a subgrid model to describe the sheath physics

Given the impossibility to resolve the sheath physics in the gyrokinetic framework, one has to find a way to account for the effect of the sheath on the quasineutral plasma, without solving the characteristic time and spatial scales of the sheath. In order to find a subgrid model for describing the sheath, one has first to describe the fundamental ingredients of the physics at play within the sheath layer. A realistic description of plasma-wall interaction involves intricate pieces of physics: the inclination of magnetic field lines with respect to the wall leads to the formation of a magnetic presheath, the interaction of charged particles with molecules of the wall gives rise to complex recombination patterns and sputtering of wall particles back into the plasma, etc. When neutrals can be found near the plasma boundary the picture becomes even more complicated as the recombination of charged particles happens within the plasma volume. Given that we cannot account for all of these phenomena within the gyrokinetic framework at once, as a first step we choose to simplify the physics at play at the plasma boundary. We therefore understand the *sheath* as the combination of the Debye sheath and magnetic presheath, that acts on the electron and ion distribution functions to ensure that the plasma remains quasineutral. As explained in section 2.1.3, when magnetic field lines are tilted, a magnetic presheath appears in addition to the Debye sheath at the plasma boundary. In the magnetic presheath the ion gyromotion becomes distorted. The combined effect of the *Debye sheath + magnetic presheath* layers remain however the same as when field lines impact the wall at normal incidence, namely to ensure quasineutrality in the plasma on scales larger than the Debye length.

Building on knowledge obtained from 2D kinetic simulations described in chapters 2 & 3 and on already-existing sheath models valid in the gyrokinetic framework [123, 124]—that we describe in the following—we choose to model the sheath with the physics represented on fig. 5.1. The left graph represents the spatial evolution of the electric potential along with electron trajectories in phase space in the vicinity of the wall. The trajectories are very similar to the ones obtained in the kinetic simulation visible on fig. 2.7. Given a cutoff velocity v_c—that we do not specify yet how to to obtain—fast electrons $v_\parallel > v_c$ overcome the sheath potential drop and are absorbed in the wall while slow electrons $0 \leq v_\parallel \leq v_c$ are reflected back into the plasma. The trajectories of ions are not represented, but consist in an acceleration in the sheath region and an absorption in the wall. The subgrid model for the sheath consists in replacing the trajectories of fig. 5.1, left graph by the ones depicted on the right graph. With this model, fast electrons are absorbed when they come into contact with the wall, while slow electrons are reflected back into the plasma with opposite parallel velocities. The difference between the left and right graph is that (i) in the subgrid model the half turn of electrons is not resolved but is operated instantly at the plasma boundary, and (ii)

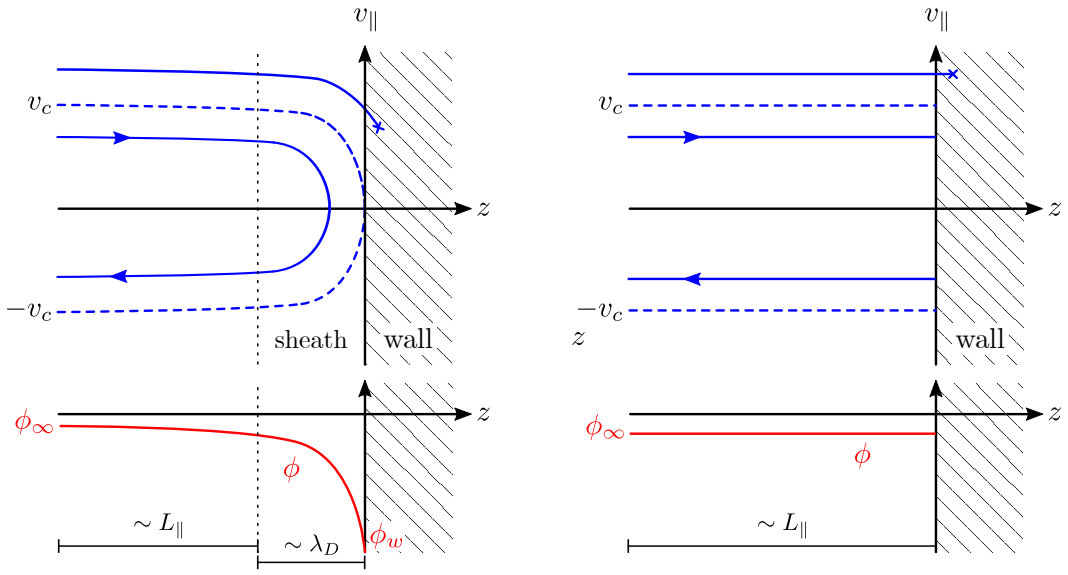

Figure 5.1: Electron trajectories in blue and electric potential variation in red in the vicinity of the wall. The z coordinate denotes the location along a given magnetic field line. The left graph represents the case of a resolved Debye sheath. The right graph corresponds to the limiting case where the sheath is infinitely small and the sheath potential drop remains not resolved. The trajectories of fast electrons have been represented to penetrate the wall region only to make more visible that these particles are absorbed there.

the potential drop that exists in the sheath is not resolved. To summarize, the right graph of fig. 5.1 corresponds to the trajectories represented on the left graph when taking the limit of an infinitely small sheath layer. A subgrid model for plasma-wall interaction valid in the gyrokinetic framework has therefore to be composed of three essential features that are

1. All ions whose trajectories intercept the material boundary should be absorbed;

2. Slow electrons with parallel velocities $0 \leq v_\parallel \leq v_c$ coming into contact with the solid boundary should be reflected back in the plasma with opposite parallel velocities. Given the characteristic frequency of the physics at play in the sheath—see Table 5.1—this reflection should happen instantly as far as the gyrokinetic theory is concerned;

3. Fast electrons with parallel velocities $v_\parallel > v_c$ should be absorbed at the plasma boundary.

Here, we considered that at the plasma boundary, particles with velocities $v_\parallel > 0$ are directed towards the solid wall.

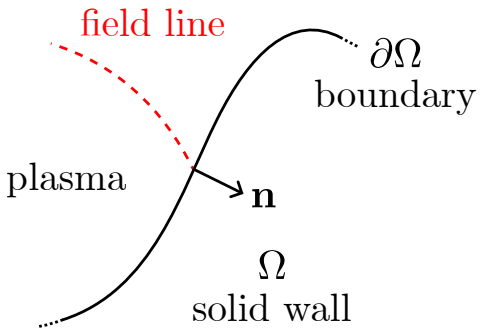

Figure 5.2: Geometry of the configuration used to illustrate the logical and conducting sheath approaches. The red dashed line represents a given magnetic field line. The normal unit vector $\mathbf{n}$ is defined on any point of the wall boundary $\partial\Omega$.

5.3.2 Two subgrid sheath models valid in the gyrokinetic framework

We describe here the so-called *logical* and *conducting* sheath approaches that propose a gyrokinetic treatment of plasma-wall interaction. The two approaches have been first presented in [123, 124]. In each paper the description of the proposed sheath treatment is quite specific to the numerical scheme of the code used to test the proposed treatment of the sheath physics. They can however be applied to virtually any numerical scheme given some small modifications. Thus in the following we give a general description of these approaches valid with any numerical scheme. We consider a magnetized plasma with field lines impacting a solid wall. The wall can have any given shape. Said differently, the magnetic configuration can be for instance a divertor or a limiter configuration. We therefore consider the general geometry represented on fig. 5.2. The solid wall region is denoted by Ω, its boundary in contact with the plasma is $\partial\Omega$. The discussion below is valid for field lines impacting the wall at any angle ψ—with $\psi = 90°$ corresponding to a field line that impacts the wall at normal incidence. The case of $\psi = 0$ is not taken into account in the following discussion as in this case the considered field line does not intercept the wall.

Particle flux at the boundary Let us consider a position on the plasma boundary $\mathbf{x} \in \partial\Omega$. The flux of particles that crosses the boundary at this location can be expressed in the gyrokinetic framework as

$$\Gamma_s^{\partial\Omega}(\mathbf{x},t) = \int_{-\infty}^{+\infty} dv_\parallel \int_0^{+\infty} d\mu\, J_v\, J_0 F_s(\mathbf{x}, v_\parallel, \mu) \left(v_\parallel \mathbf{b}_\parallel^* + \mathbf{v}_E + \mathbf{v}_D\right) \cdot \mathbf{n}, \tag{5.16}$$

where J_0 stands for the gyroaverage operator and $J_v(\mathbf{x}, v_\parallel)$ is the velocity space Jacobian that is written as $J_v = 2\pi B_\parallel^*/m_s$. In this last expression we introduced the normal unit vector $\mathbf{n}(\mathbf{x})$ as the vector orthogonal to the wall boundary at any point on the boundary. We take the following convention: the unit vector $\mathbf{n}$ points towards the inside of wall, see fig. 5.2. In eq. (5.16) the scalar product with the normal unit vector

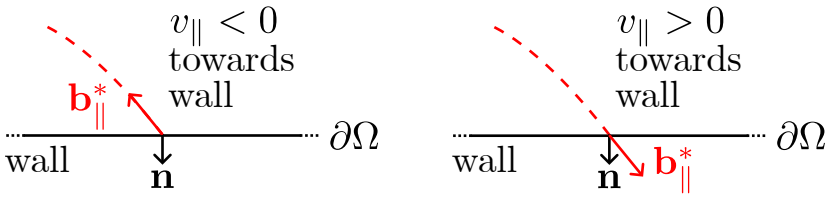

Figure 5.3: Left graph: $\varepsilon = \text{sign}(\mathbf{b}^*_\parallel \cdot \mathbf{n}) < 0$, and particles with negative parallel velocities travel towards the wall. Right graph: situation where $\varepsilon > 0$, and particles with positive parallel velocities travel towards the wall. In a limiter configuration, when the safety factor is positive $q > 0$, the left graph corresponds to the situation on the limiter surface at the low field side of the device, while the right graph corresponds to the situation on the high field side.

$\mathbf{n}$ ensures that particles crossing the boundary from plasma to solid wall give positive contributions to the flux $\Gamma_s^{\partial\Omega}$. Let us remark that the velocity used in eq. (5.16) is composed of the parallel velocity $v_\parallel \mathbf{b}^*_\parallel$ and of the perpendicular drifts $\mathbf{v}_\perp = \mathbf{v}_E + \mathbf{v}_D$: particles may cross the wall boundary as a result of their parallel or perpendicular motion. Last, as we integrate over the entire parallel velocity space $v_\parallel \in [-\infty, +\infty]$, if particles cross the boundary from the wall to the plasma—i.e. if the wall emits particles—they are included in the flux defined in eq. (5.16).

Partial flux at the boundary Given a position on the boundary $\mathbf{x} \in \partial\Omega$ and a fixed cutoff velocity $v_c > 0$ (which remains to be defined), we give hereafter an expression for the flux of particles that cross the boundary (i) with parallel velocities $v_\parallel > -v_c$ (when $v_\parallel > 0$ corresponds to particles that move towards the boundary due to their parallel motion[6]) , or (ii) with parallel velocities $v_\parallel < v_c$ (when $v_\parallel < 0$ corresponds to particles that move towards the boundary due to their parallel motion). To clarify this distinction, let us define the variable

$$\varepsilon(\mathbf{x} \in \partial\Omega) = \text{sign}(\mathbf{b}^*_\parallel \cdot \mathbf{n}). \tag{5.17}$$

This variable is positive when the parallel direction points towards the solid wall, and negative otherwise. Let us then define on any point of the boundary a generalized parallel velocity as $\bar{v}_\parallel = \varepsilon v_\parallel$. Note that this generalized parallel velocity depends on the considered position $\mathbf{x} \in \partial\Omega$. The generalized parallel velocity is positive when any of these two cases occurs:

1. When the parallel direction points towards the solid wall $\varepsilon > 0$, and the considered parallel velocity is positive $v_\parallel > 0$. In this situation, a particle with a

[6]The subtlety here is that particles may cross the material boundary surface due to their parallel or perpendicular motion. Said differently, particles with a parallel velocity directed towards the solid boundary may *miss* the solid boundary surface due to perpendicular drifts. The formulation *particles that move towards the boundary due to their parallel motion* refers to particles that would cross the boundary *in the absence of perpendicular drifts*. When drifts are included, these particles may, or may not, cross the boundary.

positive parallel velocity moves towards the limiter due to its parallel motion. This corresponds to the situation represented on fig. 5.3, right graph;

2. When the parallel direction points towards the plasma $\varepsilon < 0$ and the considered parallel velocity is negative $v_\parallel < 0$. In this situation, a particle with a negative parallel velocity moves towards the limiter due to its parallel motion. This corresponds to the situation represented on fig. 5.3, left graph;

To summarize, for any point on the boundary $\mathbf{x} \in \partial\Omega$, positive generalized velocities $\bar{v}_\parallel > 0$ correspond to particles that move towards the boundary, going from the plasma to the wall. As a consequence, particles for which $\bar{v}_\parallel > -v_c$ (with a given velocity $v_c > 0$) include (i) particles with $\bar{v}_\parallel > 0$ going towards the wall due to their parallel motion and (ii) particles coming back from the wall towards the plasma due to their parallel motion, with velocities with $-v_c < \bar{v}_\parallel < 0$. With the model for plasma-wall interaction presented on fig. 5.1 top left graph $\bar{v}_\parallel > -v_c$ corresponds to (i) electrons going towards the wall with $v_\parallel > 0$ and (ii) electrons coming back towards the plasma with parallel velocities $-v_c < v_\parallel < 0$. With these conventions, let us define the partial flux of particles with generalized parallel velocities $\bar{v}_\parallel > -v_c$ as

$$\bar{\Gamma}_s^{\partial\Omega}(\mathbf{x}, v_c, t) = \int_{-v_c}^{+\infty} d\bar{v}_\parallel \int_0^{+\infty} d\mu \, J_v \, J_0 F_s(\mathbf{x}, \bar{v}_\parallel, \mu) \left(\bar{v}_\parallel \mathbf{b}_\parallel^* + \mathbf{v}_E + \mathbf{v}_D\right) \cdot \mathbf{n}, \tag{5.18}$$

Note that in this last expression all quantities that appear in the integral and that depend on the parallel velocity—such as the Jacobian or the parallel unit vector $\mathbf{b}_\parallel^*$—should be evaluated at $\bar{v}_\parallel$ instead of $v_\parallel$.

5.3.3 Logical and conducting sheath frameworks

We detail hereafter the logical and conducting sheath techniques. With these approaches, the sheath is not resolved and its effect on the quasineutral plasma is taken into account using the subgrid model described in section 5.3.1. More precisely, the wall (i) absorbs all ions that come into contact with it, and fast electrons with velocities $\bar{v}_\parallel > v_c$, while electrons with velocities $\bar{v}_\parallel < v_c$ are reflected back to the plasma with opposite parallel velocities. The two approaches mainly differ in the way the cutoff velocity v_c is computed. For both models, the cutoff velocity v_c discriminates between fast electrons absorbed in the solid wall for which $\bar{v}_\parallel > v_c$ and slow electrons reflected in the plasma for which $0 < \bar{v}_\parallel < v_c$.

Logical sheath In the logical sheath framework, the cutoff velocity is computed so as to ensure that the fluxes of ions and electrons are equal at each position on the solid wall boundary [123]. More precisely, for any position $\mathbf{x} \in \partial\Omega$ the cutoff velocity is defined through the following implicit equation

$$Z_i \Gamma_i^{\partial\Omega}(\mathbf{x}, t) = \bar{\Gamma}_e^{\partial\Omega}(\mathbf{x}, v_c, t), \tag{5.19}$$

where $Z_i = e_i/e$ is the normalized charge of ions. With the definition given in eq. (5.19) the cutoff velocity depends on the considered position on the solid wall boundary and on time $v_c(\mathbf{x}, t)$. Note that with the logical sheath, no potential drop develops at the plasma boundary. The sheath potential drop $\Delta\phi_{\rm sh}$ is never required during the numerical treatment, but can be retrieved during the post-processing phase of the simulation. This virtual potential drop is such that it confines in the plasma all electrons crossing the wall boundary with generalized parallel velocities lower than the cutoff velocity $v_{\rm c}$. Using conservation of energy, it is therefore expressed in dimensional units as $\Delta\phi_{\rm sh} = -\frac{1}{2e} m_e v_{\rm c}^2$.
A drawback of the logical sheath is that it enforces a zero current at the boundary at each time and boundary mesh point. Such a constraint fulfills the physical requirement that the plasma charge does not build-up, and consequently that the plasma remains quasineutral. This requirement however appears too stiff. Indeed, the global constraint of quasineutrality within the plasma does not require zero current at all times and all points. The situation appears to be over constrained when considering experimental evidence, where non-vanishing currents are measured at different spatial locations of plasma facing units [137]. Enforcing the logical sheath condition may therefore modify the turbulence behavior compared to cases where the current locally fluctuates around zero net current. In the seminal paper [123] the logical sheath algorithm is presented so as to be easily implemented within a particle-in-cell code. We describe it hereafter, for a given location on the plasma boundary.

1. Starting from the particle positions at time t, apply the pusher method to compute their new position at time $t + \Delta t$. Within a particle-in-cell code, a *pusher* method moves the particles from time t to $t + \Delta t$, where Δt stands for the simulation time step.

2. As a result of step 1. particles may have crossed the simulation boundary at the considered position. Note that it is not specified whether this crossing results from the parallel or transverse motion of particles. Actually both can contribute, in agreement with the definition of the outgoing fluxes retained in eq. (5.16) and eq. (5.18). Step 2. consists then in counting the number of outgoing electrons $N_{\rm e}$ and ions $N_{\rm i}$. Then, two situations can occur:

3. More electrons than ions have crossed the boundary, i.e. $N_{\rm e} > N_{\rm i}$. In this case:

   (a) Order all $N_{\rm e}$ electrons from slowest to fastest.

   (b) Remove all $N_{\rm i}$ ions from the simulation, and the fastest $N_{\rm i}$ electrons. The velocity of the slowest electron that is absorbed in this step defines a cutoff velocity $v_{\rm c}$.

   (c) The remaining $N_{\rm e} - N_{\rm i}$ electrons that have not been absorbed have velocities lower than the cutoff velocity. These electrons are reflected back into the plasma, by flipping the sign of their parallel velocities for the next time

step[7].

4. More ions than electrons have crossed the boundary, i.e. $N_\mathrm{i} > N_\mathrm{e}$. In this case:
   (a) All these N_i ions and N_e electrons are absorbed by the wall, and are thus removed from the simulation.
   (b) To fulfill charge conservation in this case, a positive charge $N_\mathrm{i} - N_\mathrm{e}$ is attached to the plasma boundary at the considered position, for the next time step only.

Situation 3. is the most common one since electrons are more mobile than ions along field lines. In this case the net current to the wall is exactly zero. Therefore ambipolarity is ensured by the logical sheath condition. Situation 4. rarely happens, and may result from fluctuations in the system. When this case arises, at next time step the wall is positively charged. Therefore, it repels ions and attracts electrons, making situation 3. more probable again. Apart from this particular case the wall bears no charge. Finally, let us remark that this description of the logical sheath algorithm in the particle-in-cell framework is equivalent to the general definition of the cutoff velocity given in eq. (5.19). Computing a particle flux at the plasma boundary within the PIC framework involves only counting the number of outgoing particles from plasma to solid wall. When situation 4. happens however, the generalization of the PIC description is not straightforward. In this case, one could not use eq. (5.19) to define a cutoff velocity. More specifically, the following inequality would hold:

$$Z_i \Gamma_i^{\partial\Omega}(\mathbf{x}, t) > \bar{\Gamma}_e^{\partial\Omega}(\mathbf{x}, 0, t). \tag{5.20}$$

This inequality simply states that even when absorbing all electrons directed towards the wall—thus the ones with generalized velocities $\bar{v}_\parallel > 0$, the resulting electron flux would not compensate the ion flux. In this case, even though the logical sheath algorithm prescribes attaching a net positive charge to the wall for the next timestep, it remains unclear how to adapt this prescription to an Eulerian or to a semi-Lagrangian scheme.

Conducting sheath We call the boundary condition introduced in [124] *conducting sheath* in the sense that it allows finite currents to flow freely in and out of the wall, possibly forming current loops when dealing with a 2D plasma boundary. In the conducting sheath framework the potential at the plasma boundary $\phi(\mathbf{x} \in \partial\Omega)$ determines a proportion of reflected electrons. In the meantime, outgoing ions leave the simulation freely. Let us consider a point on the plasma boundary $\mathbf{x} \in \partial\Omega$. When the potential $\phi(\mathbf{x})$ is positive, the cutoff velocity is defined as

$$v_c(\mathbf{x}, t) = \sqrt{\frac{2e}{m_e}\left(\phi(\mathbf{x}) - \phi_w\right)}, \tag{5.21}$$

[7]Note that if these electrons crossed the boundary as a result of their transverse motion, flipping the sign of their parallel velocity may not be sufficient to ensure that they come back into the plasma.

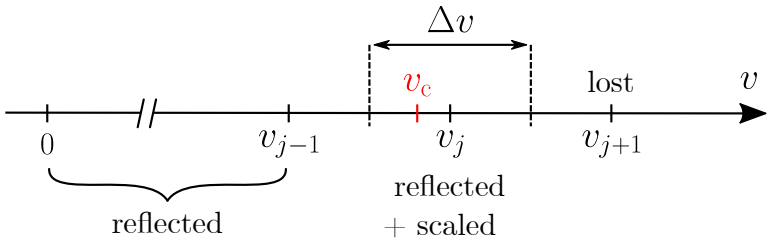

Figure 5.4: Velocity grid in the $v_\parallel$ direction at a given point on the solid wall boundary $\mathbf{x}$. Because the cutoff velocity falls inside the v_j velocity cell, when reflecting the slow electrons to the plasma the distribution function in this cell has to be rescaled.

where ϕ_w is the wall potential (taken as zero for a grounded wall). We consider the case $\phi_w = 0$ in the following. At the considered position $\mathbf{x}$, all slow electrons that have generalized velocities such that $0 \leq \bar{v}_\parallel \leq v_c$ are reflected back into the plasma. The fastest electrons are not reflected and are removed from the simulation. Let us remark that when the potential at the plasma boundary $\phi(\mathbf{x})$ is not positive then no electron is reflected and all outgoing electrons are lost to the wall. This however charges the plasma located in the vicinity of the wall positively, hence driving an increase of the potential there through the solving of quasineutrality section 5.2.2. One can therefore expect that on average the potential stays positive at the plasma boundary and the cutoff velocity given in eq. (5.21) is well defined. In [124] it is explained how to deal with the case where the cutoff velocity v_c does not coincide with a point of the mesh used to discretize the velocity direction. Let us introduce a velocity grid in the parallel direction (v_i), with i an integer. It is characterized by a discretization step Δv. The value of the distribution function $F_e(\mathbf{x}, v_i, \mu)$ accounts for the density of particles that have velocities spanning the $[v_i - \Delta v/2,\, v_i + \Delta v/2]$ interval. Since in general the cutoff velocity v_c does not lie on a specific point of the velocity grid, there exists an index j which is such that the cutoff velocity is inside the v_j cell. That is to say we have $v_c \in [v_j - \Delta v/2,\, v_j + \Delta v/2]$. For all velocities $0 \leq v_i < v_j$ the value of the distribution function $F_e(\mathbf{x}, v_i, \mu)$ is copied to the cell $v_{i'}$ which is such that $v_{i'} = -v_i$. This cell therefore stores the values of the reflected distribution function and is used as a boundary condition in the advection step of the Eulerian code, see fig. 5.4. The value of the distribution function at the particular cell $F_e(\mathbf{x}, v_j, \mu)$ is copied to the corresponding ghost cell $v_{j'} = -v_j$ and scaled by a factor c defined as

$$c(\mathbf{x}, t) = \frac{\int_{v_j - \Delta v/2}^{v_c} dv_\parallel \int_0^{+\infty} d\mu\, J_v\, F_e(\mathbf{x}, v_\parallel, \mu, t)}{\int_{v_j - \Delta v/2}^{v_j + \Delta v/2} dv_\parallel \int_0^{+\infty} d\mu\, J_v\, F_e(\mathbf{x}, v_\parallel, \mu, t)}.$$

This procedure ensures that all outgoing electrons verifying $\frac{1}{2} m_e v_\parallel^2 \leq e\phi(\mathbf{x})$ are indeed reflected back to the plasma, independently of the velocity grid in the z direction.

5.4 The GYSELA code

In this section we present the GYSELA code we use in the following sections as a framework to propose a model for plasma-wall interaction compatible with the gyrokinetic approach.

5.4.1 Code description

The GYSELA code is a gyrokinetic code that is *global*, *full-f* and that enables to perform *flux-driven* simulations. We give in the following a definition for these terms. A complete description of the code along with elements concerning its verification can be found in [138]. Two main features of the GYSELA code makes it particularly relevant to study plasma confinement:

- The GYSELA code is *global*: it describes the full torus geometry of a tokamak plasma. This is to be opposed to *local codes* that reduce the simulation domain to a smaller chunk of plasma, usually restricted in the radial direction and aligned with the magnetic field lines—the so-called *flux tubes* codes [139, 140]. A global approach is required as soon as one is interested in studying processes happening on scales comparable with the machine size, such as transport barriers for instance;
- The GYSELA code is *full-f*, it evolves the entirety of the distribution function in time. This is to be opposed to δf codes, that prescribe an equilibrium—usually Maxwellian—background distribution function and describe only the time evolution of perturbations with respect to this background equilibrium. A full-f code enables to perform *flux-driven* simulations, where the gradient of macroscopic quantities such as density and temperature evolve in time. This enables to study the self-consistent interaction between turbulence and these gradients. When performing a flux-driven simulation, a source of heat—and possibly of particles when particle transport is active, e.g. when dealing with a realistic description of the Scrape-Off Layer region—has to be included in the model otherwise the simulated turbulent state is evanescent.

Given that the GYSELA code does not make the assumption of a reduced size simulation domain, nor prescribe a background equilibrium distribution function, the computational power required to perform simulations is quite high. The GYSELA code is thus massively parallelized—simulations with 500k cores are possible—uses state-of-the-art high performance computing algorithms and is run on supercomputer architectures.

5.4.2 Numerical scheme

We detail here the numerical scheme implemented in the GYSELA code that is used to solve the gyrokinetic eq. (5.5) along with the quasineutrality eq. (5.15). This detailed breakdown of the numerical scheme is useful to understand the subgrid model presented

in section 5.5. Overall the numerical scheme is similar to the one presented in the framework of the VOICE code, and is of second order accuracy in time. In the following we omit the gyrocenter phase space variables for the sake of compactness, and write $F_s(t)$ for the gyrocenter distribution function of species s. We use the Δt notation for the timestep. The same notation is used for the electric potential that we write $\phi(t)$ at time t. The coupling between the gyrokinetic and quasineutrality equations is solved using a leap frog method, namely

1. Compute $F_s(t + \Delta t/2)$ from $F_s(t)$ by solving the gyrokinetic equation on half a timestep. The numerical scheme used for solving the gyrokinetic equation is described below. Use $F_s(t + \Delta t/2)$ in order to solve the quasineutrality equation to obtain the value of the electric potential at this intermediate time $\phi(t+\Delta t/2)$;
2. Use the intermediate electric potential $\phi(t + \Delta t/2)$ and the initial value of the distribution function $F_s(t)$ to solve the gyrokinetic equation on a full timestep to get $F_s(t + \Delta t)$.

Solving the quasineutrality equation is done using a 2D solver applied at each toroidal position. A finite differences scheme is used to discretize eq. (5.15). The gyrokinetic equation is solved using a Strang splitting [141] to separate the advections in the different directions. Sources and collisions are taken out of this splitting scheme, so as to reduce the number of computations required to solve the gyrokinetic equation. Given that the system evolves slowly under the influence of sources and collisions compared to the fast dynamics of the advections in phase space, little error is introduced in the result by taking collisions and sources out of the splitting. Overall, to advance the distribution function from time t to time $t + \Delta t$ the splitting can be summarized as

1. Advection along the $v_\parallel$ direction on a time interval $\Delta t/2$;
2. Advection along the φ direction on a time interval $\Delta t/2$;
3. Advection along the (r, θ) direction on a time interval Δt;
4. Advection along the φ direction on a time interval $\Delta t/2$;
5. Advection along the $v_\parallel$ direction on a time interval $\Delta t/2$;

This particular splitting scheme is not the only one available in the GYSELA code: it is different when using *field-aligned* coordinates for instance [142]. We do not detail the implementation of these coordinates here since the subgrid treatment of plasma-wall interaction presented in section 5.5 does not require field-aligned coordinates. We however explain how to adapt the present work to field-aligned coordinates in appendix C.1.3. A particularity of the GYSELA code is that it uses a *backward semi-Lagrangian* approach to solve for each of the advection mentioned above. The backward semi-Lagrangian method is detailed in section 5.5.2. Let us briefly recall its characteristics. It uses the invariance of the distribution function in phase space along the trajectories of particles to compute the value of the distribution function at time $t+\Delta t$

by interpolation of the distribution function at time t. One key remark for the following sections is that the semi-Lagrangian scheme requires an interpolation step. In GYSELA the interpolation procedure uses cubic b-splines. Backward semi-Lagrangian methods sit halfway between *particle-in-cells* (PIC) and *Eulerian* approaches. Compared to PIC codes, backward semi-Lagragian codes exhibit lower levels of numerical noise, allowing for reaching longer simulation times. The timestep required by semi-Lagrangian approaches is less constrained by a *Courant-Friedrich-Levy* (CFL) type condition, as compared to Eulerian approaches [49].

5.5 A penalized sheath model compatible with backward semi Lagrangian schemes

In the present section we describe a subgrid model for plasma-wall interaction that is compatible with the penalized limiter configuration of the GYSELA code. The model differs from the logical and conducting sheath approaches as it relies on matching the electron and ion fluxes *on spatial average* over the entire limiter surface. For this reason we call this model *flux-averaged sheath*. With this model global gyrokinetic simulations encompassing both core and Scrape-Off Layer regions are possible. We describe a procedure for absorbing ions in the limiter in section 5.5.1, and a procedure for reflecting at the limiter surface a fraction of the slowest electrons back into the plasma in section 5.5.2. The matching of the electron and ion fluxes on the limiter surface on spatial average is described in section 5.5.3. The difficulty of the present subgrid model lies mainly in the reflection of slow electrons on the material boundary surface. We discuss in appendix C.1 some other possible approaches to achieve such reflections. In appendix C.2 we discuss the details of the implementation of the penalized sheath model in the backward semi-Lagragian framework of the GYSELA code. A summary of the most important features of these implementation details can be found in section 5.5.4. Finally, let us remark that we take the example of a limiter configuration in the rest of this chapter since it is the current configuration of the GYSELA code. The description of the flux-average sheath technique is however valid for any magnetic configuration and shape of the material boundary—except the degenerate situation where magnetic field lines are parallel with respect to the boundary.

5.5.1 A penalization operator for ions

We consider the magnetic geometry described on fig. 5.5. We model the effect of the limiter on the ion population by introducing a penalization term $\mathcal{S}_{\text{lim}}$ in the right hand side of the gyrokinetic eq. (5.5) as

$$\frac{DF_i}{Dt} = \mathcal{C} + \mathcal{S} + \mathcal{S}_{\text{lim}}, \tag{5.22}$$

where $\mathcal{C}$ models collisional processes and $\mathcal{S}$ stands for any other source term. The penalization operator $\mathcal{S}_{\text{lim}}$ acts as a sink of particles, momentum and energy. There

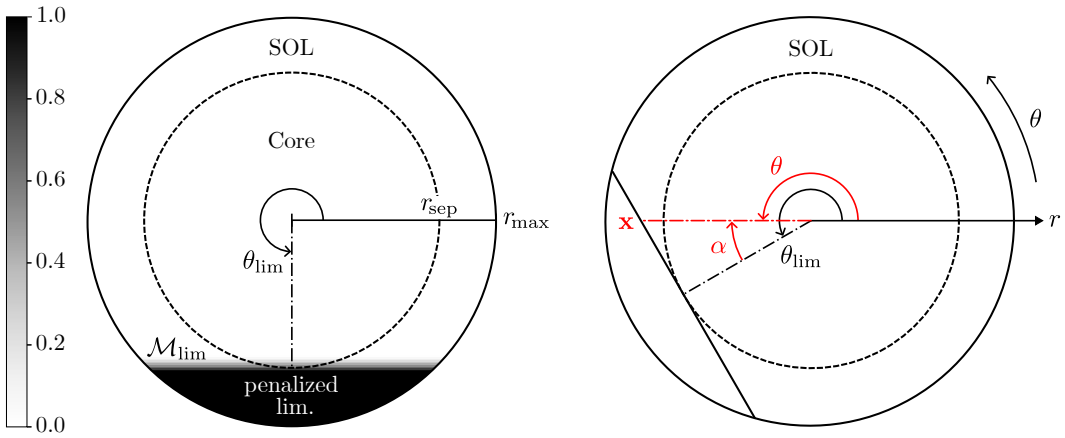

Figure 5.5: Left: poloidal cut of the limiter geometry used by the GYSELA code. The limiter mask $\mathcal{M}_{\text{lim}}$ transitions smoothly from a vanishing value (white) in the core and Scrape-Off Layer regions to a value of one (black) in the limiter region. Right: definition of the angle α used for express the limiter mask $\mathcal{M}_{\text{lim}}$ for any value of the limiter angle θ_{lim}. The definition of the angle α given in eq. (5.25) is valid for any position $\mathbf{x}$ in the plasma or limiter.

are two possible options available for this penalization operator.

Krook operator The first available penalization operator shares a common form with the sink that models the wall in the two-dimensional framework of the VOICE code, see section 2.3.1. It is a Bhatnagar-Gross-Krook operator expressed as

$$\mathcal{S}_{\text{lim}}(F_i) = -\nu \mathcal{M}_{\text{lim}} \left(F_i - F_{\text{lim}}\right). \tag{5.23}$$

This operator forces the ion distribution function to relax towards the target function F_{lim} in the limiter region. The ν coefficient is constant and sets the magnitude of the restoring force. The target function F_{lim} is an axisymmetric Maxwellian with low density and vanishing mean velocity. It can be expressed as

$$F_{\text{lim}}(r, \theta, v_{\parallel}, \mu) = \frac{n_{\text{lim}}}{\left(2\pi T_{\text{lim}}/m_i\right)^{3/2}} \exp\left(-\frac{m_i v_{\parallel}^2}{2T_{\text{lim}}} - \frac{\mu B}{T_{\text{lim}}}\right), \tag{5.24}$$

where n_{lim} and T_{lim} are constant. The target density n_{lim} is chosen to be small compared to the typical plasma density so as to ensure that the limiter effectively acts as a sink of particles, momentum and energy for the ion species. The mask $\mathcal{M}_{\text{lim}}$ defines the region where the penalization term is active. It transitions smoothly from a vanishing value in the core and Scrape-Off Layer regions to a value of one in the limiter region, see fig. 5.5, left graph. On the same figure the angle of the limiter θ_{lim} is represented, along with the separatrix radius r_{sep}. In order to give a definition of the limiter mask valid for any limiter angle $\theta_{\text{lim}} \in [0, 2\pi]$ we introduce the angle α as

$$\alpha = \theta - \theta_{\text{lim}} \left[2\pi\right]. \tag{5.25}$$

For any point in the poloidal plane $\mathbf{x}$ characterized by an angle θ, the corresponding angle α represents the angle between the normal of the limiter and the position $\mathbf{x}$, as shown on fig. 5.5. Let us additionally introduce the normalized radius as

$$\rho = r/r_{\max}, \tag{5.26}$$

and the limiter normalized radius $\rho_{\text{sep}} = r_{\text{sep}}/r_{\max}$. With these definition the penalized limiter mask is

$$\mathcal{M}_{\text{lim}}(r,\theta) = \frac{1}{2}\left(1 + \tanh\left(\frac{\rho\sin\alpha - \rho_{\text{sep}} - \rho_{\text{shift}}}{d_{\text{lim}}}\right)\right). \tag{5.27}$$

In this expression the d_{lim} parameter controls the steepness of the transition between plasma and limiter. The constant ρ_{shift} is a parameter specified at the start of the simulation that enables to shift the surface of the volume used to penalize the ion gyrocenter distribution function with respect to the separatrix. A value $\rho_{\text{shift}} = 0$ means that the mask equals one half at $\rho = \rho_{\text{sep}}$, while a value $\rho_{\text{shift}} > 0$ translates into the region where the penalization applied on ions being relegated further away in the separatrix. The necessity of such a shift is further discussed in section 5.7.

Infinite penalization The second choice for the penalization operator consists in taking the ion gyrocenter distribution function equal to the target function F_{lim} in the entire limiter region. The penalization operator consists therefore in performing the following operation at each timestep

$$F_i(\mathbf{x}, v_\parallel, \mu, t+\Delta t) = F_i(\mathbf{x}, v_\parallel, \mu, t)\,(1 - \mathcal{M}_{\text{lim}}) + F_{\text{lim}}\mathcal{M}_{\text{lim}}, \tag{5.28}$$

where $\mathbf{x}$ stands for a given position in real space, F_{lim} and $\mathcal{M}_{\text{lim}}$ are defined above in eqs. (5.24) and (5.27). With the infinite penalization operator the ion distribution function is fixed to F_{lim} in the limiter and transitions smoothly at the limiter surface towards the distribution function F_i in the plasma.

In both cases—krook or infinite penalization—the penalization operator is solved once per timestep, i.e. it is solved together with all other sources terms during an iteration of the GYSELA code, see section 5.4.2.

5.5.2 Electron reflection on the surface of the limiter

We describe here the procedure we use to reflect a portion of the slowest electrons that intercept the surface of the limiter. We work with the notation introduced in section 5.3.2. Let us recall in particular that for any point on the surface of the material boundary, the generalized parallel velocity $\bar{v}_\parallel$ is always positive for particles that move towards the solid wall due to their parallel motion, independently of the fact that $\mathbf{b}^*_\parallel$ points towards the wall or not at this position. Given a cutoff velocity $v_c > 0$, slow electrons reflected on the surface of the material boundary are such that $0 < \bar{v}_\parallel < v_c$,

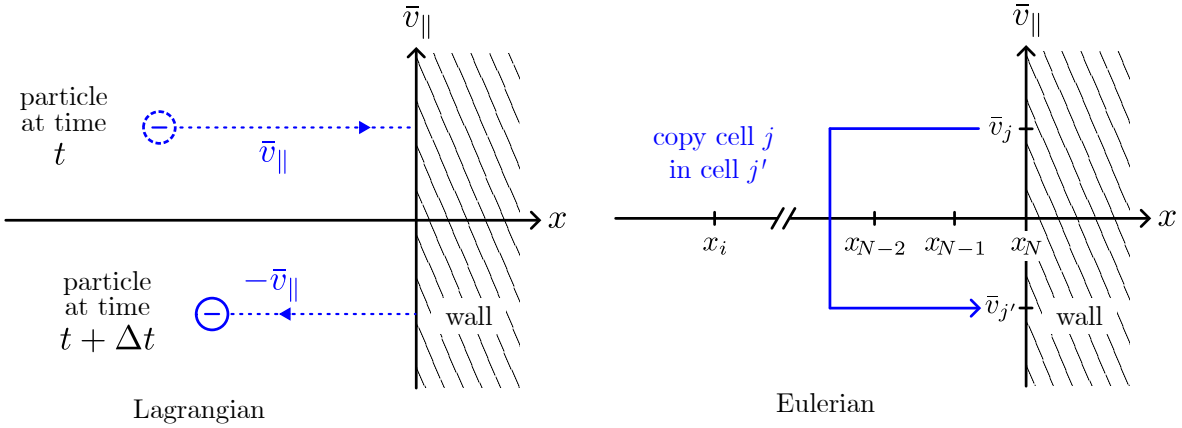

Figure 5.6: Reflection procedure for slow electrons applied to the Lagrangian framework on the left and Eulerian on the right.

while fast electrons for which $\bar{v}_\parallel > v_c$ should be absorbed in the boundary. Electrons with generalized velocities $\bar{v}_\parallel < 0$ correspond to particles with parallel velocities directed towards the plasma on the surface of the material boundary.

The procedure to reflect slow electrons on the surface of the material boundary is necessarily specific to the considered numerical scheme. In particular, the procedure differs between Lagrangian, Eulerian, and semi-Lagrangian schemes. On fig. 5.6 the reflection procedure is presented for both Lagrangian and Eulerian schemes. In both cases we considered a simplified $\left(x, \bar{v}_\parallel\right)$ geometry, where x represents the spatial position along a given magnetic field line. In the Lagrangian case the reflection procedure is straightforward: whenever a slow electron crosses the boundary of the simulation at the wall location, it is reinjected with an opposite parallel velocity in the plasma. In the Eulerian case the procedure is a bit more complex. On fig. 5.6 we introduced a discretization of $\left(x, \bar{v}_\parallel\right)$ phase space that we write $(x_i, \bar{v}_j)$. The x_N coordinate corresponds to the last resolved point in the x direction. The reflection of slow electrons consists in this case in copying the value of the distribution function at $(x_N, \bar{v}_j)$ for all indices j such that $0 < \bar{v}_j < v_c$ into the cells with oppositve parallel velocities. For instance, the value $F_e(x_N, \bar{v}_j)$ gets copied to the cell $(x_N, \bar{v}_{j'})$. The index j' is such that $\bar{v}_j = -\bar{v}_{j'}$. Values of the electron distribution function in cells $(x_N, \bar{v}_{j'} < 0)$ then propagate in the plasma when differential operators are evaluated during an iteration of the code.
We now describe the reflection procedure in the backward semi-Lagrangian (BSL) framework of the GYSELA code. The specificity of this numerical scheme is to combine elements from both Lagrangian and Eulerian schemes. In a BSL scheme, a discretization of phase space is introduced—that we denote by $(\mathbf{x}_i, v_j, \mu_k)$ with i, j, k integers. The value of the distribution function is known on points of this discretization. Backward semi-Lagrangian schemes use the invariance of the distribution function along the trajectories of particles—called the *characteristics*—to compute the value of the

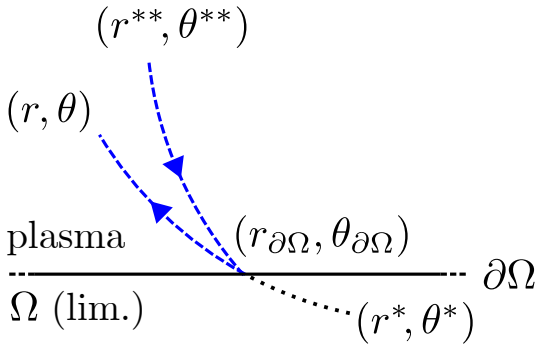

Figure 5.7: When the foot of the characteristics (r^*, θ^*) lines in the solid wall, we compute the intersection of the characteristics with the plasma boundary, denoted $(r_{\partial\Omega}, \theta_{\partial\Omega})$. Then, the foot of the characteristics obtained by flipping the parallel velocity on the surface of the limiter (r^{**}, θ^{**}) is computed.

distribution function at time $t + \Delta t$ given its value at time t. More precisely, when solving the gyrokinetic eq. (5.5) in the absence of sources and collisions one can write that[8]

$$F_s(\mathbf{x}_i, v_j, \mu, t + \Delta t) = F_s(\mathbf{x}_i^*, v_j^*, \mu, t), \tag{5.29}$$

Where the coordinate $(\mathbf{x}_i^*, v_j^*)$ is called the foot of the characteristics. It is related to the position $(\mathbf{x}_i, v_j)$ through the equations of motion

$$\mathbf{x}_i = \mathbf{x}_i^* + \int_t^{t+\Delta t} \frac{d\mathbf{x}}{dt'}\, dt' \quad \text{and} \quad v_j = v_j^* + \int_t^{t+\Delta t} \frac{dv_\parallel}{dt'}\, dt', \tag{5.30}$$

and the time derivatives of gyrocenter position $\mathbf{x}$ and parallel velocity $v_\parallel$ are given by eqs. (5.6) and (5.10). Given that the distribution function is known on points of the mesh $(\mathbf{x}_i, v_j, \mu_k)$ at time t on can infer the value of $F_s(\mathbf{x}_i, v_j, \mu, t + \Delta t)$ by interpolating the distribution function at time t to obtain $F_s(\mathbf{x}_i^*, v_j^*, \mu, t)$[9]. In our case we introduce the reflection on the limiter surface in step 3. of the splitting scheme presented in section 5.4.2, that is to say when performing the advection in the poloidal (r, θ) plane. It is indeed the only step of the splitting when particles may cross the surface of the limiter during their motion: the advection in the $v_\parallel$ direction does not account for any displacement of particles in real space, and advecting particles in the φ direction cannot make them cross the surface of the axisymmetric limiter[10]. Performing the advection step in the poloidal plane starting from a (r, θ) coordinate on a grid point involves computing the foot of the characteristics (r^*, θ^*) solving the following equations

[8] The value of μ stays constant as it is an invariant of motion in absence of sources and collisions.

[9] An interpolation is required since in general $(\mathbf{x}_i^*, v_j^*)$ does not coincide with a mesh point.

[10] The situation is different when using *field-aligned* interpolation. We touch upon the inclusion of the flux-averaged sheath model in the gyrokinetic framework when using field-aligned interpolation in appendix C.1.3

of motion from time t to time $t + \Delta t$

$$\frac{dr}{dt} = \left(v_\parallel \mathbf{b}^*_\parallel + \mathbf{v}_E + \mathbf{v}_D\right) \cdot \nabla r, \tag{5.31}$$

$$\frac{d\theta}{dt} = \left(v_\parallel \mathbf{b}^*_\parallel + \mathbf{v}_E + \mathbf{v}_D\right) \cdot \nabla \theta. \tag{5.32}$$

Some of these trajectories intercept the material boundary surface, thus (r^*, θ^*) lies inside the wall volume, as represented on fig. 5.7. For these trajectories we compute the intersection of the characteristic with the plasma boundary, denoted $(r_{\partial\Omega}, \theta_{\partial\Omega})$. Then, there exists a real number $\alpha \in [0, 1]$ such that

$$r = r_{\partial\Omega} + \int_{t+\alpha\Delta t}^{t+\Delta t} \frac{dr}{dt'}\, dt' \quad \text{and} \quad \theta = \theta_{\partial\Omega} + \int_{t+\alpha\Delta t}^{t+\Delta t} \frac{d\theta}{dt'}\, dt', \tag{5.33}$$

with the time derivatives of r and θ given by eqs. (5.31) and (5.32). By finding this α parameter using eq. (5.33) [11] one can compute the reflected foot of the characteristics (r^{**}, θ^{**}) as

$$r_{\partial\Omega} = r^{**} + \int_{t}^{t+\alpha\Delta t} \left(-v_\parallel \mathbf{b}^*_\parallel + \mathbf{v}_E + \mathbf{v}_D\right) \cdot \nabla r, \tag{5.34}$$

$$\theta_{\partial\Omega} = \theta^{**} + \int_{t}^{t+\alpha\Delta t} \left(-v_\parallel \mathbf{b}^*_\parallel + \mathbf{v}_E + \mathbf{v}_D\right) \cdot \nabla \theta. \tag{5.35}$$

In these last two integrals, all quantities that depend on $v_\parallel$ should be evaluated at $-v_\parallel$. In practice the GYSELA code computes the integrals of eq. (5.30) by approximating them using a Newton method. This makes the computation of the intersection point $(r_{\partial\Omega}, \theta_{\partial\Omega})$ and of the reflected foot (r^{**}, θ^{**}) less difficult. We describe the details of the implementation of the reflection procedure within the GYSELA code in appendix C.2. Last, let us remark that the reflection of slow electrons must be done on a boundary that is defined precisely. With the limiter geometry used in the GYSELA code, the reflection is done on the surface defined by $r\cos(\theta - \theta_{\text{lim}}) = r_{\text{sep}}$. There is therefore a difference between the definition of the limiter for the ion species, where the transition between the plasma and limiter is blurred as a result of the penalization mask introduced in eq. (5.27), and the definition of the limiter for electrons which is infinitely steep.

5.5.3 Matching the electron and ion fluxes on spatial average over the entire limiter surface

As already mentioned in the sections above, the difference between the flux-averaged sheath model detailed in the present section and the logical and conducting sheath

[11] Note that both expressions for r and θ given in eq. (5.33), along with an equation for the surface of the boundary are required to solve for the intersection point. In appendix C.2 we detail how to perform such a computation by expressing eq. (5.33) using a first-order Newton approximation as it is done in the GYSELA code, and combine the resulting expression with the equation of a flat limiter.

approaches described in section 5.3.3 lies in the definition of the cutoff velocity v_c that discriminates between slow electrons reflected on the surface of the limiter and fast electrons absorbed in the material boundary. In the present flux-averaged sheath model, we propose a definition of the cutoff velocity based on physical considerations. As mentioned in section 2.1 and confirmed by kinetic simulations investigated in Chapter 2, the most important effect that plasma-wall interaction has on the plasma is to ensure quasineutrality on scales larger than the Debye length. We further want to constrain the plasma dynamics as little as possible, so as to ensure that the plasma freely evolves according to first principles equations. Thus, the least-constraining way of ensuring quasineutrality within the plasma volume consist in matching the ion and electron fluxes *on spatial average over the entire limiter surface*. By doing so, we hope to enable for complex circulation of charges to happen in the vicinity of the limiter/divertor, possibly forming current loops between different points of the limiter.

Using the notations introduced in section 5.3.2, we introduce the average over the limiter surface of a given function f that depends on the spatial variable $\mathbf{x}$ as

$$\langle f \rangle_{\partial\Omega} = \frac{1}{\int_{\partial\Omega} d^2S} \int_{\partial\Omega} d^2S f(\mathbf{x}). \tag{5.36}$$

We recall here that $\partial\Omega$ denotes the surface of the limiter—or of any boundary that intercepts magnetic field lines, such as a divertor surface for instance. The d^2S element is the infinitesimal surface element of the limiter. We use eq. (5.16) that defines the flux of ions crossing the limiter at a given position on the limiter surface $\Gamma_i^{\partial\Omega}(\mathbf{x} \in \partial\Omega, t)$, and eq. (5.18) that defines the flux of electrons crossing the limiter at a given position on the limiter surface with generalized parallel velocities higher than a cutoff velocity $\bar{v}_\parallel > -v_c$ that we write $\bar{\Gamma}_e^{\partial\Omega}(\mathbf{x} \in \partial\Omega, v_c, t)$. We write as usual v_c the cutoff velocity, such that on the surface of the limiter (i) electrons with generalized velocities $\bar{v}_\parallel > v_c$ are absorbed and (ii) electrons for which $0 < \bar{v}_\parallel < v_c$ are reflected with opposite parallel velocities $-\bar{v}_\parallel$ in the plasma. A definition of such a cutoff velocity v_c ensuring that the electron and ion fluxes are matched on average over the entire surface of the limiter surface is therefore

$$\left\langle \Gamma_i^{\partial\Omega}(\mathbf{x}, t) \right\rangle_{\partial\Omega} = \left\langle \bar{\Gamma}_e^{\partial\Omega}(\mathbf{x}, v_c, t) \right\rangle_{\partial\Omega}, \tag{5.37}$$

or equivalently

$$\begin{aligned} &\int_{\partial\Omega} d^2S \int_{-\infty}^{+\infty} dv_\parallel \int_0^{+\infty} d\mu\, J_v\, J_0 F_i(\mathbf{x}, v_\parallel, \mu) \left(v_\parallel \mathbf{b}_\parallel^* + \mathbf{v}_E + \mathbf{v}_D \right) \cdot \mathbf{n} \\ &= \int_{\partial\Omega} d^2S \int_{-v_c}^{+\infty} d\bar{v}_\parallel \int_0^{+\infty} d\mu\, J_v\, F_e(\mathbf{x}, \bar{v}_\parallel, \mu) \left(\bar{v}_\parallel \mathbf{b}_\parallel^* + \mathbf{v}_E + \mathbf{v}_D \right) \cdot \mathbf{n}, \end{aligned} \tag{5.38}$$

with $\varepsilon(\mathbf{x} \in \partial\Omega) = \mathrm{sign}(\mathbf{b}_\parallel^* \cdot \mathbf{n})$ and $\bar{v}_\parallel = \varepsilon v_\parallel$. All quantities that depend on $v_\parallel$ in the right-hand-side of eq. (5.37) are evaluated at $\bar{v}_\parallel$. Note that because the sign of the $\bar{v}_\parallel$ variable depends on the considered position on the material boundary, it is not

possible to switch the integral in $\bar{v}_\parallel$ and on the surface $\partial\Omega$ in this equation[12]. Last, let us remark that the quantities $\left\langle \Gamma_i^{\partial\Omega}(\mathbf{x},t)\right\rangle_{\partial\Omega}$ and $\left\langle \bar{\Gamma}_e^{\partial\Omega}(\mathbf{x},v_c,t)\right\rangle_{\partial\Omega}$ only depend on time as a result of the successive integrations.

5.5.4 Implementation of the penalized sheath model in the GYSELA framework

The details of the implementation of the penalized sheath model in the GYSELA code are given in appendix C.2. We give a summary of the most important points hereafter.

1. To reflect slow electrons on the limiter surface, it is required to compute the interception of the characteristics with the surface of the limiter. The characteristics are computed in the GYSELA framework by approximating eq. (5.30) using a first order approximation of the integral. The interception point defined in eq. (5.33) can then be computed using a Newton method, and then the reflection of the characteristics foot is given by approximating the integral in eqs. (5.34) and (5.35) with a first order approximation. Note that this step is very costly numerically, as for all characteristics it is required to check whether or not the foot is inside the limiter. Then, for characteristics for which it is the case, the Newton method must be performed to find the interception point with the solid boundary;

2. Once the foot of the reflected characteristics is known, it is required to perform an interpolation of the distribution function at time t, for an opposite value of the parallel velocity $-v_\parallel$. More precisely one has to compute

$$F_e(r,\theta,\varphi,v_\parallel,\mu,t+\Delta t) = F_e(r_i^{**},\theta_j^{**},\varphi,-v_\parallel,\mu,t),$$

   for all characteristic feet (r_i^{**},θ_j^{**}) that are reflected on the solid boundary. Performing this interpolation step requires to have on the same MPI process the value of the distribution function for both velocities $v_\parallel$ and $-v_\parallel$. This remark involved a modification of the usual parallelization scheme of the GYSELA code;

3. In order to perform the aforementioned interpolation step, 2D spline representations of the distribution $F_e(r,\theta,\varphi,v_\parallel,\mu,t)$ has to be constructed for every triplet $(\varphi,v_\parallel,\mu)$. A boundary condition for the spline has therefore to be specified in the limiter since the electron distribution function is undefined in the solid boundary (there are by definition no electrons there). A possible boundary condition that ensures a smooth interpolation and does not require to rewrite the entire 2D spline representation consists in defining the spline representation on the entirety of the (r,θ) plane—limiter included—and copying adapted chunks of the distribution function in the solid boundary;

[12] This however does not cause any difficulty in the numerical evaluation of eq. (5.37), see appendix C.2

4. As fast electrons should be absorbed in the solid boundary, a relevant boundary condition is imposed in the solid wall to perform the interpolation step for fast electrons while ensuring their absorption on the material boundary. The reflection of slow electrons and absorption of fast electrons creates a discontinuity in the distribution function in the $v_\parallel$ direction. To minimize the interpolation errors created by interpolating a discontinuous distribution function, a smoothing procedure has been introduced between fast and slow electrons;

5. The computation of the electrons and ion fluxes on the surface of the limiter can be easily done by interpolating the distribution functions on the limiter surface (taking the same precautions as detailed in the last two steps above for the electron distribution function to ensure a smooth interpolation), and computing the integral using an appropriate coordinate system on the solid boundary surface.

5.6 Adapting the quasineutrality equation for the penalized sheath model

In this section we describe how to adapt the quasineutrality eq. (5.15) for the penalized sheath model described in section 5.5. We first explain why a kinetic electron response is required in the Scrape-Off Layer, before presenting some necessary adjustments to the quasineutrality equation to account for the limiter.

5.6.1 On the necessity of a fully kinetic electron response in the Scrape-Off Layer

We first recall here the quasineutrality equation expressed within the gyrokinetic framework as

$$-\nabla_\perp \cdot \left(\frac{m_i \bar{n}_{eq,i}}{eZ_i B^2} \nabla_\perp \phi \right) = Z_i \int d^3v \, \mathcal{J} F_i(\mathbf{x}, v_\parallel, \mu, t) - n_e, \tag{5.39}$$

There exist several ways of expressing the electron density n_e. The most important ones are the so-called *adiabatic*, *fully kinetic* and *trapped kinetic* electron responses. These three responses are detailed in appendix C.3. We focus hereafter on the fully-kinetic and trapped kinetic electron responses, the problem of the integration of plasma-wall interaction in the gyrokinetic framework has already been discussed in section 5.1.3. As explained in appendix C.3 the trapped kinetic response considers that trapped electrons—which do not explore the whole poloidal $[0, 2\pi]$ domain—have a kinetic response in the quasineutrality equation, whereas passing electrons are treated as being adiabatic. The main reason for using a trapped-kinetic electron response as compared to a fully kinetic one reads as follows. When magnetic fluctuations are not taken into account, and the electron response is considered fully-kinetic, spurious modes appear when evolving the electrostatic potential in time. These modes due to passing electrons correspond to the electrostatic limit of Alfvén waves, and are called ω_H modes [143]. To get rid of these spurious modes, two solutions can be imagined. The first one

consists in solving an Ampère equation along with the quasineutrality equation to solve electromagnetic fluctuations, effectively resulting in the damping of the ω_H modes. For the inclusion of an Ampère solver in the GYSELA code the reader can see [144]. The other solution consists in using a trapped-kinetic response for electrons, that does not allow for the growth of spurious ω_H modes. In the following, we however show that a fully-kinetic response of electrons is required in the Scrape-Off Layer.

Electron response with poloidal variations of the ion density

Let us consider a tokamak magnetic geometry. The magnetic field can be approximated as

$$\mathbf{B} = B_0 \left(\frac{r}{qR} \mathbf{e}_\theta + \frac{R_0}{R} \mathbf{e}_\varphi \right),$$

where $R = R_0 + r\cos\theta$ with a the minor radius and R_0 the major radius of the device. The safety factor q measures the helicity of the field lines and is defined in eq. (1.14). In the limit of a large aspect ratio $a/R_0 \ll 1$, the norm of the magnetic field is approximately constant since in this case

$$\|\mathbf{B}\|^2 = B_0^2 \left(\frac{r^2}{q^2 R^2} + \frac{R^2}{R_0^2} \right) \approx B_0^2,$$

indeed, $r \ll R$ and $R \approx R_0$ in this case. Given that the norm of the magnetic field is constant, the mirror force $-\mu \mathbf{b} \cdot \nabla B$ vanishes thus all particles can be considered passing. We investigate in the following the electric potential computed from the quasineutrality equation in the simplified magnetic geometry presented above. In particular we are interested in the electric potential response when significant poloidal gradients of the ion and electron densities exist. This is of interest since in the sheath-limited Scrape-Off Layer, one expects the density at the limiter/divertor target to be approximately half of the upstream density, see [23]. We consider a plasma with an ion gyrocenter density that depends on the poloidal angle as

$$n_{Gi} = n_0 \left(1 + \cos\theta\right), \tag{5.40}$$

where n_0 is a constant. We consider singly-charged ions $Z_i = 1$ and a constant plasma temperature $T_e = T_i = T_0$. Let us further suppose that at initial time $t = 0$ the electron density is slightly perturbed from the ion gyrocenter density, such that

$$n_e = n_0 \left(1 + (1 - \varepsilon)\cos\theta\right), \tag{5.41}$$

with ε a small parameter. To simplify the calculations we suppose that the plasma is homogeneous in both radial and toroidal directions. Thus the potential resulting from a mismatch between the electron and ion gyrocenter densities will only depend on the poloidal angle, i.e. $\phi(\theta)$. The perpendicular Laplacian operator is therefore $\nabla_\perp = \partial_\theta / r$ with r the considered radial position.

With the fully-kinetic electron response: the quasineutrality equation can be rewritten as

$$-\frac{m_i n_0}{e(rB_0)^2}\partial_{\theta\theta}\phi = n_0\varepsilon\cos\theta, \tag{5.42}$$

Which gives after double integration

$$\phi = \frac{e\varepsilon(rB_0)^2}{m_i}\cos\theta + K\theta + Q. \tag{5.43}$$

The periodicity condition in the poloidal direction imposes that $K = 0$, while Q is simply the flux surface average of the potential $Q = \langle\phi\rangle$. With the present magnetic geometry this average is simply $\langle\cdot\rangle = \int_0^{2\pi}\cdot\, d\theta/2\pi$. Thus one obtains

$$\phi = \frac{e\varepsilon r^2 B_0^2}{m_i}\cos\theta + \langle\phi\rangle\,. \tag{5.44}$$

With the trapped-kinetic electron response: as the norm of the magnetic field is constant, all electrons are passing. Thus one obtains from flux-surface averaging the electron density given in eq. (5.41) the quantity $\langle n_e^{\text{pass.}}\rangle = n_0$. The quasineutrality equation can therefore be rewritten as

$$-\frac{m_i n_0}{e(rB_0)^2}\partial_{\theta\theta}\tilde{\phi} + \frac{en_0}{T_0}\tilde{\phi} = 0, \tag{5.45}$$

where we have defined the fluctuations of the potential as $\tilde{\phi} = \phi - \langle\phi\rangle$. Integrating eq. (5.45) yields

$$\phi = \langle\phi\rangle + Ae^{\gamma_0\theta} + Be^{-\gamma_0\theta}, \tag{5.46}$$

with

$$\gamma_0 = \frac{erB_0}{\sqrt{m_i T_0}}.$$

The periodicity condition in the poloidal direction gives $A = B = 0$.

The main difference between the potentials obtained with the fully-kinetic electron and trapped kinetic response is that in the fully-kinetic model, the potential exhibits a poloidal variation and is in phase with the poloidal variation of the ion gyrocenter density. This variation of the electric potential translates into an electric field that tends to confine electrons to regions of high ion density, so that the plasma remains quasineutral. On the contrary, when the electron response is trapped-kinetic, the electric potential does not depend on the poloidal angle. Thus electrons are free to travel to low ion density regions, breaking quasineutrality. To further highlight this difference, let us write a fluid equation that expresses the conservation of electron momentum in the parallel direction. By neglecting momentum transfer with adjacent field lines, collisional interaction with ions, assuming steady state and neglecting the

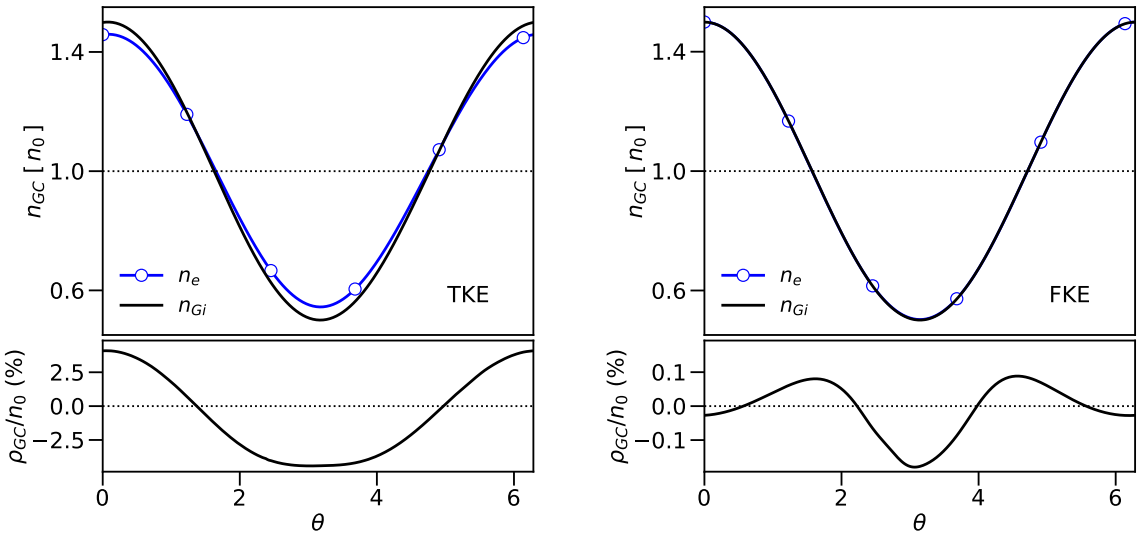

Figure 5.8: Top graphs: electron and ion gyrocenter densities n_e and n_{Gi}, bottom graphs: gyrocenter charge density $\rho_{GC} = n_{Gi} - n_e$ expressed in percentage of the equilibrium density n_0 defined in eq. (5.40). On the left the simulation is performed with a trapped-kinetic electron response (TKE) while on the right the response is fully-kinetic (FKE).

inertia of electrons compared to the electron pressure $p_e \gg \frac{1}{2} m_e n_e u_e^2$ the momentum conservation equation given in eq. (3.12) reduces to

$$e n_e \nabla_\parallel \phi = \nabla_\parallel p_e. \tag{5.47}$$

When the plasma is axisymmetric $\nabla_\parallel \propto \partial_\theta$, therefore with the model introduced above when the electric potential has no poloidal variation the volumetric force balance eq. (5.47) cannot be satisfied. We illustrate this fact in the GYSELA framework by performing a 5D gyrokinetic simulation of an axisymmetric plasma initialized with an equal electron and ion density given by eq. (5.40). The minor radius is set by $1/\rho^* = a/\rho_i = 150$, and the aspect ratio is $R_0/a = 3$. We perform two simulations, one with fully-kinetic electron response and the other with trapped-kinetic electron response. On fig. 5.8 the gyrocenter densities and charge densities are plotted at time $t = 20\Omega_{ci}^{-1}$ as a function of the poloidal angle. We clearly see that the trapped-kinetic response on the left leads to larger gyrocenter charge densities as compared to the fully-kinetic response on the right. The ratio of the maximum gyrocenter charge density between the two electron responses is approximately $\max \rho_{GC}^{\mathrm{TKE}} / \max \rho_{GC}^{\mathrm{FKE}} \approx 25$. Let us remark that the aspect ratio used in the simulation is not very large, thus some electrons are trapped on the low field side of the plasma. These electrons are therefore treated with a kinetic response when computing the electron density in the quasineutrality equation, with the trapped-kinetic electron model. These trapped electrons can therefore contribute to the establishement of an electric field with a poloidal variation that tends to confine electrons to regions of high ion density, in a similar fashion to the electron dynamic in the fully-kinetic model. This effect seems however not to be suffi-

cient to ensure quasineutrality within the plasma. As a conclusion, it seems important to consider a kinetic response for electrons as soon as non-negligible poloidal gradients exist. In particular, taking into account a kinetic response for passing particles seems to be crucial so as to ensure that the plasma stays quasineutral.

5.6.2 Adapting the quasineutrality equation for the immersed limiter

Given the analysis of the previous section, one cannot use a trapped-kinetic electron response in the Scrape-Off Layer. Indeed, the physics at play at the plasma boundary leads to the formation of gradients in the poloidal direction. In order to ensure quasineutrality within the SOL region, a fully kinetic electron model is required there. Two solutions are possible.
The first one is the simplest and consists in using a fully kinetic electron response in the entirety of the simulation domain. To account for the fact that the limiter is immersed within the simulation domain, the quasineutrality equation with the fully-kinetic electron response is modified such that

$$-\nabla_\perp \cdot \left(\frac{m_i \bar{n}_{eq,i}}{e Z_i B^2} \nabla_\perp \phi \right) = \left(Z_i \int d^3v \, \mathcal{J} F_i - n_e \right) \times (1 - \mathcal{H}_{\text{lim}}), \tag{5.48}$$

where we introduced the discontinuous limiter mask $\mathcal{H}_{\text{lim}}$ as

$$\mathcal{H}_{\text{lim}}(r, \theta) = \begin{cases} 1 & \text{if} \quad r \cos(\theta - \theta_{\text{lim}}) > r_{\text{sep}}, \\ 0 & \text{otherwise.} \end{cases} \tag{5.49}$$

This mask equals unity in the limiter, and vanishes in the plasma. Note that it is different from the limiter mask $\mathcal{M}_{\text{lim}}$ defined in eq. (5.27) that transitions smoothly from zero in the plasma to one in the limiter region. The reason for using a different mask in the quasineutrality and in the penalization term for ions in eq. (5.23) reads as follows. The ion dynamics is resolved by solving the gyrokinetic equation in the limiter, however there are no electrons in the limiter, given that they are either reflected or absorbed at the limiter surface. The charge density in the interior of the limiter is therefore quite high since there are no electrons there. We thus hide this charge density by introducing the steep mask $\mathcal{H}_{\text{lim}}$ that defines the limiter in the electron sense[13]. Last, let us remark that the definition of the $\bar{n}_{\text{eq},i}$ density that appears in the polarization term in eq. (5.48) is not so straightfoward in the Scrape-Off Layer. In the core, $\bar{n}_{\text{eq},i}$ is the equilibrium ion density on a given magnetic flux surface. In the Scrape-Off Layer given that magnetic flux surfaces intercept the plasma solid boundary, this definition cannot be applied. The alternative definition is to use the density averaged over the flux surface without the limiter, i.e.

$$\bar{n}_{\text{eq},i} = \int_{\text{FS}} n_i \left(1 - \mathcal{H}_{\text{lim}}\right), \tag{5.50}$$

[13]For electrons, the definition of the limiter is $r \cos(\theta - \theta_{\text{lim}}) > r_{\text{sep}}$, given that a smooth definition of the limiter surface cannot be used to reflect electrons, see section 5.5.2.

where the $\int_{\text{FS}}$ refers to the integration over a magnetic flux surface.
The alternative solution consists in modifying the trapped-kinetic electron model so as to give a fully kinetic response for electrons in the Scrape-Off Layer only. We present this solution here. Let us first recall that the trapped-kinetic electron model is described in appendix C.3. The expression of the trapped electron density is

$$n_e^{\text{trap.}}(r,\theta,\varphi) = \int_0^{+\infty} d\mu \int_{-v_\parallel^\pm}^{v_\parallel^\pm} dv_\parallel 2\pi B_\parallel^* F_e(r,\theta,\varphi,\mu,v_\parallel). \tag{5.51}$$

The cutoff velocity $v_\parallel^\pm$ discriminates trapped electrons for which $|v_\parallel| \leq v_\parallel^\pm$ and passing electrons for which $|v_\parallel| > v_\parallel^\pm$. To give a fully-kinetic response to electrons in the Scrape-Off Layer, the definition of the usual trapped-passing boundary $v_\parallel^\pm$ is modified as

$$v_\parallel^\pm = \sqrt{\frac{2\mu}{m_e}\left(B_{\max}(r) - B(r,\theta)\right)}\left(1 - \mathcal{H}_{\text{SOL}}\right) + \mathcal{H}_{\text{SOL}} v_\parallel^{\max}. \tag{5.52}$$

Where the $v_\parallel^{\max}$ velocity is the highest parallel velocity resolved in the code, and $\mathcal{H}_{\text{SOL}}$ is a mask that defines the Scrape-Off Layer region. Two options are available for the definition of this mask: either to use a discontinuous mask similar to the one given in eq. (5.49), or a smooth mask such as the one given in eq. (5.27). With this modified version of the trapped-kinetic electron response it should be possible to perform a turbulent simulation encompassing both core and Scrape-Off Layer regions.

5.7 Results and discussion

In this section we perform GYSELA simulations encompassing both core and Scrape-Off Layer using the penalized limiter model described in section 5.5. We first show that the limiter surface effectively acts as required; it reflects slow electrons and absorbs fast ones. The penalization operator acting on ions results in the limiter being a sink of particles, momentum and energy.

5.7.1 Simulation without quasineutrality equation

We first perform a simulation by solving the gyrokinetic equation given in eq. (5.5) for both ion and electron gyrocenter distribution functions, without solving the quasineutrality equation, hence $\mathbf{E} = 0$ in the plasma. The simulation is axisymmetric with respect to the toroidal direction. The parameters used in this reference simulation are visible in Table 5.2. The separatrix is located at normalized radius $\rho_{\text{sep}} = r_{\text{sep}}/r_{\max} = 0.8$, so that the core extends from $\rho = r/r_{\max} = 0$ up to ρ_{sep}, and the $\rho \in [0.8, 1.]$ region stands for the Scrape-off Layer. The limiter is located at a poloidal angle $\theta_{\text{lim}} = 3\pi/2$. Note that any limiter angle could have been used instead.

$1/\rho^*$	A	N_r	N_θ	$N_{v_\parallel}$	N_μ	$\mu_{\max}$	$v_{\max}$	ν_0^*	m_i/m_e	$\rho_{\max}$	ρ_{sep}	θ_{lim}
150	3	127	256	127	64	20	5	0.1	100	1	0.8	$3\pi/2$

Table 5.2: Reference simulation parameters. The ν_0^* coefficient defines the plasma collisionality, $\rho^* = \rho_i/a$ defines the radial extent the plasma, and $A = R_0/a$ is the aspect ratio. The safety factor is positive in the whole simulation domain. The timestep used in the simulation is $\Delta t = 1$.

Electron reflection on the limiter surface

To highlight the correct implementation of the reflection procedure for electrons on the surface of the limiter we consider a fixed cutoff velocity $v_c = \frac{1}{6}v_{\max} \approx 1.67\, v_{T_0 e}$ with $v_{T_0 e} = \sqrt{T_0/m_e}$ the electron thermal velocity. The distribution function for both species is initialized as a Maxwellian with uniform density and temperature $n_0 = 1$, $T_0 = 1$ at the initial time. On fig. 5.9 the electron distribution function F_e is plotted at a given radial position in the Scrape-Off Layer $\rho = 0.85$, as a function of the angle $\theta_{\text{lim}} - \theta$ $[2\pi]$ and parallel velocity $v_\parallel$. Two plots are visible, that correspond to two different values of the magnetic moment $\mu = 0$ (top graph) and $\mu = 10.2$ (bottom graph). The simulation has been evolved up to $t = 15\Omega_{ci}^{-1}$ only, to highlight the selective reflection procedure for electrons.
On both graphs, electrons with positive parallel velocities travel towards increasing values of the poloidal angle—i.e. towards the right part of the graphs—as the safety factor is positive everywhere in the simulation domain. Looking first at the top graph for $\mu = 0$, we see that

1. On the rightmost side of the limiter: electrons with parallel velocities $0 \leq v_\parallel \leq v_c$, i.e. generalized parallel velocities $0 \leq \overline{v}_\parallel \leq v_c$ are reflected in the plasma when their trajectories intercept the limiter surface. The reflection procedure is highlighted by the white arrow.

2. On the rightmost side of the limiter, electrons with velocities $v_\parallel \geq v_c$, are absorbed when their trajectories intercept the limiter surface. This absorption creates a gap in phase space for velocities $v_\parallel \leq -v_c$ and angle $\theta - \theta_{\text{lim}}$ approximately in the range [4.6, 6]. Note that the selective absorption of fast electrons creates two discontinuities in the distribution function. The first one is found at $v_\parallel = v_c$, and is horizontal on the figure. This discontinuity is smoothened by the procedure described in appendix C.2, and as such, no interpolation error can be found close to $v_\parallel \approx v_c$. Interpolation errors can be spotted easily on a logarithmic scale graph, as one of their consequence is the appearance of negative values that are represented in white on the figures. The second discontinuity can be found close to the dotted red line on fig. 5.9, top graph. This discontinuity originates from the initialization of the distribution function, that is Maxwellian everywhere

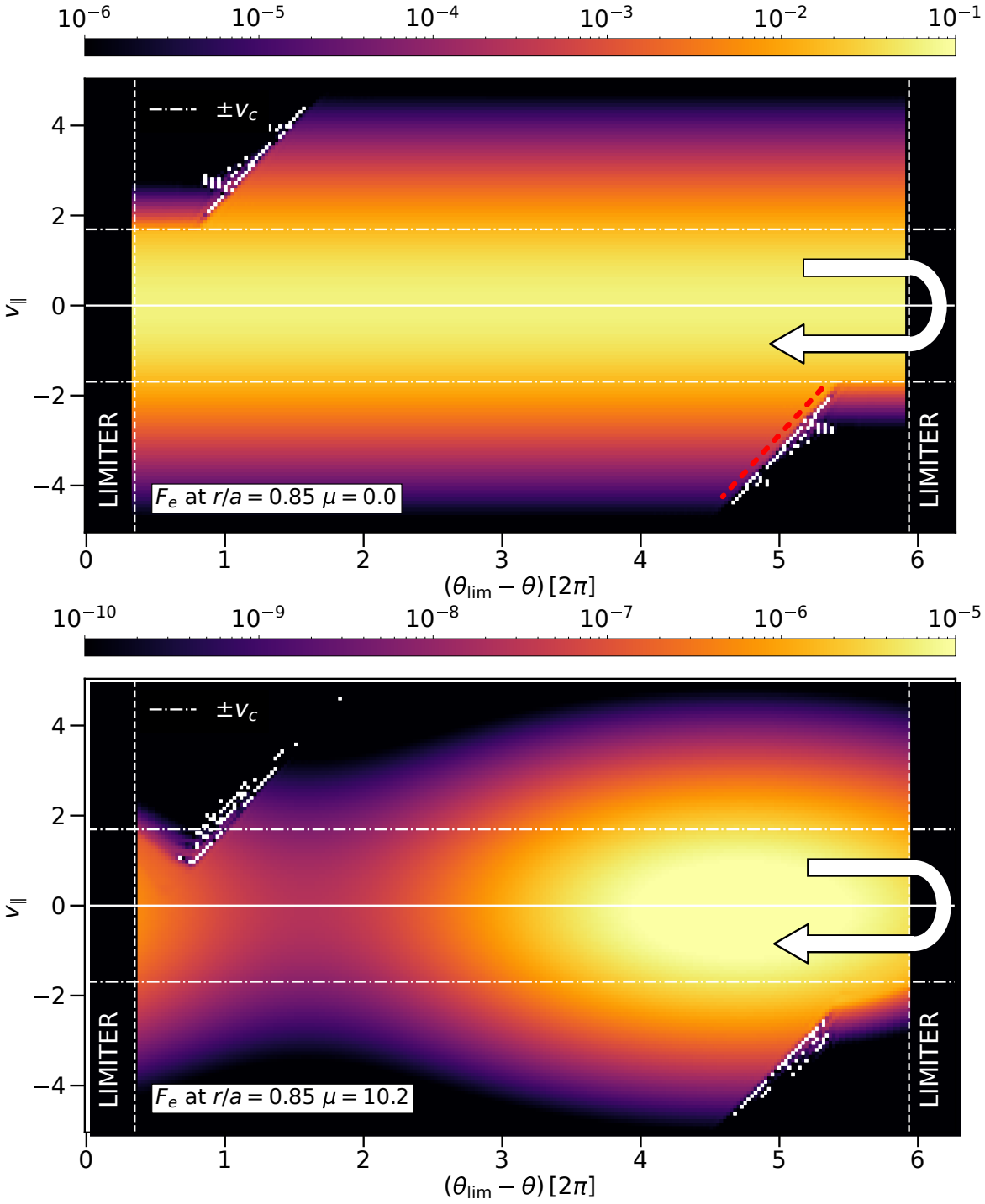

Figure 5.9: Electron distribution function at time $t = 15\Omega_{ci}^{-1}$, for $\mu = 0$ (top graph) and $\mu = 10.2$ (bottom graph), with the simulation parameters presented in Table 5.2. The maximum of the electron distribution function for $\mu = 10.2$ is located where the magnetic field is the weakest, i.e. at $\theta = 0$, since $\theta_{\rm lim} = 3\pi/2$.

at time $t = 0$, even in the region of phase space $v_\parallel < -v_c$. This discontinuity gets tilted as the simulation time increases. It is not smoothened by the procedure described in appendix C.2 as the negative values remain small compared to the values of the distribution function (typically the ratio between the largest negative value in absolute value and the maximum value of the distribution function is close to 10^{-4}, for all values of μ).

3. On the leftmost part of the limiter, the situation is almost the symmetrical of the one described on the rightmost part of the limiter. The two sides of the limiter are however not perfectly symmetrical due to the toroidal geometry of the magnetic configuration.

Looking now at the bottom graph of fig. 5.9, we observe a similar dynamics for electrons with magnetic moment $\mu = 10.2$ compared to $\mu = 0$: slow electrons are reflected on the surface of both sides of the limiter, while fast electrons are absorbed. Similarly to the $\mu = 0$ case, the initial Maxwellian value of the distribution function leads to negative values that propagate inside the plasma. The main difference between the $\mu = 0$ and $\mu = 10.2$ cases lies in the fact that electrons for $\mu = 10.2$ are subject to the mirror force $-\mu\nabla B$. We thus see that on the low field side of the device around $\theta = 0$, i.e. $\theta - \theta_{\text{lim}}\ [2\pi] \approx 3\pi/2$ more electrons can be found as compared to the high field side of the device $\theta - \theta_{\text{lim}}\ [2\pi] \approx \pi/2$. To summarize, the reflection and selective absorption procedure implemented for electrons interacts with the electron trajectories at the surface of the limiter as expected. Slow electrons are reflected into the plasma, while fast ones are absorbed in the limiter volume. This selective absorption leads to a discontinuity in the $v_\parallel$ direction, that is smoothened by the procedure described in appendix C.2. The initial Maxwellian distribution function results in a discontinuity with small negative values that propagate within the plasma. Last, let us note that the smoothing results in the presence of electrons with velocities $\bar{v}_\parallel < -v_c$ in the vicinity of the limiter. This re-injection of fast electrons does not impact significantly the value of the electron flux at the surface of the limiter.

Ion absorption in the limiter

The gyrocenter ion density is plotted on fig. 5.10, in the poloidal plane on the left graph, and as a function of the angle $\theta - \theta_{\text{lim}}$ on the right graph, for several values of the normalized radius ρ. The simulation time is $t = 15\,\Omega_{\text{ci}}^{-1}$. The ion distribution function is penalized in the limiter volume using the infinite penalization operator described in section 5.5.1. The infinite penalization boundary condition is defined in eq. (5.28). The target gyrocenter density for the limiter volume is set to $n_{\text{lim}} = 10^{-2}$ in the target Maxwellian given in eq. (5.24). As can be seen on fig. 5.10, left graph the gyrocenter ion density drops from a close-to-unity value in the plasma—the initial distribution functions at $t = 0$ have a unitary density and are radially and poloidally symmetric—to a value close to $n_{\text{lim}} = 10^{-2}$ in the limiter volume, as expected. The penalized limiter mask has a steepness of $d_{\text{lim}} = 3\Delta r/r_{\text{max}} \approx 0.023$,

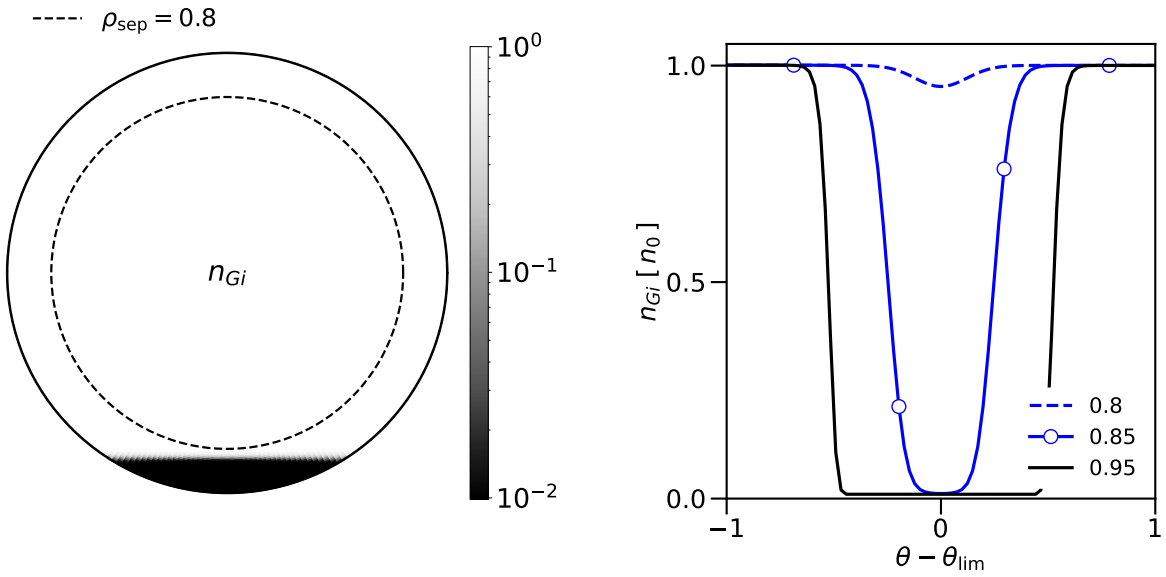

Figure 5.10: Left: ion gyrocenter density n_{Gi} in the poloidal plane, at time $t = 15\,\Omega_{ci}$. Right: ion gyrocenter density at different values of the normalized radius $\rho = r/r_{max}$, as a function of the angle $\theta - \theta_{lim}$ in the vicinity of the limiter.

with $\Delta r = a/N_r$. The penalized limiter appears to be shifted with respect to the separatrix at $\rho_{sep} = r_{sep}/r_{max} = 0.8$. This is done on purpose, by using a shift $\rho_{shift} = 3d_{lim} > 0$ in the definition of the penalized limiter mask $\mathcal{M}_{lim}$ given in eq. (5.27). The justification of such a shift is the following. As stated in section 5.5.2, the reflection of slow electrons must be performed on the surface of the limiter, which is defined by $r\sin(\theta - \theta_{lim}) = r_{sep}$. With this definition, the limiter is defined unambiguously: during its trajectory, an electron does, or does not intercept the limiter surface. Said differently, an electron whose trajectory satisfies $r\sin(\theta - \theta_{lim}) < r_{sep}$ is left unchanged by the limiter, as this electron does not intercept its surface. The definition of the limiter for the ion species is different, as for this species it is defined through the limiter mask $\mathcal{M}_{lim}$ defined in eq. (5.27). Given that the steepness of the limiter mask d_{lim} is finite, there exists a blurred region where the mask transitions from a vanishing value in the plasma to a unity value in the limiter region. This is a direct consequence of the penalization method. It implies that the infinite penalization operator described in eq. (5.28) has an effect on the ion distribution function even for values of the radius $r\sin(\theta - \theta_{lim}) < r_{sep}$, i.e. the penalization influences the plasma. Given that the main effect of the penalization operator acting on ions is to absorb particles, with a vanishing shift $\rho_{shift} = 0$, some ions are absorbed in the plasma volume above the limiter—above in the sense $r\sin(\theta - \theta_{lim}) < r_{sep}$—whereas electrons are not influenced by the limiter in this region, as explained above. To avoid the build up of a negative charge density at the boundary with the limiter, a strictly positive shift $\rho_{shift} > 0$ is taken. This reduces the absorption of ions in the plasma close to the limiter surface. This shift is clearly visible

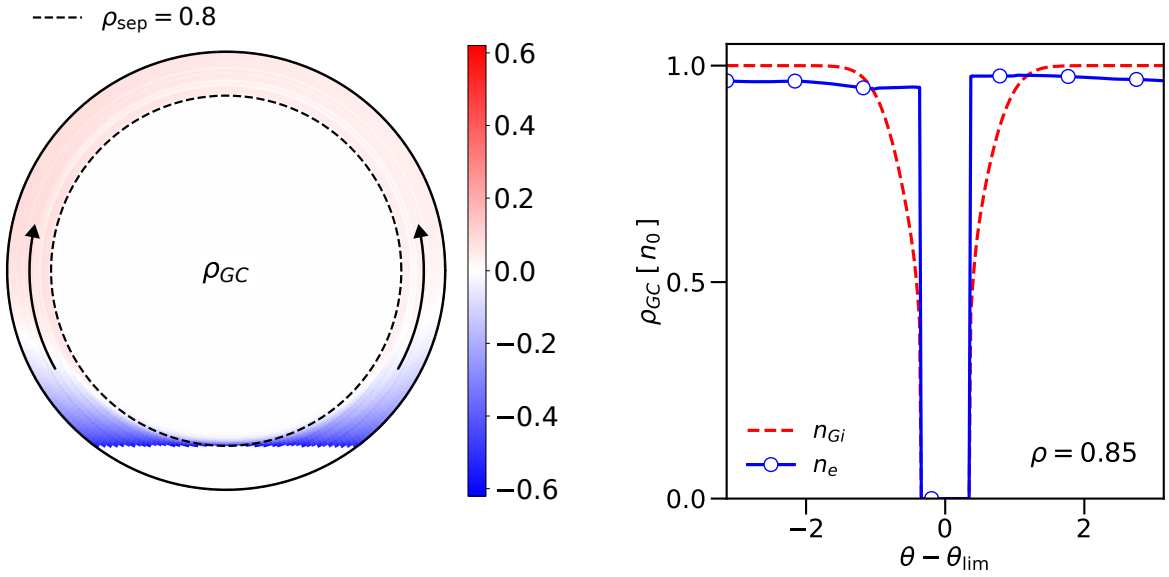

Figure 5.11: Left: gyrocenter charge density in the poloidal plane. Right: gyrocenter ion density and electron density at the normalized radius $\rho = 0.85$ in the Scrape-Off Layer, as a function of the poloidal angle. On both graphs, the gyrocenter charge density $\rho_{\mathrm{GC}} = n_{Gi} - n_e$ has been set to zero in the limiter region in the post-processing phase of the simulation. Thus, on the right graph, the limiter region is defined by the steep transition of the electron density to a vanishing value.

on fig. 5.10, left graph. On the same figure, right graph, we see that the ion gyrocenter density remains close to the initial unity value at normalized radius $\rho_{\mathrm{sep}} = 0.8$, due to the positive parameter $\rho_{\mathrm{shift}} > 0$. For large values of the normalized radius, the gyrocenter ion density drops towards the target value $n_{\mathrm{lim}} = 10^{-2}$ as expected in the limiter volume, with a smooth transition between plasma and limiter regions. Last, note that with the current values of the penalized limiter steepness $d_{\mathrm{lim}} = 3\Delta r / r_{\mathrm{max}}$ and shift $\rho_{\mathrm{shift}} = 3 d_{\mathrm{lim}}$ when increasing the discretization in the radial direction the width of the transition between plasma and penalized limiter region decreases, as does the shift. In the limit of a simulation with a large number of points used to discretize the radial direction the penalized limiter mask converges towards the definition of the limiter for electrons that is infinitely steep.

Gyrocenter charge density

In this section we investigate the gyrocenter charge density defined as $\rho_{GC} = Z_i n_{Gi} - n_e$. The simulation uses the same parameters as the one described in the beginning of section 5.7.1, in particular the quasineutrality equation is not solved hence $\mathbf{E} = 0$ in the simulation domain. The cutoff velocity v_c however is not fixed anymore, but is adapted at each timestep so as to ensure on spatial average over the entire limiter surface the equality of the ion and electron gyrocenter fluxes. The definition of this cutoff velocity

is given in section 5.5. On fig. 5.11 the gyrocenter charge density is represented in the poloidal plane on the left—the simulation is axisymmetric in the toroidal direction. On the right graph the gyrocenter ion density and electron density are represented at several radial locations as functions of the poloidal angle $\theta - \theta_{\text{lim}}$. The charge density and gyrocenter densities have been set to zero in the limiter on both graphs—i.e. for positions $r \sin(\theta - \theta_{\text{lim}}) > r_{\text{sep}}$—during the post-processing phase of the simulation, as the discussion below focuses on the plasma region. The simulation is run until $t = 250\,\Omega_{\text{ci}}^{-1}$. Looking at the left graph of fig. 5.11 we see that the core plasma remains quasineutral, while the Scrape-Off Layer becomes negatively charged in the vicinity of the limiter, while it is positively charged far away from the limiter. We now discuss the reason for this change of sign of the gyrocenter charge density in the Scrape-Off Layer region. Given that the cutoff velocity v_c is adapted at each timestep, the total charge density of the plasma remains close to a vanishing value. Therefore, the negative gyrocenter charge density in the vicinity of the limiter is compensated by the positive gyrocenter charge density in the far-SOL region. Given that the initial state of the system is Maxwellian, and that the limiter absorbs ions that enter the region where the penalization operator is active, a depletion of ions propagates upstream in the Scrape-Off Layer, following the black arrows on fig. 5.11. The front of the depletion region—where the gyrocenter charge density flips sign—propagates in the parallel direction with a velocity close to the ion thermal velocity. The absorption of ions in the limiter volume is compensated by the absorption of the fastest electrons at the surface of the limiter. Given that these absorbed electrons have a larger parallel velocity than the majority of ions—because of their light inertia—the depletion of electrons propagates upstream very rapidly as compared to the depletion front of ions. Thus, the Scrape-Off Layer region far from the limiter appears positively charged, as this region is depleted from fast electrons, whereas the ions in this far-SOL region have not yet been influenced by the limiter. The vicinity of the limiter is also depleted of fast electrons, but most importantly, of ions, and thus appears as negatively charged. This fact can be seen as well on the right graph of fig. 5.11, where the ion density drops close to the limiter, whereas the electron density remains approximately constant in the whole Scrape-Off Layer.

What the present simulation shows is that when including a model for plasma-wall interaction within a global gyrokinetic simulation without solving the quasineutrality equation, large charge densities appear in the Scrape-Off Layer. This is the direct consequence of the inertia difference between ions and electrons, and of the selective absorption of fast electrons. Solving the quasineutrality equation for the electric potential is therefore required so as to ensure that ions and electrons interact through a Coulomb-like force and that no charge density appears on scales comparable to the parallel connection length as it is the case in the simulation investigated in the present section.

5.7.2 Simulation with quasineutrality equation

We now describe GYSELA simulations performed with the flux-averaged sheath model and the adaptation of the quasineutrality equation for the limiter described in section 5.6.2. We perform two simulations with different discretizations of the $v_\parallel$ dimension. The first simulation is performed with $N_v = 128$ points in the $v_\parallel$ dimension, while and the second one is performed with $N_v = 512$ points. A critical feature of the flux-averaged sheath model is that it must ensure that quasineutrality holds in the plasma. So as to test the validity of this feature in the simulation, we plot on fig. 5.12 the gyrocenter electron and ion fluxes on the surface of the limiter, for the $N_v = 128$ simulation on the left and for the $N_v = 512$ simulation on the right. More precisely, the graph shows

1. The time evolution of the gyrocenter ion flux averaged over the limiter surface $\left\langle \Gamma_i^{\partial\Omega} \right\rangle_{\partial\Omega}$. We recall that the gyrocenter flux of species s computed at a given point on the surface of the limiter $\Gamma_i^{\partial\Omega}$ is defined in eq. (5.16). The average over the limiter surface $\langle\cdot\rangle_{\partial\Omega}$ is defined in eq. (5.36) and eq. (C.25);

2. The time evolution of two partial electron fluxes averaged over the limiter surface $\left\langle \bar{\Gamma}_e^{\partial\Omega+} \right\rangle_{\partial\Omega}$ and $\left\langle \bar{\Gamma}_e^{\partial\Omega-} \right\rangle_{\partial\Omega}$. These quantities are defined as follows. Given a positive velocity $v_{\parallel 0}$ and a spatial coordinate on the surface of the limiter $\mathbf{x}$, the partial flux of electrons with generalized parallel velocities $\bar{v}_\parallel > -v_{\parallel 0}$ written $\bar{\Gamma}_e^{\partial\Omega}(\mathbf{x}, v_{\parallel 0}, t)$ is defined in eq. (5.18)[14]. The precise definition of the generalized parallel velocity $\bar{v}_\parallel$ is given in section 5.3.2. Let us consider a cutoff velocity v_c a solution of eq. (5.37), i.e. a cutoff velocity that matches the limiter-averaged flux of ions and the limiter-averaged partial flux of electrons at time t as

$$\left\langle \Gamma_i^{\partial\Omega} \right\rangle_{\partial\Omega}(t) = \left\langle \bar{\Gamma}_e^{\partial\Omega} \right\rangle_{\partial\Omega}(v_c, t). \tag{5.53}$$

   Let us write $\left\{ v_{\parallel k} = k\Delta v_\parallel \right\}$ the discretization of the $v_\parallel$ dimension, with $-\lfloor N_v/2 \rfloor \geq k \leq \lfloor N_v/2 \rfloor$ a relative integer, $\Delta v_\parallel = 2v_{\max}/N_v$ and $v_{\max}$ is the maximum parallel velocity resolved by the code. In general, the parallel velocity v_c solution of eq. (5.53) does not coincide with a grid point $v_{\parallel k}$. Thus there exists an integer $k_0 \geq 0$ which is such that

$$\left\langle \bar{\Gamma}_e^{\partial\Omega} \right\rangle_{\partial\Omega}(v_{\parallel k_0}, t) \leq \left\langle \Gamma_i^{\partial\Omega} \right\rangle_{\partial\Omega}(t) < \left\langle \bar{\Gamma}_e^{\partial\Omega} \right\rangle_{\partial\Omega}(v_{\parallel k_0+1}, t). \tag{5.54}$$

   The $\left\langle \bar{\Gamma}_e^{\partial\Omega+} \right\rangle_{\partial\Omega}$ and $\left\langle \bar{\Gamma}_e^{\partial\Omega-} \right\rangle_{\partial\Omega}$ quantities are thus defined as

$$\left\langle \bar{\Gamma}_e^{\partial\Omega+} \right\rangle_{\partial\Omega}(t) = \left\langle \bar{\Gamma}_e^{\partial\Omega} \right\rangle_{\partial\Omega}(v_{\parallel k_0}, t), \tag{5.55}$$

$$\left\langle \bar{\Gamma}_e^{\partial\Omega-} \right\rangle_{\partial\Omega}(t) = \left\langle \bar{\Gamma}_e^{\partial\Omega} \right\rangle_{\partial\Omega}(v_{\parallel k_0+1}, t). \tag{5.56}$$

[14] Note that even though the quantity $\bar{\Gamma}_e^{\partial\Omega}$ has the dimensionality of a particle flux, it depends on the parallel velocity. Indeed, this quantity stands for the flux of electrons directed towards the limiter with velocities higher than a certain threshold.

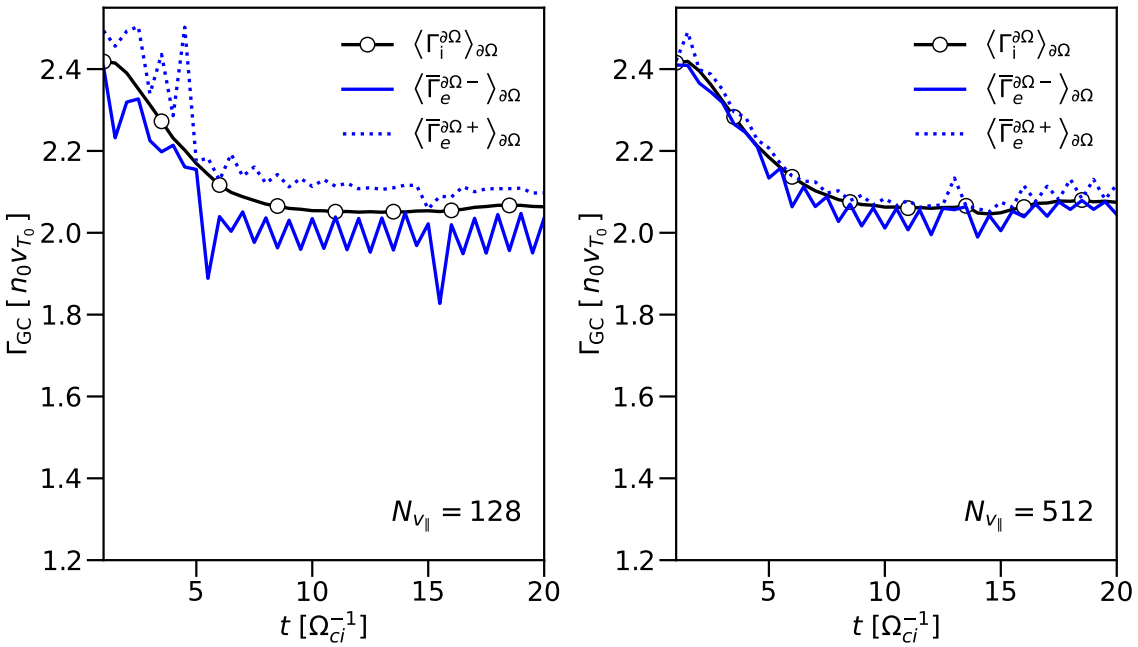

Figure 5.12: Time evolution of the gyrocenter ion flux averaged on the surface of the limiter $\langle \Gamma_i^{\partial\Omega} \rangle_{\partial\Omega}$, and of the partial electron fluxes $\langle \bar{\Gamma}_e^{\partial\Omega+} \rangle_{\partial\Omega}$ and $\langle \bar{\Gamma}_e^{\partial\Omega-} \rangle_{\partial\Omega}$. On the left graph, the simulation is run with $N_v = 128$ points in the $v_\parallel$ direction and on the right $N_v = 512$. Note that both simulations are initialized with a ion gyrocenter distribution function shifted towards positive generalized parallel velocities in the vicinity of the limiter. This explains why the limiter-averaged ion gyrocenter flux is strictly positive at the beginning of the plotted time interval.

Thus the $\langle \bar{\Gamma}_e^{\partial\Omega+} \rangle_{\partial\Omega}$ represents the partial flux of electrons on the limiter surface that overestimates the ion flux on the limiter surface, obtained by taking a cutoff velocity slightly lower than what would be obtained by solving eq. (5.53). The $\langle \bar{\Gamma}_e^{\partial\Omega-} \rangle_{\partial\Omega}$ represents the partial flux of electrons on the limiter surface that underestimates the ion flux on the limiter surface. Note that the cutoff velocity used to reflect or absorb electrons on the limiter surface has to lie on a point of the mesh used to discretize the parallel velocity dimension. Indeed, when performing the reflection of the electron characteristics on the limiter surface described in section 5.5.2, the parallel velocity used to compute the characteristic foot remains constant during the (r, θ) advection, and lies on a grid point. One has therefore to choose for each grid point of the parallel velocity mesh and each electron characteristics that intercepts the limiter whether the characteristics should be reflected on the limiter surface—slow electrons—or if the corresponding particles should be absorbed in the limiter—fast electrons.

Looking at fig. 5.12 we see that (i) in both $N_v = 128$ and $N_v = 512$ cases the limiter-averaged gyrocenter ion flux $\langle \Gamma_i^{\partial\Omega} \rangle_{\partial\Omega}$ is bounded by the two partial electron fluxes $\langle \bar{\Gamma}_e^{\partial\Omega+} \rangle_{\partial\Omega}$ and $\langle \bar{\Gamma}_e^{\partial\Omega-} \rangle_{\partial\Omega}$, and the inequality given in eq. (5.54) is fulfilled at all times.

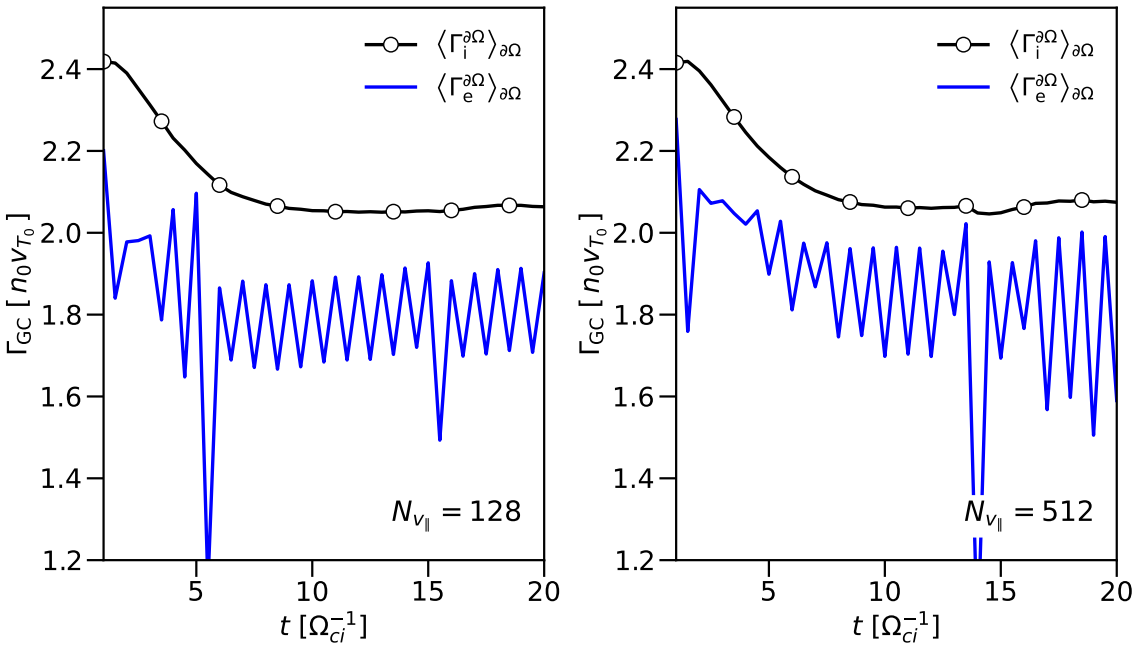

Figure 5.13: Time evolution of the gyrocenter ion and electron flux averaged on the surface of the limiter $\langle\Gamma_i^{\partial\Omega}\rangle_{\partial\Omega}$ and $\langle\Gamma_e^{\partial\Omega}\rangle_{\partial\Omega}$. Simulation with $N_v = 128$ on the left graph, and $N_v = 512$ on the right.

In both cases the partial electron fluxes stay close to the limiter-averaged gyrocenter ion flux. More importantly, when refining the discretization of the velocity dimension, the limiter-averaged gyrocenter ion flux and the partial electron fluxes match with a better precision. This is expected, given that the finer the discretization of the $v_\parallel$ dimension, the better the solution of eq. (5.53) can be approximated with a cutoff velocity that lies on a grid point.

Even though the ion and electron gyrocenter fluxes appear to be well matched by the computation of the cutoff velocity as shown on fig. 5.12, we are unable to run the simulation after a time $t \approx 100\,\Omega_{\mathrm{ci}}{}^{-1}$[15]. As the number of iterations performed by the code increases, a negative charge develops on the surface of the limiter, builds up over time and eventually leads to the breakdown of quasineutrality. This behavior appears to be independent of the discretization of the poloidal plane, μ dimension and of the timestep—the discretization of the toroidal direction does not play a role either given that the cases considered in the present section are axisymmetric. More interestingly, refining the mesh discretization in the parallel velocity direction does not allow for higher simulation times. To illustrate this point and the negative charge that appears on the limiter surface, we plot on fig. 5.13 the time evolution of the limiter-averaged gyrocenter ion and electron fluxes. The ion flux $\langle\Gamma_i^{\partial\Omega}\rangle_{\partial\Omega}$ is essentially the

[15]This simulation end time is an approximation and may vary with simulation parameters such as the minor radius, etc.

same quantity as the one plotted on fig. 5.12. The quantity $\left\langle \Gamma_e^{\partial\Omega} \right\rangle_{\partial\Omega}$ is defined by eq. (5.16) and represents the electron flux averaged over the limiter surface—with no cutoff, contrary to the $\left\langle \bar{\Gamma}_e^{\partial\Omega+} \right\rangle_{\partial\Omega}$ and $\left\langle \bar{\Gamma}_e^{\partial\Omega-} \right\rangle_{\partial\Omega}$ quantities plotted on fig. 5.12. Another difference is that the $\left\langle \Gamma_i^{\partial\Omega} \right\rangle_{\partial\Omega}$ and $\left\langle \Gamma_e^{\partial\Omega} \right\rangle_{\partial\Omega}$ fluxes plotted on fig. 5.13 are computed at different locations in the code with respect to the splitting scheme as compared to the quantities represented on fig. 5.12. More precisely

1. Before the (r, θ) advection—that we abusively refer to as the *poloidal advection* step in the following—the quantities $\left\langle \Gamma_i^{\partial\Omega} \right\rangle_{\partial\Omega}$ and $\left\langle \bar{\Gamma}_e^{\partial\Omega-} \right\rangle_{\partial\Omega}$ visible on fig. 5.12 are computed. This defines a cutoff velocity v_c;
2. During the poloidal advection slow electrons with generalized parallel velocities $\bar{v}_\parallel < v_c$ are reflected on the surface of the limiter;
3. After the poloidal advection, the quantities $\left\langle \Gamma_i^{\partial\Omega} \right\rangle_{\partial\Omega}$ and $\left\langle \Gamma_e^{\partial\Omega} \right\rangle_{\partial\Omega}$ represented on fig. 5.13 are computed. Given that ions have a high inertia, the ion flux $\left\langle \Gamma_i^{\partial\Omega} \right\rangle_{\partial\Omega}$ computed in this step is approximately the same as the one computed in step 1. described above.

The electron flux $\left\langle \Gamma_e^{\partial\Omega} \right\rangle_{\partial\Omega}$ computed in step 3. above represents the surface-averaged flux of electrons that cross the limiter after the poloidal advection. If the cutoff procedure for fast electrons were to be effective in the poloidal advection step 2. above, then the $\left\langle \Gamma_i^{\partial\Omega} \right\rangle_{\partial\Omega}$ and $\left\langle \Gamma_e^{\partial\Omega} \right\rangle_{\partial\Omega}$ quantities should remain close when computed in step 3—indeed after step 3 the electron distribution function on the surface of the limiter is already truncated for fast electrons $\bar{v}_\parallel < -v_c$. On fig. 5.13 we see a clear imbalance between the limiter-averaged ion and electron fluxes. The quantity $\left\langle \Gamma_e^{\partial\Omega} \right\rangle_{\partial\Omega}$ is systematically lower than the limiter-averaged ion flux $\left\langle \Gamma_i^{\partial\Omega} \right\rangle_{\partial\Omega}$. Increasing by a factor of four the number of points in the parallel velocity direction does not lead to a significant reduction of the mismatch between the two fluxes. We believe that this mismatch is the cause for the crash of the simulations. The oscillations of the electron fluxes that can be observed on fig. 5.12 are found again on fig. 5.13 in an amplified fashion. When refining the discretization in the parallel velocity dimension, the amplitude of these oscillations appears to increase. The cause for the mismatch between the electron and ion gyrocenter fluxes is not clear yet. Note that it is not due to the choice of either the $\left\langle \Gamma_e^{\partial\Omega+} \right\rangle_{\partial\Omega}$ or $\left\langle \Gamma_e^{\partial\Omega-} \right\rangle_{\partial\Omega}$ quantities as a definition for the cutoff velocity. Said differently, in either cases where the limiter-averaged ion flux is (i) overestimated by the partial electron flux $\left\langle \Gamma_e^{\partial\Omega+} \right\rangle_{\partial\Omega}$ or (ii) underestimated by $\left\langle \Gamma_e^{\partial\Omega-} \right\rangle_{\partial\Omega}$ we observe a mismatch $\left\langle \Gamma_e^{\partial\Omega} \right\rangle_{\partial\Omega} < \left\langle \Gamma_i^{\partial\Omega} \right\rangle_{\partial\Omega}$ when computing these quantities during step 3. described above.

5.8 Conclusion of the chapter

In the present chapter we introduced some necessary elements to include a plasma-wall interaction model valid in the GYSELA code. More precisely, the model is compatible with (i) global simulations encompassing all three core-edge-Scrape-Off Layer

regions, (ii) immersed boundary conditions and (iii) Backward semi-Lagrangian numerical schemes. The present *flux-averaged* sheath model shares similarities with the *logical* and *conducting* sheath approaches, in the sense that it enables for the material boundary to absorb all incoming ions, and a fraction of the fastest electrons. The slowest electrons are reflected back in the plasma. All these models ensure that quasineutrality holds within the plasma, without solving the characteristic time and spatial scales of the sheath. The *flux-averaged* sheath model differs from the logical and conducting approaches in the sense that the electron and ion fluxes are matched on spatial average over the entire material boundary surface. More precisely, with the analysis developed in the above sections

1. We have introduced a simple penalization operator that acts as a sink of particles, momentum and energy for ions which is localized in the limiter region;
2. We have described a reflection procedure for electrons that is compatible with Backward semi-Lagragian numerical schemes. The procedure takes advantage of the computation of the characteristics feet required to update the distribution function in time, by reflecting the slow electron trajectories on the material boundary surface;
3. We have depicted a new technique for computing the cutoff velocity that distinguishes between slow and fast electrons, based on matching the electron and gyrocenter ion fluxes on spatial average over the entire limiter surface.

The penalization operator for ions and the selective reflection procedure for electrons have been shown to perform as required, see section 5.7.1. As explained in section 5.7.2 the aforementioned procedure for computing the cutoff velocity does not however lead to the electron and ion fluxes matching accurately enough on the limiter surface, and the simulation cannot reach time long enough for turbulence to be studied. We list hereafter a few remarks concerning the difficulty of performing such simulations.

1. While subgrid models for gyrokinetic plasma-wall interaction have been tested in various codes and give satisfactory results—see [93, 123] for the logical and conducting sheath approaches—, the present work is the first attempt at introducing such a model in the Backward semi-Lagrangian framework, with a penalized limiter. The mismatch of the electron and ion flux observed in the simulation could be a consequence of the subgrid model being incompatible with the penalization, with the semi-Lagrangian framework, or relate to the splitting procedure becoming questionable.
2. The limiter being immersed in the simulation domain raises some difficulties for solving the quasineutrality equation properly. Even though the adaptation of the quasineutrality solver described in section 5.6.2 seems to allow for performing short simulations with an immersed limiter, it is not clear whether or not the flux mismatch is the result of the limiter being immersed in the region where quasineutrality is solved.

3. Last, a thorough assessment of the convergence of the flux-averaged sheath technique with the timestep and the discretization of phase space is at the moment difficult because of the increase in computational time due to the reflection of slow electrons—each characteristics has to be checked to intercept the limiter, and then reflected if needed. An optimization of this reflection procedure would certainly help assessing whether or not the flux-averaged sheath technique is faulty or viable.

Generally speaking, going from a core-only gyrokinetic simulation—or a core, edge and Scrape-Off Layer gyrokinetic simulation with adiabatic electrons—to a global core-edge-SOL simulation with kinetic electrons is a big step. Breaking this step into smaller chunks would help, even though they would require more work. In particular, working in a simplified gyrokinetic Scrape-Off Layer only geometry with no immersed boundary conditions—hence a material boundary located on the edge of the resolved model would enable for testing the flux-averaged sheath method in the Backward semi-Lagrangian frawework and comparing it with techniques such as the conducting sheath, that has proven to be relevant in edge gyrokinetic codes. Lastly, a general criticism that can be addressed to the flux-averaged sheath is that it does not ensure that the mismatch between the electron and ion fluxes on the surface of the limiter will remain bounded and close to zero over time. With the simulations investigated in section 5.7.2 the mismatch is for instance always negative. More generally, such a mismatch will always be non-vanishing due to the finite number of grid points used to discretize the parallel velocity dimension. If the mismatch is always of the same sign—for instance, an additional small fraction of electrons gets reinjected in the simulation compared to the strict equality of electron and ion fluxes—the quasineutrality of the plasma may become invalid on the long run. The question is whether this drift of the error can be kept small so a statistically converged turbulence regime can be achieved before quasineutrality breaks down[16].

[16]Concerning this last point and from the author's current understanding, the conducting sheath may allow for achieving the compensation of the mismatch between electron and ion fluxes on the limiter surface. Indeed, in this framework any polarization of the plasma results in a modification of the electric potential at the material boundary, which thus in turn results in the adaptation of the electron and ion fluxes. While this statement is not a proper proof that the conducting allows for no drift of the mismatch error over time, it shows at least that such an auto-corrective feedback loop may exist and could be the reason for the conducting sheath to have proven usable in turbulent edge gyrokinetic simulations.

6

Conclusion

The present work aims at improving the description of the edge plasma region in the gyrokinetic framework, and in particular in the GYSELA code. One of the main players in the Scrape-Off Layer region that influences key observables such as turbulence levels is the interaction between the plasma and the target plates at the extremities of magnetic field lines. In this thesis, we have proposed a model for plasma-wall interaction that ensures quasineutrality of the plasma without solving the characteristic time and spatial scales of the sheath—that are incompatible with assumptions of the gyrokinetic theory. The model relies on immersed boundary conditions, is compatible with Backward semi-Lagrangian numerical schemes, and could be adapted to other numerical schemes such as the Lagrangian or Eulerian schemes.

Prior to describing such a model, the interaction between a plasma and a solid surface has been investigated by means of the two-dimensional (one dimension of space and one dimension of velocity) VOICE kinetic code. A particularity of the code is that uses immersed boundary conditions to model the wall region. The kinetic Vlasov-Poisson model describes a single magnetic field line that intercepts the solid wall at normal incidence in both of its ends. The case of oblique incidence could be investigated in future work, but does not modify the prescribed subgrid sheath model described in the present work. Curvature effects of the magnetic field and interactions with adjacent field lines are neglected. Non-uniform spline interpolation has been investigated within the VOICE code, showing that this scheme helps in reducing the memory requirement of a simulation. We have investigated two different penalized wall models that either allow—in the conducting wall model—or forbid—in the insulating wall model—charge sources to exist within the wall region. When no charge source exists within the wall, the penalized operator active in the wall region mimics a recombination process. In this case a negative charge develops in the wall, of greater magnitude than when allowing charge sources to exist in the wall. In this latter case the penalization operator can absorb each and every ion and electron that enters the wall region, provided the strength of the operator is high enough. The immersed boundary condition technique proved to be robust in the sense that with both wall models, we retrieve key aspects of the Debye sheath physics. A positively charged region of a few Debye lengths wide develops in front of the walls, which is reminiscent of a Debye sheath. This boundary region is accompanied by a drop of the electric potential, that accelerates ions and

reflects a portion of the slowest electrons in the plasma. Due to this selective electron absorption, the electron and ion fluxes match at the plasma boundary on timescales typically larger than the inverse of the electron plasma frequency. We retrieve a fundamental feature of plasma-wall interaction: it ensures that quasineutrality holds within the plasma on scales larger than the Debye length. We performed scans of relevant parameters such as the electron-to-ion mass ratio, electron temperature and magnetic connection length, and by doing so we assessed the dependence of the sheath potential drop with these parameters. By comparing this drop with an analytic prediction derived from a simple sheath model, we showed that there exist discrepancies between the prediction and the simulated potential drop. The discrepancies can be attributed to the departure of the electron distribution function from a Maxwellian state, and to the presence of fast electrons at the entrance of the sheath that are re-emitted from the wall region. This re-emission of electrons is more important in the insulating wall case compared to the conducting wall, given that with the former model more electrons can be found in the wall region as compared to the latter. More generally, the re-emission of fast electrons can be attributed to (i) collisional reorganization processes at play in the sheath region, (ii) to the finite strength of the penalization operator in the conducting wall case, and (iii) to the presence of electrons in the wall region in the insulating wall case. On the contrary to the insulating wall model, the electron re-emission in the conducting wall framework can be controlled and reduced by increasing the strength of the penalization operator and the steepness of the mask that defines the transition between the plasma and the wall region, at the cost of a reduced timestep and finer discretization. The conducting wall model thus appeared as more relevant to describe plasma-wall interaction as compared to the insulating wall model.

We then investigated kinetic features of simulations performed in the conducting wall framework using predictions obtained from the hierarchy of fluid equations. Even with the simple kinetic model considered here—1D-1V Vlasov-Poisson system with collisions—spatial variations of fluid quantities in the kinetic simulation revealed to be not straightforward to predict in the fluid framework. Total heat flux levels—electron plus ions—measured in the kinetic simulation revealed to account for nearly 30% of the total energy flux. The electron heat flux accounts for nearly 50% of the electron energy flux. Such heat flux levels can only be explained by collisional reorganization of distribution functions between the source region—modelling the region where particles are injected as a result of cross-field transport—and the wall region where they are absorbed. Collisional processes tend to drive the system back to thermal equilibrium, whereas the injection of particles by the source and the sheath physics at play in the wall region pushes the system away from such thermal equilibrium. Collisions further appear as a key mechanism in the simulation in the sense that without this mechanism no steady state can be reached. The competition between collisions and the source and sheath physics results in a complex self-organization of the plasma in steady state. This self-organization is difficult to capture within the fluid framework. Computing the sheath heat transmission factors when such steady state is reached shows that the

electron and ion factors obtained in the simulation exceed the prediction by 35% and 60% respectively. These increased values with respect to the prediction are directly caused by kinetic effects, in particular the fact that at the entrance of the sheath the ion distribution function is not a Maxwellian shifted towards positive velocities and the electron distribution function is not a Maxwellian truncated for fast electrons coming back from the wall region. As stated above, as a result of the kinetic physics at play, the variations of fluid quantities in the plasma obtained by integrating the distribution function against powers of the velocity variables reveal difficult to predict in the fluid framework. In particular, the prescription of a closure for the fluid hierarchy—on either the heat flux or a higher-order moment—that allows for retrieving the kinetic features of the simulation did not prove conclusive. A strong implication of this fact is that the spatial variation of the Mach number in the kinetic simulation does not enable for retrieving the marginal Bohm criterion $M = u_i/c_s = 1$ at the entrance of the sheath. Moreover, depending on the chosen closure scheme, the expression of the speed of sound waves c_s changes. This observation may have implications for fluid codes, that usually impose the Bohm criterion $M \geq 1$ at the plasma facing units—where one is especially interested in assessing particle and heat flux levels correctly. In general fluid codes do not take an expression for the speed of sound that is compatible with the closure scheme used to solve the hierarchy of fluid equations. We detailed in the corresponding section a technique that could in principle be adapted to a three-dimensional geometry to compute a speed of sound coherent with a given closure scheme. From a kinetic standpoint, the Bohm criterion does not appear as a condition that bears any predictive capability for a kinetic code. The problem is mainly that the expression of the speed of sound waves is *a priori* unknown in the kinetic framework. We investigate the validity of the vanishing heat flux closure by performing high collisionality simulations. At high-collisionalities, distribution functions remain close to Maxwellians and thus heat flux levels are small. One could therefore reasonably expect the fluid prediction for the speed of sound derived when considering a vanishing heat flux to be valid. However, even at collisionalities 5×10^4 times higher than usual sheath-limited Scrape-Off Layer conditions, we do not retrieve the marginal Bohm criterion $M = 1$ at the entrance of the sheath.

So as to prepare for future extension of the edge description of the GYSELA code to describe the dynamics of plasma-neutral interaction, we detailed a pressure-diffusion fluid model for neutral particles that could be adapted to the gyrokinetic framework. Through the rewriting of the `Fortran 90` version of the VOICE code in the `C++` language, we implemented and tested the pressure-diffusive fluid model for neutrals. We detailed in particular the coupling between the fluid model for neutrals and the kinetic description of the plasma through a source term added to the Vlasov equation. This work has been performed partly through the supervision of the internship of a second-year Master student. Running simple proof-of-concept GPU simulations of plasma with the neutral model highlights qualitative modifications of the plasma behavior as compared to a reference simulation without neutrals. More precisely, in the investi-

gated regime where ionization is dominant, this reaction leads to the build-up of plasma density in front of the immersed wall region. Given that the source term added to the Vlasov equation to couple the plasma and neutral dynamics has a vanishing momentum, the ionization process leads to a decrease of the ion Mach number in the vicinity of the wall. One can reasonably expect this behavior to change when considering improvements for the coupling between plasma and neutrals. One of these improvements would consists in modifying the coupling term so as to account for momentum transfer.

Last, we presented a new approach that enables including the most important feature of plasma-wall interaction—the fact that it ensures quasineutrality in the plasma on time and spatial scales larger than the electron plasma frequency and Debye length—in the gyrokinetic framework. This sheath model is *subgrid* in the sense that it does not resolve the characteristic spatial and time scales of the sheath layer. This subgrid model shares similarities with the already existing *logical* and *conducting* sheath approaches, that we reviewed and that are models for plasma-wall interaction valid in the gyrokinetic framework. The main difference between our present model—that we called *flux-averaged* sheath—and the logical and conducting approaches lies in the way the cutoff velocity that distinguishes between slow (reflected) and fast (absorbed) electrons is computed. So as to constrain the dynamics of the quasineutral plasma as little as possible, we proposed to compute this threshold velocity so that on spatial average over the entire limiter surface the electron and ion fluxes are equal. We detailed how to perform such a computation of the cutoff velocity. The present flux-averaged sheath model is compatible with immersed boundary conditions. A penalization operator active in the material boundary region stands as a sink of particles, momentum and energy for ions. A reflection procedure for slow electrons on the material boundary surface has been described, which is compatible with Backward semi-Lagragian schemes and that could be adapted to other numerical schemes. This reflection proved to be the most complicated feature of the flux-averaged sheath model as it involves reflecting the characteristics of electrons on the surface of the material boundary, and modifying the boundary condition used for the interpolation step required by Backward semi-Lagrangian schemes. We carefully detailed in appendices the implementation of such flux-averaged sheath model. Overall, the flux-averaged sheath model has exhibited the expected behavior concerning the absorption of ions in the limiter volume, the reflection of slow electrons and the absorption of fast electrons at the limiter surface. Even though the cutoff velocity was computed at each timestep to ensure the equality of the gyrocenter ion and electron particles fluxes, a mismatch was observed between these two quantities after the poloidal advection process, where the reflection of slow electrons is implemented. This mismatch was such that too many electrons were reflected into the quasineutral plasma, which lead to the breakdown of quasineutrality on short timescales compared to turbulent timescales. The origin of such a mismatch remains yet unclear. We detail possible origins of such a mismatch in section 5.8.

Overall, improving the description of the edge and Scrape-Off Layer regions in gy-

rokinetic codes is of great interest since properties of turbulence and transport at the separatrix in tokamak plasmas are influenced by the physics at play in these regions. The Scrape-Off Layer is by nature a difficult region to handle from the gyrokinetic standpoint since (i) key assumptions of the gyrokinetic theory may become invalidated in the Scrape-Off Layer and (ii) the physics at play at the plasma-wall interface cannot be directly resolved by means of the gyrokinetic theory. Such physics is however crucial for setting the dynamics of the Scrape-Off Layer and edge regions. The interaction between the plasma and its material boundaries ensures that quasineutrality remains valid on time and spatial scales described by the gyrokinetic theory—and sets the radial electric field in sheath-limited Scrape-Off Layer regimes—while the interaction between charged and neutral particles influences greatly heat and particle fluxes at the target plates. So as to embark these crucial pieces of edge physics in gyrokinetic codes, plasma-wall and plasma-neutral interactions must be described by means of efficient and robust models. Regarding plasma-wall interaction investigated in detail in the present work, the most important feature to be recovered in the gyrokinetic framework, as explained above, is the quasineutrality of the plasma. More precisely, the present work showed that the procedure used to compute the cutoff velocity that distinguishes reflected and absorbed electrons must be accompanied by means of assessing the precision and convergence of such a method. In particular, a nice improvement of the flux-averaged sheath would consist in ensuring that the mismatch between the electron and ion gyrocenter fluxes at the material boundary surface compensates over time, so as to ensure that turbulent simulations can be performed on timescales comparable with the energy confinement time. The development of such verification tools and autocorrection methods is still ongoing work in the Gysela framework, but stands as a crucial step, so that subgrid plasma-wall interaction models can influence the edge physics as expected, without hampering the efficiency and convergence of the code. In the perspective of porting the Gysela code to the `c++` programming language, this involves in particular designing simple test cases for gyrokinetic plasma-wall interaction, for instance in simplified cylindrical geometries or in reduced 4D drift kinetic dimensionalities.

Bibliography

[1] Y. Munschy *et al.* 2024 *Nuclear Fusion* 64 056027.
[2] Y. Munschy *et al.* 2024 *Nuclear Fusion* 64 046013.
[3] E. Bourne *et al.* 2023 *Journal of Computational Physics* 488 112229.
[4] G. Dif-Pradalier *et al.* 2022 *Communications Physics* 5.
[5] S. M. Motevalli and F. Fadaei 2015 *Zeitschrift für Naturforschung A* 70 79–84.
[6] F. Belloni 2021 *Plasma Physics and Controlled Fusion* 63 055020.
[7] Wikipedia contributors. *Nuclear binding energy*. Accessed 20-Aug-2024.
[8] J. Lawson 1955 *Atomic Energy Research Establishment*.
[9] M. Greenwald 2002 *Plasma Physics and Controlled Fusion* 44 R27.
[10] J. M. Rax *Physique des tokamaks*, Editions de l'Ecole polytechnique, 2011.
[11] P. C. Liewer 1985 *Nuclear Fusion* 25 543.
[12] X. Garbet, 2023, HAL lecture.
[13] E. Westerhof 2012 *Fusion Science and Technology* 61 312–319.
[14] P. Helander *Collisional Transport in Magnetized Plasmas*, 2005.
[15] Nuclear Info website Accessed: 2024-04-23.
[16] X. Garbet *et al.* 2010 *Nuclear Fusion* 50 043002.
[17] W. M. Tang and V. S. Chan 2005 *Plasma Physics and Controlled Fusion* 47 R1.
[18] Y. Idomura *et al.* 2006 *Comptes Rendus. Physique* 7 650–669.
[19] L. Villard *et al.* 2004 *Plasma Physics and Controlled Fusion* 46 B51.
[20] B. Kadomtsev and O. Pogutse 1971 *Nuclear Fusion* 11 67.
[21] T. Eich *et al.* 2013 *Nuclear Fusion* 53 093031.
[22] *Summary of the ITER Final Design Report*, IAEA, Vienna, 2001.
[23] P. C. Stangeby *The Plasma Boundary of Magnetic Fusion Devices*, 2000.
[24] R. Pitts *et al.* 2019 *Nuclear Materials and Energy* 20 100696.
[25] F. Wagner *et al.* 1982 *Physical Review Letters* 49 1408–1412.
[26] P. Lang *et al.* 2013 *Nuclear Fusion* 53 043004.
[27] J. Kinsey *et al.* 2011 *Nuclear Fusion* 51 083001.
[28] H. Zohm 1996 *Plasma Physics and Controlled Fusion* 38 105.
[29] A. W. Leonard 2014 *Physics of Plasmas* 21 090501.
[30] D. Whyte *et al.* 2010 *Nuclear Fusion* 50 105005.
[31] C. M. Greenfield *et al.* 2001 *Phys. Rev. Lett.* 86 4544–4547.
[32] A. J. Brizard and T. S. Hahm 2007 *Rev. Mod. Phys.* 79 421–468.
[33] S. Ku *et al.* 2009 *Nuclear Fusion* 49 115021.

[34] P. H. Diamond *et al.* 2005 *Plasma Physics and Controlled Fusion* 47 R35.
[35] B. N. Rogers *et al.* 2000 *Phys. Rev. Lett.* 85 5336–5339.
[36] Y. Sarazin *et al.* 2010 *Nuclear Fusion* 50 054004.
[37] Wikipedia contributors. *Exascale computing*. Accessed 23-Aug-2024.
[38] *The DDC library*. Github repo. accessed 23-Aug-2024.
[39] *The Kokkos library*. Accessed 23-Aug-2024.
[40] *The GoogleTest framework*. Accessed 23-Aug-2024.
[41] V. Grandgirard *et al.* 2016 *Computer Physics Communications* 207 35–68.
[42] R. Chodura 1982 *The Physics of Fluids* 25 1628–1633.
[43] A. Paredes *et al.* 2014 *Journal of Computational Physics* 274 283–298.
[44] P. Ghendrih *et al.* 2011 *Plasma Physics and Controlled Fusion* 53 54019.
[45] P. L. Bhatnagar *et al.* 1954 *Physical Review* 94 511–525.
[46] D. R. Nicholson *Introduction to plasma theory*, John Wiley & Sons, 1983.
[47] G. Dif-Pradalier *et al.* 2011 *Physics of Plasmas* 18 62309.
[48] D. Estève *et al.* 2015 *Physics of Plasmas* 22 122506.
[49] E. Sonnendrücker *et al.* 1999 *J. Comput. Phys.* 149 201–220.
[50] G. Manfredi *et al.* 2010 *Plasma Physics and Controlled Fusion* 53 015012.
[51] B. Afeyan *et al.* 2014 *The European Physical Journal D* 68 295.
[52] F. M. Poli 2018 *Physics of Plasmas* 25 055602.
[53] V. Zhdanov *Transport Processes in Multicomponent Plasma*, CRC Press, 2002.
[54] S. Wiesen *et al.* 2015 *Journal of Nuclear Materials* 463 480–484.
[55] N. Rivals *et al.* 2022 *Contributions to Plasma Physics* 62 e202100182.
[56] H. Bufferand *et al.* 2021 *Nuclear Fusion* 61 116052.
[57] A. Taroni *et al.* 1995 *Journal of Nuclear Materials* 220-222 1086–1090.
[58] M. Giacomin *et al.* 2022 *Journal of Computational Physics* 463 111294.
[59] B. Dudson *et al.* 2009 *Computer Physics Communications* 180 1467–1480.
[60] M. Wiesenberger and M. Held 2020 *Nuclear Fusion* 60 096018.
[61] A. Stegmeir *et al.* 2018 *Plasma Physics and Controlled Fusion* 60 035005.
[62] H. Bufferand *et al.* 2019 *Nuclear Materials and Energy* 18 82–86.
[63] E. Serre *et al.* 2012 *Contributions to Plasma Physics* 52 401–405.
[64] N. Li *et al.* 2018 *Computer Physics Communications* 228 69–82.
[65] M. Z. Tokar' 1994 *Contributions to Plasma Physics* 34 139–144.
[66] J. Loizu *et al.* 2012 *Physics of Plasmas* 19 122307.
[67] D. Bohm *The Characteristics of Electrical Discharges in Magnetic Fields*, p 77, 1949.
[68] G. W. Hammett and F. W. Perkins 1990 *Phys. Rev. Lett.* 64 3019–3022.
[69] Y. Sarazin *et al.* 2009 *Plasma Physics and Controlled Fusion* 51 115003.
[70] P. Ghendrih *et al.* 2011 *Plasma Physics and Controlled Fusion* 53 054019.
[71] Y. Shimomura *et al.* 1983 *Nuclear Fusion* 23 869.
[72] V. Quadri *et al. Contributions to Plasma Physics* n/a e202300146.
[73] D. Reiter *et al.* 2005 *Fusion Science and Technology* 47 172–186.

[74] N. Horsten *et al.* 2017 *Nuclear Fusion* 57 116043.
[75] M. Umansky *et al.* 2003 *Journal of Nuclear Materials* 313-316 559–563.
[76] J. Riemann *et al.* 2004 *Contributions to Plasma Physics* 44 35–38.
[77] K. Hoshino *et al.* 2008 *Contributions to Plasma Physics* 48 136–140.
[78] M. Furubayashi *et al.* 2009 *Journal of Nuclear Materials* 390-391 295–298.
[79] W. V. Uytven *et al.* 2022 *Nuclear Fusion* 62 086023.
[80] F. Wising *et al.* 1996 *Contributions to Plasma Physics* 36 309–313.
[81] M. E. Rensink *et al.* 1998 *Contributions to Plasma Physics* 38 325–330.
[82] R. Schneider *et al.* 2006 *Contributions to Plasma Physics* 46 3–191.
[83] D. A. Knoll *et al.* 1996 *Physics of Plasmas* 3 293–303.
[84] C. F. F. Karney *et al.* 1998 *Contributions to Plasma Physics* 38 319–324.
[85] G. Dimarco and L. Pareschi 2008 *Multiscale Modeling & Simulation* 6 1169–1197.
[86] H. P. Summers. *The ADAS User Manual, version 2.6.* 2004.
[87] J. Candy *et al.* 2016 *Journal of Computational Physics* 324 73–93.
[88] T. Görler *et al.* 2011 *Journal of Computational Physics* 230 7053–7071.
[89] K. Obrejan *et al.* 2015 *Plasma and Fusion Research* 10 3403042–3403042.
[90] A. Peeters *et al.* 2009 *Computer Physics Communications* 180 2650–2672.
[91] Y. Idomura *et al.* 2008 *Computer Physics Communications* 179 391–403.
[92] S. Jolliet *et al.* 2012 *Journal of Computational Physics* 231 745–758.
[93] E. L. Shi *et al.* 2017 *Journal of Plasma Physics* 83 905830304.
[94] A. Hakim *et al.* 2020 *Physics of Plasmas* 27 042304.
[95] M. Boesl *et al.* 2019 *Physics of Plasmas* 26 122302.
[96] R. Hager *et al.* 2022 *Physics of Plasmas* 29 112308.
[97] M. Dorf and M. Dorr 2021 *Physics of Plasmas* 28 032508.
[98] H. Biglari *et al.* 1990 *Physics of Fluids B: Plasma Physics* 2 1–4.
[99] E. J. Kim and P. H. Diamond 2003 *Phys. Rev. Lett.* 90 185006.
[100] R. C. Wolf 2002 *Plasma Physics and Controlled Fusion* 45 R1.
[101] J. Connor *et al.* 2004 *Nuclear Fusion* 44 R1.
[102] T. Tala *et al.* 2006 *Comptes Rendus. Physique* 7 622–633.
[103] P. W. Terry 2000 *Rev. Mod. Phys.* 72 109–165.
[104] J. Schirmer *et al.* 2006 *Nuclear Fusion* 46 S780.
[105] Y. B. Kim *et al.* 1991 *Physics of Fluids B: Plasma Physics* 3 2050–2060.
[106] S. I. Itoh and K. Itoh 1988 *Phys. Rev. Lett.* 60 2276–2279.
[107] R. W. Brzozowski *et al.* 2019 *Physics of Plasmas* 26 042511.
[108] K. C. Shaing and E. C. Crume 1989 *Phys. Rev. Lett.* 63 2369–2372.
[109] L. Chôné *et al.* 2014 *Physics of Plasmas* 21 070702.
[110] B. D. Scott 2007 *Plasma Physics and Controlled Fusion* 49 S25.
[111] C. P. Ritz *et al.* 1989 *Phys. Rev. Lett.* 62 1844–1847.
[112] X. Garbet and M. Lesur *Gyrokinetics*, Doctoral, 2023.
[113] P. Donnel *et al.* 2020 *Plasma Physics and Controlled Fusion* 63 025006.

[114] G. Dif-Pradalier *et al.* 2009 *Phys. Rev. Lett.* 103 065002.
[115] C. Peskin 2002 *Acta Numerica* 11 479–517.
[116] R. Mittal and G. Iaccarino 2005 *Annu. Rev. Fluid Mech.* 37 239–261.
[117] L. Isoardi *et al.* 2010 *Journal of Computational Physics* 229 2220–2235.
[118] A. Paredes Cabrel *et al.* 2014 *Journal of Computational Physics* 274 283–298.
[119] E. Caschera *et al.* 2018 *Journal of Physics: Conference Series* 1125 12006.
[120] G. Dif-Pradalier *et al.* 2021.
[121] G. D. Giannatale *et al.* 2022 *Journal of Physics: Conference Series* 2397 012002.
[122] C. Holland *et al.* 2011 *Physics of Plasmas* 18 056113–056113.
[123] S. E. Parker *et al.* 1993 *Journal of Computational Physics* 104 41–49.
[124] E. L. Shi *et al.* 2015 *Physics of Plasmas* 22 22504.
[125] S. Ku *et al.* 2016 *Journal of Computational Physics* 315 467–475.
[126] S. Ku *et al.* 2018 *Physics of Plasmas* 25 056107.
[127] C. S. Chang *et al.* 2017 *Phys. Rev. Lett.* 118 175001.
[128] Q. Pan *et al.* 2018 *Physics of Plasmas* 25 062303.
[129] N. R. Mandell *et al.* 2020 *Journal of Plasma Physics* 86 905860109.
[130] F. Halpern *et al.* 2016 *Journal of Computational Physics* 315 388–408.
[131] P. Ulbl *et al.* 2023 *Physics of Plasmas* 30 052507.
[132] G. Merlo *et al.* 2021 *Physics of Plasmas* 28.
[133] J. Cheng *et al.* 2020 *Physics of Plasmas* 27 122510.
[134] J. A. Krommes 2012 *Annual Review of Fluid Mechanics* 44 175–201.
[135] I. P. B. Editors *et al.* 1999 *Nuclear Fusion* 39 2137.
[136] J. Dominski *et al.* 2017 *Physics of Plasmas* 24 022308.
[137] P. Ghendrih *et al.* 2003 *Nuclear Fusion* 43 1013.
[138] V. Grandgirard *et al.* 2006 871.
[139] F. Jenko 2000 *Computer Physics Communications* 125 196–209.
[140] J. Candy and R. E. Waltz 2003 *Phys. Rev. Lett.* 91 045001.
[141] G. Strang 1968 *SIAM Journal on Numerical Analysis* 5 506–517.
[142] G. Latu *et al.* 2018 *Journal of Scientific Computing* 74 1601–1650.
[143] W. Lee 1987 *Journal of Computational Physics* 72 243–269.
[144] C. Gillot. Theses. PhD thesis. Aix Marseille Université, Dec. 2020.
[145] E. R. Harrison and W. B. Thompson 1959 *Proceedings of the Physical Society* 74 145.
[146] K. U. Riemann 1991 *Journal of Physics D: Applied Physics* 24 493–518.

A

Immersed boundary conditions

A.1 Collisions

All of the quantities described in the following are normalized unless the contrary is explicitly specified. The intra species collision operator $\mathcal{C}_{ss}(f_s)$ is defined in eq. (2.16). This operator automatically ensures particle conservation since $\int dv\, \mathcal{C}_{ss}(f_s) = 0$. To furthermore fulfill momentum and kinetic energy conservation, we adjust the fluid moments of the kernel Maxwellian f_{Ms}. We set the density of f_{Ms} as equal to the density of f_s. Then, its two other moments u_{Ms} and T_{Ms} are adapted at each time step and spatial position. More precisely, the two equations $\int dv_s\, v_s \mathcal{C}_{ss}(f_s) = 0$ and $\int dv_s\, v_s^2 \mathcal{C}_{ss} = 0$ are solved for u_{Ms} and T_{Ms}. This gives

$$u_{Ms} = \frac{-\langle v_s D_v\rangle\langle\partial_{v_s}(v_s D_v)\rangle + \langle v_s^2 D_v\rangle\langle\partial_{v_s} D_v\rangle}{\langle v_s D_v\rangle\langle\partial_{v_s} D_v\rangle - \langle D_v\rangle\langle\partial_{v_s}(v D_v)\rangle}, \tag{A.1}$$

$$T_{Ms} = \frac{\langle v_s D_v\rangle^2 - \langle D_v\rangle\langle v_s^2 D_v\rangle}{\langle v_s D_v\rangle\langle\partial_{v_s} D_v\rangle - \langle D_v\rangle\langle\partial_{v_s}(v_s D_v)\rangle}, \tag{A.2}$$

where the bracket notation is defined as the integral against f_s, for instance $\langle D_v\rangle = \int dv_s\, f_s D_v$. Note that these two moments depend on both space and time. In the case where f_s itself is a Maxwellian, then u_M^s and T_{Ms} are its actual mean velocity and temperature. The diffusion coefficient in velocity space D_v depends on the velocity and space variables. It is defined as

$$D_v = D_0 \frac{\Phi - G}{y_s}, \tag{A.3}$$

with $D_0 = 3\sqrt{2\pi}\nu_{ss}^\star T_s/4$ and $y_s = |v_s|/\sqrt{2T_s}$. The Φ and G functions are defined as

$$\Phi(y_s) = \frac{2}{\sqrt{\pi}} \int_0^{y_s} e^{-z^2}\, dz,$$

$$G(y_s) = \frac{\Phi - y_s \Phi'}{2y_s^2}.$$

The self-collision frequency $\nu_{ss}^\star$ is derived from the classical expression of the two-species collisions frequency $\nu_{ss'}^\star$ defined in appendix A.1. This frequency is expressed in normalized units as

$$\nu_{ss'}^\star = \sqrt{A_s}\, Z_s^4\, \frac{n_s}{T_s^{3/2}}. \tag{A.4}$$

See eq. (2.20) for the definition of $\nu_0^\star$. The two species collision operator is defined in eq. (2.17). The inter species collision frequency is written in normalized units as:

$$\nu^\star_{ss'} = \sqrt{2A_s}\frac{n_{s'}Z_s^2Z_{s'}^2}{T_s^{3/2}}\left(1+\frac{A_{s'}}{A_s}\right)\left(1+\frac{A_{s'}T_{s'}}{A_sT_s}\right)^{-3/2} \tag{A.5}$$

The friction term describing the momentum exchange is thus a restoring force proportional to $u_s - u_{s'}$, which consequently vanishes when $u_s = u_{s'}$. Similarly, the energy equipartition term exhibits a thermal equipartition part acting as a restoring force proportional to $T_s - T_{s'}$, hence vanishing when $T_s = T_{s'}$ together with a term describing the energy exchange governed by the momentum exchange. The correctness of the implementation of the collision operator can be checked by deriving the rate of change of thermal energy and mean velocity of a quasineutral plasma homogeneous along the parallel dimension. Indeed, under these circumstances and in the absence of any source term the Boltzmann equation reduces to $\partial_t f_s = C_{ss}(f_s) + C_{ss'}(f_s)$. By integrating this equation against powers of the velocity variable, and combining the resulting equations for both species we obtain in normalized units

$$\partial_t \log\left(u_s - \sqrt{A_{s'}/A_s}u_{s'}\right) = -\nu_{ss'}\left(1+\frac{A_{s'}}{A_s}\right) \tag{A.6}$$

$$\partial_t(T_s - T_{s'}) = -12\nu_{ss'}\frac{A_{s'}}{A_{s'}+A_s}(T_s - T_{s'}) + 2\nu_{ss'}\left(u_s - \sqrt{A_{s'}/A_s}u_{s'}\right)^2. \tag{A.7}$$

These two equations describes the relaxation of both species mean velocities and temperatures towards a common value due to collisional processes. The typical timescale over which this relaxation occurs is controlled by the plasma collisionality parameter $\nu_0^\star$, as the collision frequency $\nu_{ss'}$ is proportional to this parameter—see section 2.4.2. We use these two equations to verify the correct implementation of the collision operator.

A.2 Verification of the code

Verification of the Voice code is provided by checking conservations properties of the plasma, of fluid quantities such as density, temperature, etc. Checking that fluid moments exhibit the correct conservations properties gives confidence in the correct implementation of the numerical scheme, as if one solves a Boltzmann equation correctly, then fluid conservation equations should be automatically satisfied as well. We show below that the electron energy is well conserved in the simulation box. A similar verification has been done concerning the conservation of density and momentum for both species. The equation that expresses the conservation of electron energy is defined in normalized units as

$$\partial_t \mathcal{E}_e + \partial_x Q_e = \Gamma_e \partial_x \phi + C^e_{\mathcal{E}} + S^e_{\mathcal{E}} \tag{A.8}$$

See section 3.1 for the definition of the terms that appear in this equation. All the terms involved in this conservation equations are shown on fig. A.1. The accuracy of

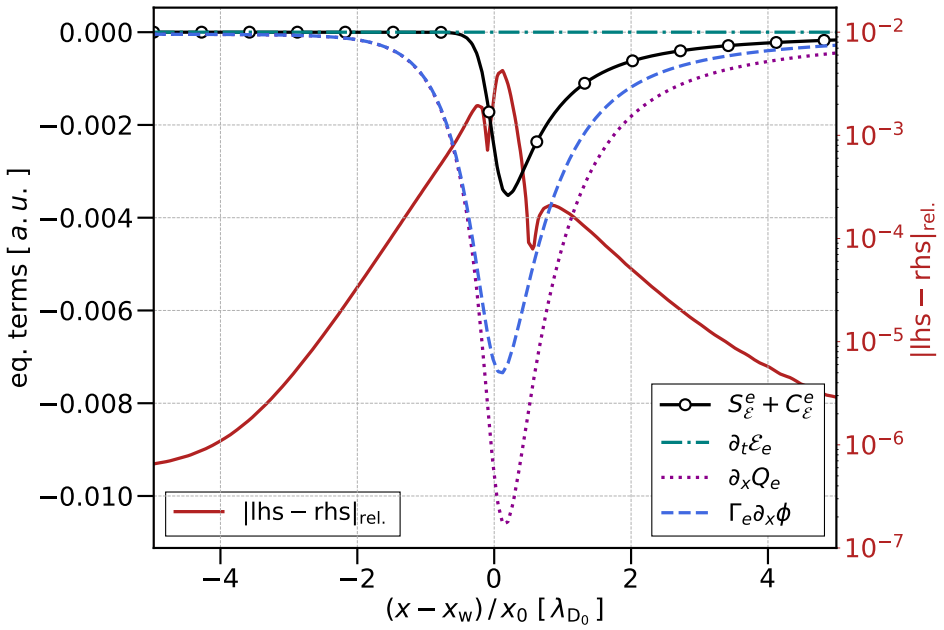

Figure A.1: Conservation of the electron energy in the vicinity of the wall, whose position is denoted by x_w. The magnitude of the normalized error is visible on the right axis.

the simulation can be checked by looking at the value of the relative error term denoted by $|\text{lhs} - \text{rhs}|_{\text{rel.}}$ on the same figure, right axis. This term is computed by substracting the right-hand side part from the left-hand side part of the conservation equation. Then, this term is divided by the maximum value of its constituents. Concretely, for the conservation eq. (A.8) it is defined as

$$|\text{lhs} - \text{rhs}|_{\text{rel.}} = \frac{|\partial_t \mathcal{E}_e + \partial_x Q_e - \Gamma_e \partial_x \phi - C^e_{\mathcal{E}} - S^e_{\mathcal{E}}|}{\max_{x\in[0,L_x]} \{|\partial_t \mathcal{E}_e|, |\partial_x Q_e|, |\Gamma_e \partial_x \phi|, |C^e_{\mathcal{E}}|, |S^e_{\mathcal{E}}|\}},$$

We see on fig. A.1 that this error term never exceeds 10^{-2}, hence the numerical error is under a percent. It is of similar amplitude for the other conservation equations, for both species. Along with assessing the correct conservation property, such a graph allows for checking that the simulation has reached a steady state, as the time derivative term $\partial_t \mathcal{E}_e$ is negligible compared to the other terms that appear in the equation.

A.3 Prediction of the potential drop in the sheath

A.3.1 Classical potential drop prediction

The sheath potential drop prediction detailed below is presented in [23]. Let us consider a perfectly absorbing wall at position x_{w}, bounding a semi infinite plasma located at $x \leq x_{\text{w}}$. The model is one-dimensional in real space and one dimensional in velocity space. We consider the wall to be grounded and to not emit any secondary particles.

In front of the wall a sheath develops to ensure in steady state the equality of ion and electron fluxes. In the following $x_{\rm sh}$ refers to the position of the sheath entrance. The flux of ions computed at this position can be written as

$$\Gamma_{\rm i}^{\rm sh} = n_{\rm i}^{\rm sh} M c_{\rm s}. \tag{A.9}$$

The Mach number M and sound speed velocity $c_{\rm s}$ are taken at the sheath entrance as well. We ignore the effects of collisions in the sheath. Under these assumptions the Hamiltonian function for electrons is simply $H_{\rm e} = \frac{1}{2} m_{\rm e} v^2 - e\phi$. Since this quantity does not explicitly depend on time it is conserved along the electrons trajectories. On a particular trajectory connecting the sheath entrance to the wall we can therefore write that

$$\frac{1}{2} m_{\rm e} v(x_{\rm sh})^2 - e\phi(x_{\rm sh}) = \frac{1}{2} m_{\rm e} v(x_{\rm w})^2 - e\phi(x_{\rm w}),$$

or equivalently

$$v(x_{\rm w})^2 = v(x_{\rm sh})^2 + \frac{2e\Delta\phi_{\rm sh}}{m_{\rm e}}.$$

Here we see that a necessary condition for the electrons to reach the wall is $v(x_{\rm sh}) \geq v_{\rm c} = \sqrt{-2e\Delta\phi_{\rm sh}/m_{\rm e}}$. The electrons that are faster than the velocity $v_{\rm c}$ at the sheath entrance are therefore absorbed in the wall. The rest of the electrons are reflected back into the plasma. Since the wall does no emit any secondary electron, the above calculation shows that there are no electrons with velocities $v(x_{\rm sh}) < -v_{\rm c}$ at the sheath entrance. We therefore assume that the electron distribution function at the sheath entrance is a Maxwellian truncated for velocities $v \leq -v_{\rm c}$. This truncated Maxwellian is characterized by a density $\overline{n}_{\rm e}$ and a temperature $T_{\rm e}^{\rm sh}$. It is written as

$$\begin{aligned} f_{\rm e}(x_{\rm sh}, v) &= \overline{n}_{\rm e} \sqrt{\frac{m_{\rm e}}{2\pi T_{\rm e}^{\rm sh}}}\, e^{-\dfrac{m_{\rm e} v^2}{2T_{\rm e}^{\rm sh}}}\, {\rm H}(v + v_{\rm c}), \\ &= \overline{f_{\rm e}}(v)\, {\rm H}(v + v_{\rm c}), \end{aligned} \tag{A.10}$$

where ${\rm H}(v+v_{\rm c})$ is the Heaviside function that has a value of one when $v \geq -v_{\rm c}$, and zero otherwise. For the sake of compactness of the following computation we introduced the $\overline{f_{\rm e}}$ notation that stands for the non-truncated Maxwellian

$$\overline{f_{\rm e}} = \overline{n}_{\rm e} \sqrt{\frac{m_{\rm e}}{2\pi T_{\rm e}^{\rm sh}}}\, e^{-\dfrac{m_{\rm e} v^2}{2T_{\rm e}^{\rm sh}}}.$$

Note that the quantity $\overline{n}_{\rm e}$ is not the electron density at the sheath entrance $n_{\rm e}^{\rm sh}$. The density at sheath entrance $n_{\rm e}^{\rm sh}$ can be found by integrating against velocity ap-

pendix A.3.1. By doing so, we find

$$\begin{aligned} n_{\mathrm{e}}^{\mathrm{sh}} &= \int_{-v_{\mathrm{c}}}^{+\infty} dv\, \overline{f_{\mathrm{e}}} \\ &= \int_{-\infty}^{+\infty} dv\, \overline{f_{\mathrm{e}}} - \int_{-v_{\mathrm{c}}}^{+\infty} dv\, \overline{f_{\mathrm{e}}} \\ &= \overline{n}_{\mathrm{e}} - \int_{v_{\mathrm{c}}}^{+\infty} dv\, \overline{f_{\mathrm{e}}} \end{aligned}$$

In the following we neglect the contribution of the density of the tail of the electron distribution in the overall electron density at the entrance of the sheath, i.e. we assume that $\overline{n}_{\mathrm{e}} \approx n_{\mathrm{e}}^{\mathrm{sh}}$. In the simulations this assumption is not always valid. We observed nevertheless that taking into account the correct density at the sheath entrance $n_{\mathrm{e}}^{\mathrm{sh}} = \overline{n}_{\mathrm{e}} - n_{\mathrm{e}}(x_{\mathrm{w}})$ did not change noticeably the computed value of the potential drop from the simulations. We therefore consider in the following that $\overline{n}_{\mathrm{e}} \approx n_{\mathrm{e}}^{\mathrm{sh}}$. The expression of the electron flux at the sheath entrance is therefore

$$\begin{aligned} \Gamma_{\mathrm{e}}^{\mathrm{sh}} &= \int_{-v_{\mathrm{c}}}^{+\infty} dv\, v n_e^{\mathrm{sh}} \sqrt{\frac{m_{\mathrm{e}}}{2\pi T_{\mathrm{e}}^{\mathrm{sh}}}} e^{-\frac{m_{\mathrm{e}} v^2}{2T_{\mathrm{e}}^{\mathrm{sh}}}} \\ &= n_{\mathrm{e}}^{\mathrm{sh}} e^{\frac{e\Delta\phi_{\mathrm{sh}}}{T_{\mathrm{e}}^{\mathrm{sh}}}} \sqrt{\frac{T_{\mathrm{e}}^{\mathrm{sh}}}{2\pi m_{\mathrm{e}}}}. \end{aligned} \tag{A.11}$$

By equating the ion flux eq. (A.9) and electron flux appendix A.3.1 we find the classical expression of the potential drop in the sheath region

$$\Delta\phi_{\mathrm{sh}} = \frac{T_{\mathrm{e}}^{\mathrm{sh}}}{2e} \log\left(2\pi \frac{m_{\mathrm{e}}}{m_{\mathrm{i}}} M^2 \left(1 + \frac{T_{\mathrm{i}}^{\mathrm{sh}}}{T_{\mathrm{e}}^{\mathrm{sh}}}\right)\right). \tag{A.12}$$

A.3.2 On the electron re-emission from the wall

When assuming that the wall emits electrons back into the plasma, the prediction for the potential drop that exists in the sheath given in eq. (A.12) is modified. We include this electron re-emission by rewriting the equality of the ion and electron fluxes at the sheath entrance as

$$\Gamma_{\mathrm{i}}^{\mathrm{sh}} = \int_{-v_{\mathrm{c}}}^{+\infty} dv\, v n_e^{\mathrm{sh}} \sqrt{\frac{m_{\mathrm{e}}}{2\pi T_{\mathrm{e}}^{\mathrm{sh}}}} e^{-\frac{m_{\mathrm{e}} v^2}{2T_{\mathrm{e}}^{\mathrm{sh}}}} - \Gamma_{\mathrm{e}}^{-},$$

where the integral corresponds to the electron flux originating from a Maxwellian distribution function truncated for velocities $v \leq -v_c$, and the Γ_{e}^{-} accounts for the flux of

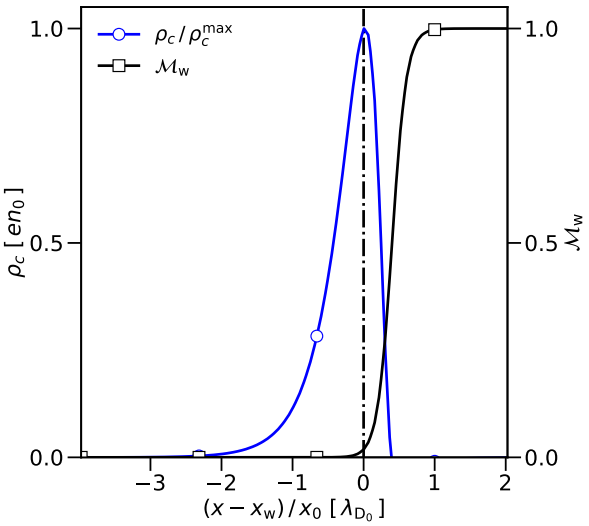

Figure A.2: Charge density $\rho_c = e(n_i - n_e)$ normalized to its maximum $\rho_c^{\max} = \max_x \rho_c$, and wall mask $\mathcal{M}_\mathrm{w}$. The dashed line marks the wall position $x = x_w$.

electron re-emission from the wall at the sheath entrance. This corresponds to a non vanishing electron distribution function for $v \leq -v_c$. That is to say

$$\Gamma_\mathrm{e}^- = -\int_{-\infty}^{-v_\mathrm{c}} dv\, v f_\mathrm{e}^\mathrm{sh}. \tag{A.13}$$

In this expression f_e^sh is the distribution function at the sheath entrance. Note that Γ_e^- is a positive quantity, therefore the corrected electron flux at the sheath entrance is lower than the value obtained with a perfectly truncated Maxwellian. Thus the potential drop required to ensure $\Gamma_e^{sh} = \Gamma_i^{sh}$ is smaller in absolute value. After some calculations we find the prediction for the potential drop in the sheath taking the re-emission into account

$$\Delta\phi_\mathrm{sh}^\mathrm{ref.} = \frac{T_\mathrm{e}^\mathrm{sh}}{e} \log\left(\sqrt{2\pi\frac{m_\mathrm{e}}{m_\mathrm{i}}M^2\left(1+\frac{T_\mathrm{i}^\mathrm{sh}}{T_\mathrm{e}^\mathrm{sh}}\right)}\left(1+\frac{\Gamma_\mathrm{e}^-}{\Gamma_\mathrm{i}^\mathrm{sh}}\right)\right). \tag{A.14}$$

A.4 On the definition of the entrance of the sheath and wall positions

In this section we detail the definition of the entrance of the sheath and wall positions in the reference simulation.

A.4.1 Definition of the wall position

When considering the interaction between a plasma along a given magnetic field line and a solid surface, a positive charge density builds up as the considered position

approaches the wall. The charge density is maximum at the wall position. This is the definition we adopt for the wall: it is located at the position of the maximum charge density. The resulting position is visible on fig. A.2. Note that this position corresponds approximately to the location where the wall mask $\mathcal{M}_w$ takes a non-zero value, i.e. where the sink of particles active in the wall region given in eq. (2.10) becomes active. Formally the wall position for the right half of the plasma is defined through the following implicit relationship

$$\rho_{\mathrm{c}}(x_{\mathrm{w}}) = \max_{x \geq L_x/2} \rho_{\mathrm{c}},$$

and a similar definition is adopted for the left half of the simulation box $x \in [0,\, L_x/2]$.

A.4.2 Definition of the sheath entrance

As shown in Chapter 3 Bohm criterion is invalid in the set of investigated kinetic simulations. As a consequence, one cannot use the equality $M = 1$ to define the entrance of the sheath. We derive in the following kinetic equivalents to Bohm criterion, before discussing their applicability in the kinetic simulations.

Kinetic equivalent to Bohm criterion

In this section we derive a kinetic constraint that has to be verified at the entrance of the sheath. It is a general constraint that is derived from Poisson equation, and that assumes that the wall is located at $x = 0$ while the quasineutral plasma horizon is relegated at $x \to +\infty$. Thus the entirety of the spatial domain is the sheath. The potential at $x \to +\infty$ is written ϕ_∞ and stands for the potential of the quasineutral plasma. We write a Poisson equation to relate the potential ϕ to the charge density ρ_c as

$$\varepsilon_0 \frac{\mathrm{d}^2\phi}{\mathrm{d}x^2} = -\rho_c.$$

Interestingly enough, the above equation can be seen as a Newton equation with effective mass ε_0, position ϕ, time x and applied force $-\rho_c$. In classical mechanics, starting from Newton's equation to find a conserved quantity one has to multiply both sides of the equation by the velocity, and then integrate with respect to time. In our case we multiply the above equation by $\mathrm{d}\phi/\mathrm{d}x$ and integrate with respect to the x variable between the sheath horizon and a general coordinate inside the sheath to get

$$\frac{1}{2}\varepsilon_0 \left(\frac{\mathrm{d}\phi}{\mathrm{d}x}\right)^2 - \frac{1}{2}\varepsilon_0 \left(\frac{\mathrm{d}\phi}{\mathrm{d}x}\right)^2 \Bigg|_{x_\infty} = -\int_{\phi_\infty}^{\phi} \rho_c \,\mathrm{d}\phi'.$$

Let us define $G(\phi) = -\int_{\phi_\infty}^{\phi} \rho_c \,\mathrm{d}\phi'$. At the sheath horizon the plasma potential is finite thus the derivative of ϕ vanishes there. By asymptotically expanding the G function in powers of $\phi - \phi_\infty$ at second order we arrive to

$$\frac{1}{2}\varepsilon_0 \left(\frac{\mathrm{d}\phi}{\mathrm{d}x}\right)^2 \approx G(\phi_\infty) + G'(\phi_\infty)\,(\phi - \phi_\infty) + \frac{1}{2}G''\,(\phi - \phi_\infty)^2$$

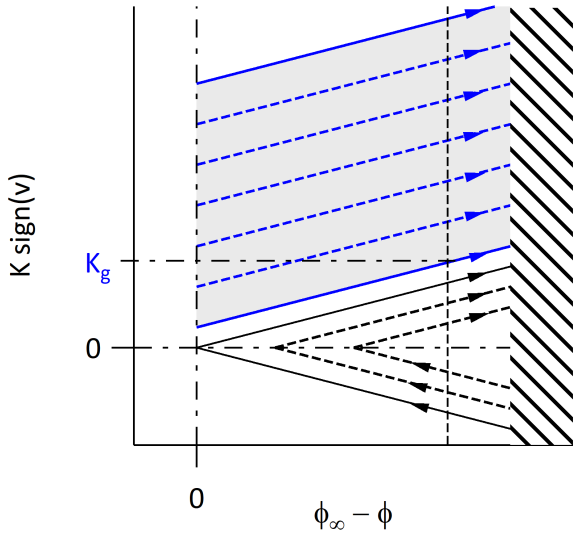

Figure A.3: Particles trajectories in phase space as a function of the (K, ϕ) set of variables. When no collisions nor source terms are found in the sheath, the negative potential drop that exists there creates a gap in the ion distribution function as going towards the wall.

From the definition of G we have $G(\phi_\infty) = 0$ and $G'(\phi_\infty) = -\rho_c(\phi_\infty) = 0$ since the plasma is quasineutral at the entrance of the sheath. Therefore a necessary condition at the entrance of the sheath is $G''(\phi_\infty) \geq 0$. This condition can be rewritten as

$$\left.\frac{\mathrm{d}n_i}{\mathrm{d}\phi}\right|_{\phi_\infty} \leq \left.\frac{\mathrm{d}n_e}{\mathrm{d}\phi}\right|_{\phi_\infty} \tag{A.15}$$

One can formally show that this condition is equivalent to the classical Bohm criterion $M \geq 1$ at the sheath entrance when assuming a vanishing heat flux closure, see [2]. Assuming that the electric potential decreases monotonically in the sheath, this criterion simply tells that the spatial derivative of the ion density has to be larger than the space derivative of the electron density. In other words, in order to have a decreasing electric potential, the ion density must depart from the electron density and the charge separation must be of positive sign.

Harrison-Tompson criterion

When the sheath can be considered as collisionless, we may rewrite eq. (A.15) as a criterion on the ion distribution function taken at the entrance of the sheath. This criterion has first been derived by Harrison and Thompson [145] and then revisited by Riemann [146]. Let us consider the ion distribution function at the entrance of the sheath $f_i(v, \phi_\infty)$. Assuming a perfectly absorbing wall and neglecting collisional

processes within the sheath region, then at the entrance of sheath ϕ_∞ there shall be no ion with negative velocities $f_i(v \leq 0, \phi_\infty) = 0$. By further assuming a negative electric potential gradient in the sheath region we have that the acceleration of ions must create a gap in the distribution function, see fig. A.3. Writing the energy conservation between the entrance of the sheath and at a general position ϕ within the sheath we have $e\phi + K = e\phi_\infty + K_\infty$, where we defined the ion kinetic energy $K = \frac{1}{2}m_i v^2$. Therefore a particle with a vanishing velocity at the entrance of the sheath will have a kinetic energy $K_g = \phi_\infty - \phi > 0$ at position ϕ, and therefore $f_i(K < K_g, \phi) = 0$. The ion density at position ϕ can therefore be found by integrating the distribution function as

$$n_i(\phi) = \int_{v_g}^{+\infty} dv\, f_i(v, \phi), \tag{A.16}$$

where $\frac{1}{2}m_i v_g^2 = K_g$. Using now the kinetic energy K as the integration variable the integral can be rewritten as

$$n_i(\phi) = \int_{K_g}^{+\infty} dK\, \frac{f_i(K, \phi)}{\sqrt{2m_i K}}. \tag{A.17}$$

Since the distribution function vanishes for all values of $K < K_g$ with $K_g > 0$ we can safely replace the lower integration bound by zero in the above integral. Futhermore, the distribution function is constant along the characteristics, therefore the equality $f_i(K, \phi) = f_i(K_\infty, \phi_\infty)$ for all values of the potential and kinetic energy such that $K + e\phi = K_\infty + e\phi_\infty$. Moreover the element of volume dK of phase space is conserved when the system evolves, therefore $f_i(K, \phi)dK = f_i(K_\infty, \phi_\infty)dK_\infty$. The ion density can therefore be expressed as

$$n_i(\phi) = \int_0^{+\infty} dK_\infty \frac{f_i(K_\infty, \phi_\infty)}{\sqrt{2m_i(K_\infty + \phi_\infty - \phi)}}. \tag{A.18}$$

Now differentiating the above expression with respect to the electric potential ϕ one gets

$$\frac{\mathrm{d}n_i}{\mathrm{d}\phi} = \int_0^{+\infty} dK_\infty \frac{f_i(K_\infty, \phi_\infty)}{\sqrt{8m_i}(K_\infty + \phi_\infty - \phi)^{3/2}}, \tag{A.19}$$

that is to say

$$\frac{\mathrm{d}n_i}{\mathrm{d}\phi} = \int_0^{+\infty} dv_\infty \frac{f_i(K_\infty, \phi_\infty)}{m_i v_\infty^2}. \tag{A.20}$$

Setting $\phi \to \phi_\infty$ and combining this last expression with the condition given in eq. (A.15), we arrive to a kinetic condition that has to be satisfied at the entrance of the sheath

$$\int_0^{+\infty} dv\, \frac{f_i(v, \phi_\infty)}{v^2} \leq \frac{\mathrm{d}n_e}{\mathrm{d}\phi}. \tag{A.21}$$

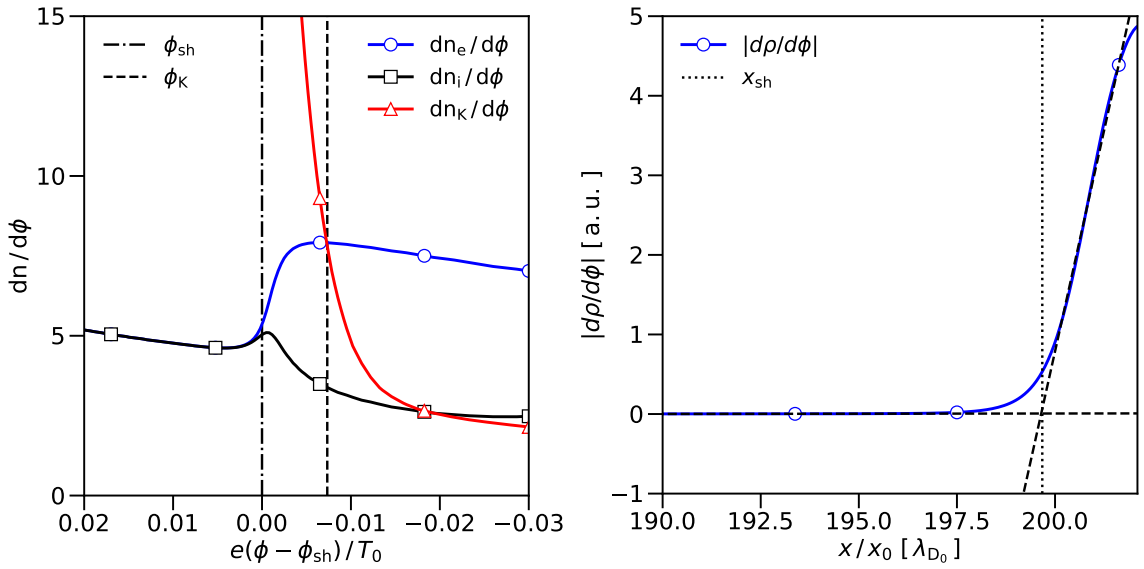

Figure A.4: Left: derivatives of electron and ion densities with respect to the potential. The derivative defined in eq. (A.22) is represented as well. Right: intersection of two linear fit of the $d\rho_c/d\phi$ quantity performed in the quasineutral plasma and the positively charged region. The intersection between the two fits is taken as the position of the entrance of the sheath.

Discussion on the definition of the sheath entrance

We found in eq. (A.15) and eq. (A.21) two criteria for defining the entrance of the sheath. On fig. A.4, left graph the derivative of the electron density with respect to the potential $dn_e/d\phi$ is plotted along with $dn_i/d\phi$, and a third quantity $dn_K/d\phi$ which is defined as the integral over the ion distribution function that appears in eq. (A.21), i.e.

$$\frac{\mathrm{d}n_K}{\mathrm{d}\phi} = \int_0^{+\infty} dv\, \frac{f_i(v,\phi)}{v^2}. \tag{A.22}$$

The x-axis shows decreasing values of the potential ϕ so that the wall is effectively located on the right side of the graph as usual. The ϕ_{sh} position corresponds to the entrance of the sheath that we define below. We first see that the inequality $dn_e/d\phi \geq dn_i/d\phi$ is satisfied everywhere on the graph—it is obvious for $\phi \leq \phi_{\mathrm{sh}}$, but also true for $\phi > \phi_{\mathrm{sh}}$ even though the $dn_e/d\phi$ and $dn_i/d\phi$ quantities seem to overlap on the graph. This is a consequence of the fact that there is no precise transition in the kinetic simulation between a quasineutral plasma and a positively charged sheath region. Rather, the plasma is slightly positively charged—a positive charge which is reminiscent of the presheath charge—and this positive charge grows as going towards the wall. Therefore, there is no precise position in the simulation box where the inequality $dn_e/d\phi \geq dn_i/d\phi$ becomes satisfied. This can be understood as a consequence of the fact that this inequality that should be verified at the entrance of the sheath has been derived assuming a quasineutral plasma relegated infinitely far away from the wall. This is obviously not the case in the simulation. Second, on fig. A.4 we see that

the $dn_K/d\phi$ and $dn_e/d\phi$ cross at a given position labeled ϕ_K. The Harrison-Tompson criterion of eq. (A.21) becomes satisfied for $\phi < \phi_K$. We however observe that the $dn_K/d\phi$ quantity diverges in the quasineutral plasma where $\phi > \phi_K$. This is a direct consequence of collisional processes taking place in the sheath. The derivation of the Harrison-Tompson criterion assumes that one cannot find ions with velocities $v \approx 0$ at the entrance of the sheath, so that the integral present in eq. (A.21) can be safely evaluated. In the investigated kinetic simulations this is clearly not the case, as collisional processes replenish the $v \approx 0$ part of the ion distribution function, see section 2.7.1, effectively leading to the divergence of $dn_K/d\phi$ in the quasineutral plasma. For this reason, we choose to not rely on the Harrison-Tompson criterion to define the entrance of the sheath. Instead, we define this position as the approximate location where the quantity $d\rho_c/d\phi$ becomes non negligible, or said differently where the condition given in eq. (A.15) becomes oversatisfied. To define such a position, one possible choice is to perform a linear fit of $d\rho_c/d\phi$ in the quasineutral plasma and positive charge region, and find the intersection of the two fits. This is done on fig. A.4, right graph. The intersection position x_{sh} of the two linear fits corresponds to a potential ϕ_{sh} that is marked on the same figure, left graph. We see that the x_{sh} position indeed corresponds to the approximate location where the kinetic criterion given in eq. (A.15) becomes satisfied.

B

Plasma-wall interaction: fluid and kinetic analysis

B.1 Bohm criterion with cold ions

This demonstration assumes monoenergetic ions, also called cold ions characterized by a vanishing temperature $T_i = 0$. In this framework the speed of sound waves in the plasma is simply $c_s^{\text{cold}} = \sqrt{T_e/m_i}$. Let us consider a magnetic field line in the Scrape-Off Layer of a tokamak. The magnetic field line impacts the divertor plate at both of its ends. We denote by the superscript $\star$ the quantity taken at the entrance of the sheath where quasineutrality breaks down. In the absence of any source or sinks of particles in the sheath region, the energy of the ions is a constant of motion. Thus the following quantity is conserved

$$E = \frac{1}{2} m_i u_{\parallel i}^2 + e\phi,$$

Where $u_{\parallel i}$ is the velocity of ions in the parallel direction. Writing the conservation of energy between the entrance of the sheath and a particular spatial location inside the sheath leads to

$$\frac{u_{\parallel i}}{u_{\parallel i}^\star} = \sqrt{1 + \frac{2e}{m_i u_{\parallel i}^{\star 2}} (\phi^\star - \phi)}.$$

We additionally assume that electrons are adiabatic, so that the electron density within the sheath is given by a Boltzmann response of the form

$$n_e = n_e^\star \exp\left(-e\delta\phi/T_e\right),$$

Where we introduced $\delta\phi = \phi^\star - \phi$. Then, combining the last two expressions in Poisson equation leads to

$$\begin{aligned} \partial_x^2 \delta\phi &= \frac{e}{\varepsilon_0} (n_i - n_e) \\ &= e n_i^\star \left(\left(1 + \frac{2e}{m_i u_{\parallel i}^{\star 2}} \delta\phi \right)^{-\frac{1}{2}} - e^{-e\delta\phi/T_e} \right). \end{aligned}$$

In the latter expression we used the fact that the plasma is quasineutral at sheath entrance—therefore $n_i^\star = n_e^\star = n^\star$—along with the conservation of the particle flux in the sheath which can be written as $n_i = n_i^\star u_{\parallel i}^\star / u_{\parallel i}$. Then near the entrance of the sheath we have $\delta\phi \to 0$ and by Taylor expanding the above expression we get

$$\begin{aligned}\partial_x^2 \delta\phi &\approx \frac{e n^\star}{\varepsilon_0}\left(\frac{e}{T_e} - \frac{e}{m_i u_{\parallel i}^\star}\right)\delta\phi \\ &\approx \frac{1}{\lambda_D^2}\left(1 - \frac{T_e}{m_i u_{\parallel i}^{\star 2}}\right)\delta\phi,\end{aligned}$$

with $\lambda_D = \sqrt{\varepsilon_0 T_e / e^2 n^\star}$ the Debye length. The previous equation is simply

$$\lambda_D^2\, \partial_x^2 \delta\phi - \left[1 - \left(\frac{c_s}{u_{\parallel i}^\star}\right)^2\right]\delta\phi = 0.$$

Therefore, in order to have non-oscillatory solutions for the potential within the sheath region, we find that the Bohm criterion must be satisfied at the sheath entrance as

$$u_{\parallel i}^\star \geq c_s.$$

This derivation has several limitations. First, there is nothing forbidding an oscillatory potential at the entrance of the sheath, as pointed out by Riemann [146]. With the above hypothesis, such a peculiar solution could in theory allow the ions for reaching the entrance of the sheath without a supersonic velocity. Second, ions are far from cold in tokamak plasma; in typical sheath-limiter Scrape-Off Layer plasma the ion temperature is of the order of 100 eV.

B.2 Bohm criterion from matching sheath and presheath regions

In this section we perform an asymptotic expansion of fluid quantities at the entrance of the sheath. By doing so, we find that the Bohm criterion must apply there, and we obtain asymptotic formulas giving the variation of fluid moments at the entrance of the sheath. We consider in the following that the sheath horizon is relegated at $x \to +\infty$, while the $x = 0$ coordinate defines the wall position. In the whole Scrape-Off Layer—quasineutral plasma and sheath region—the plasma momentum flux $\Pi = \Pi_{qn} - \eta T_e$ is a constant. Therefore, since the density difference $\eta = n_i - n_e$ increases at the entrance of the sheath, then this has to be compensated by an equal decrease of the Π_{qn} quantity. We will therefore expand Π_{qn} and ηT_e in powers of $1/x$ at the entrance of the sheath, and match the coefficients of the expansion. To make the computation easier to follow, we first rewrite the quasineutral momentum flux Π_{qn} as a function of the particle flux

and convective energy flux Γ and Q_c. Within the sheath region, these quantities stay constant: from the fluid eqs. (3.11) to (3.13) we see that the variation of these two terms come mainly from the source of particle that exists along the SOL magnetic field line. The typical scale of this source term is $L_\parallel$, the length of the magnetic field line, which is large as compared to the sheath size λ_D. We therefore identify Q_c and Γ with their values at the sheath horizon Q_c^∞ and Γ_∞. In all the following quantities evaluated at the sheath horizon are denoted by the ∞ subscript. The quasineutral momentum flux is therefore

$$\begin{aligned}\Pi_{qn} &= n_i T + n_i m_i u_i^2 \\ &= \frac{2Q_c^\infty}{3u_i} + \frac{2}{3}\Gamma_\infty m_i u_i,\end{aligned} \tag{B.1}$$

provided that $Q_c^\infty = Q_c = \Gamma(\frac{3}{2}T + \frac{1}{2}m_i u_i^2)$ where $T = T_i + T_e$. From the above expression we see that the decrease of the quasineutral momentum flux Π_{qn} at the sheath entrance is driven by the increase of the ion fluid velocity u_i. Expressing this last variable as

$$\frac{1}{u_i} = \frac{n_i}{\Gamma_\infty}, \tag{B.2}$$

we therefore seek an expansion of the ion density n_i. To do so, we use Poisson's equation to write

$$\frac{n_i}{n_\infty} = \frac{n_e}{n_\infty} - \frac{\varepsilon_0}{n_\infty e}\Delta\phi.$$

We further assume that electron temperature is constant and that electrons respond to the variations of the electric potential through a Boltzmann response $n_e = n_\infty \exp(e\delta\phi/T_e)$, where $\delta\phi = \phi - \phi_\infty < 0$. We can replace ϕ by its fluctuations $\delta\phi$ in the Laplacian of the above Poisson equation. We arrive to

$$\frac{n_i}{n_\infty} = 1 + F(\delta\phi) - G(\delta\phi), \tag{B.3}$$

with $F(\delta\phi) = e^{\delta\phi} - 1$ and $G(\delta\phi) = \Delta\delta\phi$. These two functions are useful for the present calculation since at the entrance of the sheath, $\delta\phi \to 0$ and $F(\delta\phi) \to 0$, $G(\delta\phi) \to 0$ as well. Combining eq. (B.3) and eq. (B.2) with the expression of the quasineutral momentum flux Π_{qn} given in eq. (B.1) we get

$$\Pi = \Pi_\infty = \Pi_Q\left(1 + F(\delta\phi) - G(\delta\phi)\right) + \Pi_\Gamma\left(1 + F(\delta\phi) - G(\delta\phi)\right) + \Pi_\eta G(\delta\phi),$$

where we introduced the notations $\Pi_Q = 2Q_c^\infty/(3u_\infty)$, $\Pi_\Gamma = 2/3 m_i \Gamma u_\infty$ and $\Pi_\eta = n_\infty T_e$. Expanding the above expression into powers of $F(\delta\phi) - G(\delta\phi)$ at the sheath horizon leads to

$$\begin{aligned}\Pi_\infty = &\Pi_Q\left(1 + F(\delta\phi) - G(\delta\phi)\right) + \Pi_\eta G(\delta\phi) \\ &+ \Pi_\Gamma\left(1 + F(\delta\phi) - G(\delta\phi)\right) \\ &+ \Pi_\Gamma\left(F(\delta\phi) - G(\delta\phi)\right)^2 + \dots\end{aligned} \tag{B.4}$$

Thus

$$\begin{aligned}\Pi_\infty = &\Pi_Q + \Pi_\Gamma + (\Pi_Q - \Pi_\Gamma)\, F(\delta\phi) \\ &- (\Pi_Q - \Pi_\Gamma - \Pi_\eta)\, G(\delta\phi) \\ &+ \Pi_\Gamma \left(F(\delta\phi)^2 - 2F(\delta\phi)G(\delta\phi) + G(\delta\phi)^2\right) + \dots \end{aligned} \tag{B.5}$$

We now expand $F(\delta\phi)$ in powers of $1/x$. Assuming the leading order term to be of order K we have

$$F(\delta\phi) = A_K^F \frac{1}{x^K} + \dots,$$

and therefore

$$G(\delta\phi) = K\,(K+1)\, A_K^F \frac{1}{x^{K+2}} + \dots$$

Therefore by injecting these expansions into eq. (B.5) we get two constraints regarding the coefficients of the zeroth-order and K-th order terms as

$$\Pi_\infty = \Pi_Q + \Pi_\Gamma, \quad 0 = \Pi_Q - \Pi_\Gamma \tag{B.6}$$

and the remaning of eq. (B.5) is at leading order

$$0 = \Pi_\eta G(\delta\phi) + \Pi_\Gamma F(\delta\phi)^2. \tag{B.7}$$

From the constraint $\Pi_Q = \Pi_\Gamma$ we get that $Q_c^\infty = m_i \Gamma_\infty u_\infty^2$ and therefore by replacing with the expression of the convective energy flux

$$3T_\infty = m_i u_\infty^2,$$

with T_∞ is the plasma temperature $T_e + T_i$ at the sheath horizon. This last equality expresses nothing else than the marginal Bohm criterion: the ion mean velocity must equal the sound speed—here computed in the framework of the vanishing heat flux closure—at the entrance of the sheath. From eq. (B.6) we also get the value of the plasma momentum flux $\Pi_\infty = 4 n_\infty T_\infty$. In eq. (B.7) we enforce that the solution of the expansion is not the trivial one $G = F = 0$. This leads to $K = 2$ and

$$6\Pi_\eta + \frac{1}{2}\Pi_\infty A_2^F = 0.$$

In other words

$$A_2^F = -3\frac{T_e}{T_\infty}.$$

B.3 Plasma sound waves with the polytropic closure

In this section we investigate the so-called polytropic closure, which assumes that the variations of pressure and density are linked through a polytropic coefficient γ_p as

$$\frac{dp}{p} = \gamma_p \frac{dn}{n}. \tag{B.8}$$

To find the value of the sound speed within the polytropic closure framework, let us use the equality above to rewrite the spatial derivative of the total pressure $\Pi = p + m_i n u^2$ as

$$\partial_x \Pi = \gamma_p \frac{p}{n} \partial_x n + m_i \partial_x (\Gamma^2 / n).$$

Then, we inject this expression into the equation of momentum conservation (3.19), and linearize the obtained expression in a similar fashion to what is done in section 3.4.2. After linearizing and stepping to Fourier space, the first two fluid equation describing the evolution of the fluctuating parts of the fluid moments are

$$-c\hat{n} + \hat{\Gamma} = 0 \tag{B.9}$$

$$-c\hat{\Gamma} + \gamma_p \frac{p_0}{m_i n_0} + 2\frac{\Gamma_0}{n_0}\hat{\Gamma} - \frac{\Gamma_0^2}{n_0^2}\hat{n} = 0, \tag{B.10}$$

where we used the hat notation $\hat{n}$ to denote the fourier transform of the fluctuation $\tilde{n}$. By combining these two equations and assuming that the density fluctuations are not vanishing $\hat{n} \neq 0$, we find the dispersion relation

$$(c - u_0)^2 - \gamma_p T_{eq}/m_i = 0,$$

and thus the sound speed in the polytropic framework is

$$c_s = \sqrt{\frac{\gamma_p \left(T_e + T_i\right)}{m_i}}. \tag{B.11}$$

For $\gamma_p = 3$ we retrieve the expression of the sound speed obtained in the framework of vanishing heat flux. Setting the polytropic coefficient to one, we have $dp/p = dn/n$ and thus the quantity $p/n = T$ is a constant. In this case we recover the expression of the sound speed obtained when assuming isothermality which is $c_s^{\text{iso.}} = \sqrt{(T_e + T_i)/m_i}$. For more details of the isothermal closure one can see [44]. On fig. B.1 the polytropic index is plotted, using the pressure and density from the kinetic simulation and eq. (B.8). We see that this index is not constant in the plasma, hence questioning the validity of the polytropic closure.

B.4 Plasma sound waves with higher moment closure

In this section we investigate the velocity of sound waves in the plasma by closing the system of fluid equation by setting to zero the moment of the distribution function of arbitrary order ℓ. Let us define two moments M_ℓ^s and N_ℓ^s of order ℓ for species s as

$$M_\ell^s = \int_{-\infty}^{+\infty} dv\, v^\ell f_s \tag{B.12}$$

$$N_\ell^s = \int_{-\infty}^{+\infty} dv\, (v - u_s)^\ell f_a. \tag{B.13}$$

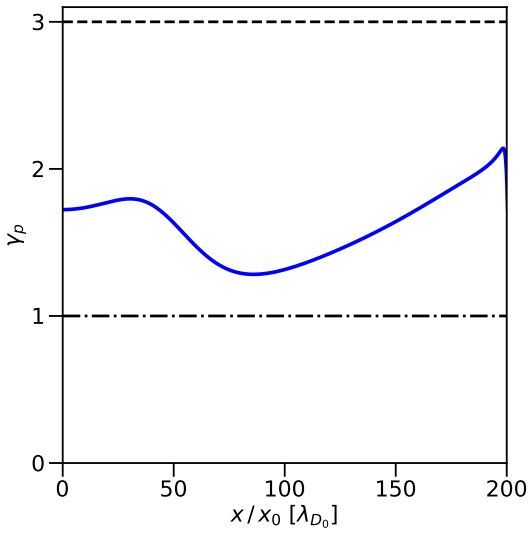

Figure B.1: Polytropic index in the right half of the simulation box. $x = 0$ corresponds to the position of the stagnation point and $x \approx 200$ is the sheath entrance position. The dashed line corresponds to the polytropic index computed when assuming a Maxwellian plasma, while the dashdotted line corresponds to the isothermal plasma.

As we do not possess any insight on the meaning of M_ℓ^s or N_ℓ^s when $\ell > 3$, the only reasonable closure is to assume that the fluid moment of order ℓ vanishes as $N_l^s = 0$. We ignore in the following the effect of the parallel electric field and work in a quasineutral plasma, and work in a region of the magnetic field line where there is no source nor sink, thus $\mathcal{S}(f_s) = 0$ in the Vlasov equation eq. (2.6). We neglect any collisional effect as well, thus $\mathcal{C}(f_s) = 0$. With this set of hypothesis the conservation equation of order ℓ—that is to say the conservation equation obtained by multiplying the Vlasov equation by v^ℓ in integrating against v—simply reads

$$\partial_t M_\ell^s + \partial_x M_{\ell+1}^s = 0.$$

We then define the combined moments M_ℓ and N_ℓ as

$$M_\ell = \frac{m_i}{m_e + m_i} M_\ell^i + \frac{m_e}{m_e + m_i} M_\ell^e \tag{B.14}$$

$$N_\ell = \frac{m_i}{m_e + m_i} N_\ell^i + \frac{m_e}{m_e + m_i} N_\ell^e, \tag{B.15}$$

and by summing the two conservation equations for M_ℓ^i and M_ℓ^e we obtain the conservation equation for the combined moment

$$\partial_t M_\ell + \partial_x M_{\ell+1} = 0. \tag{B.16}$$

From eq. (B.13) the following equality holds

$$N_\ell = \sum_{j=0}^{\ell} \binom{j}{\ell} (-u)^j M_{\ell-j},$$

where we used the fact that for a quasineutral plasma without any ionization source the fluid velocity for both species must be equal, thus $u_i = u_e = u$, see section 3.4.2. Then we expand all moments between a mean and fluctuating part as $M_\ell = M_\ell^0 + \tilde{M}_\ell$, $N_\ell = N_\ell^0 + \tilde{N}_\ell$, $u = u_0 + \tilde{u}$ etc. As in the previou sections the 0 subscript or superscript denotes the mean part of the considered fluid moment and the tilde is the fluctuating part. We assume again that the fluctuations are small an linearize the $(-u)^j M_{\ell-j}$ term in the sum above to get

$$\tilde{N}_\ell = \sum_{j=0}^{\ell} \binom{j}{\ell} (-u_0)^j \, \tilde{M}_{\ell-j} + \sum_{j=1}^{\ell} j \binom{j}{\ell} (-u_0)^{j-1} \, M_{\ell-j}^0 \tilde{u},$$

By using the fact that $j\binom{j}{\ell} = \ell\binom{j-1}{\ell-1}$ and by rearranging the rightmost sum in the last equality we find

$$\tilde{N}_\ell = \sum_{j=0}^{\ell} \binom{j}{\ell} (-u_0)^j \, \tilde{M}_{\ell-j} + \ell N_{\ell-1}^0 \tilde{u},$$

Now let us Fourier transform in space and time the fluctuations and denote by the hat the Fourier transform of the corresponding fluctuating quantity, for instance $\hat{M}_\ell$ is the Fourier transform of $\tilde{M}_\ell$. In Fourier space the conservation equation of order ℓ written in eq. (B.16) is simply $c\hat{M}_\ell = \hat{M}_{\ell+1}$, with the phase velocity $c = \omega/k$. By using this property in the above equation the Fourier transform $\hat{N}_\ell$ can be recast as

$$\hat{N}_\ell = (c - u_0)^\ell \hat{M}_0 - \ell N_{\ell-1}^0 \hat{u}.$$

To find the expression of $\hat{u}$ we write this last equality for $\ell = 1$ and we get

$$\hat{u} = \frac{1}{n_0}(c - u_0)\hat{M}_0,$$

since $N_0^0 = n_0$ and $N_1 = \hat{N}_1 = 0$ from the definitions of eqs. (B.12) to (B.13). Thus by using this expression for $\hat{u}$

$$\hat{N}_\ell = (c - u_0)^\ell \hat{M}_0 - \ell \frac{N_{\ell-1}^0}{n_0}(c - u_0). \tag{B.17}$$

If we choose to close the fluid hierarchy at order ℓ by imposing $\hat{N}_\ell = 0$ we obtain the dispersion relation

$$(c - u_0)^{\ell-1} - \ell \frac{N_{\ell-1}^0}{n_0} = 0. \tag{B.18}$$

Thus the speed of sound obtained in the framework of the high order closure is

$$c_s^\ell = \left(\ell \frac{N_{\ell-1}}{M_0} \right)^{1/(\ell-1)}, \tag{B.19}$$

where we assumed $N_{\ell-1} \approx N_{\ell-1}^0$.

B.5 Prediction for the sheath heat transmission factors

We recall in the following a derivation of the sheath heat transmission factor for both electrons and ions species. This derivation is well known in the literature and can be found for instance in [23, p. 92]. The ion and electron sheath heat transmission coefficients are defined respectively as

$$Q_e = \gamma_e \Gamma T_e$$
$$Q_i = \gamma_i \Gamma T_i,$$

where the energy flux Q_s for species s is defined in eq. (3.4) as $Q_s = \int dv\, \frac{1}{2} m_s v^3 f_s$. Note that electron and ion particle fluxes are assumed to be equal at the plasma boundary, i.e. $\Gamma_i = \Gamma_e = \Gamma$. In the following of this section all quantities are taken at the entrance of the sheath. As explained in appendix A.3, we use the conservation of energy for electrons to define the critical velocity v_c. This quantity represents the minimal velocity an electron must have at sheath entrance to overcome the repulsive electric field of the sheath and hit the wall and is written as

$$v_\mathrm{c} = \sqrt{\frac{-2e\Delta\phi_\mathrm{sh}}{m_e}}, \tag{B.20}$$

where $\Delta\phi_\mathrm{sh}$ is the negative electric potential drop in the sheath region. We consider the wall as perfectly absorbent. At the entrance of the sheath electron velocities satisfy $v \geq -v_\mathrm{c}$. It follows that the electron distribution function at sheath entrance is necessarily truncated for velocities $v \leq -v_\mathrm{c}$. Further assuming a Maxwellian shape leads to

$$f_e(x_\mathrm{sh}, v) = n_e \sqrt{\frac{m_e}{2\pi T_e}}\, e^{-\frac{m_e v^2}{2T_e}}\, \mathrm{H}(v + v_\mathrm{c}),$$

where $\mathrm{H}(v + v_\mathrm{c})$ is the Heaviside function that equals zero for $v \leq -v_\mathrm{c}$ and one otherwise. n_e is the electron density at sheath entrance. After some straightforward calculations and using the definition of v_c given by eq. (B.20) we find the energy flux of this distribution function

$$Q_e = T_e \Gamma_e - \ e\Delta\phi_\mathrm{sh}\, n_e e^{\frac{e\Delta\phi_\mathrm{sh}}{T_e}} \sqrt{\frac{T_e}{2\pi m_e}} \tag{B.21}$$

Using the expression of the electron flux at sheath entrance given in appendix A.3.1 we rewrite this energy flux as

$$Q_e = T_e \Gamma_e - e\Delta\phi_\mathrm{sh} \Gamma_e.$$

And therefore the electron heat transmission factor is in the case of a Deuterium plasma

$$\gamma_e = 1 - \frac{e\Delta\phi_\mathrm{sh}}{T_e} \approx 4.$$

The last equality is justified by the prediction of the potential drop in the sheath given in eq. (A.12) that yields for a Deuterium plasma $-e\Delta\phi_{\rm sh}/T_e \approx 3$. In the case of reduced ion-to-electron mass ratio, for $m_i/m_e = 400$ we find $\gamma_e \approx 2.7$. One should keep in mind that the expression obtained for the electron energy flux in appendix B.5 is only valid in a simplified 1D geometry. When going towards more realistic 3D models one has to also take into account the component of the velocity vector perpendicular to the magnetic field along with its parallel component. This leads to a factor 2 in front of the $T_e\Gamma_e$ term of appendix B.5. Consequently, the prediction for the electron heat transmission factor is modified so that $\gamma_e^{\rm 3D} \approx 5$ for a Deuterium plasma.

Regarding the ion distribution function at sheath entrance, we consider a Maxwellian of temperature T_i with a mean velocity $u_i = Mc_{\rm s}$, where $c_{\rm s}$ is the plasma sound wave velocity. Without any loss of generality the sound speed can be defined as $m_i c_{\rm s} = \chi T$, with $T = T_e + T_i$ and χ is a coefficient that depends on the chosen closure of the fluid hierarchy, Chapter (3). For instance, with an isothermal closure $T_e = T_i$ and we find $\chi = 1$. The energy flux associated to such a distribution function reads

$$Q_i = \Gamma T_i \left(\frac{3}{2} + \frac{\chi M^2}{2} \left(\frac{T_e}{T_i} + 1 \right) \right). \tag{B.22}$$

Therefore with we find the ion heat transmission factor at the sheath entrance

$$\gamma_i = \frac{3}{2} + \frac{\chi M^2}{2} \left(\frac{T_e}{T_i} + 1 \right).$$

Assuming an isothermal closure of the fluid hierarchy we further get $\chi = 1$, and $T_e = T_i$, thus $\gamma_i^{\rm isoth.} = 5/2$. In this case the total sheath heat transmission factor is

$$\gamma = \gamma_i^{\rm isoth.} + \gamma_e \approx 5.2.$$

Lastly, the same remark as the one formulated for the electrons applies here. The value found above for the ion sheath heat transmission factor depends on the dimensionality of the model. When going towards a 3D model, the ion energy flux expression is modified as

$$Q_i^{\rm 3D} = \Gamma T_i \left(\frac{5}{2} + \frac{\chi M^2}{2} \left(\frac{T_e}{T_i} + 1 \right) \right).$$

Thus with the isothermal closure one would get $\gamma_i^{\rm 3D,isoth.} = 3.5$ and then $\gamma^{\rm 3D} \approx 7.5$ for a Deuterium plasma, and $\gamma^{\rm 3D} \approx 6.2$ for $m_i/m_e = 400$.

C

A subgrid model for gyrokinetic treatment of plasma-wall interaction



C.1 Alternative models for gyrokinetic plasma-wall interaction

In this section we present a few alternative models to the one already presented in section 5.5 for modeling the effect of the sheath on the quasineutral plasma. In the following sections we focus mainly on solutions for achieving the reflection of slow electrons at the plasma boundary since it is the most difficult property of plasma-wall interaction to include within the gyrokinetic framework. In the first model presented in appendix C.1.1, the equation describing the time evolution of the parallel velocity of gyrocenters is penalized to account for the influence of the sheath on the plasma. In the second model presented in appendix C.1.2 the (r, θ) advection is further split into a radial advection and a poloidal advection to make the computation of the intersection of the electron characteristics with the limiter easier as compared to a (r, θ) advection. These first two models were implemented in the Gysela code but failed to describe properly the plasma-wall interaction dynamic we wanted to retrieve. We detail the reasons why in the corresponding sections. Lastly, in appendix C.1.3 we present an adaptation of the flux-averaged sheath model described in section 5.5 in the case were field-aligned interpolation is used.

C.1.1 Penalization of parallel force balance equation

In this section we describe how to achieve a reflection of electrons on the surface of the limiter geometry of the Gysela code by using a pure penalization method. Let us first remark that even though the influence of the limiter on the ion dynamics can be modeled by a sink of particles, momentum and energy added to the right-hand-side of eq. (5.5), achieving the required reflection of slow electrons by means of a similar source term seems quite arduous. Indeed, a source term accounts for either an absorption or an injection of particles, momentum and/or energy. A reflection is fundamentally different as it involves a modification of the trajectory of a given particle. Therefore, if one wants to model the reflection of electrons by means of penalization the technique employed must take a different form than source term. We describe below only the reflection of electrons. A possible solution for this is to penalize the equation expressing

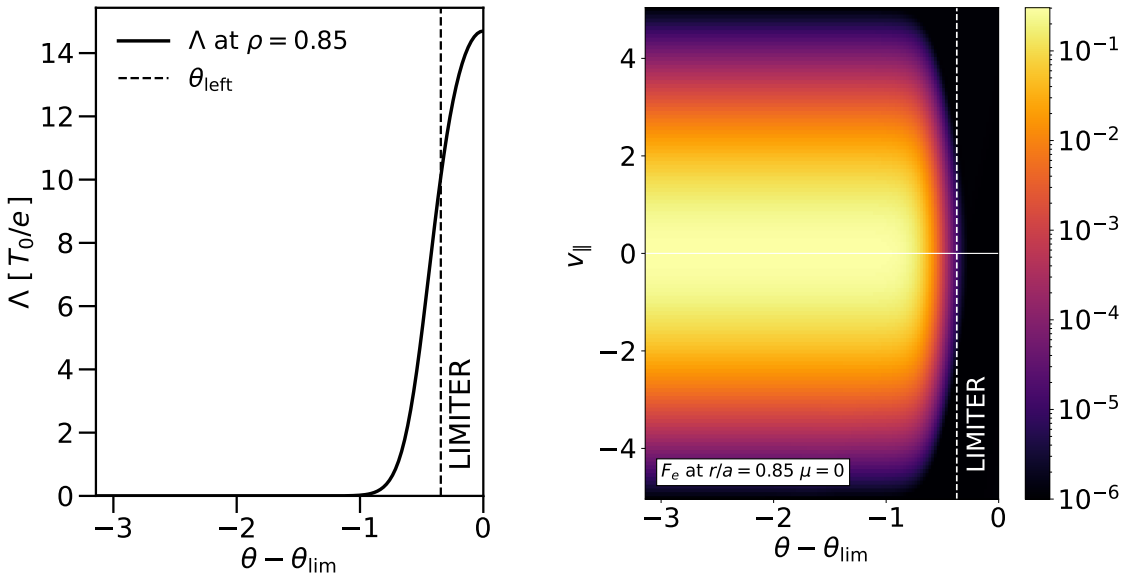

Figure C.1: Left: limiter potential defined in eq. (C.2) in the high field side of the magnetic configuration for a given value of the radius r. The values $\Lambda_0 = 20$ and $d_\Lambda = 15$ have been used to define the limiter potential Λ. Right: electron distribution function at the same radius for $\mu = 0$, as a function of the poloidal angle and parallel velocity, at a time t comparable to the transit time for electrons from one side of the limiter to the other, see below. The simulation has been performed with parameters comparable to the reference simulation presented in section 5.7. The quasineutrality equation is not solved in this case, thus $\phi = 0$ in the simulation domain. The θ_{left} angle corresponds to the poloidal angle at which the magnetic field line located at $r/r_{\max} = 0.85$ intercepts the limiter in the high field side part of the plasma.

the time evolution of the parallel velocity of gyrocenters, so as to reflect electrons on the surface of the limiter. Such a penalized equation can be written as

$$m_s \frac{dv_\parallel}{dt} = -\mu \mathbf{b}^*_\parallel \cdot \nabla B - e_s \mathbf{b}^*_\parallel \cdot \nabla \bar{\phi} + \frac{m_s v_\parallel}{B} \mathbf{v}_E \cdot \nabla B + e_s \mathbf{b}^*_\parallel \cdot \nabla \Lambda, \tag{C.1}$$

where the penalization has been introduced through the $e_s \mathbf{b}^*_\parallel \cdot \nabla \Lambda$ term. The potential Λ is taken as function that is constant in time and depends on space such that its gradient $\nabla \Lambda$ vanishes in the plasma and increases monotonically in the limiter. This ensures that the $e_s \mathbf{b}^*_\parallel \cdot \nabla \Lambda$ term effectively accounts for a repulsive force that tends to repel electrons in the plasma. Note that since this term depends on the charge of the considered species e_s, the effect on the ion species is the opposite: it accelerates ions towards the limiter, similarly to the potential drop that exists within the sheath. Various expressions for the limiter potential Λ are possible, one of them is

$$\Lambda(r, \theta) = \frac{1}{2} \Lambda_0 \left(1 + \tanh \left(\frac{z - r_{\text{sep}}}{d_\Lambda} \right) \right), \tag{C.2}$$

where $z = r\cos(\theta - \theta_{\text{lim}})$ is the distance to the limiter surface, θ_{lim} is the limiter angle and r_{sep} is the radius of the separatrix. The d_Λ parameter sets the steepness of the limiter potential, whereas the Λ_0 parameter sets the maximum value of this potential. On fig. C.1, left graph the value of the limiter potential Λ is plotted as a function of the angle $\theta - \theta_{\text{lim}}$ in the vicinity of the limiter, for a radial position such that $\rho = r/r_{\max} = 0.85$. The interval $\theta - \theta_{\text{lim}} \in [-\pi, 0]$ stands for the high field side of the magnetic configuration. On the same figure, right graph a slice of the distribution function at the same radial position is plotted, for $\mu = 0$, as a function of the poloidal angle $\theta - \theta_{\text{lim}} \in [-\pi, 0]$ and of the parallel velocity $v_\parallel$, i.e. the quantity $F_e(\rho = 0.85, \theta, v_\parallel, \mu = 0, t)$ has been represented. The time t at which the electron distribution function is plotted is taken as approximately equal to the transit time of electrons from one side of the limiter to the other, i.e. $t \approx L_\parallel / v_{T_0 e}$, with $L_\parallel = 2\pi q R$, $v_{T_0 e} = \sqrt{T_0/m_e}$ and the radius $R = R_0 + r$ with $r/r_{\max} = 0.85$. We see that electrons with positive parallel velocities directed towards the limiter are reflected back towards the plasma, as required. The penalization given in eq. (C.1) does not seem to give a satisfactory method for modeling the sheath physics in the gyrokinetic framework, for the following reasons:

1. When the sheath is resolved, the reflection of slow electrons happens within the sheath, on a spatial scale comparable to the Debye length, which is very small as compared to the typical discretization of a gyrokinetic simulation. The procedure described in the current section translates into a reflection of slow electrons on a scale typically given by the d_Λ parameter given in eq. (C.2), thus $d_\Lambda \gg \lambda_D$. It is not clear if and how this reflection on a large scale will influence the global dynamic of the plasma;

2. In order to perform a reflection of slow electron on a smaller scale, one has to reduce the d_Λ parameter. Consequently, the timestep of the simulation has to be reduced to resolve the reflection. This can be very costly numerically. In the limit $d_\Lambda \to 0$ the reflection happens on a scale infinitely thin as compared to ρ_i. This situation is given by the subgrid sheath model presented in section 5.3, thus this last model appears more relevant;

3. The reflection of electrons on a typical distance d_Λ translates into a drop of the electron density in the vicinity of the limiter: the more electrons have been reflected by the potential, the less remaining electrons there is, thus the density is lower at the surface of the limiter as compared to a location far from the limiter. It is not clear how to deal safely with such a decrease of the electron density without introducing large charge densities within the quasineutrality equation, effectively creating spurious $E \times B$ transport in the vicinity of the limiter.

C.1.2 Splitting of poloidal advection

Another possible description for the reflection of slow electrons at the plasma boundary consists in rewriting the (r, θ) advection step within the splitting presented in

section 5.4.2 to further separate it between a radial and a poloidal advection. More precisely, one would replace the step n°3 *advection along the* (r, θ) *direction on* Δt by the following substeps

1. Advection along the poloidal θ direction on $\Delta t/2$;
2. Advection along the radial direction on Δt;
3. Advection along the poloidal θ direction on $\Delta t/2$.

This sub-splitting scheme has the advantage of making the calculation of the intersection point between a characteristics that intercepts the limiter and the limiter surface very easy. Indeed, in substeps 1. and 3. the foot of the characteristics is computed through

$$\theta = \theta^* + u_\theta \Delta t/2,$$

where u_θ is the poloidal velocity computed using eq. (5.32). In this case the condition for assessing whether or not the characteristics intercepts the limiter is simply $\theta \notin \left[\theta^\ell_{\text{lim}}, \theta^r_{\text{lim}}\right]$, and $\theta^* \in \left[\theta^\ell_{\text{lim}}, \theta^r_{\text{lim}}\right]$. The angles θ^ℓ_{lim} and θ^r_{lim} correspond to the left and right limiter angles at the considered radial position, see eqs. (C.14) and (C.15). Similarly, during the radial advection substep 2. above, the characteristics foot is computed using $r = r^* + u_r \Delta t/2$, where the radial velocity is computed using eq. (5.31). In this case a condition for intercepting the limiter surface can be as simple as $r < r_{\text{sep}}$ and $r^* > r_{\text{sep}}$. Even though the computation of the interception between characteristics and the plasma boundary can be expressed easily within the framework of the sub-splitting described in the present section, rewriting the entire (r, θ) only for account for this reflection on the material boundary is excessive. Besides, it is not so sure that the performance gained from computing the interception with the limiter in the sub-splitting framework will be compensated by the increased computational power required to replace a single 2D (r, θ) advection by two one-dimensional advections.

C.1.3 Reflection of electrons in field-aligned coordinates

We discuss here some aspects concerning the adaptation of the flux-averaged sheath model described in section 5.5 to *field-aligned interpolation*. More precisely we only focus on the implementation of the reflection of slow electrons within a field-aligned interpolation scheme. Other parts of the flux-averaged sheath model, such as the absorption of ions and the computation of fluxes on the material boundary surface, can be treated similarly as described in section 5.5.
The field-aligned interpolation technique is based on the observation that in tokamak plasmas, gradients are typically much smaller in the direction parallel to magnetic field lines as compared to gradients in directions perpendicular to field lines. When applied to the semi-Lagrangian framework, the technique consists in coupling a one-dimensional advection along field lines with a two-dimensional advection in the poloidal plane. Field-aligned interpolation allow for a reduction of computational cost with

an equivalent precision as compared to a non field-aligned simulation. A thorough description of the field-aligned technique along with details concerning its justification and implementation in the GYSELA code can be found in [142]. Within the field-aligned framework, the usual splitting scheme used in GYSELA—described in section 5.4.2—is rewritten as

1. Advection on a magnetic flux surface (θ, φ) on $\Delta t/2$ following the advection equation

$$\partial_f F_s + \left[\left(v_\parallel \mathbf{b}^*_\parallel + \mathbf{v}_D\right) \cdot \nabla\theta\right] \partial_\theta F_s + \left[\left(v_\parallel \mathbf{b}^*_\parallel + \mathbf{v}_D + \mathbf{v}_E\right) \cdot \nabla\varphi\right] \partial_\varphi F_s = 0.$$

   During this advection step the interpolations required to update the distribution function are performed along magnetic field lines.

2. Advection on the (r, θ) plane on Δt following the advection equation

$$\partial_f F_s + \left[\left(\mathbf{v}_D + \mathbf{v}_E\right) \cdot \nabla r\right] \partial_r F_s + \left[\mathbf{v}_E \cdot \nabla\theta\right] \partial_\theta F_s = 0.$$

3. Same as Step 1.

We did not include the advection along $v_\parallel$ in this description since it remains unchanged between a field-aligned and non-field-aligned advection scheme. When trying to include the flux-averaged sheath model in the advection scheme above, one must first notice that electrons may cross the limiter surface as a result of either step 1 or step 2, i.e. as a result of their parallel or transverse motion. Note that this fact is true regardless of the chosen advection scheme: electrons cross the surface of the limiter due to their motion in the poloidal plane (r, θ). The poloidal motion of electrons is the result of the projection in the (r, θ) plane of their transverse drift velocities, and of their parallel velocity. As explained in appendix C.2, a consequence of this is that when using non-field-aligned interpolation, flipping the parallel velocity to compute the reflection of a given characteristics on the limiter surface does not ensure that the foot of the reflected characteristics is located outside of the limiter volume. When using field-aligned coordinates, this issue becomes even more obvious. Indeed, when performing the advection described in step 1, the reflection of characteristics on the surface of the limiter can be performed similarly as described in section 5.5 and appendix C.2. Namely, the intersection of each characteristics with the limiter surface can be computed, and the reflected characteristics foot can be obtained by flipping the sign of the parallel velocity. As stated above, this does not ensure that the reflected foot ends up outside of the limiter. When looking at step 2 above, given that the parallel velocity does not contribute to the advection equation, one cannot reflect the characteristics on the limiter surface by flipping the sign of the parallel velocity. It is therefore unclear how to deal with electrons crossing the limiter surface during this advection step. Two solutions could however be thought of to deal with such electrons:

1. The first one consists in absorbing electrons that cross the limiter surface due to their transverse drifts. It is this solution that is implicitly chosen in the penalized sheath model implemented in the GYSELA framework, see appendix C.2. This solution is consistent with the fact that when considering the physics at play within the Debye sheath, one observes that slow electrons come back to the plasma with a parallel velocity in the opposite direction as compared to their motion prior to entering the sheath. One therefore concludes that the action of the subgrid sheath on slow electrons should be only to flip the sign of their parallel velocity when the trajectory of these electrons intercept the limiter.
2. The other solution consists in reflecting slow electrons on the surface of the limiter by flipping the sign of their total velocity $v_\parallel \mathbf{b}^*_\parallel + \mathbf{v}_\perp$. This solution is coherent with the observation that the sheath physics results in the plasma remaining quasineutral on scales larger than the Debye length, therefore the most important feature of a subgrid sheath model should be that this quasineutrality property remains verified at all times. Thus, no electrons should be lost in the limiter volume as a result of their transverse motion.

Given that the subgrid sheath model has not been implemented in the field-aligned version of GYSELA it is not clear if considering one solution or the other has a noticeable impact on the plasma dynamics. Let us however remark that when considering a non-field-aligned interpolation, the situation where slow electron cross the surface of the limiter and flipping the sign of their parallel velocity does not result in the foot of the reflected characteristics being located in the plasma seldom happens. One could therefore hope that the same observation applies to field-aligned interpolation, i.e. that the choice of one or the other solution mentioned above does not have a noticeable impact on the plasma dynamics.

C.2 Numerical implementation of the penalized sheath model

In this section we detail some aspects of the implementation of the penalized sheath model described in section 5.5 within the GYSELA framework. We focus on the following aspects this sheath model: the reflection of slow electrons, absorption of fast electrons, and the computation of the flux-averaged cutoff velocity v_c. The other elements of the model such as the penalization sink acting on ions and the modification of the quasineutrality equation do not cause any difficulty in the implementation.

C.2.1 Reflection of slow electrons

The reflection of slow electrons is performed within the (r, θ) advection step of the splitting scheme. Let us introduce a uniform discretization of the poloidal plane $r_i = i\Delta r$ and $\theta_j = j\Delta\theta$ with i, j integers and Δr, $\Delta\theta$ are the discretization step in the radial and poloidal direction. During this advection step the $(\varphi, \mu, v_\parallel)$ coordinates of the particles remain constant—except for electrons that are reflected on the limiter

surface and whose parallel velocity is reversed, see below. Let use fix a $(\varphi, \mu, v_\parallel)$ triplet such that the generalized parallel velocity[1] $\bar{v}_\parallel = \varepsilon v_\parallel$ is lower than the cutoff velocity v_c, thus electrons with this parallel velocity are reflected on the surface of the limiter.

Intersection with the limiter surface

To perform the advection, for each point (r_i, θ_j) of the mesh used to discretize the poloidal plane, one must first find the foot of the characteristics using the equation of motion given in eq. (5.30). In the GYSELA code these equations of motion are approximated using a first order Newton method such that

$$r_i = r_i^* + u_r \Delta t \tag{C.3}$$
$$\theta_j = \theta_j^* + u_\theta \Delta t \tag{C.4}$$

where (r_i^*, θ_j^*) is the foot of the characteristics, and the velocities u_r, u_θ are

$$u_r = \left(v_\parallel \mathbf{b}_\parallel^* + \mathbf{v}_E + \mathbf{v}_D\right) \cdot \nabla r \tag{C.5}$$
$$u_\theta = \left(v_\parallel \mathbf{b}_\parallel^* + \mathbf{v}_E + \mathbf{v}_D\right) \cdot \nabla \theta \tag{C.6}$$

The equation that defines the surface of the limiter is $r\cos(\theta - \theta_{\text{lim}}) = r_{\text{sep}}$. The intersection between the characteristics and the surface of the limiter is therefore given by

$$(r_i - u_i \alpha \Delta t)\cos\left(\theta_j - u_\theta \alpha \Delta t - \theta_{\text{lim}}\right) = r_{\text{sep}}. \tag{C.7}$$

with α a parameter in the $[0, 1]$ interval. Equation (C.7) can be solved for the value of α, using a Newton method for instance. Let us remark that finding the value of α for every characteristics that intercepts the limiter represents a great deal of computation, slowing down the (r, θ) advection significantly compared to a situation without limiter. When the value of the α parameter is know, the foot of the characteristics reflected on the surface of the limiter can be computed using

$$r_i = r_i^{**} + \tilde{u}_r(1 - \alpha)\Delta t + u_r \alpha \Delta t, \tag{C.8}$$
$$\theta_i = \theta_i^{**} + \tilde{u}_\theta(1 - \alpha)\Delta t + u_\theta \alpha \Delta t, \tag{C.9}$$

with

$$\tilde{u}_r = \left(-v_\parallel \mathbf{b}_\parallel^* + \mathbf{v}_E + \mathbf{v}_D\right) \cdot \nabla r, \tag{C.10}$$
$$\tilde{u}_\theta = \left(-v_\parallel \mathbf{b}_\parallel^* + \mathbf{v}_E + \mathbf{v}_D\right) \cdot \nabla \theta. \tag{C.11}$$

In these last two expressions for $\tilde{u}_r$ and $\tilde{u}_\theta$ all quantities that depend on $v_\parallel$ should be evaluated at $-v_\parallel$. Note that the reflection of the characteristics presented in eqs. (C.8) and (C.9) does not ensure that the reflected foot $(r_i^{**}, \theta_j^{**})$ is located in the plasma and not in the limiter volume. In particular, electrons with $v_\parallel \approx 0$ may cross the limiter

[1] See section 5.3.2 for the definition of the generalized parallel velocity

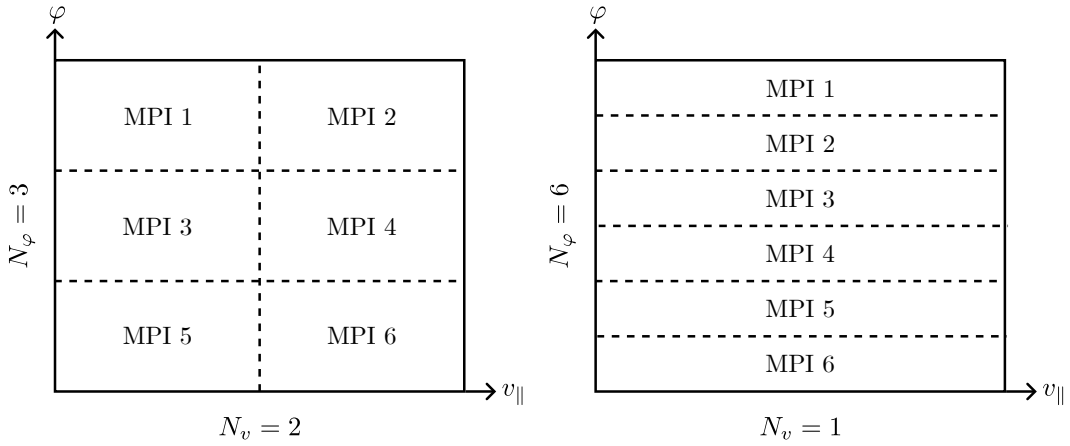

Figure C.2: Parallelization schemes in the $(v_\parallel, \varphi)$ directions in the usual GYSELA scheme on the left, and with the scheme adapted for the reflection on the limiter surface. A number $N_v = 2$ and $N_\varphi = 3$ chunks have been used as an example.

surface due to their transverse drifts. For these electrons, flipping the sign of their parallel velocity does not lead to a reflection of the trajectory on the limiter surface: $v_\parallel \approx 0$ implies that the trajectory of such electrons is at first order independent of their parallel velocity. Let us however remark that this case seldom happens in the GYSELA code. This is a good indication that (i) for most electrons the projection of the parallel dynamic in the (r, θ) plane is dominant as compared to the transverse dynamics, and (ii) electron with $v_\parallel \approx 0$ somehow do not cross the limiter surface so that the situation where the reflected foot $(r_i^{**}, \theta_j^{**})$ is located in the limiter volume almost never happens. When this situation happens nonetheless, we consider that the electron should be removed from the simulation. The electron distribution function at time $t + \Delta t$ for trajectories that intercepts the limiter can therefore be computed as

$$F_e(r_i, \theta_j, \varphi, v_\parallel, \mu, t + \Delta t) = F_e(r_i^{**}, \theta_j^{**}, \varphi, -v_\parallel, \mu, t). \tag{C.12}$$

From this last expression we see that updating the value of the electron distribution function at time $t+\Delta t$ for a given parallel velocity involves interpolating the distribution function at time t for the opposite parallel velocity $-v_\parallel$: the point $(r_i^{**}, \theta_j^{**})$ does not indeed lie in general on a mesh point. Thus, in order to perform this interpolation a given MPI processor must contain information about the distribution function at both velocities $v_\parallel$ and $-v_\parallel$. This requirement involves modifying the parallelization scheme of the GYSELA code. Given that the whole 5D distribution function cannot be stored in memory on a single processor, different chunks of the distribution function are stored on different MPI processes, each of them running in parallel. The usual parallelization scheme of the GYSELA code is such that during the (r, θ) advection each MPI process has access to the information of the distribution function on the whole (r, θ) poloidal plane, but to a limited chunk of the distribution function in the $(\varphi, v_\parallel)$ direction[2]. To

[2]The distribution function is also parallelized in the μ direction, each MPI process having access to a single value of μ during the poloidal advection process. The choice of the parallelization along

make sure that a single MPI process can have access to the value of the distribution function at both $v_\parallel$ and $-v_\parallel$ values of the parallel velocity, the simplest way consists in modifying the parallelization scheme such that each MPI process has access to the whole $v_\parallel$ direction. To ensure that this reorganization does not lead to a saturation of the memory, with the updated parallelization scheme each MPI process has access to a smaller chunk of the distribution function in the φ direction. The regular and adapted parallelization schemes are represented on fig. C.2. Let us denote by N_v and N_φ the number of processes used to discretize the $v_\parallel$ and φ direction in the usual parallelization scheme, and N'_v and N'_φ the number of processes to discretize these two directions in the adapted parallelization scheme. The new parallelization scheme is therefore defined by

$$N'_v = 1 \quad \text{and} \quad N'_\varphi = N_v N_\varphi. \tag{C.13}$$

So that the amount of memory required to store each chunk of the distribution function on each MPI process remains the same with the usual and adapted parallelization schemes.

Boundary condition for the interpolation step

Given the foot of the characteristics $(r_i^{**}, \theta_j^{**})$ does not lie on a point of the mesh used to discretize the poloidal plane, an interpolation is required to evaluate eq. (C.12). Within the GYSELAcode, this step is performed using two-dimensional *b-splines* of third degree. More specifically, for each point $(\varphi, v_\parallel, \mu)$ the distribution function $F_e(r, \theta, \varphi, v_\parallel, \mu, t)$ is projected on a basis composed of these two dimensional b-splines, so that eq. (C.12) involves a two-dimensional interpolation in the (r, θ) poloidal plane. To ensure that this interpolation step is performed correctly, the choice of the boundary condition imposed on the limiter surface at $r\cos(\theta - \theta_{\text{lim}})$ to build the spline representation of F_e is critical. Indeed, the feet of characteristics that are located very close to the limiter surface are influenced by the value given to F_e inside the limiter. Given that electrons are either absorbed in the limiter or reflected at its surface, there are no electrons in the limiter volume. The value of the electron distribution function in the limiter volume is therefore undefined. We take advantage of this observation to impose a boundary condition on the electron distribution function within the limiter volume. The problem consists therefore in finding values for F_e in the limiter volume such that the poloidal advection of electrons in the plasma is carried accurately, and in particular such that the reflection of slow electrons on the limiter surface is carried correctly. In the following we take a given position of the mesh used to discretize the radial direction.

the μ direction does not however impact the discussion given in the present section.

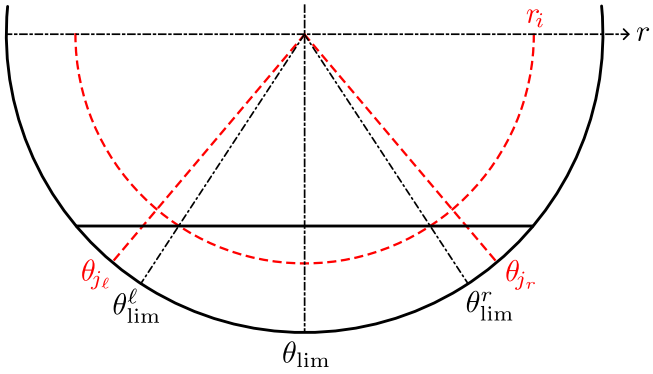

Figure C.3: Given a radial position r_i on the radial mesh, the $\theta^\ell_{\rm lim}$ and $\theta^r_{\rm lim}$ angle define the intersection of the field line at r_i with the limiter. The θ_{j_ℓ} and θ_{j_r} are the angles of the discretization of the poloidal direction that are the closest to the limiter surface.

We denote by r_i this position. We then define the following poloidal positions

$$\theta^\ell_{\rm lim} = \theta_{\rm lim} - \operatorname{acos}\left(\frac{r_{\rm sep}}{r_i}\right)[2\pi]\,, \tag{C.14}$$

$$\theta^r_{\rm lim} = \theta_{\rm lim} + \operatorname{acos}\left(\frac{r_{\rm sep}}{r_i}\right)[2\pi]\,. \tag{C.15}$$

With $\theta_{\rm lim}$ the limiter angle. The $\theta^\ell_{\rm lim}$ and $\theta^r_{\rm lim}$ quantities correspond to the angles at which a field line at radius r_i intercepts the limiter, see fig. C.3. In general $\theta^\ell_{\rm lim}$ and $\theta^r_{\rm lim}$ do not lie in points of the mesh used to discretize the poloidal direction. From these angles we define the following integers

$$j_\ell = \left\lceil \frac{\theta^\ell_{\rm lim}}{\Delta\theta} \right\rceil \quad \text{and} \quad j_r = \left\lfloor \frac{\theta^r_{\rm lim}}{\Delta\theta} \right\rfloor, \tag{C.16}$$

where $\Delta\theta$ is the discretization step in the poloidal direction. The integers defined in eq. (C.16) are such that the angle θ_{j_ℓ} (respectively θ_{j_r}) is the point of the mesh closest to the limiter surface and $\theta_{j_\ell} \leq \theta^\ell_{\rm lim}$ (respectively $\theta_{j_r} \geq \theta^r_{\rm lim}$). Note that all angles $\theta^\ell_{\rm lim}$, $\theta^r_{\rm lim}$, θ_{j_ℓ} and θ_{j_ℓ} depend on the considered radial position r_i. For more clarity all these angles are represented on fig. C.3. Let us define in a similar fashion

$$j_{\rm lim} = \left\lfloor \frac{\theta_{\rm lim}}{\Delta\theta} \right\rfloor. \tag{C.17}$$

In order to design the boundary condition of the interpolation step in the limiter volume, let us consider that electrons move mainly due to their parallel velocities in the poloidal plane, and thus neglect the influence of the $\mathbf{v}_E$ and $\mathbf{v}_D$ drifts. In the simulations presented in section 5.7 these two drifts are taken into account to evolve the electron distribution function, but the boundary condition designed by neglecting these two drifts is still effective enough. We use fig. C.4 to highlight the boundary

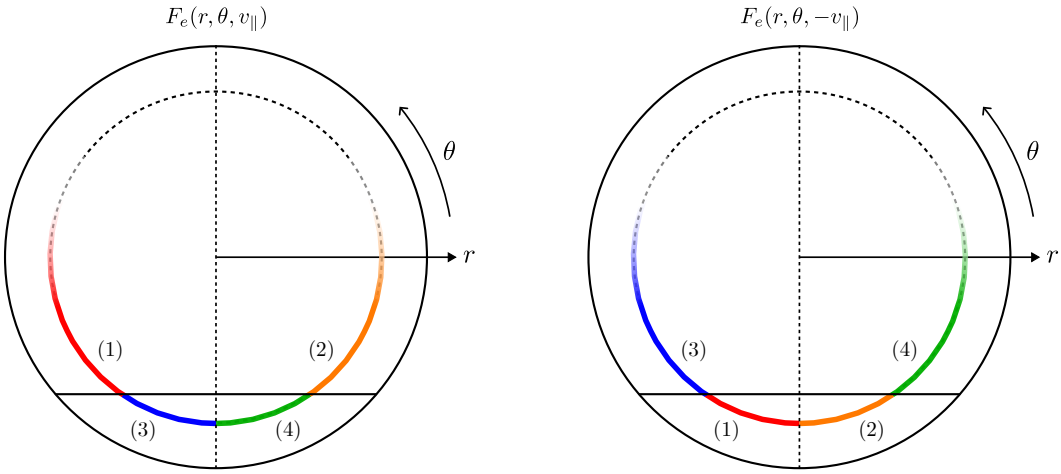

Figure C.4: Boundary condition used in the limiter volume to ensure a smooth reflection procedure of slow electrons. The different colors stand for different values taken by the electron distribution function at different locations.

condition in the limiter. The left graph represents to the electron distribution in the poloidal plane for a given parallel velocity $v_\parallel$, while the right graph stands for the distribution at the opposite parallel velocity $-v_\parallel$. The colors stand for values taken by the distribution function at the considered radius. For the sake of clarity the only part of the electron distribution function shown is its values at a given radius r_i, and close to the limiter. Let us assume a positive value for $v_\parallel$ and for the safety factor q. Neglecting the drifts the electrons travel in the clockwise direction on the left graph, and counter clockwise on the right graph. Thus, the red part of the distribution function marked (1) on the left graph tend to be reflected in the region marked by (3) on the right graph. The boundary condition imposed in the limiter for this reflection process is therefore

$$\begin{aligned} &F_e(r_i,\theta_j \in [\theta_{j_\ell+1},\, \theta_{j_{\rm lim}}]\,,\varphi,v_\parallel,\mu,t) = F_e(r_i,\theta_{j'},\varphi,-v_\parallel,\mu,t) \\ &\text{with} \quad j' = 2j_\ell - j - 1 \end{aligned} \tag{C.18}$$

With a similar line of reasoning one obtains the boundary condition in the limiter volume for the "right" part of the limiter

$$\begin{aligned} &F_e(r_i,\theta_j \in]\theta_{j_{\rm lim}},\, \theta_{j_r-1},]\,,\varphi,v_\parallel,\mu,t) = F_e(r_i,\theta_{j'},\varphi,-v_\parallel,\mu,t) \\ &\text{with} \quad j' = 2j_r - j + 1 \end{aligned} \tag{C.19}$$

To summarize, the part of the distribution function denoted by (1) on the left graph is reversed in the θ direction and copied to the (1) location on the right graph. Same for the part number (2), on the left that gets reversed and copied to the part (2) on the right. The part (3) on the right gets reversed and copied to the part (3) on the left, the part (4) on the right gets reversed and copied to the part (4) on the left. This boundary condition is applied within the limiter volume for all values of r_i such that field lines at r_i intercept the limiter. The boundary condition is valid as well for the

first resolved radius associated with a field line that intercepts the limiter, given that there are at least two poloidal points located inside the limiter.

C.2.2 Absorption of fast electrons

We consider the characteristics of fast electrons $\bar{v}_\parallel > v_c$ that intercept the limiter, i.e. such that (r_i^*, θ_j^*) in eqs. (C.3) and (C.4) is located in the material boundary region. These fast electrons should be absorbed in the limiter volume, hence the electron distribution function is updated following

$$F_e(r_i, \theta_j, \varphi, v_\parallel, \mu, t + \Delta t) = f_{\text{lim}}(r_i, \theta_j, \varphi, \mu), \tag{C.20}$$

where f_{lim} is a coefficient close to zero (typically we take the value of the distribution function at initial time and at the maximum resolved parallel velocity, i.e.

$$f_{\text{lim}}(r, \theta, \varphi, \mu) = F_e(r, \theta, \varphi, v_{\parallel\text{max}}, \mu) \ll 1, \tag{C.21}$$

where $v_{\parallel\text{max}}$ is the highest parallel velocity resolved by the code. For fast electrons it is still necessary to perform an interpolation step given that not all fast electrons intercept the limiter. The value of the electron distribution function in the limiter volume must therefore be prescribed, in a similar fashion as when performing the advection for slow electrons, see the previous section. In the present case the boundary condition for electrons is simply

$$F_e(r_i, \theta_j \in [\theta_{j_\ell+1}, \theta_{j_r-1}], \varphi, v_\parallel, \mu, t) = f_{\text{lim}}(r_i, \theta_j, \varphi, \mu). \tag{C.22}$$

The absorption of fast electrons above a cutoff velocity v_c creates a discontinuity in the electron distribution function in the vicinity of the limiter. This discontinuity leads to interpolation error when performing interpolation steps later on during the execution of the code. An illustration of this problem is depicted on fig. C.5. The figure show the electron distribution function as a function of the parallel velocity, at a given radial position in the Scrape-Off Layer, at a given poloidal angle close to the left part of the limiter $\theta \approx \theta_{\text{lim}}^\ell$, and at given toroidal and magnetic moment coordinates. The left graph correspond to the absorption of fast electrons with the procedure described above. We see that some oscillations appeared in the distribution function. They are due to the interpolation of the discontinuity at $v_\parallel = v_c$. To avoid this effect, we implemented a smoothing procedure that acts on the part of the electron distribution function corresponding to fast electrons that have been absorbed in the limiter—i.e. the part $v_\parallel > v_c$ on fig. C.5. Let us introduce a discretization $v_k = k\Delta v$ of the parallel direction, with k an integer and Δv the discretization step. The smoothing procedure reads as follows

$$\begin{aligned} F_e(r_i, \theta_j, v_k > v_c, \varphi, v_\parallel, \mu, t + \Delta t) =& (1 - \alpha) F_e(r_i, \theta_j, v_{k-1}, \varphi, v_\parallel, \mu, t + \Delta t) \\ &+ \alpha f_{\text{lim}}(r_i, \theta_j, \varphi, \mu), \end{aligned} \tag{C.23}$$

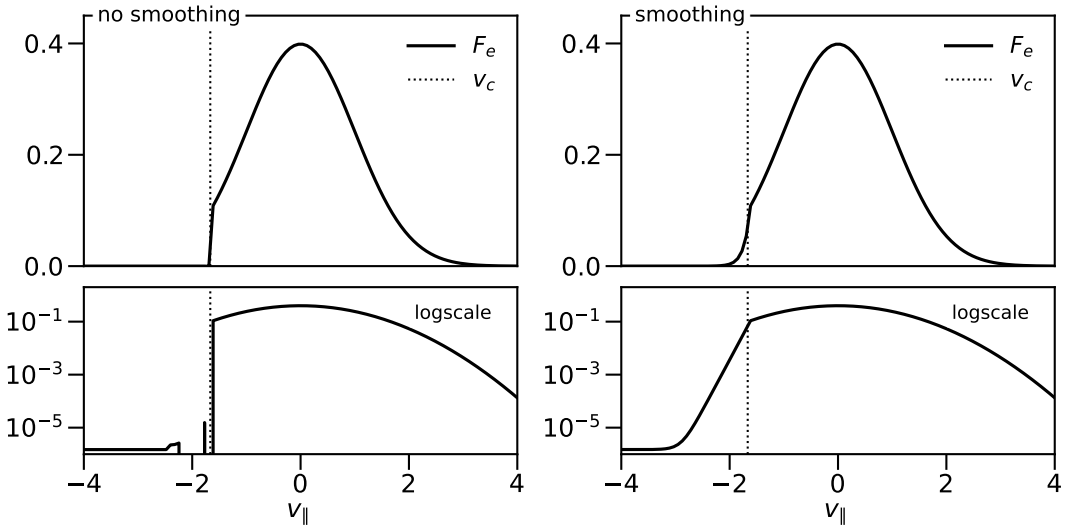

Figure C.5: Electron distribution function in the vicinity of the limiter for $\mu = 0$, as a function of the parallel velocity. Positive parallel velocities correspond to electrons going towards the limiter. A fixed cutoff velocity v_c has been used in the simulation. A single iteration of the GYSELA code has been performed to get these results. The left graph shows the distribution function when no smoothing procedure is applied to fast electrons, in both normal and log scales (top and bottom graphs). The right graphs shows the simulation result with the smoothing procedure described by eq. (C.23).

where α is a coefficient, we typically take $\alpha = 0.5$. This smoothing procedure is applied for all (r_i, θ_j) coordinates such that the foot of the characteristics (r_i^*, θ_j^*) is inside the limiter. It does not therefore affect the rest of the distribution function, for instance the parts corresponding to slow electrons reflected on the limiter surface, or electrons that do not intercept the limiter during the poloidal advection step. An example of the resulting smoothened distribution function can be viewed on fig. C.5, right graph. We see that the smoothing reduces greatly the oscillations of the interpolation observed in the non-smoothened case. Several other smoothening processes other than the one given in eq. (C.23) could have been envisaged. In particular, the most correct one from physical considerations would consist in applying collisions to the distribution function. This would result in an effective smoothening of the electron distribution function in the parallel direction. This process has requires however to apply the collision operator at every timestep, right after the poloidal advection. In general, to save computational time, the collision operator is applied every few timesteps.

C.2.3 Particle fluxes on the limiter surface

We describe hereafter how to perform a spatial integration on the surface of the limiter. This step is required to compute the limiter fluxes expressed in eqs. (5.16) and (5.18). We work with the limiter geometry depicted on fig. C.6. The unit vector $\mathbf{u}$ is associated

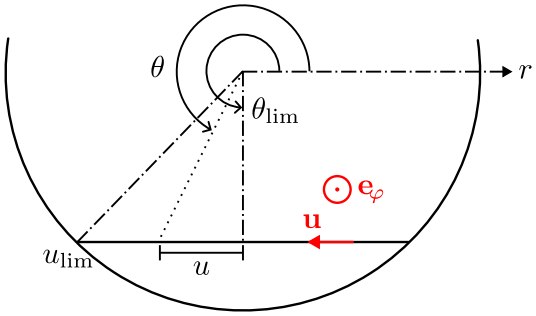

Figure C.6: Limiter geometry and adapted coordinates.

to the coordinate

$$u = -r \sin\left(\theta - \theta_{\text{lim}}\right) \tag{C.24}$$

The u coordinate stands for the horizontal distance to the limiter center in the direction marked by $\mathbf{u}$. The (u, φ) coordinate system can be used to express the integral on the surface of the limiter as

$$\int_{S_{\text{lim}}} d^2S = \int_{-u_{\text{lim}}}^{u_{\text{lim}}} du \int_0^{2\pi} R d\varphi, \tag{C.25}$$

with u_{lim} the width of the limiter which is $u_{\text{lim}} = \sqrt{a^2 - r_{\text{sep}}^2}$. The Jacobian in the above integral is simply $R = R_0 + r\cos\theta$, see below for a demonstration of this statement. With this expression of the integral on the surface of the limiter the fluxes given in eqs. (5.16) and (5.18) can be computed easily. First, one introduces a discretization of the $\mathbf{u}$ direction that we denote by (u_i). The distribution function can then be interpolated at each of the u_i points, and then the integration along the u_i direction can be performed with a trapezoid quadrature method for instance.

Jacobian on the limiter surface We denote by $\{x^i\}$ the (r, θ, φ) coordinates, with $i \in [0, 2]$ and $x^0 = r$, $x^1 = \theta$, $x^2 = \varphi$. The covariant metric tensor in the $\{x^i\}$ system of coordinates is

$$g = \begin{pmatrix} 1 & 0 & 0 \\ 0 & r^2 & 0 \\ 0 & 0 & R^2 \end{pmatrix}. \tag{C.26}$$

The components of this covariant metric tensor are denoted by g_{ij}. We want to express the jacobian in the system of coordinates (u, φ) that is adapted to the limiter surface. We denote by $\{y^i\}$ this limiter surface coordinate system. The next step is to write a parametrization of the $\{x^i\}$ coordinates on the limiter surface by the $\{y^i\}$ coordinates. This gives

$$r = \sqrt{r_{\text{sep}}^2 + u^2} \tag{C.27}$$

$$\theta = \theta_{\text{lim}} + \tan^{-1}\left(\frac{u}{r_{\text{sep}}}\right) \tag{C.28}$$

The elements g^{lim}_{pq} of the metric tensor g^{lim} in the $\{y^i\}$ system of coordinates are then given by

$$g^{\mathrm{lim}}_{pq} = \sum_{i,j} g_{ij} \frac{\partial x^i}{\partial y^p} \frac{\partial x^j}{\partial y^q}. \tag{C.29}$$

This yields

$$g^{\mathrm{lim}} = \begin{pmatrix} 1 & 0 \\ 0 & R^2 \end{pmatrix}. \tag{C.30}$$

Therefore the infinitesimal surface element of the limiter is simply $d^2S = R dud\varphi$.

C.3 Electron response in the quasineutrality equation

We present here different possible expressions for the electron density n_e that appears in the quasineutrality eq. (5.15). We first recall the expression of the quasineutrality equation here that is

$$-\nabla_\perp \cdot \left(\frac{m_i \bar{n}_{\mathrm{eq},i}}{e Z_i B^2} \nabla_\perp \phi \right) = Z_i \int d^3v \, \mathcal{J} F_i - n_e, \tag{C.31}$$

The equilibrium ion density $\bar{n}_{\mathrm{eq},i}$ is defined in eq. (5.14).

Fully kinetic electron model

The simplest way of expressing the electron density n_e consists in considering a fully kinetic electron response, that is to say integrating the electron distribution function over velocity space to get for any position $\mathbf{x}$

$$n_e(\mathbf{x}, t) = \int_0^{+\infty} d\mu \int_{-\infty}^{+\infty} dv_\parallel \, J_v F_e(\mathbf{x}, v_\parallel, \mu, t), \tag{C.32}$$

where $J_v = 2\pi B^*_\parallel / m_e$ is the velocity Jacobian for the electron species.

Adiabatic electron model

A second option for computing the electron density consists in assuming an adiabatic electron response. When electrons are adiabatic, they respond infinitely fast to any fluctuation of the electric potential following a Boltzmann response of the form

$$n_e = \langle n_e \rangle_{\mathrm{FS}} \exp\left(\frac{e\left(\phi - \langle \phi \rangle_{\mathrm{FS}}\right)}{\langle T_e \rangle_{\mathrm{FS}}} \right). \tag{C.33}$$

where the $\langle \cdot \rangle_{\mathrm{FS}}$ notation stands for the average of the considered quantity on a given magnetic field surface. Note that quite surprisingly when computing the flux-surface

average of the left and right-hand-side of eq. (C.33) one does not find that the flux-surface average of n_e is $\langle n_e \rangle_{\rm FS}$. This inconsistency disappears when expanding the Boltzmann response as done in the following. By considering small fluctuations of the electric field $e\left|\phi - \langle\phi\rangle_{\rm FS}\right| / \langle T_e \rangle_{\rm FS} \ll 1$ one may Taylor-expand eq. (C.33) around $\phi - \langle\phi\rangle_{\rm FS} \approx 0$ as

$$n_e \approx \langle n_e \rangle_{\rm FS} \left(1 + \frac{e\left(\phi - \langle\phi\rangle_{\rm FS}\right)}{\langle T_e \rangle_{\rm FS}}\right),$$

With this last expression one recovers as expected that the flux-surface average of n_e is $\langle n_e \rangle_{\rm FS}$. The quasineutrality equation can then be rewritten as

$$-\nabla_\perp \cdot \left(\frac{m_i \bar{n}_{{\rm eq},i}}{e Z_i B^2} \nabla_\perp \phi\right) + \langle n_e \rangle_{\rm FS} \frac{e\left(\phi - \langle\phi\rangle_{\rm FS}\right)}{\langle T_e \rangle_{\rm FS}} = Z_i \int d^3v\, \mathcal{J} F_i - \langle n_e \rangle_{\rm FS}\,. \tag{C.34}$$

Trapped kinetic electron model

A third model for computing the electron density is the so-called trapped-kinetic model. It assumes an adiabatic response for passing electrons—passing in the sense that they have enough kinetic energy to explore both high and low field side of the magnetic configuration. The electrons that are trapped by the mirror force $-\mu \mathbf{b} \cdot \nabla B$, see section 1.2.2 that we call trapped electrons are treated as kinetic. More precisely, the trapped kinetic model consists in separating the electron density as $n_e = n_e^{\rm trap.} + n_e^{\rm pass.}$. The trapped electron density is computed as

$$n_e^{\rm trap.}(r,\theta,\varphi) = \int_0^{+\infty} d\mu \int_{-v_\parallel^\pm}^{v_\parallel^\pm} dv_\parallel 2\pi B_\parallel^* F_e(r,\theta,\varphi,\mu,v_\parallel). \tag{C.35}$$

Where the cutoff velocity $v_\parallel^\pm$ separates trapped electrons for which $\left|v_\parallel\right| \leq v_\parallel^\pm$ and passing electrons for which $\left|v_\parallel\right| > v_\parallel^\pm$. This cutoff velocity is expressed as

$$v_\parallel^\pm = \sqrt{\frac{2\mu}{m_e}\left(B_{\rm max}(r) - B(r,\theta)\right)}, \tag{C.36}$$

where

$$B_{\rm max}(r) = \max_{\theta \in [0,2\pi]} B(r,\theta).$$

The passing electron density is computed assuming an adiabatic response that can be written as

$$n_e^{\rm pass.} = \langle n_e^{\rm pass.} \rangle_{\rm FS} \left(1 - \frac{e\left(\phi - \langle\phi\rangle_{\rm FS}\right)}{\langle T_e \rangle_{\rm FS}}\right),$$

with $\langle n_e^{\rm pass.} \rangle_{\rm FS} = \langle n_e - n_e^{\rm trap.} \rangle_{\rm FS}$. Thus the quasineutrality equation can be rewritten in the trapped kinetic electron framework as

$$-\nabla_\perp \cdot \left(\frac{m_i \bar{n}_{{\rm eq},i}}{e Z_i B^2} \nabla_\perp \phi\right) + \langle n_e^{\rm pass.} \rangle_{\rm FS} \frac{e(\phi - \langle\phi\rangle_{\rm FS})}{\langle T_e \rangle_{\rm FS}} = Z_i \int d^3v\, \mathcal{J} F_i - n_e^{\rm trap.} - \langle n_e^{\rm pass.} \rangle_{\rm FS}\,. \tag{C.37}$$